Sticking and deposition of atoms in the sub-monolayer range

Arindam Jana

▶ **To cite this version:**

Arindam Jana. Sticking and deposition of atoms in the sub-monolayer range. Other. Université de Lorraine, 2014. English. NNT : 2014LORR0074 . tel-01750797

HAL Id: tel-01750797
https://hal.univ-lorraine.fr/tel-01750797v1

Submitted on 29 Mar 2018

HAL is a multi-disciplinary open access archive for the deposit and dissemination of scientific research documents, whether they are published or not. The documents may come from teaching and research institutions in France or abroad, or from public or private research centers.

L'archive ouverte pluridisciplinaire **HAL**, est destinée au dépôt et à la diffusion de documents scientifiques de niveau recherche, publiés ou non, émanant des établissements d'enseignement et de recherche français ou étrangers, des laboratoires publics ou privés.

AVERTISSEMENT

Ce document est le fruit d'un long travail approuvé par le jury de soutenance et mis à disposition de l'ensemble de la communauté universitaire élargie.

Il est soumis à la propriété intellectuelle de l'auteur. Ceci implique une obligation de citation et de référencement lors de l'utilisation de ce document.

D'autre part, toute contrefaçon, plagiat, reproduction illicite encourt une poursuite pénale.

Contact : ddoc-theses-contact@univ-lorraine.fr

LIENS

Code de la Propriété Intellectuelle. articles L 122. 4
Code de la Propriété Intellectuelle. articles L 335.2- L 335.10
http://www.cfcopies.com/V2/leg/leg_droi.php
http://www.culture.gouv.fr/culture/infos-pratiques/droits/protection.htm

UNIVERSITE DE LORRAINE

Ecole Doctorale : **É**nergie **M**écanique **Ma**tériaux

Institut **J**ean **L**amour
Département Chimie et Physique des Solides et des Surfaces

THESE
résumé étendu

présentée le 18/07/2014

pour obtenir le grade de Docteur de l'Université de Lorraine
Spécialité Science des matériaux

par

Arindam JANA

Collage et adhérence de particules dans le domaine de la sous-monocouche

Jury

Président :	**Mohammed BELMAHI**	Professeur, Université de Lorraine
Rapporteurs:	**Laurent HOUSSIAU**	Professeur, Université de Namur, Belgique.
	Pascal BRAULT	Directeur de recherches CNRS, GREMI, Université d'Orléans.
Examinateur:	**Kai NORDLUND**	Professeur, Université de Helsinki, Finlande.
Encadrants :	**Gérard HENRION**	Directeur de recherches CNRS, IJL, Université de Lorraine
	Patrick PHILIPP	Chargé de projets, CRP Gabriel Lippmann, Belvaux, Luxembourg.

Sommaire

Préambule

Le manuscrit original étant écrit en langue anglaise, nous présentons ici un résumé étendu du travail de thèse. Le manuscrit original figure en seconde partie de ce document.

Nous tenons à remercier ici le Président de l'Université de Lorraine et la Vice-Présidente du Conseil Scientifique de l'Université de Lorraine de nous avoir permis de déroger à la règle de rédaction en langue française.

1 Introduction - Contexte

Dans le domaine des traitements de surface, le collage et le réarrangement d'atomes dans le domaine de la sous-monocouche revêtent une importance essentielle, la première monocouche définissant les propriétés de l'interface entre la couche déposée et le substrat.

La maitrise de cette interface est primordiale, en particulier pour la réalisation reproductible de dépôts possédant une bonne adhérence. Ceci représente en effet un enjeu industriel dans de nombreux secteurs d'activité tels que la micro-électronique, le photovoltaïque, la protection contre l'usure ou la corrosion, les barrières thermiques, la décoration, etc.

Ces aspects sont au cœur du projet "Sub-ML" qui constitue la cadre de cette thèse et dont les objectifs principaux visent à une meilleure compréhension des mécanismes de dépôt, et plus particulièrement du comportement de particules arrivant sur une surface de silicium. Dans ce cadre, l'objectif de cette thèse - partie intégrante de Sub-ML - est d'étudier le collage et le réarrangement d'atomes et l'effet de certains paramètres sur le processus de dépôt et les propriétés d'interface.

Pour atteindre ces objectifs, nous avons utilisé une approche multidisciplinaire combinant simulations numériques (dynamique moléculaire, calculs DFT), études expérimentales (dépôts PVD) et caractérisation des matériaux (SIMS).

Les études de collage et de réorganisation de surface ont concernées trois espèces particulières, carbone, titane et tungstène, présentant un intérêt particulier pour la croissance de couches minces de type carbure. Le dépôt de carbone a été étudié uniquement de manière numérique ; titane et tungstène ont fait l'objet d'une étude numérique et expérimentale.

Le mémoire complet comporte 150 pages et 158 références bibliographiques. Il est structuré en cinq chapitres. Le premier dresse un état de l'art des différentes techniques utilisées avec une attention particulière aux travaux publiés concernant l'interaction d'un atome-projectile avec une surface cible.

Les détails des techniques expérimentales et numériques mises en œuvre au cours de cette thèse font l'objet du second chapitre. Les trois chapitres suivants traitent du collage d'atomes sur une surface de silicium : carbone (chap. 3), titane (chap. 4) et tungstène (chap. 5).

Une conclusion générale et des perspectives à ce travail complètent le mémoire.

2 Aspects expérimentaux et numériques

Les études expérimentales ont été réalisées grâce à l'instrument storing matter qui permet de réaliser des dépôts par pulvérisation cathodique sur un collecteur en silicium. Ce collecteur est ensuite analyser par SIMS. L'analyse se fait ainsi en connaissant parfaitement le support du dépôt et donc en s'affranchissant des effets de matrice. Toutefois, les particules pulvérisées de la cible arrivent sur le collecteur avec une distribution d'angles d'incidence (en fait dans un certain angle solide) et une distribution en énergie inconnue. De ce fait, les comparaisons avec les résultats de simulation numériques peuvent parfois être délicates.

Concernant les études de simulations numériques, celles-ci ont été réalisées par dynamique moléculaire, cette méthode étant un outil des plus prometteurs pour aboutir à une description prédictive du système étudié sur un court intervalle de temps. Elle fournit également des informations détaillées des mécanismes à l'échelle atomique durant le processus de dépôt. Nous avons utilisé le code de dynamique moléculaire FLX développé par J. Kieffer *et al.*[1] pour modéliser le comportement des matériaux ayant un caractère mixte covalent-ionique. FLX offre un choix de modèles d'interaction incluant Lennard-Jones, Coulomb, Born-Mayer-Huggins, trois corps ainsi que le model de Kieffer de transfert de charge. FLX utilise un algorithme correcteur-prédicteur de vitesse du cinquième ordre pour l'intégration des équations de mouvement.

Le champ de potentiel de Kieffer prend la forme suivante :

$$\varphi_i = q_i \sum_{j=1}^{N} \frac{q_j}{4\pi\epsilon_0 r_{ij}} + \sum_{j=1}^{NC} C_{ij} e^{\frac{\sigma_i+\sigma_j-r_{ij}}{\rho_{ij}}} + \sum_{j=1}^{NC-1} \sum_{k=j+1}^{NC} (\phi_{ik} + \phi_{ik})\chi_{ijk}$$

où le premier terme du membre de droite représente l'interaction coulombienne, le second est le potentiel répulsif de Born-Huggins-Mayer et le troisième terme représente le potentiel d'interaction (attractif) à trois corps.

Les simulations ont été réalisées pour les conditions des particules incidentes suivantes :

- Substrat : Si (100) et Si amorphe.
- Espèces incidentes : C (unique et continu) ; Ti ; W.
- Energie incidente : < 100 eV.
- Angle d'incidence par rapport à la normale à la surface : 0 – 60°.
- Paramètres calculés : rétrodiffusion, implantation, déplacement latéral, coordination, collage.

[1] L. P. Huang, J. Kieffer, J. Chem. Phys. 2003, 118 (3), 1487-1498.

3 Simulation par dynamique moléculaire du dépôt de carbone

L'étude du dépôt et du collage d'atomes de carbone sur une surface de silicium a été menée en deux parties. Dans un premier temps, nous nous sommes intéressés au comportement d'un atome de carbone unique bombardant la surface du substrat. Dans une seconde partie, l'étude a été réalisée pour un flux d'atomes de carbone (100 atomes dans les simulations).

3.1 Atome de carbone unique

Dans le cas de l'impact d'un atome de carbone unique, les résultats numériques obtenus à l'aide du champ de forces défini par Kieffer ont été comparés à ceux obtenus avec ceux issus d'un calcul utilisant les potentiels interatomique bien établis de Erhart-Albe afin de valider la méthode. Notons que les calculs utilisant les potentiels Erhart-Albe ont été réalisés par le groupe de Kai Nordlund à l'université d'Helsinki[2]

Un atome est considéré comme implanté dès lors que sa position finale dans le matériau (Si) est est au-delà de 0,5 Å de l'extrême surface (position à 0 Å). Si la position est comprise entre 0 Å et 0,5 Å, l'atome est considéré comme déposé. Si la position finale est inférieure à 0 Å, il s'agit alors des atomes rétrodiffusés.

La profondeur moyenne de pénétration de l'atome de carbone est peu sensible à l'incidence de celui-ci par rapport à la normal à la surface tant que l'énergie d'impact reste inférieure à 20 eV (fig. 1). Pour des énergies incidentes plus élevées, la profondeur de pénétration des atomes de carbone montre une dépendance en angle d'incidence ; pour les angles d'incidence de 30° et 45°, les atomes pénètrent plus profondément dans le réseau cristallin de silicium alors qu'en incidence quasi-normale (0° et 15°) les atomes pénètrent moins dans le matériau.

Un effet de canalisation a été observé lors du dépôt d'un atome de carbone unique sur la surface de silicium cristallin pour des valeurs de l'énergie incidente supérieures à 10 eV. En effet, pour une incidence de 45° par rapport à la normale à la surface, les atomes pénètrent plus profondément dans le réseau cristallin du fait de la structure-même du matériau dont la direction [100] émerge à la surface avec un angle de 45°, présentant de ce fait un axe préférentiel de pénétration (fig. 2). Cet effet est également observé, dans une moindre mesure, pour une incidence de 60°.

[2] L. G. V. Briquet *et al.*, J. Phys. : Condens. Matter **24,** 395004 (2012)

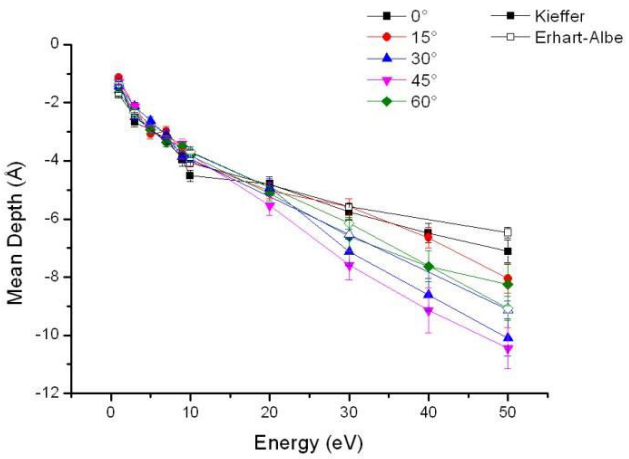

Figure 1 : Variation de la profondeur de pénétration moyenne d'un atome de carbone dans le réseau cristallin de silicium en fonction de son énergie et pour plusieurs angles d'incidence ; simulations effectuées avec les potentiels de Kieffer et ceux de Erhart-Albe.

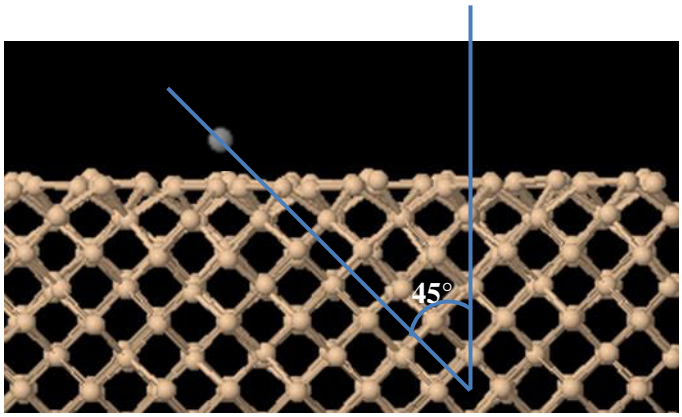

Figure 2: Illustration de l'effet de canalisation pour une surface de silicium dans la direction [100].

Quels que soient l'angle d'incidence et l'énergie d'impact, il y a toujours de la rétrodiffusion, celle-ci étant particulièrement marquée pour des angles d'incidence élevés, tout en n'excédant pas 25% (fig. 3).

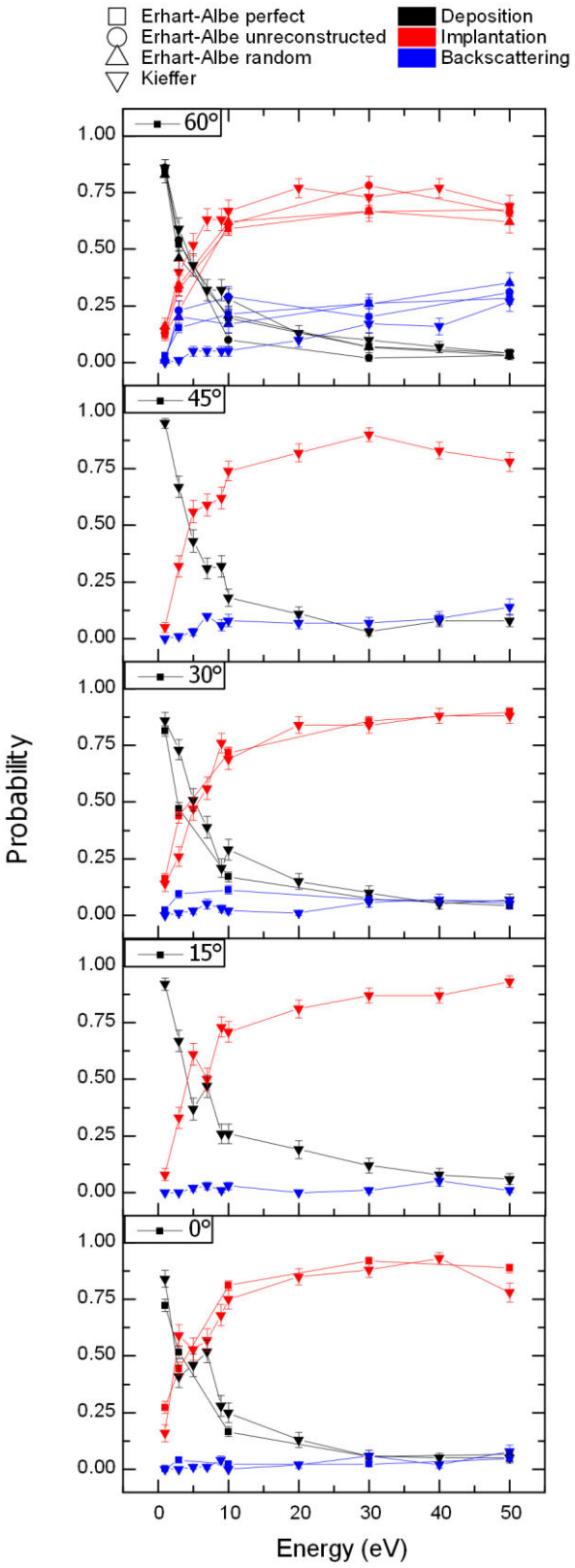

Figure 3 : Probabilité de dépôt (noir), d'implantation (rouge) ou de rétrodiffusion (bleu) d'un atome de carbone sur une surface de silicium (100).

3.2 Flux d'atomes de carbone

Dans une seconde étape, nous nous sommes intéressés au dépôt de carbone en continu, c'est-à-dire en simulant l'impact de plusieurs atomes successivement sur la surface de silicium cristallin. Les simulations ont été réalisées pour les énergies d'impact de 1 à 30 eV et des angles d'incidence de 0°, 30°, 45° et 60° par rapport à la normale à la surface. Le nombre total d'atomes bombardant la surface a été fixé à 100. Les résultats de simulation, comparé pour différentes énergies et incidences, concernent la distribution en profondeur d'implantation, le coefficient de collage des atomes de carbone sur silicium, la distribution de C en position radiale et angulaire par rapport au point d'impact, ainsi que le nombre de coordination c'est-à-dire le nombre de plus proches voisins estimé par le nombre d'atomes auxquels le carbone incident est lié à la fin de son trajet dans le matériau. De même, les simulations permettent d'obtenir des informations précieuses sur les modifications et la réorganisation de la surface du matériau résultant du dépôt et de l'implantation de C. En effet, la zone en surface proche de l'impact subit de profondes modifications, jusqu'à une certaine amorphisation (fig. 4).

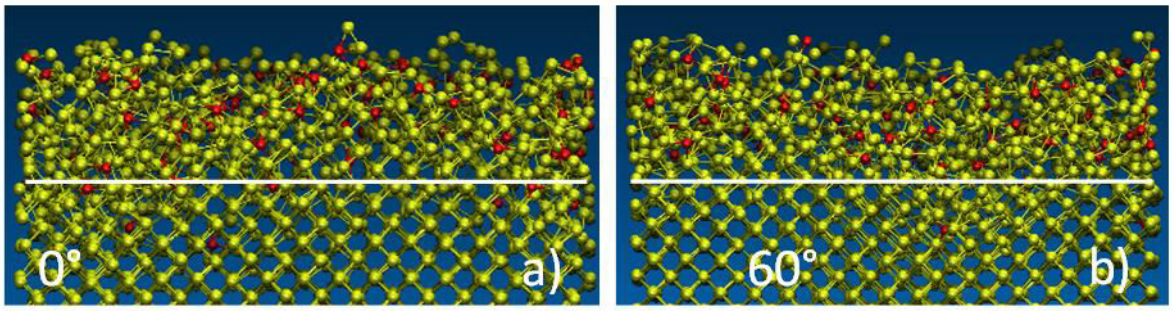

Figure 4 : Structure de la surface de silicium après l'impact de 100 atomes de carbone possédant une énergie de 5 eV pour deux angles d'incidence : 0° (a) et 60° (b).

La déformation de la structure cristalline en profondeur peut être étudiée à l'aide la fonction de distribution radiale g(r) calculée pour différentes couches de matériau chacune ayant une épaisseur de 5 Å d'épaisseur. La figure 5 montre les variations de g(r) selon l'angle d'incidence des atomes de carbone pour différentes profondeurs en sous-surface. Les pics de distribution radiale bien mieux définis pour de grandes profondeurs (17,5 Å) indiquent que la structure est moins endommagée en profondeur. En revanche, plus on s'approche de la surface, plus la modification de structure est importante, ce qui se traduit par un élargissement et une moins bonne résolution des pic de g(r). De plus, l'influence de l'angle d'incidence sur g(r) est visible sur la figure 5. En effet, si l'interaction Si-Si et Si-C dans une zone proche de la surface (7,5 Å) semble peu dépendre de l'angle d'incidence, cette influence se fait sentir pour des profondeurs plus importantes sous la surface. En effet, les pics

correspondants aux second plus proches voisins Si-Si (pics à 3.8 Å et 4.4 Å) sont mieux discriminés à 60° d'incidence qu'aux autres incidences pour la couche à 12,5 Å. Cette influence est encore plus marquée à 17,5 Å de profondeur (pics de second et de troisièmes plus proches voisins Si-Si). Du fait d'une plus faible pénétration à 60°, l'énergie déposée au cours de l'impact reste au voisinage de la surface, ce qui explique la plus forte perturbation du réseau cristallin en surface par rapport aux couches plus profondes.

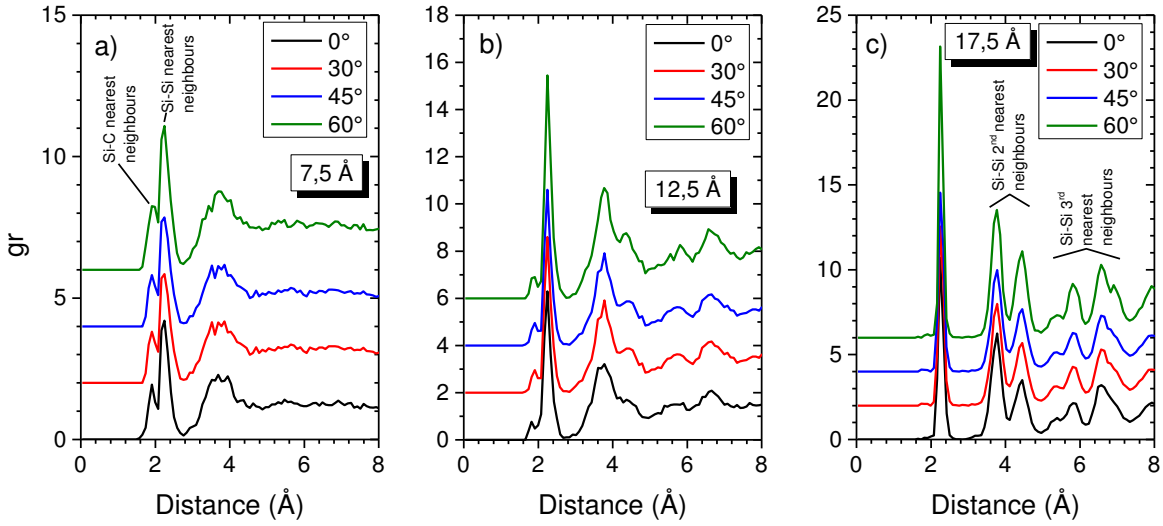

Figure 5 : Fonction de distribution radiale pour différents angles d'incidence pour des couches à différentes profondeurs : a) 7,5Å ; b) 12,5Å ; c) 17,5Å. Energie incidente = 5 eV. L'indexation des pics est donnée sur la figure.

Intéressons-nous maintenant à l'influence de l'énergie incidente sur les modifications de structure. La fonction de distribution radiale (fig. 6) montre que, au voisinage de la surface (2,5 Å), la probabilité de liaison Si-C est plus élevée à basse énergie d'impact (1 eV). Ceci est dû au fait que, dans ces conditions, la plupart des atomes de carbone incidents sont faiblement implantés et demeurent en surface. Pour des énergies d'impact plus élevées, le rapport des pics Si-C sur Si-Si en proche surface (2,5 Å) est plus élevé qu'à 1 eV, montrant ainsi que l'énergie d'incidence influe sur les modifications du matériau.

Comme précédemment, l'analyse des pics de seconds voisins Si-Si à 3,8 Å et 4,4 Å montre que les modifications de structure en profondeur sont moindres.

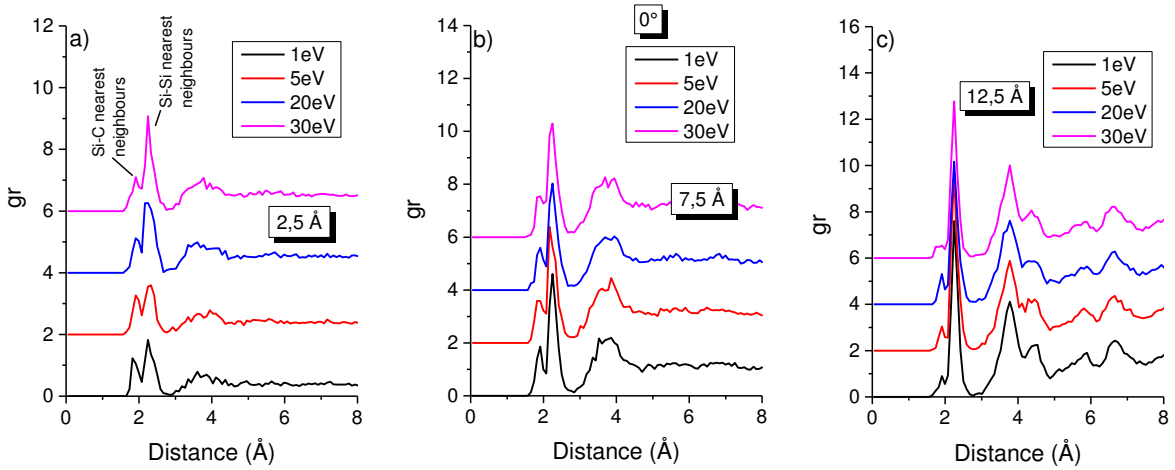

Figure 6 : Fonction de distribution radiale pour différentes valeurs de l'énergie incidente pour des couches à différentes profondeurs : a) 7,5Å ; b) 12,5Å ; c) 17,5Å. Angle d'incidence = 0° d'incidence. L'indexation complète des pics est donnée sur la figure 5.

Les figures 7 et 8 montrent la distribution en profondeur des atomes de carbone implantés après 30, 50, 70 et 100 atomes déposés. Outre une idée sur la nature du matériau après dépôt, cette distribution indique clairement comment les atomes de carbone sont répartis dans le matériau silicium selon la dose que celui-ci reçoit. Sur la figure 8, il apparaît clairement que presque tous les atomes de carbone incidents sont déposés/implantés dans les premières couches du réseau cristallin (< 5 Å) pour des doses de 30 et 50 atomes incidents. A mesure que la dose d'atomes incidents augmente, la probabilité de présence en profondeur se décale vers les couches plus internes. Des atomes C peuvent ainsi être implantés jusqu'à 15,5 Å de profondeur, même pour des énergies incidentes faibles. Cela peut s'expliquer par le fait que, à mesure que la dose de C augmente, les atomes C déjà déposés/implantés en surface sont poussés vers l'intérieur. Ce mécanisme peut être confirmé en suivant la trajectoire des atomes c précédemment déposés.

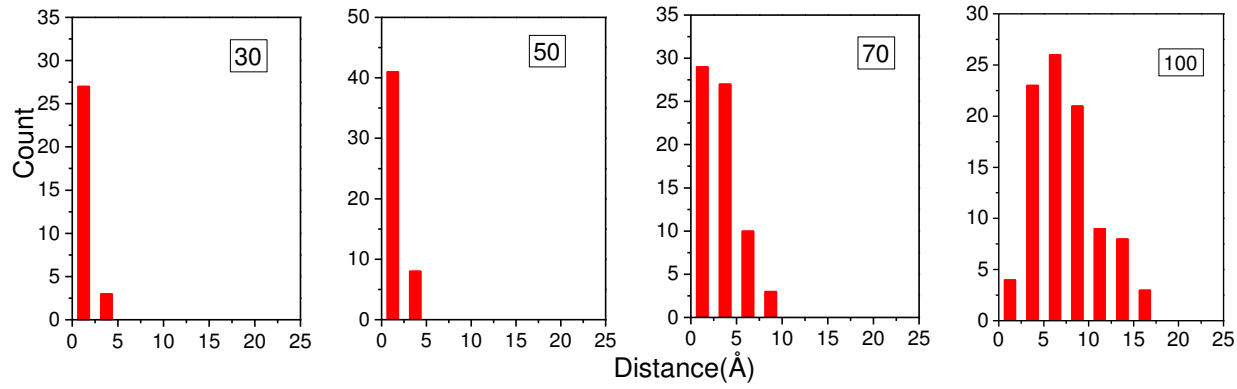

Figure 7 : Distribution en profondeur des atomes c implantés dans Si (100) après différentes doses. 1 eV ; 0°.

Des résultats similaires sont obtenus à plus forte énergie d'impact (fig. 8). Toutefois, pour des énergies plus élevées, les atomes C s'implantent dans les couches plus profondes (> 2,5 Å) pour des doses plus faibles (> 30 at.). C'est une conséquence directe de l'augmentation de l'énergie d'impact.

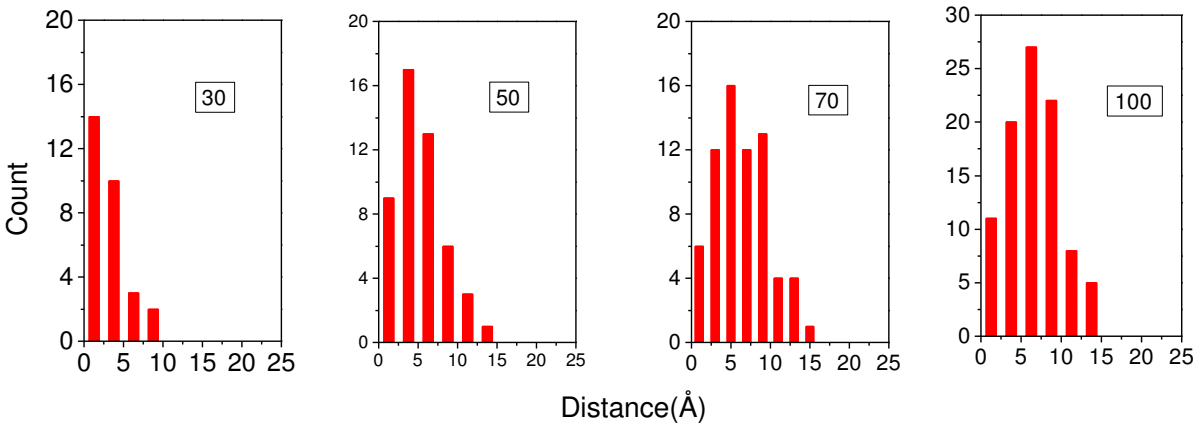

Figure 8 : Distribution en profondeur des atomes c implantés dans Si (100) après différentes doses. 30 eV ; 0°.

4 Dépôt de titane sur silicium

L'un des objectifs de la partie expérimentale de ce travail est la détermination des coefficients de collage d'atomes sur une surface de silicium cristallin. Pour cette détermination, du titane a été déposé sur du silicium dans l'instrument Storing Matter en utilisant un faisceau d'ions argon de 10 keV. Après transfert sous ultravide, les échantillons ont été analysés par SIMS afin de déterminer la forme des dépôts et le coefficient de collage. Un balayage de l'analyse sur la surface de l'échantillon permet, dans un premier temps, de détermine la localisation du dépôt. Dans un second temps, les profils de dépôt sont ensuite ajustés à une fonction de Lorentz[3] puis intégrés pour déterminer le nombre total d'atomes déposés. Un exemple de profil en profondeur sur plusieurs lignes de balayage ainsi que le résultat de l'intégration et de l'ajustement par une fonction de Lorentz est donné sur la figure 9. Cette procédure est utilisée pour déterminer le nombre total d'atomes déposés en 3 dimensions, l'ajustement lorentzien et l'intégration étant réalisées en 2 dimensions pour chaque dépôt.

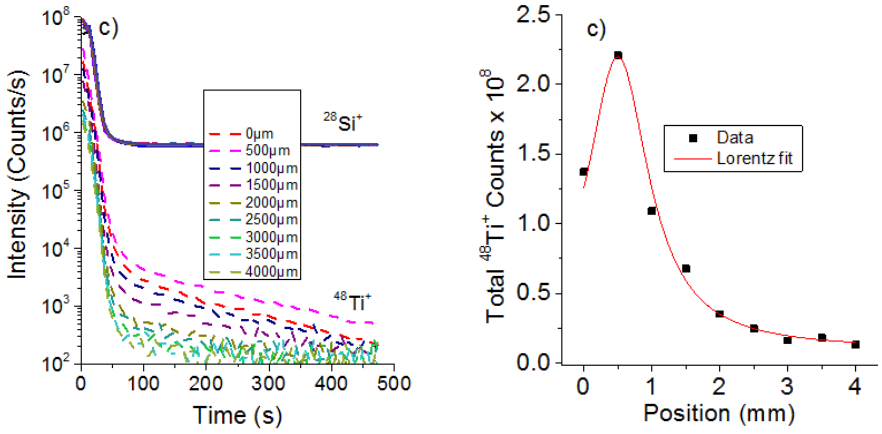

Figure 9 : Exemple de profil en profondeur mesurés par SIMS selon une ligne de balayage du collecteur (gauche) et valeurs intégrées et interpolées du nombre d'atomes déposés (droite).

Le coefficient de collage est ensuite déterminé à partir des taux de sputtering de l'instrument storing matter et de l'analyseur SIMS :

$$SC = \frac{N_{Ti\ deposited}}{N_{Ti\ sputtered}} = \frac{C_{SIMS}}{UY_{SIMS} * Y * N_{Ar+}}$$

où C_{SIMS} est le nombre total d'atomes détectés (nombre d'atomes obtenu par intégration 2D de l'interpolation lorentzienne), UY_{SIMS} est le taux effectif de pulvérisation de l'instrument d'analyse

[3] Fonction de Lorentz car c'est la forme analytique de la projection sur une surface plane de la distribution en cosinus, dans l'espace, des particules pulvérisées par bombardement ionique

SIMS, *Y* est le taux de pulvérisation de l'instrument storing mater et N_{Ar+} le nombre d'ions Ar^+ utilisés pour réaliser le dépôt dans la chambre storing mater. $N_{Ti\ sputtered}$ et $N_{Ti\ deposited}$ représentent respectivement le nombre d'atomes de titane pulvérisés de la cible et le nombre d'atomes de titane effectivement déposés dans la chambre storing matter.

Malgré une forte dispersion, les mesures montrent que le coefficient de collage ne dépend pas du taux de couverture de la surface (fig. 10). La dispersion est principalement due à plusieurs causes. Tout d'abord, le balayage de l'analyse se fait par pas de 500 µm, ce qui confère à la mesure spatiale une précision maximale de 500 µm. Ensuite, le jeu mécanique du manipulateur dans la chambre d'analyse SIMS est également une source d'erreur, difficile à quantifier. Enfin, le positionnement du collecteur dans la chambre de dépôt, avec une précision de +/- 500µm conduit, dans certains cas, à une forte sous-estimation du coefficient de collage. Toutefois, comme nous le verrons ci-après, les valeurs de coefficient de collage comprises entre 0,8 et 1 semblent les plus réalistes.

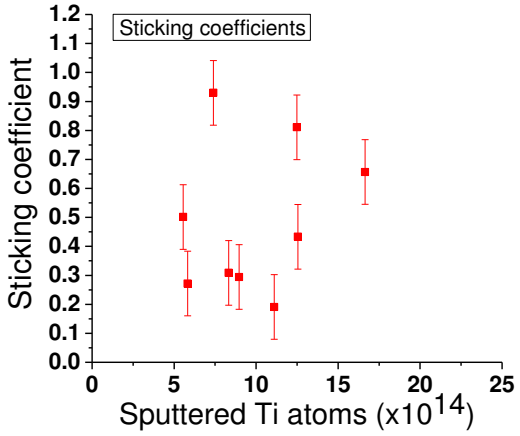

Figure 10 : Variation du coefficient de collage des atomes de Ti sur Si en fonction de la dose d'atomes de titane pulvérisés de la cible lors du dépôt dans la chambre storing matter.

Des simulations de dynamique moléculaire ont ensuite été réalisées afin de valider les résultats expérimentaux et obtenir des renseignements complémentaires des mécanismes à l'échelle atomique, en particulier comment et où s'adsorbent les atomes déposés. Comme dans le cas du carbone, les simulations ont été réalisées pour différentes énergies et différents angles d'incidence. Les résultats concernent des substrats cristallins et des substrats de Si amorphe.

La figure 11 montre les variations de la profondeur de pénétration moyenne en fonction de l'énergie des atomes incidents pour différents angles et natures de substrat. A faible énergie (typ.

< 10 eV), la profondeur d'implantation est indépendante de l'angle d'incidence des particules ; on note cependant une profondeur légèrement supérieure pour le substrat cristallin, ce qui peut s'expliquer par des effets de canalisation favorisés par l'arrangement régulier des atomes de silicium dans le cas d'un substrat cristallisé. A plus forte énergie incidente, la profondeur d'implantation augmente avec l'énergie et dépend de l'angle d'incidence. La profondeur moyenne est la plus élevée à incidence normale et la plus limitée à 60° d'incidence. Cela s'explique par le fait que la composante de la vitesse normale à la surface est plus élevée à incidence normale.

Ces résultats de simulation numérique montrent également que, contrairement au cas du carbone, il n'y a pas ou peu d'effet de canalisation pour une direction incidente donnée.

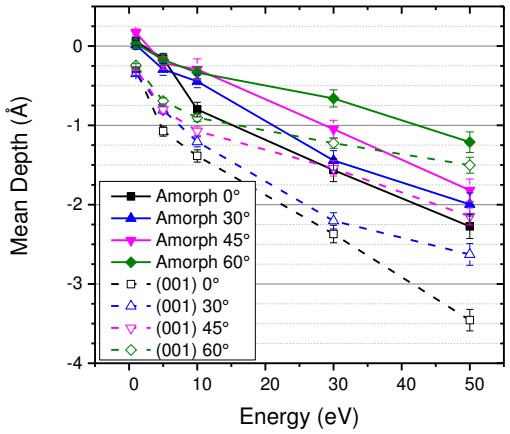

Figure 11 : Variation de la profondeur de pénétration moyenne des atomes de titane dans le réseau cristallin de silicium en fonction de son énergie et pour plusieurs angles d'incidence et de la structure du matériau.

Du point de vue numérique, le coefficient de collage (*SC*) des atomes de titane sur le substrat de silicium est calculé à partir du taux d'atomes rétrodiffusés (Y_{BS}): $SC = 1 - Y_{BS}$. Les résultats du calcul du coefficient de collage présentés sur la figure 12 appellent deux remarques :

- quels que soient l'angle d'incidence et la nature du substrat (amorphe ou cristallin), la probabilité de collage présente une particularité à 5 eV, énergie pour laquelle la probabilité de collage est sensiblement plus faible.

- à cette particularité près (5 eV), la probabilité de collage des atomes de titane sur silicium semble indépendante de l'énergie incidente et du substrat sauf pour les fortes incidences (60°).

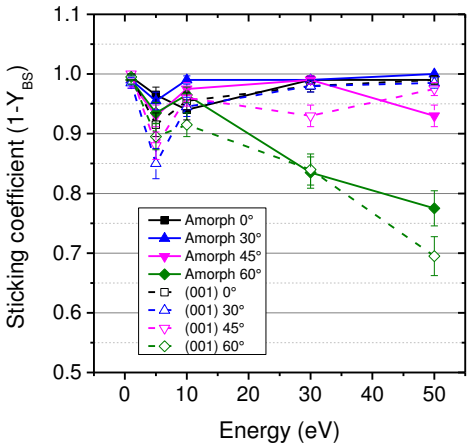

Figure 12 : Variation de la probabilité de collage des atomes de titane sur silicium (cristallin et amorphe) en fonction de l'énergie des atomes incidents et pour différentes incidences.

Cela s'explique en comparant l'énergie d'impact et l'énergie de liaison. Pour les faibles valeurs d'énergie incidente (typ. < 5 eV), inférieures à l'énergie de liaison Ti-Si, les atomes de titane incident vont simplement s'adsorber en extrême surface, soit sur une rangée d'atomes Si entre deux atomes Si (fig. 13a), soit entre deux rangées d'atomes Si (fig. 13b).

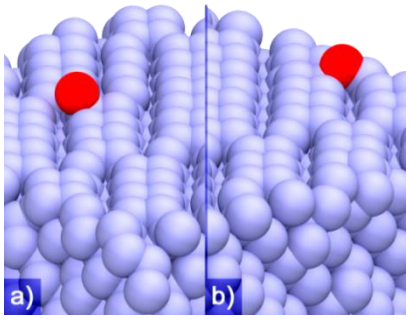

Figure 13 : Sites d'adsorption du titane déposé à 1 eV sur silicium. a) adsorption entre deux atomes sur une rangée externe ; b) adsorption entre deux rangées d'atomes.

A 5 eV, l'énergie de liaison Si-Ti est proche de l'énergie des atomes incidents. Lorsque l'atome Ti approche de la surface, il peut y avoir un effet de résonnance si l'atome incident impact juste sur le dessus d'un atome de silicium. Dès lors, la probabilité de rétrodiffusion est plus forte dans ce cas, et par conséquence, la probabilité de collage est plus faible. A 10 eV, les atomes incidents ont suffisamment d'énergie pour franchir la barrière de potentiel formée par les liaisons Si-Si et peuvent alors s'implanter sous la première couche d'atomes de Si d'extrême surface. Pour des énergies plus élevées, le scénario est sensiblement le même, les atomes incidents pouvant alors s'implanter plus profondément dans le substrat. A 60° d'incidence, et au-delà probablement, la composante de la vitesse parallèle à la surface devient prépondérante dans les mécanismes et augmente la rétrodiffusion, d'autant plus que cette composante est élevée (i.e. que l'énergie incidente augmente). On notera que la probabilité de collage de Ti sur Si est proche de l'unité (comprise entre 0,95 et 0,99) avec une valeur sensiblement inférieure à 5 eV pour laquelle le coefficient de collage est compris entre 0,85 et 0,96.

5 Dépôt de tungstène sur silicium

Comme dans le cas du dépôt de titane, des dépôts de tungstène ont été réalisés par pulvérisation cathodique dans l'instrument storing matter avec des ions Ar^+ de 10 keV. Les conditions de dépôt et les procédures d'analyse sont similaires à celles utilisées dans le cas du titane. Toutefois, dans ce cas, les mesures sont beaucoup plus sensibles aux effets de matrice qui conduisent à sous-estimer les valeurs du coefficient de collage.

Les mesures de coefficient de collage montrent également une dispersion, bien que celle-ci soit moins marquée que dans le cas du titane (fig. 14). Dans ce cas également, les causes d'incertitude sont nombreuses, comme dans le cas du dépôt de Ti.

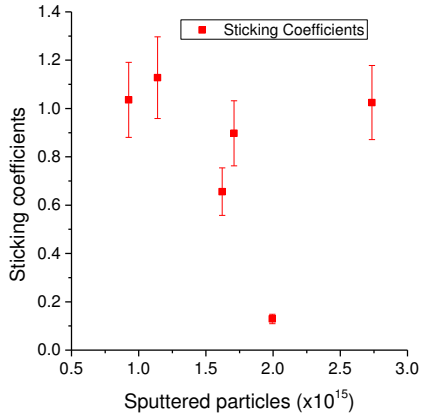

Figure 14 : Variation du coefficient de collage des atomes de W sur Si en fonction de la dose d'atomes de tungstène pulvérisés de la cible lors du dépôt dans la chambre storing matter. Les barres d'erreur ne prennent en compte que les incertitudes sur la mesure. Les incertitudes dues au positionnement et au balayage ne sont pas quantifiées.

La simulation numérique par dynamique moléculaire a également été réalisée pour le dépôt de tungstène sur silicium, en fonction de l'angle d'incidence (0°, 30°, 45° and 60°) et de l'énergie (1, 5, 10, 30, 50, 100eV) des atomes incidents.

La figure 15 montre la variation de la profondeur d'implantation moyenne des atomes W à la surface cristalline de Si en fonction de l'énergie incidente et pour différents angles d'impact. Comme dans le cas du titane, la profondeur d'implantation est indépendante de l'angle d'impact pour des valeurs d'énergie incidente inférieures à 10 eV ; la plupart des atomes de W restent adsorbés en extrême surface. A 30 eV d'énergie d'impact, la profondeur moyenne de pénétration atteint 2,5 Å et augmente progressivement à mesure que l'énergie d'impact augmente, avec une influence significative de l'angle d'impact des particules incidentes.

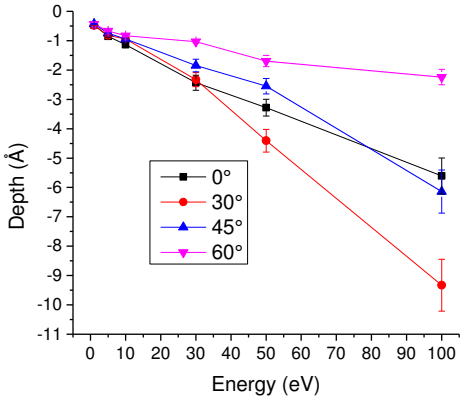

Figure 15: ***Variation de la profondeur de pénétration moyenne des atomes de W dans le réseau cristallin de silicium en fonction de l'énergie d'impact et pour plusieurs angles d'incidence***

Jusqu'à 30 eV d'énergie d'impact, la profondeur moyenne d'implantation est maximale pour une incidence normale, et minimale pour une incidence de 60° par rapport à la normale à la surface. Cela est dû à la prédominance de la composante normale de la vitesse des atomes incidents. A 100 eV, la pénétration du W dans Si est maximale et atteint une profondeur maximale de 9,5 Å à 30°.

A 30° d'incidence et 50 eV et 100 eV d'énergie d'impact, on observe un effet de canalisation comparé aux autres angles d'impact (fig. 16).

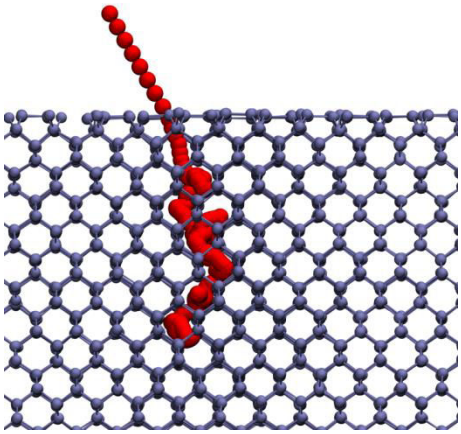

Figure 16 : Effet de canalisation des atomes de W déposés à 30° d'incidence et 30 eV d'énergie.

Même à forte énergie d'impact (100 eV) et à 60° d'incidence, la plupart des atomes de W s'adsorbent en extrême surface. Cela montre que l'angle d'incidence à une forte influence sur les processus de dépôt et d'implantation.

La probabilité de collage des atomes de tungstène sur silicium a été calculée comme précédemment, à partir du nombre d'atomes W rétrodiffusés. Dans le cas du tungstène, quasiment tous les atomes incidents restent à la surface ou pénètrent dans les premières couches atomiques du substrat. Il en résulte que le coefficient de collage reste sensiblement constant et proche de 1 quels que soient les paramètres d'incidence et d'énergie (fig. 17). Cette valeur élevée s'explique par l'énergie élevée de la liaison W-Si (10,6 eV) comparée aux énergies de liaison Ti-Si (5,5 eV) et C-Si (4,6 eV). Ainsi, dès qu'un atome W approche de la surface avec une énergie relativement faible (< 100 eV), sa probabilité de former une liaison W-Si est grande, conduisant au collage de l'atome à la surface.

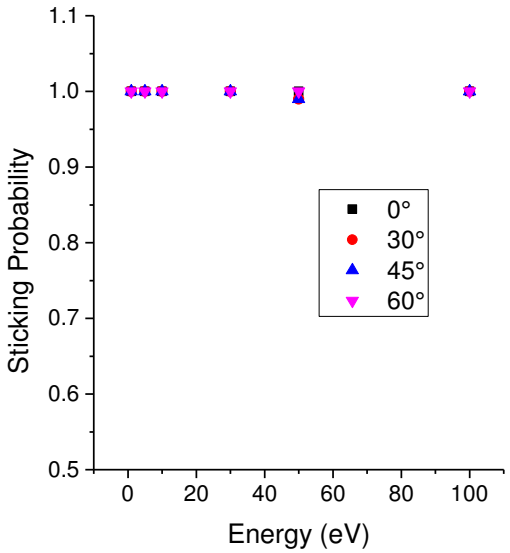

Figure 17 : variation de la probabilité de collage de W sur Si (100).

6 Conclusion et perspectives

6.1 Conclusion

Le collage, le dépôt et la réorganisation d'atomes dans le domaine de la sous-monocouche sont de grande importance dans le domaine de la science des surfaces. L'adhérence d'un matériau quelconque à la surface d'un produit est une problématique industrielle majeure avec de nombreuses applications dans les industries de l'emballage, de l'électronique et des matériaux. Afin de bien cerner les phénomènes d'interaction entre un atome et une surface, comme ceux rencontrés par exemple en traitement de surface assistés par plasma, il est essentiel d'avoir une parfaite connaissance des mécanismes de collage dès les premiers stades de l'interaction, ces mécanismes contrôlant les propriétés d'interface.

Le principal objectif de ce travail était d'étudier le dépôt et le collage de particules inorganiques sur des surfaces de silicium pendant la croissance de l'interface dans le régime de la sous-monocouche et le domaine des faibles énergies (quelques eV).

Outre des investigations expérimentales, une approche de simulation numérique a été utilisée pour atteindre ces objectifs. Des simulations par dynamique moléculaire à grande échelle, utilisant les champs de forces réactifs ont été utilisées pour décrire et comprendre les processus à l'échelle atomique qui sous-tendent l'adhérence et la réorganisation des atomes à la surface du substrat. Seule cette approche permet une meilleure compréhension et un meilleur contrôle des propriétés d'interface telles que souhaitées.

De plus, ces études améliorent notre compréhension des processus de dépôts dans le régime de la sous-monocouche durant les étapes de préparation du collecteur et de l'analyse de surface via la technique et l'instrument storing matter. Les résultats obtenus apportent des éléments pour améliorer cette technique.

L'influence de l'énergie et de l'angle d'incidence des particules sur le collage et la diffusion de surface a été étudiée selon le taux de couverture de la surface. Aucune étude de plasma n'a été entreprise dans ce travail, le plasma étant considéré uniquement comme une source de particules. Les principaux paramètres explorés dans ce projet concernent tant les particules incidentes (énergie, angle d'incidence et taille) que la composition et structure cristallographique des substrats.

Le collage et les mécanismes de dépôt ont été étudiés et discutés pour C, Ti et W par une double approche combinant expériences et simulation numérique de dynamique moléculaire, cette dernière permettant d'obtenir des informations sur les mécanismes de dépôt et d'implantation à l'échelle atomique. Aucune étude expérimentale n'a été réalisée pour ce qui concerne le carbone. En

effet, notre système expérimental est tel que la contamination par le carbone ne peut pas être réduite à un niveau où elle n'interférerait pas significativement avec les dépôts en régime de sous-monocouche. En conséquence, des travaux de simulation supplémentaires ont été faits dans le cas du carbone, à savoir l'étude de l'interaction d'un flux continu de carbone avec la surface.

Dans le cas du carbone, la simulation de dynamique moléculaire fournit des renseignements sur l'interaction carbone silicium à faible énergie d'impact. Qu'il s'agisse d'un atome de carbone unique ou d'un flux d'atomes, les simulations décrivent plusieurs aspects des mécanismes d'adhérence et d'implantation. Le champ de force développé par John Kieffer a été choisi pour les simulations car il permet de prendre en considération la formation et la rupture des liaisons atomiques via les transferts de charge en fonction de l'environnement des atomes.

Les résultats pour l'interaction d'un atome C unique concernent les variations dela profondeur moyenne de pénétration, la distribution en profondeur d'implantation, le ratio dépôt/implantation et la probabilité de rétrodiffusion. Les résultats correspondants ont été validés par comparaison avec une autre simulation faites en utilisant les potentiels bien établis de Erhart-Albe. Malgré quelques légères divergences - pour des incidences rasantes et les énergies les plus élevées - entre les résultats issus des deux modèles, l'accord entre les deux est plus que satisfaisant.

Ces études de dynamique moléculaire ont été étendues au cas de l'interaction d'atomes de carbone en continu afin d'appréhender et de mieux cerner non seulement le dépôt et l'implantation de carbone dans le silicium, mais également la formation de défauts et la réorganisation des atomes en surface du substrat au cours de l'interaction d'atomes de faible énergie avec une surface de silicium (100).

Les fonctions de distribution radiale et angulaire des atomes révèlent les modifications de la structure Si-C selon l'énergie et l'angle d'incidence des particules, la dose d'atomes reçue et la profondeur de pénétration dans le matériau. Il apparaît que la structure est fortement perturbée en extrême surface alors qu'elle reste bien ordonnée à des profondeurs au-delà de 10 Å. Des conclusions similaires peuvent être tirées des résultats portant sur les concentrations, la distribution en profondeur ou encore les calculs de coordination. Il a été montré que l'énergie incidente des particules a plus d'effet que l'angle d'incidence sur la réorganisation de surface du matériau.

L'analyse de résultats à différent étapes en faisant varier la dose d'atomes reçus fournit également plusieurs aspects concernant les processus de dépôt et d'implantation. A 1 eV, des atomes

de carbone peuvent atteindre jusqu'à 15 Å de profondeur ce qui est principalement dû à des mécanismes de diffusion.

Plusieurs aspects concernant le collage et l'adhérence du titane sur silicium ont fait l'objet d'un chapitre dédié. Des résultats expérimentaux couplés à des simulations numériques ont permis d'appréhender les mécanismes d'interaction d'atomes de titane avec une surface de silicium. Les mécanismes aux interfaces durant le dépôt ont été discutés. Néanmoins, les investigations expérimentales du coefficient de collage Ti sur Si n'ont pas montré de tendance particulière avec les paramètres d'incidence. En revanche, les calculs de dynamique moléculaire ont conduit à des valeurs de probabilité de collage comprises entre 0,8 et 0,99, et un effet de résonance a été mis en évidence autour de 5 eV, qui conduit à une augmentation sensible du taux d'atomes rétrodiffusés, et diminution en conséquence du coefficient de collage.

Une approche similaire a été réalisée dans le cas du dépôt d'atomes de tungstène sur silicium. Les études expérimentales ont montré que les valeurs du coefficient de collage sont élevées, malgré une certaine dispersion des résultats, cependant moindre que dans le cas du titane. Ces valeurs expérimentales ont pu être corrélées aux résultats numériques avec un accord satisfaisant. Les valeurs élevées de la probabilité de collage (proches de 1) sont probablement due à l'énergie élevée de la liaison W-Si (10,6 eV), favorisant le collage d'atomes ayant une énergie d'impact modérée (< 100 eV). Plusieurs autres investigations ont pu être menées par dynamique moléculaire, concernant par exemple le déplacement latéral des atomes ou encore l'implantation. En particulier, il a été montré que lorsque le déplacement latéral est important, la profondeur de pénétration est faible et vice versa.

D'une manière générale, on peut conclure que ce travail apporte une contribution significative à la description et la compréhension des mécanismes de collage et de dépôt de particules inorganiques (C, Ti, W) dans le régime de la sous-monocouche.

6.2 **Perspectives**

Les coefficients de collage ont été déterminés par la technique couplée storing matter / SIMS. Toutefois, il est nécessaire d'améliorer la précision des mesures, en particulier pour ce qui concerne le positionnement du collecteur dans l'instrument stroring matter et son repérage dans l'analyseur SIMS.

De même, les problèmes de contamination rencontrés avec les outils expérimentaux utilisés limitent les mesures expérimentales à quelques éléments. L'utilisation d'une chambre sous ultra vide unique pour le dépôt et pour l'analyse permettrait de s'affranchir des contaminations (a minima de les limiter).

Un autre aspect qui se doit d'être considéré concerne la couche d'oxyde natif inévitable qui se forme à la surface du silicium, malgré les conditions d'ultravide utilisées pour nos dépôts expérimentaux. En effet, cette couche d'oxyde n'est pas prise en compte dans les simulations numériques qui considèrent une surface parfaitement propre et exempte de toute contamination ou oxydation.

De même, les simulations sont réalisées avec des angles d'incidence parfaitement déterminés alors que ceux-ci sont inconnus dans l'expérience, les atomes pulvérisés étant émis dans un certain angle solide. Il en est de même pour ce qui concerne l'énergie des particules incidentes, bien fixée dans les simulations numériques, mais distribuées sur une gamme d'énergie plus ou moins large dans l'instrument storing matter.

Le dépôt de carbone a été étudié pour un atome unique et pour un flux d'atomes. Cette étude pour plusieurs atomes doit également être réalisée pour ce qui concerne le titane et le tungstène. Cela permettra d'avoir des points de comparaisons plus réalistes par rapport aux techniques de dépôt par pulvérisation à faible énergie.

Ce travail est une première étape vers une description des mécanismes de dépôts de SiC, TiC et WC, matériaux dont les applications sont nombreuses. Ainsi une prochaine étape pourrai être d'étudier les mécanismes afférents à ces carbures.

Enfin, après avoir étudié l'interaction d'un atome (même en flux continu), il serait intéressant de s'intéresser au comportement des particules et de la surface sous l'impact d'agrégats d'atomes au lieu d'atomes isolés.

Plusieurs autres aspects enfin pourraient être étudiés tels que la formation d'îlots, la diffusion lors de l'analyse, etc. ; cela apporterait des renseignements quant aux processus fondamentaux impliqués dans les processus d'émission d'ions secondaires

Collage et adhérence de particules dans le domaine de la sous-monocouche

Résumé

Au cours d'un traitement de surface de type dépôt assisté par plasma, les caractéristiques et propriétés de l'interface entre le dépôt et le substrat sont déterminées par la première couche atomique du dépôt, voire les premiers atomes qui commencent à recouvrir la surface du substrat. Aussi, la parfaite connaissance du comportement des particules incidentes et du réarrangement des atomes suite à l'impact d'une particule du plasma est-elle un élément essentiel à la description du comportement de la surface en cours de traitement et donc de ses propriétés ultérieures. Au cours de cette thèse, nous avons entrepris d'étudier, par une approche combinant expériences et simulation numérique par dynamique moléculaire, l'interaction d'espèces (C, Ti, W) avec une surface de silicium en fonction de paramètres tels que l'énergie, la fluence ou encore l'incidence des particules arrivant sur la surface. Une part importante de ce travail a consisté à adapter les codes de dynamique moléculaire (utilisation des champs de force réactifs) aux systèmes étudiés. La partie expérimentale a nécessité la mise en place de procédures spécifiques pour l'utilisation de l'équipement *Storing Matter*. Les résultats montrent que, quelle que soit l'espèce incidente, parmi celles étudiées, le coefficient de collage (SC) est dans la gamme [0.7 – 1] ; dans le cas de W, quasiment tous les atomes incidents restent sur la surface (SC≈1). Outre la détermination du coefficient de collage, pour différentes conditions initiales des espèces incidentes (énergie, incidence, fluence) les modifications apportées à la surface ont également été déterminées en termes d'implantation et de trajectoire dans le matériau des espèces incidentes, et de pulvérisation de la surface du substrat.

Mots-Clés : Dynamique moléculaire, coefficient de collage, SIMS, Storing Matter, sous-monocouche.

Sticking and deposition of atoms in the sub-monolayer range

Abstract

During plasma assisted deposition, properties of the coating substrate interface depend on the first atomic layer of the deposit, or the atoms that first start to cover the surface. Therefore the good knowledge of the sticking coefficient and the reorganization of the surface following particle impact is an essential issue to achieve the description of the behavior of the processed surface and, therefore, its expected properties. Consequently, we investigated the interaction between incoming particles (C, Ti, W) and a silicon surface by using an approach combining molecular dynamic simulations and experiments. Various initial conditions were studied, energy, fluence and incidence angle of the incoming particles. An important part of this work has consisted in adapting the molecular dynamic codes (using reactive force fields) to the investigated systems. Meanwhile, experimental procedure specifically devoted to the use of the *Storing Matter* facility was also developed. Results show that the sticking coefficient (SC) value is in the range [0.7 – 1] irrespectively of the incoming species; in the case of W, almost all atoms stick on the surface (SC≈1). Besides the determination of sticking coefficient, the surface modification resulting from the particles impingement were determined for various initial conditions (energy, fluence, angle) in terms of implantation and displacement of the incoming species, and surface sputtering as well.

Keywords: Molecular dynamic simulations, sticking coefficient, SIMS, Storing matter, Sub monolayer.

UNIVERSITE DE LORRAINE

Ecole Doctorale : **É**nergie **M**écanique **Ma**tériaux

Institut **J**ean **L**amour
Département Chimie et Physique des Solides et des Surfaces

THESIS

defended on 18/07/2014

to obtain the degree of Doctor of the University of Lorraine
in material science and engineering

by

Arindam JANA

Sticking and deposition of atoms in the sub-monolayer range.

Jury

President:	**Mohammed BELMAHI**	Professor, University of Lorraine
Reviewers:	**Laurent HOUSSIAU**	Professor, University of Namur, Belgium.
	Pascal BRAULT	Senior researcher (DR) CNRS, GREMI, University of Orléans.
Examiners:	**Kai NORDLUND**	Professor, University of Helsinki, Finland.
Supervisors :	**Gérard HENRION**	Senior researcher (DR) CNRS, IJL, University of Lorraine
	Patrick PHILIPP	Project leader, CRP Gabriel Lippmann, Belvaux, Luxembourg.

Dedicated to my parents and my family

Acknowledgements

After working for more than three and half years in a PhD research, I would compare this experience to a maze in where colleagues and other professionals as well as friends and family, are posted in many intersections to guide you through many corridors and towards the exit. With this thesis, I finally managed to get out of this maze and I would like, now, to thank all the people who made me follow the path I used.

First, I wish to express my hearty gratitude to Dr. Tow Wirtz and Dr. Patrick Philipp who believed in me by accepting me within their team at UIS group. I am really grateful to Dr. Patrick Philipp for his constant guidance and his constructive attitude, which was always driving me to go further. I would like to express my hearty gratitude and many thanks to Dr. Gérard Henrion for his constant support and valuable guidance. Without his comments and modifications, the thesis would never have been the same. I am grateful as well to Prof. Laurent Houssiau and Dr. Pascal Brault who accepted to be my reviewer, and for their strong commitment in reading my thesis. I also wish to express my gratitude to Prof. Kai Nordlund and Prof. Mohammed Belmahi to make time and be part of my defense committee.

This work was financially supported by Fonds National de la Recherche, Luxembourg (FNR) by means of an AFR grant (grant number: PHD-MARP-05) and without their money, this thesis would not exist, so: thank you.

I really appreciate the help of Dr. Ludovic Briquet who constantly guided me through the puzzle of computation since my first day at UIS group. Also I would like to express many thanks to Dr. Jean Nicolas Audinot and Brahime Eladib for their constant help while I was working in dynamic SIMS. I am also really grateful to Samir Menaouli, Arnaud Moschetta, and Alain Robert for their efficient engineering support and valuable technical assistance whenever it was required.

I am also very grateful to Ben, Canan, David, Hung, Ioana, Lukasz, Olivier de Castro, Olivier Bouton Mathieu, Marina, Nimer, Rachid, Roch, Santhana and Yves for their precious suggestions, refreshing discussions, and pleasant humours. I would like to thank other actual or former colleagues of UIS group, with whom I shared so many outings, leisure times as well as many discussions regarding how to solve biggest problems of the world. I really had a good time while sharing those discussions with so many cultures and different opinions within the whole SAM.

I also would like to express my gratitude and thanks to all those whose names are not mentioned here but who provided support of personal, scientific, technical, or in administrative nature.

Table of contents

Chapitre 0.

General scope and content of the thesis

The investigation of sticking, deposition and reorganization of atoms or molecules in the sub-monolayer range has a great importance in the surface treatment field, where the first monolayer describes the interface characteristics and structure between substrate and deposited layer as well as the adhesion properties of this deposited layer on the substrate surface. The properties of the interface are of great significance as interface is often the site where fracture of multi-layered systems originates.

In order to well understand the interactions between atoms and surfaces, as could be the case in plasma surface treatments, it is essential to get a perfect knowledge on the sticking mechanisms during the early stage of growth since these mechanisms control the interface properties. Therefore deposition mechanisms are fundamental in understanding how the atomic interactions influence the interface properties. At the same time understanding of atomic scale behavior during sub-monolayer or monolayer growth is also fundamental for basic and applied problems of surface science.

In this work, plasmas are not investigated by themselves but this work brings more fundamental understanding on the interaction of few-eV energy atoms, i.e. energies similar to those found in plasmas.At the same time, sputter deposition process is a very attractive well established technique for the formation of metal thin films and it has lots of applications in various fields of interest like electronic, optical, medical, and automobile industries. A reproducible realization of a good adhesion and sticking of any material to a product surface is an important industrial problem with many applications like decoration of plates, integrated circuits, photoconductive materials, protection from corrosion, abrasion or thermal resistance. Sticking and adhesion then, is important as soon as one wants to combine homogeneous or heterogeneous materials together without help of any mechanical fixation.

The main objective of this PhD work is to better investigate and understand the deposition, sticking and reorganization behaviour of inorganic particles on silicon surfaces during the growth of interface in sub monolayer range at low energies, i.e. energies found in magnetron sputtering and similar plasma deposition techniques and how some parameters (angle, energy, dose) influence the deposition, implantation and interface properties. To attain these objectives, a multidisciplinary approach involving, experimental investigations and numerical simulations have been incorporated to

investigate the sticking and deposition mechanism of atoms during the sub-monolayer growth in order to obtain detailed description of the atomistic-scale mechanisms controlling the deposition of the very first monolayers in particle-surface treatments. Large-scale MD simulations based on first-principle reactive force fields are utilized to describe and understand the atomistic behaviour underlying the reorganization and adhesion of atoms on the substrates. In this way, a better comprehension and control of tailor-designed surface characteristics can be achieved. In addition, these studies will contribute towards a better understanding of the deposition process in the sub-monolayer range during the deposit preparation for the promising and new surface analysis technique "Storing Matter". The results achieved during this PhD work contribute to further enhance of this technique in terms of sensitivity and quantification. The sticking properties and surface diffusion have been investigated for different surfaces with respect to surface coverage varying the incidence angle and incident energy of the atoms. In addition to MD simulations, sputter deposition technique (storing matter instrument) is utilized to deposit matter in the sub-monolayer range. At the same time, secondary ion mass spectroscopy has been used to characterize the deposits and to estimate the total amount of matter deposited. Although plasma by itself is not studied in this project but it is consideredas a source of atoms. The crucial parameters studied in this project comprise the particle properties (such as energy and angular distributions) along with substrate composition and roughness.

In the first chapter, a general introduction to MD simulations, plasma treatments, SIMS and the storing matter technique as well as literature studies regarding projects of interest are provided.

The second chapter deals with the details of simulation and experimental conditions along with MD force field and instrumental descriptions.

The third chapter presents several sticking and deposition aspects of carbon on silicon (100). The first section of this chapter deals with single carbon deposition followed by continuous carbon deposition on silicon in the second part.

The fourth chapter describes the sticking behaviour of Ti on a silicon surface by sputter deposition technique and also validated by MD simulation results.

The fifth and final chapter consists of sticking and deposition of tungsten on silicon surface done by both MD simulation and storing matter combined with SIMS techniques.

State of Art

"Sticking and deposition during the initial stages of growth of any material to a product surface is an important industrial problem with many applications. A molecular dynamics simulation along with plasma deposition technique has been integral part of this work. A literature review related to this work has been presented in this chapter."

Chapitre 1.
State of the art

1) Introduction

In this chapter existing literature studies related to fundamentals of the SubML project will be presented. There will be four sections for the literature studies, which will complete the main overview of the thesis. These four sections will consist of literature studies of molecular dynamics simulations, plasma treatment, secondary ion mass spectroscopy and storing matter deposition technique. In the molecular dynamics (MD) simulation section, we described past literature studies on growth mechanism, microstructure, epitaxial growth, angle and energy dependence, etc. During the deposition, examples of compound materials which may form include SiC, TiSi, WSi etc. So, in this section we describe an overview of the different properties, characteristics and applications of these materials and a comparison with past literature review. Special attention will be given to the different parameters affecting the deposition mechanism at atomic scale.

2) Molecular Dynamics simulations: a literature review

i) Introduction

SubML project is executed in a multidisciplinary approach and MD simulation is one of the major approaches used to reach the objectives of the project. Before describing literature studies on MD simulations, we will have a look into several other simulation techniques, their use and why MD simulations are most suitable for the SubML project. Several simulation techniques exist to investigate plasma deposition processes. They include kinetic models, fluid models, Monte Carlo, particle-in-cell Monte Carlo collision simulations and MD simulations. Depending on the phenomena and the parameters to be investigated, the one or other technique is better suited. Fluid models are used to study the discharge and to understand the complex and coupled interactions and how they are affected by the design of the experimental setup and the operation conditions [1,2]. Kinetic models are used in a diversity of physico-chemical areas in which kinetic measurement provide significant physical insight [3]. Particle-in-cell simulations are widely used for the application to partially ionized gases. They have the advantage of providing kinetic information such as velocities of the species in the plasma [4,5]. Plasma–surface interactions are best described by Monte Carlo (MC) and MD simulations [6]. Examples for the MC method include among other studies on the discharge [7,8]. MD studies report on the sticking on surfaces [9], the growth of diamond carbon films [10] and others.

Computer simulations in surface science have grown rapidly during the past decades. Modelling with molecular dynamics simulation is considered as a beneficial complementary technique to several experimental approaches as it explores detailed understanding of chemical and physical processes at atomic and molecular level where the system properties can be controlled precisely and according to wish. The analytical results and the understanding from MD simulation are as valuable as experimental technique and can give a detailed insight into the phenomena when only limited information can be obtained from experimental conditions. In the molecular dynamics simulation of film deposition, an interatomic potential model is used and from the beginning of the simulations the system is then followed by Newtonian physics as the time progresses. Incoming atoms impinging the surface can be added to the system and the trajectories of atoms of the system can be followed till the system relaxes. In general, the processes occurring during the MD simulations vastly depend on the accuracy of the interatomic potentials which means that the latter need careful adjustment. The direct effect of energy of incident atoms on film structures can be achieved by MD simulation analysis. The results after the collisions give insights into atomic scale mechanism of low-energy many-body collisions during the thin film growth [11,12]. While dealing with low impact energies, MD simulations are the best suitable method as they produce a fully deterministic description of the studied system over short periods of time. The interactions between all the deposited atoms and the neighbouring atoms are thoroughly considered, which is very important because the projectiles with such low velocities experience the neighbouring chemical environment. During molecular dynamics simulations, atom trajectories can be traced, which is a great interest for particle surface interactions.

As numerical simulation is one of the major parts of the project, we will focus now on papers involving Monte Carlo (MC), Kinetic Monte Carlo (KMC), Density Functional Theory (DFT) and also MD simulations. Gleason et al. did a study on the growth of hydrogenated Si from SiH_3 and SiH_2 radicals (derived from silane) while choosing the location of impacts of the precursor on the surface arbitrarily [13]. They observed that the state of the final film is mainly determined by the surface diffusion of silicon containing species. McCaughey et al. did other investigations on the bulk and surface characteristics of amorphous hydrogenated Si deposition from silane plasmas [14]. They concluded that the physical characteristics of the film mainly are determined by the relative fraction of the radicals in the incident flux as well as the rate at which the radicals arrive on the surface. They also observed that the roughness of the films mainly rely on the sticking coefficients of the incident radicals as well as on the deposition rate to a lesser extent [14]. Several current studies involve DFT calculations, MD simulations, or KMC simulations or a combination of them. Ohira et al. performed MD simulations studies with a many-body semi-classical potential to observe the basic processes regarding microcrystalline silicon deposition with SiH_4 diluted by H_2 in a plasma enhanced chemical vapour deposition (PECVD) [15]. They observed the processes of crystallization of SiH_3 radicals, the processes of hydrogen desorption and Si structure stability at 500K substrate temperature. Bakos et

al. performed DFT calculations to understand pathways of reaction for the SiH_3 radical with Si as a function of the temperature and proved that SiH_3 inserted into strained Si-Si bonds is free of barrier [16]. They justified those results by MD simulation studies. In another paper, the aforesaid authors did studies on the formation of disilane and its responses with the sample surface by using the similar techniques [17]. Pandey et al. performed KMC simulations as well as DFT calculations and studied several surface kinetic events (radical-surface diffusion, surface hydride dissociation reactions, radical surface and adsorbed radical-radical interactions) to investigate the growth processes of amorphous silicon as a function of the substrate temperature [18]. Valipa et al. performed MD simulations along with DFT calculations to understand the surface smoothening processes in hydrogenated amorphous Si thin film deposition [19]. Gordiets et al. described a kinetic model to explain the process of thin film growth for films consisting of two components, like for example H terminated Si films [20]. Molecular dynamics studies regarding other materials involve surface migration and adsorption processes on α-Al_2O_3 by DFT calculations [21], sputtering and deposition on a polystyrene surface by CF_3^+ and $C_3F_5^+$ ions [22], the 3D distributions of sputtered and scattered products from Cu^+ and Ar^+ ion bombardment on Cu [23] or the energetic fluorine etching of SiC [24]. Other materials, which have been investigated by simulations involved diamond growth [25-27] or film growth of hydrocarbon on SiC [28].

For any molecular dynamics calculation, molecular mechanics force field is the most important form. It defines the forces between the particles in the system and the potential energy can be derived from the forces. If the force field is known for a system, successively momentum, acceleration, velocity and finally position of the particles can be deduced and determined.

ii) The choice of the appropriate force field

Force fields used during MD simulation studies are mostly classical force fields, where interactions depend only on the interacting elements and on interatomic distance. At the same time, interactions during such MD simulations are independent of chemical environment. The description of the plasma-surface interactions needs information on the deposition and reorganization of particles at a sample surface and also information of the particle energy and angle, as well as backscattering and etching. Therefore, it is necessary to consider the formation and breaking of bonds while doing MD simulations. Reactive force fields that include coulomb interactions with adjustable transfer of partial charges and environment-dependent covalent bonding are better suited than classical force fields (coulomb interactions with fix charges, or 2-body and 3-body interactions which do not depend on the chemical environment) to observe systems going under structural change. There are several such force fields which have been developed for different materials.

In recent years there has been a significant increment of interest for carbon film growth by low energy carbon plasma and ion beam deposition. Several experimental studies of carbon film growth provide

important data of surface structure, bonding state and properties of the film deposited by different techniques. MD simulation is one of the methods to understand atomic scale mechanism to get details of the structural descriptions. Pailthorpe et al. developed a Stillinger-Weber (SW) [29] class of interatomic potential for the modelling of both sp^2 and sp3 interactions in diamond like carbon [30]. They actually derived the potential from Hartree-Fock calculations for small carbon clusters in tetrahedral and trigonal configurations. The model has been applied for bulk diamond, carbon clusters and thin film forms of high density amorphous carbon. The SW potential is an empirical inter-atomic potential which was originally developed for silicon and is a sum over physically intuitive two body bond stretching and three body bond bending interactions [29]. This potential has been applied successfully to the study of bulk and surface properties of silicon, to the sputtering of silicon surfaces, to small silicon clusters and to bulk germanium [31-34].

Another interatomic potential developed by Tersoff [35,36,36], which includes the effects of coordination number to improve the description of silicon clusters and surfaces, has been successfully used to simulate the growth of amorphous carbon, and has been extended by Brenner to study carbon film growth from hydrocarbon species [27]. The REBO potential second-generation reactive empirical bond order potential energy, originally evolves from the Brenner potential and has been extended for hydrocarbon molecules and solid carbon [37]. It enables covalent bond breaking and formation with related changes in atomic hybridization based on a classical potential. This is related to the Abell-Tersoff bond order potential [38] which has already been utilized in preceding version of this potential [27]. Afterwards, this potential has been modified to incorporate oxygen, i.e. H-O, C-O and O-O bonds to the already presented C-C, C-H and H-H bonds [39]. This potential has been employed to the investigation of the chemical stability and structure of various polymer chains and molecules and to the modelling of chemical interactions within a series of molecules inside the limits of classical MD simulations [39-45].

Another reactive force field associating hydrocarbons has been derived by van Duin et al. [46]. The ReaxFF force field utilizes a general association between bond order and bond distance on one hand and between bond energy and bond order on the other hand which guides to proper dissociation of bonds to discrete atoms. In addition to the Brenner potential [27], it involves Coulomb and van der Waals interactions with a formerly developed approach to estimate charge distributions in molecules [47]. The charges within the system are permitted to evolve dynamically with the modification of atomic environment. The reaction and dissociation curves are obtained from quantum chemistry computations [46]. The force field developed has been continued to various systems, including silicon oxide and silicon [48,49], hydride of magnesium[50], materials with ferroelectric properties [51], platinum [52], nickel [53], gold [54] and to catalytic reactions [55-57]. This potential has been developed to include full chemistry of the breaking and formation of bonds, in addition to a proper description of the fully bound equilibrium geometry of complex molecules. However, its charge-equilibrium method, which

needs significantly larger computational efforts than classical force fields, limits the use of this force field to relatively small systems. Yu et al. [58,59] described a charge optimized many-body (COMB) potential for the Si/SiO_2 system, which is based on the modified Tersoff potential described by Yasukawa [60] to reduce the drawbacks of the ReaxFF potential (vast computational resources), and yet produce correct results for the Si/SiO_2 system. The effect of charge transfer is accounted by the many-body interactions and electronegativity equalization principle.

There is another reactive force field which is developed by Kieffer et al. at the University of Michigan [61,62]. This potential involves Coulomb interactions, directional covalent bonds, a torsion term and van der Waals interactions. Important traits regarding this force field during simulating of systems which undergo substantial structural changes are (i) the capability to consider for the redistribution of density of electrons upon formation, ionization, or breaking of bonds, within a charge transfer term, and (ii) the characteristics that the change in the coordination number of an atom arises because of dynamical angular constraints.

In fact, the potential by Kieffer et al. was originated and successfully applied for inorganic materials [61,63-68,68,69]. Within the Kieffer potential, a large number of silica polymorphs, including α- and β-quartz , α- and β-cristobalite, stishovite, X-I silica, high-stishovite, and amorphous silica can be computed with a single parameterization demonstrates to the transferability of the potential [62]. Later on, the force field was adjusted for the computation of polyamorphic transitions in vitreous B_2O_3 under pressure [65] and polyhedral oligomeric silsesquioxane POSS nano-assemblies [70] multiscale simulations have been studied.

iii) MD studies on epitaxial growth, reaction mechanisms and adhesion

Several studies are done to observe how the energy affects the atomic scale mechanism during the film deposition. For example during the deposition of silver atoms on a Ag(111) substrate, it was found that increasing the energy of the depositing Ag atoms from 0.1 to 10 eV altered the film growth mechanism from an island-growth mode toward a layer-by-layer mode[71]. The primary mechanism for the redistribution of deposited atoms was found to be the collapse of unstable clusters for the 0.1 eV deposition and displacements of surface atoms by ballistic collisions at 10 eV[71]. For energies of l0, 20 and 40 eV, further simulations showed that an interface mixing phenomenon occurred via an atom exchange mechanism at the surface. The mechanism of this surface exchange was activated by ballistic collisions, but was also assisted by thermal vibrations of the substrate lattice [72]. Epitaxial growth can be achieved by using the energetic atoms for depositions [73]. Some studies by molecular dynamics simulations have been done also at different temperatures to observe the temperature influence on growth mechanisms. J. Tarus and K. Nordlund did a molecular dynamics simulation study on Si_{20} cluster deposition on Si(001) at two different temperatures (300K and 1000K) [74]. They found a significant change in epitaxial growth at 1000K but they did not find any kind of epitaxial

growth at 300K. In addition, their study reveals that there is an amorphous film on the substrate and an advancing crystalline amorphous interface below it. Biswas et al. did a study for single cluster impacts on the Si(111) surface by assuming the fact that a high surface diffusion and spreading of clusters are needed to achieve the epitaxial growth [75]. There are several important technological interests to grow a film in layer by layer formation. G. Betz and W. Husinsky studied the sputtering and ion assisted deposition by molecular dynamics simulation along with kinetic Monte Carlo (KMC) simulations for Cu ion bombardment on Cu (100) surface [76]. In their study they found that the energy required per atom for homo-epitaxial growth of Cu on Cu (100) is around 20 eV. Shin-PonJu carried out a general molecular dynamics study of the deposition rate dependence of film morphology on the sputtering process [77]. In his study, the impact of incident atoms is modelled by using rescaling technique. He showed that the influence of the deposition rate on the thin film morphology is more significant at high incident energy (sputtering) than at low incident energy (evaporation) and he found also that the incidence energy has a significant influence on the coverage percentage (Fig. I-1).

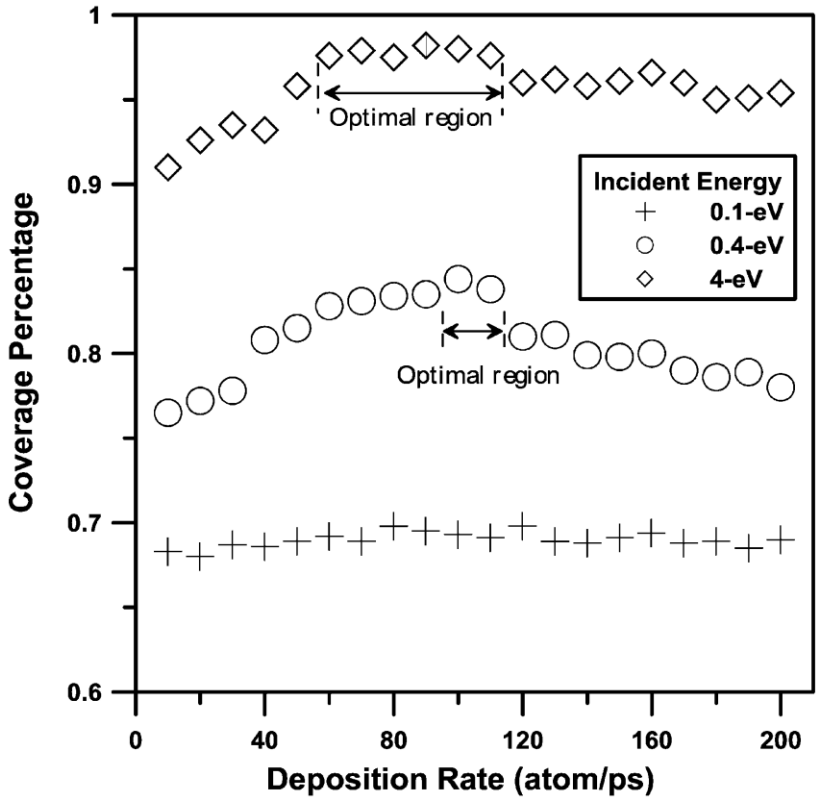

Fig. I-1: Change in coverage with energy of the incident particles [77]. Y axis represents coverage and not coverage percentage as marked on figure.

Yanhong Hu et al. used a molecular dynamics study to estimate the percentage of adhesion of carbon atoms in the incident C_{20} beam as a function of incidence angle [78]. The study revealed that the amount of adhesion decreases as the angle increases and is insensitive to cluster energy. H. Lan and Z. Kang

performed a molecular dynamics study of the growth of amorphous carbon films with a modified Tersoff potential with impact varied from 1 eV to 50 eV [79]. They investigated the effects of the incident energy on growth dynamics and film structure. According to their study, the mobility of surface atoms in the cascade regime is enhanced by the impact of energetic carbon atoms. They showed how the distribution of DLC films varies with incident energies (Fig. I-2).

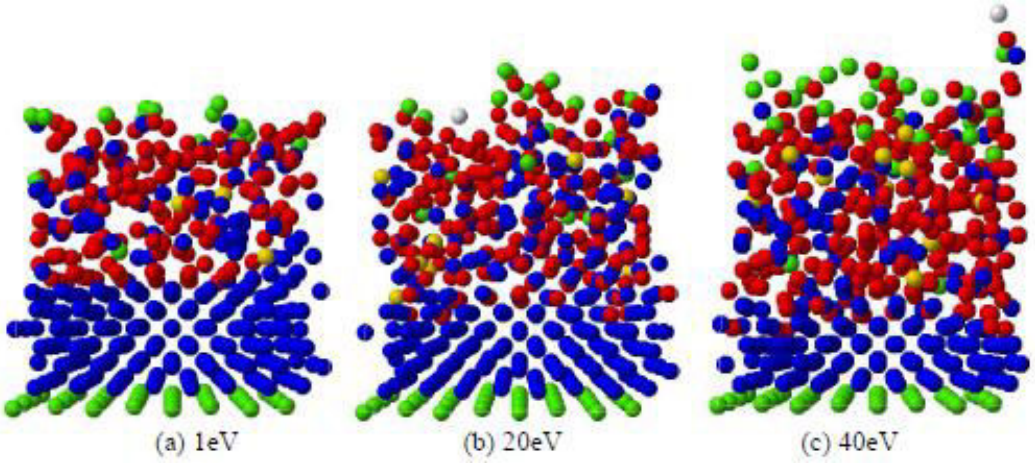

Fig. I-2: Comparison of growth dynamics and film structures with energy .yellow, blue, red, green and grey spheres are sp^4, sp^3, sp^2, sp^1 and sp^0 hybrid carbons respectively [79].

H. Chen et al have investigated deposition of Cu clusters on a pristine Cu substrate and on a substrate partially covered by Cu clusters by molecular dynamics simulations. They mainly focussed on three quantitative items: flatness of primary deposition, adhesion between cluster and substrate, and degree of epitaxial growth to get the characteristics of thin film [80]. Some molecular dynamics studies are carried out also to investigate the reaction mechanism at the interface while doing deposition of one material on a substrate. Y. Ishikawa et al. did a study by a combined approach of MD and DFT to observe the insight of reaction mechanism while doing electro-oxidation of hydrogen at the Pt(111)/water interface [81]. E. Zaminpayma et al. did an investigation to understand quantitatively the interaction mechanism between the cluster atoms and the substrate atoms by molecular dynamics simulation with EAM potential. They described the interactions of Co clusters with an Al (100) substrate and influence of cluster size and the initial velocity of clusters [82]. S.G. Lee et al. investigated a quantitative approach for the surface characterization during the early stages of epitaxial growth of Fe and Cu on Cu(111) substrate using molecular dynamics and molecular statics methods at low incidence energy 0.1 eV [83]. H. Zhang and Z.N. Xia described a simulation study on thin film properties and formation of Al cluster beam on a Si(100) substrate [84]. They describe in details the cluster migration distance and Al thin film structure in different conditions.

iv) MD studies on angle dependence

T.H. Fang et al. described an investigation of deposition mechanism of ionic beam sputtering (IBS) with incident energy, incident angle and deposition temperature for nickel films deposited on substrate of Si (100), Indium Tin Oxide (ITO) and glass [85].

The authors showed how the surface roughness, grain size and density of the film change with energy and angle (Fig. I-3). They explained that higher incident energy provides an opportunity for surface diffusion reconstruction to obtain a smother surface and a smaller average grain size as shown in Fig. I-3a. In the other figures, while the incident energy is higher, the sputtering rate is higher, which prompts rising density of the thin film.

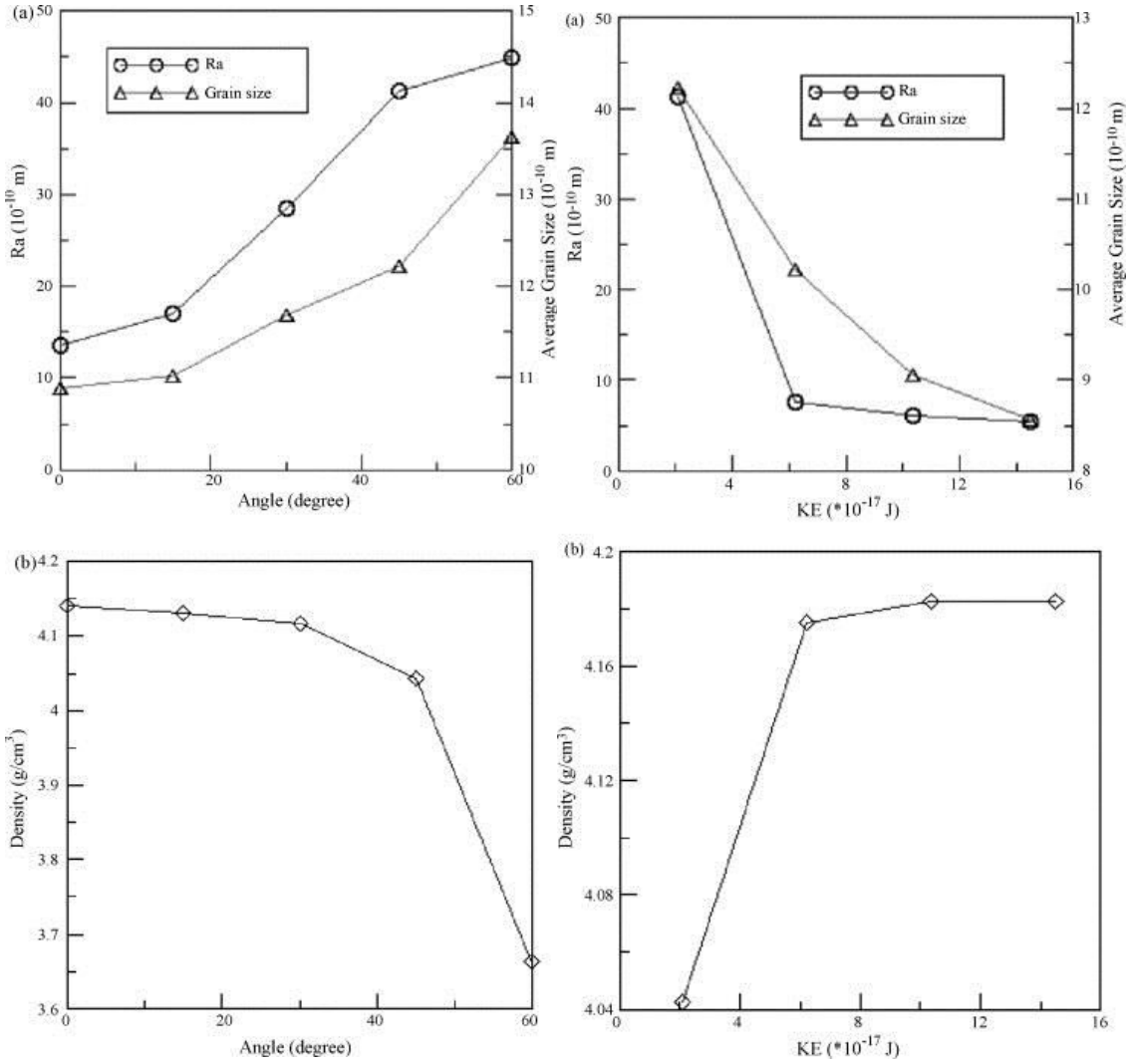

Fig. I-3: Dependence of grain size, roughness (a) and density of the film (b) with incidence angle with respect to the surface normal (left) and kinetic energy (right) of incoming ions [85].

v) MD studies on film microstructure

The bombardment of energetic particles during the deposition might significantly change the film's microstructure and its properties during sputter deposition. Several effects have been studied while doing the deposition of film atoms with essentially thermal energies and bombardment by reactive inert gas ions in ion beam assisted deposition (IBAD), ion beam sputtering deposition (IBSD), and energy filtered ion beam deposition(IBD)[86,87]. A wide change in energies from eV to keV was done while doing IBAD processes and the effect of activation of surface processes at the growth surface, lattice displacements and ion implantation well below the first monolayer have been observed [72]. In recent time, the low-energy ion assisted depositions values (<100 eV) for the interest of relative activation of surface processes were used, which results in the improvement of film properties [72]. Furthermore, increasing the energy induces bulk lattice displacements and sputtering of deposited atoms.

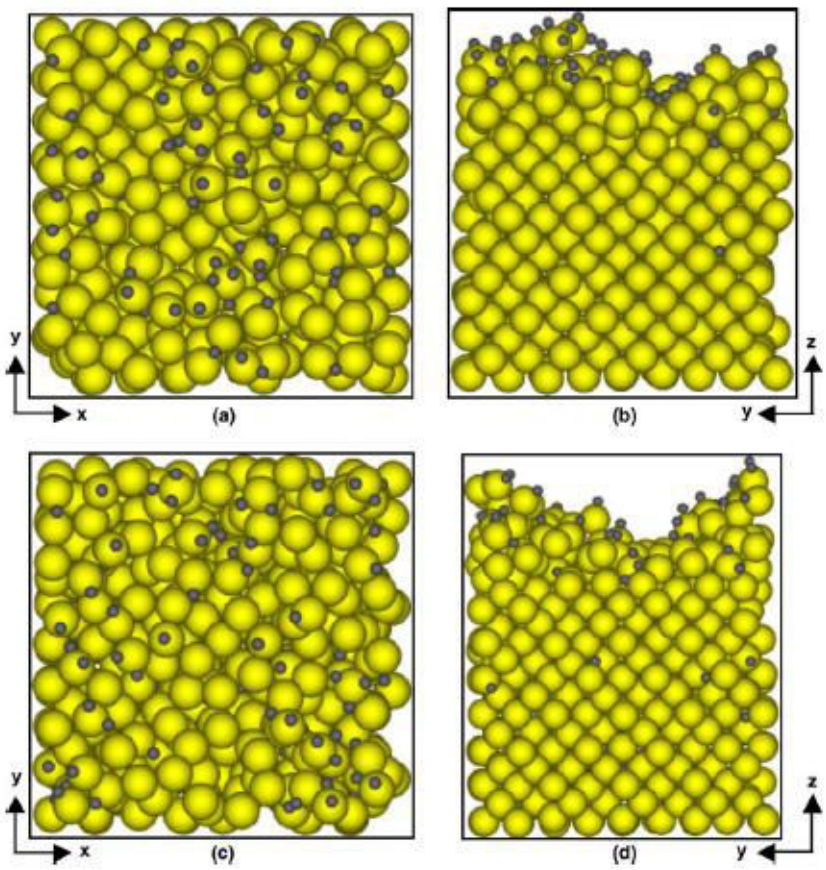

Fig. I-4: Evolution of (a) and (c) surface structure as viewed along the [001] direction and (b) and (d) film structure as viewed along the [100] direction, during MD simulation of a-Si:H film growth at a substrate temperature of 773K. The corresponding duration of simulated film growth is (a) and (b) 1ns and (c) and (d) 2ns. In (a), (b), (c), and (d), large yellow spheres and smaller dark-gray spheres represent Si atoms and H atoms bound to the Si atoms, respectively. In (a) and (c) the surface area shown is 21.7 Å x 21.7 Å. The areas shown in (b) and (d) are 27.7 Å x 21.7 Å, and 30.3 Å x 21.7 Å, respectively [19].

M. S. Valipa et al. did a study on atomic scale analysis of fundamental processes that determine the surface structure and smoothness during plasma deposition of hydrogenated amorphous silicon thin films [19]. They investigated the surface smoothness over different period of simulated growth time and compare the results. Fig. I-4 gives the surface structures viewed along different directions and for different growth times.

Several other cluster depositions are done by molecular dynamics simulations. J. C. Jimenez-Saez did a molecular dynamics simulation study for Ni cluster deposition on a Cu (001) surface [88]. The study was mainly focusing on the understanding of the relation between the number of grown monolayers and changes in the atomic positions near the interface. A low energy ion radiation study by molecular dynamics simulation of Cu deposition on Mo (100) substrate has investigated by B.S. Bunnik et al. [89]. Due to the energetic impact of incident atoms, wetting phenomenon and different film structure were observed

3) Plasma treatment

i) Introduction

Plasma can be defined as an ionized gas phase with a mixture of ions, electrons, photons, radicals and neutral atoms. In this work, they are not investigated by themselves, or used during experiments. However, the PhD work is a fundamental study on the interaction of few-eV energy atoms, i.e. energies similar to those found in plasmas, with surfaces in order to understand the sticking and deposition mechanisms with perspective to obtain results which could be used in later steps to improve plasma processes.

In most of the cases in laboratory, plasmas are formed by applying an electric field which produces accelerated electrons. Through collisions with atomic and molecular species, these electrons dissociate, ionize and excite the gas phase species and form plasmas. Plasma occupies more than 99% of the Universe, and we are living (on Earth) in the 1% where plasma does not predominate [90,91]. Various kinds of plasma exist. They can be classified according to their electron density and electron energy (or temperature).

Due to the presence of various products issued from the plasma kinetics (dissociation, ionization, recombination, excitation, etc.), plasmas are much more reactive than the natural gas mixture in which they are sustained. So, such reactive plasmas are of great interest in plasma surface interaction and therefore in surface processing.

Plasma based processes are efficient, environmental functional, non-polluting and economical tools for surface treatment. The use of plasma-assisted surface treatments has been explored over many decades in various application fields like textile industry, solar cell industry, semiconducting industry,

medicine, aeronautics, automotive, plasma display, etc. In more, plasma process is a very easy and flexible method, where modifications of surface properties can be made for different materials within a certain experimental device.

In order to have a better understanding of plasma – surface interactions, experimental studies as well as numerical studies can be very efficient ways to explore where early stages of deposit, island formation, roughness etc. can be detailed by varying different significant parameters.

K. Fukushima et al. investigated the effect of plasma conditions on the ion fraction and the ion energy distribution of Ti flux in RF-plasma enhanced magnetron sputtering [92]. Fig. I-5(a) shows that the ion energy distribution shifts to higher energies as the coil power increases. Fig. I-5(b) describes that the number, the mean energy and the ion power of the Ti^+ flux all increase monotonically with increasing the coil radio frequency power.

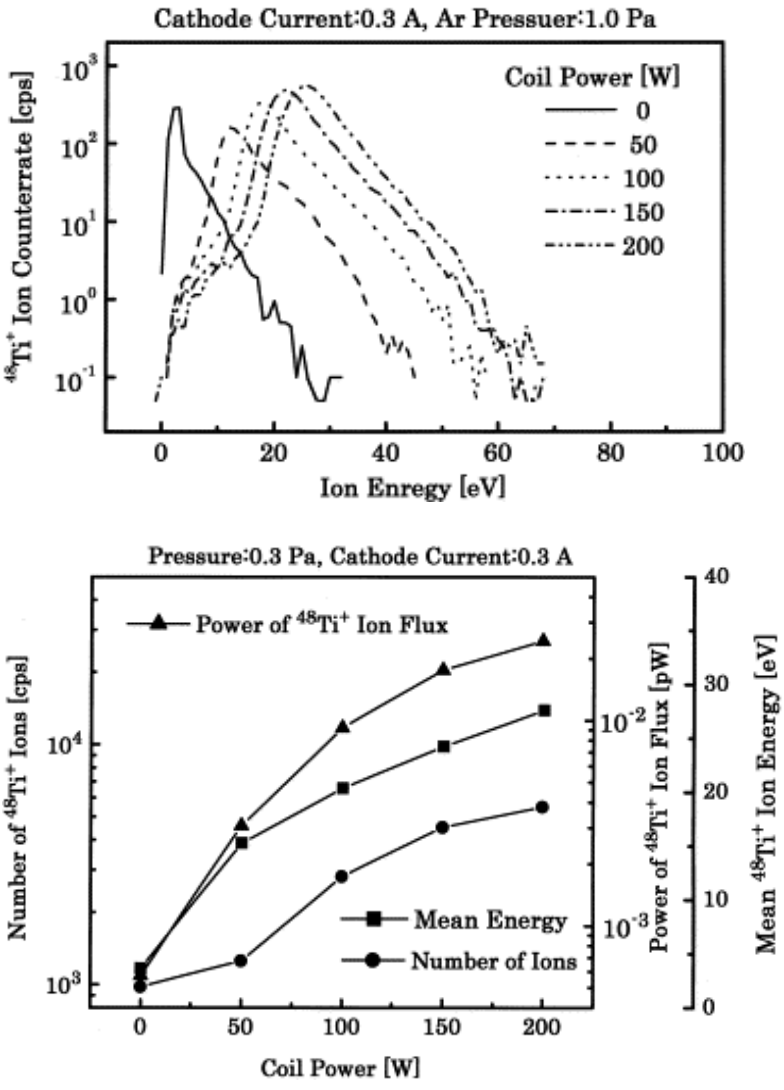

Fig. I-5: (a): Ti^+ flux energy distributions for various RF coil powers. (b): Number, mean energy, and ion power of Ti^+ flux arriving to the substrate as a function of coil RF power.

Another study for plasma surface treatment effect on TiO_2 thin film was carried out by Y. Chiba et al. [93]. In this study, the TiO_2 thin film surface formed by RF reactive ion planting was bombarded by the plasma which consisted of Ar, H_2 and CH_4. After the bombardment they found out that the adsorption edge of the TiO_2 film is shifted to the visible light. G. J. Wan et al. investigated the characteristics and surface energy of silicon doped diamond like carbon films fabricated by plasma immersion ion implantation and deposition [94]. They showed that the sp3 configuration including Si–C bonds increases with higher silicon content, and oxygen incorporates more readily into the silicon and carbon interlinks on the surface of the more heavily silicon-doped DLC films. X. Zhang et al. described a process of surface modification of carbon fibers by plasma graft of silsesquioxane [95]. They showed that the oxygen/carbon and silicon/carbon ratios increased rapidly after the plasma graft silsesquioxane treatment, which results in the improvement of interfacial bonding between carbon fibre and polyarylacetylene (PAA) and enhances the weight of wetting.

P. Rai et al. studied the influence of carbon precursors on thermal plasma assisted synthesis of SiC nanoparticles [96]. They investigated the effect of plasma processing on the structure and morphology of SiC where SiC is synthesized by two solid state methods (a) carbon black and (b) activated carbon. Fig. I-6 shows that the intensity of diffraction peaks for SiC synthesized by activated carbon is higher than the carbon black which means that crystallinity is higher in case of activated carbon.

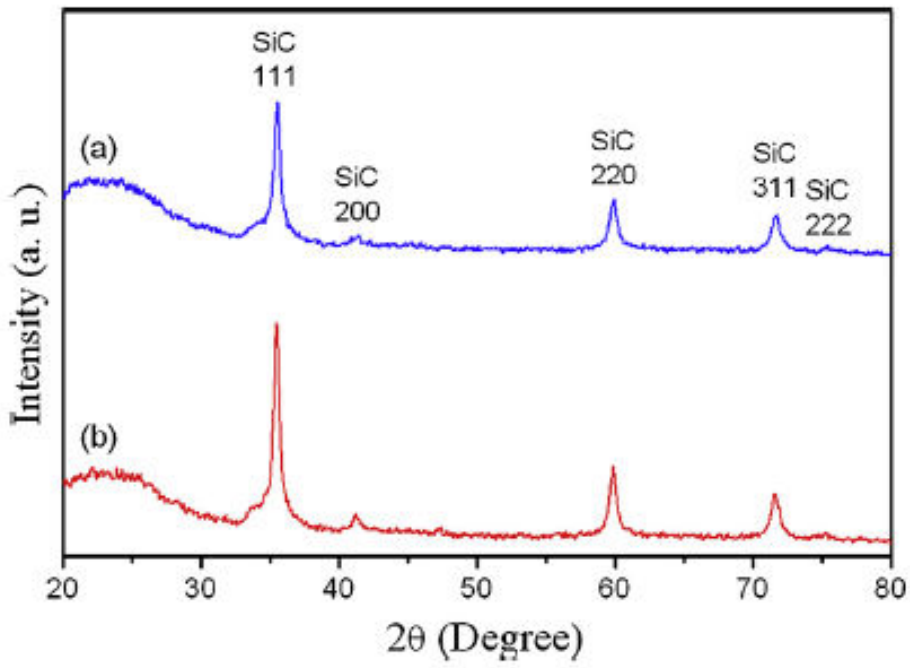

Fig. I-6: XRD peaks for the verification of crystallinity of activated carbon and carbon black [96].

4) Secondary Ion Mass Spectroscopy and sputtering processes

i) SIMS analysis for inorganic materials

Secondary Ion Mass Spectroscopy is a very sensitive and powerful technique with a large dynamic range and a good mass resolution for the characterization of thin films and bulk systems. It is widely used in various fields to investigate phenomena such as implants and thin films in the semiconducting industry, the chemical mapping of biological samples etc [97,98]. The whole concept of SIMS is about bombarding the sample surface by an ion beam, called primary ion beam, and to detect the sputtered ions which are called secondary ions. During the analysis the secondary ion counts of the different masses are recorded sequentially as a function of depth, which is called a depth profile. To obtain a depth profile, a higher primary ion fluence is used which leads to the erosion of the sample. Detection limits can be as low as in the ppb range. Depending on the analytical conditions, the depth resolution can be below 1 nm.

ii) Sputtering by ion/particle bombardment

When the surface of a solid is bombarded by energetic particles, surface atoms are removed due to series of interactions between the primary ions and the target atoms. This phenomenon is usually called sputtering. The surface becomes eroded and morphology of the surface may change depending on the irradiation conditions. The sputtering of a target atom occurs only if it gains an energy component normal to the surface greater than the binding energy of the surface. This explains also why the sputtering is mainly limited to atoms of the two topmost atomic layers of the sample. These processes are mainly called physical sputtering [99]. Depending upon the energy of the incident ion/particles and the collision cross section between the incident atoms and the atoms on the surface of the solid, several collision regimes have been identified during physical sputtering [100,101].

The sputtering yield is defined as the numbers of atoms sputtered from the surface of the solid per incident ions:

$$Y = \frac{Number\ of\ sputtered\ atoms}{Number\ of\ primary\ ions} \qquad \text{(I-1)}$$

The sputtering yield depends on several parameters of the primary ions (impact energy, incidence angle, mass) and also on the solid target properties [99].

For SIMS analyses, several key points can be noted:

(a) The ion beam should be well focused and well defined in terms of energy width and in terms of angular divergence. This leads to a homogeneous erosion of the sample. The primary beam should be mass analysed in order to discriminate molecular ions from atomic ions.

(b) During the initial stage of bombardment, the amount of primary ions being implanted into the target material is higher than the one being sputtered, which will modify the secondary ion yield depending on the reactivity of the primary ion species. Indeed, ionisation processes in SIMS depend on the local sample composition. Therefore, any change in the surface atom environment may result in a change in the secondary ion yields and also the sputtering yield. Similarly, in the case of thin film analysis, if the investigated layer is too thin, the underlying substrate may influence the secondary ion yield and sputtering yield [102].

Besides experimental observations, several computer simulations by binary collision approximations have been done to measure the sputtering yield. B. Guzmán de la Mata et al. investigated sputter yield variations of diamond films under bombardment with low energy ions. Fig. I-7 describes the sputter yield variations as a function of angle for cesium beam at 500 eV [103]. The behaviour has almost same trend for three different materials. The sputter yield increases for lower range of angles (<50°) and becomes maximum between 40° and 70°. This behaviour is true for any analytical conditions in dynamic SIMS, i.e. monatomic primary ions and energy in the keV range. They explained that the decrease is due to enhanced scattering of the caesium at glancing angles and may also be due to onset of roughness. In their work, they observed also the variation of the sputter yield by using 500 eV O_2 beam. In this case they found only increasing nature of sputter yield with angle even at 70°. Data for larger angles is not available, but the sputter yield is expected to decrease at some point [103].

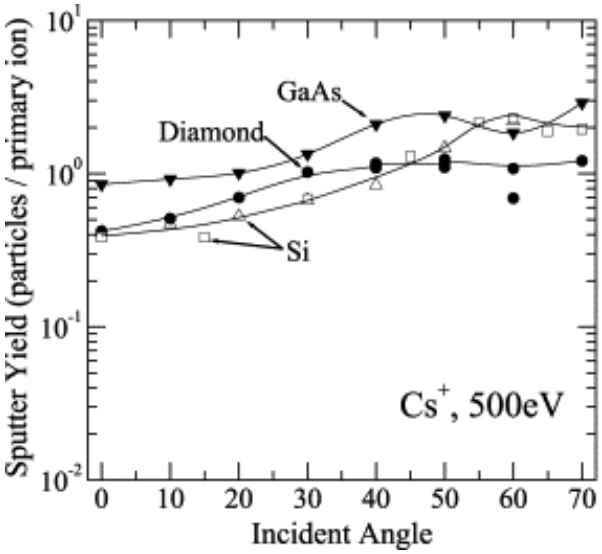

Fig. I-7 : Sputter yield dependence on angle for several materials bombarded with a 500eV caesium beam taken from reference [103].

Fig. I-8 describes the dependence of sputter yield on impact energy. The experiment was done at 50° incidence angle with respect to the surface normal for a caesium beam by B.G. Mata et al. In the energy range for SIMS, the sputter yield increases with energy for all the materials [103].

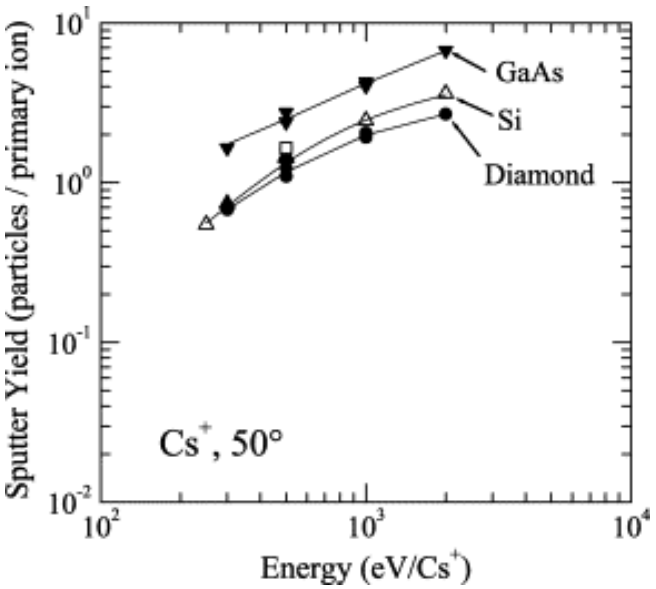

Fig. I-8: Sputter yield dependence on energy for GaAs, Si and diamond bombarded with a caesium beam at 50° to normal incidence as taken from reference [103].

iii) Angular distributions of the emitted particles:

Under ion bombardment, both the collision cascade theory and the linear transport theory of sputtering give cosine like angular distributions:

$$\frac{dY}{d\Omega} \propto cos^n \theta \qquad \text{(I-2)}$$

Where Y is the sputtering yield, Ω is the solid angle, θ is the polar angle of the emitted particles and exponent n varies between 1 and 2. It is important to notice that the equation of the emitted particles is independent of the incident angle. Scharmann's group [104-106] showed the polycrystalline angular distribution of differential sputter yield in the energy range of 100-1000keV. Fig. I-9b shows an example of the angular distribution up to 130 keV. As seen above, the angular distributions of the sputtered species reflect the atomistic process occurring during the sputter event to some extent. Therefore, it is important to have information about the angular distribution of the sputtered species. In literature several experimental observations with different species for determining angular and energy distribution can be found for different bombardment conditions.

During the sputtering process, the sputtered flux consists of several species. The species may include neutral atoms and molecules, ions, charged fragments, radicals, as well as excited atoms. The angular distribution varies due to the structure of the solid material. The emission characteristics may change because of the orderings of the crystalline lattice sites of the species to be sputtered. This property is well observed in case of single crystalline sputtered species but the case might be different for polycrystalline materials. If the sputtering specie is amorphous, this effect will be null [107].

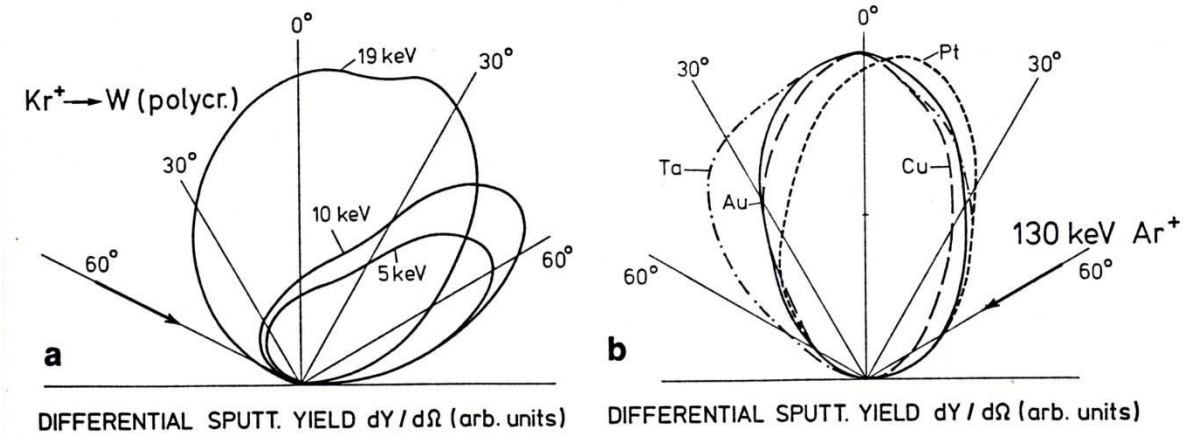

Fig. I-9: Emission distribution from various polycrystalline targets at oblique projectile incidence. With increasing energy, ejection is determined more and more by random collision cascades, resulting in axially symmetric intensity distributions around the surface normal [107].

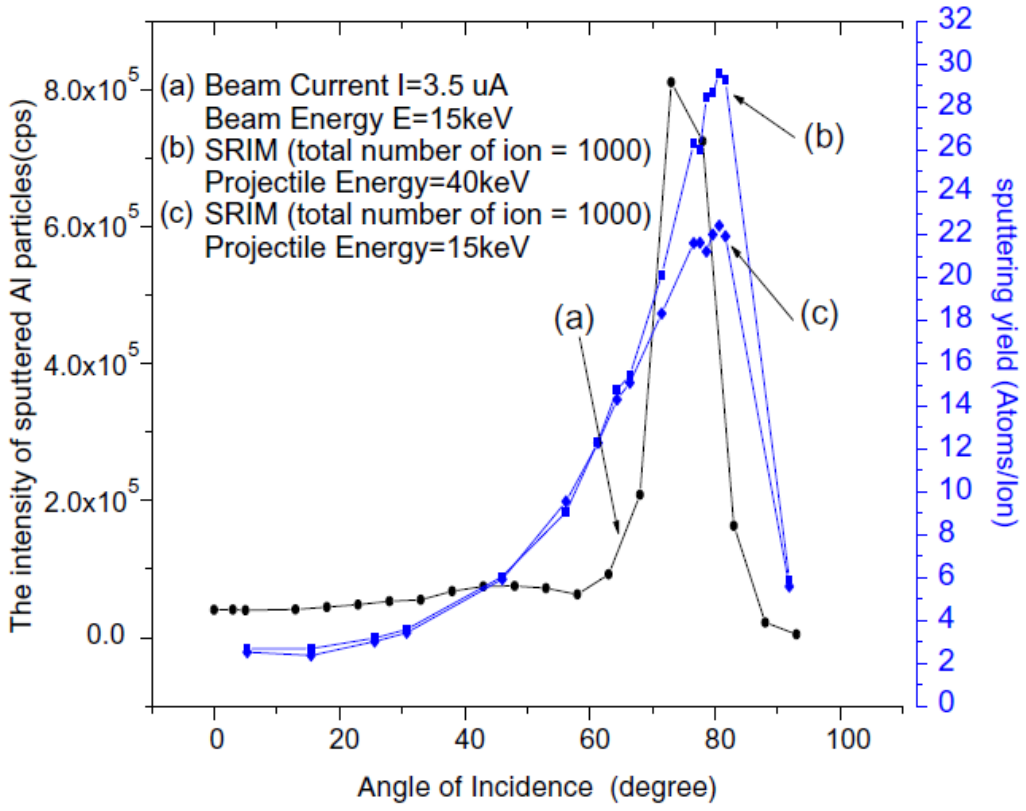

Fig. I-10. (a) The intensities of sputtered Al particles versus the angle of incidence induced by a 15 keV Ar bombardment of Al target. (b, c) The SRIM-based simulation obtained sputtering yields for Al polycrystalline target by 40 and 15 keVAr$^+$, respectively [108].

Along with the experimental observations, several computer simulation studies have been done also to specify the emission characteristics. Classical molecular dynamics simulations can be used to illustrate the phenomenon of sputtering. Also TRIM/SRIM software using the binary collision

approximation is also used to describe the sputtering processes. C.S. Lee et al. investigated the angular distribution of Al and Ar sputtered particles induced by ion bombardment using a 15 keV argon ion beam [108]. They employed the SRIM simulation program also to obtain the sputtering yield of Al atoms. They compared the angular distribution of sputtered Al particles and sputter yields for both experiment and SRIM simulation shown in Fig. I-10. They described that the maximum intensities of sputtered Al particles come at 75° and 78° respectively. The shift in the maximum of the angular distribution might come from the binary collision approximation in SRIM. There are differences in the slope between experimental curve and simulated curve. The difference arose mainly due to the difference in cleanliness of the target surfaces used in two conditions. [108]

5) The Storing Matter technique

The Science and Analysis of Material (SAM) department at CRP-Gabriel Lippmann is well organized with many high quality instruments for surface and bulk analysis and it acquired a wide range of experiences in instrumental development relating quantification issues in SIMS. The storing matter technique is one of the important examples to resolve the quantification problems in SIMS.

The storing matter technique is a newly developed analytical technique in SAM [109]. It has applications to both organic and inorganic materials [110,110,111,111-113,113]. It decouples the sputtering event of the element from the subsequent analysis step,. At the beginning, the surface of target material is sputtered by a well-focused ion beam, and the ejected sputtered particles (ions, neutrals, radicals) are collected and deposited at a sub-monolayer level on a dedicated collector. The full process remains under UHV condition to minimise contamination and oxidation issues. In the next step, the sub-monolayer deposits are characterized in an analytical instrument (basically static and dynamics SIMS). The transfer carried out also under UHV condition from deposition chamber analytic instrument. As the deposit is in sub-monolayer range, the matrix of the collector surface is controlling the ionisation processes during the SIMS analyses. Hence, the secondary ion ionization probabilities do not depend on the composition of the initial sample, but only on the collector surface. As the collector surface composition is well known, the matrix effect can be avoidable and quantification in SIMS can be enhanced. At some point also, the sensitivity can be kept high by choosing the right collector material which will allow for the optimisation of the subsequent SIMS analysis of the deposit. For example, the ionisation yields of positive secondary ions in SIMS are enhanced by substrates with a high work function. Thus to make the quantification easier, the different SIMS analysis mode (M^+, M^-, cf. chapter 2) and the collector surface (or matrix) are chosen according to the element(s) to be analysed.

This new analytical technique was first described by T. Wirtz and H.N. Migeon in 2008 [109]. In the successive years, several developments for different applications have been published [110,110,112,112,114,115]. The idea of assembling this prototype instrument was first proposed by G. Slodzian

[116]. As previously mentioned, the composition of the collector surface is important for the control of the ionisation processes in SIMS. In this regard, the collector treatment is an important aspect to optimize the chemical state of the collector surface. Metal surfaces with high work function can enhance the positive secondary ion emission and metal surfaces with a low work function can enhance the negative secondary ion emission[113]. Gold or silver coated collector surfaces can produce cationisation for organic information [112,117]. These are the factors which can influence while choosing the collector material for getting higher sensitivity.

The sensitivity of the Storing Matter technique is given by the Storing Matter useful yield UY_{StoMat}. Before this parameter can be defined, the classical SIMS useful yield needs to be defined:

$$UY_{SIMS} = \frac{N_{detected}}{N_{sputtered}} \quad \text{(I-3)}$$

where $N_{detected}$ is the number of secondary ions of a given species detected during the SIMS analysis and $N_{sputtered}$ is the number of atoms of the same species sputtered during the same analysis.

As not all atoms sputtered during the deposition process stick on the collector surface, the sticking coefficient γ needs to be defined. Finally, the storing matter useful yield is given by the equation below:

$$UY_{StoMat} = \gamma \cdot UY_{sims} \quad \text{(I-4)}$$

For this thesis work, the main parameter of interest to investigate was γ. The relationship between the different parameters and the Storing Matter process is depicted in Fig. I-11 below.

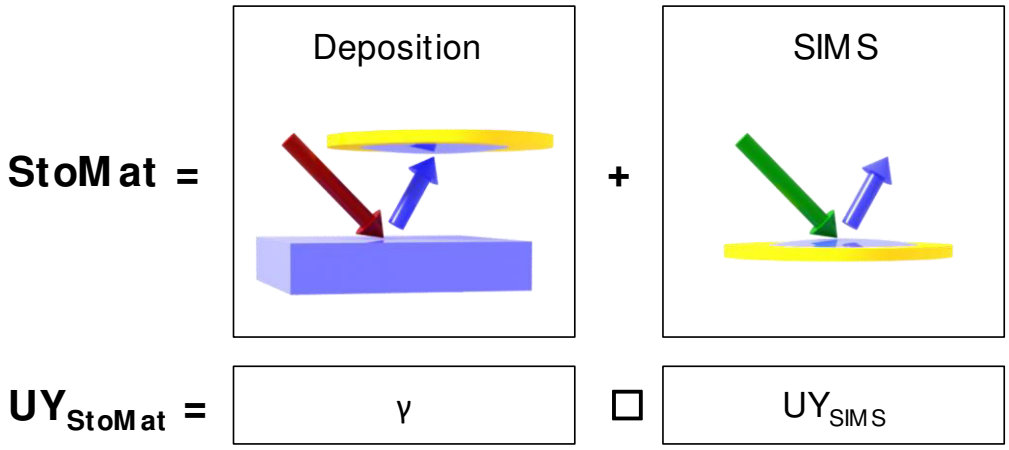

Fig. I-11: relation between useful yield of storing matter and SIMS.

The useful yield of storing matter technique on Ge(100) was determined by C. Mansilla et al. While doing this study, they investigated the influence of several different collector surfaces (W, Ta and Al) on the storing matter useful yield. They found that the collector surface with low work function has

the highest useful yield. According to their study, the useful yield for these materials on Ge (100) varies between 10^{-5} to 10^{-6} (Fig. 1-12) [113].

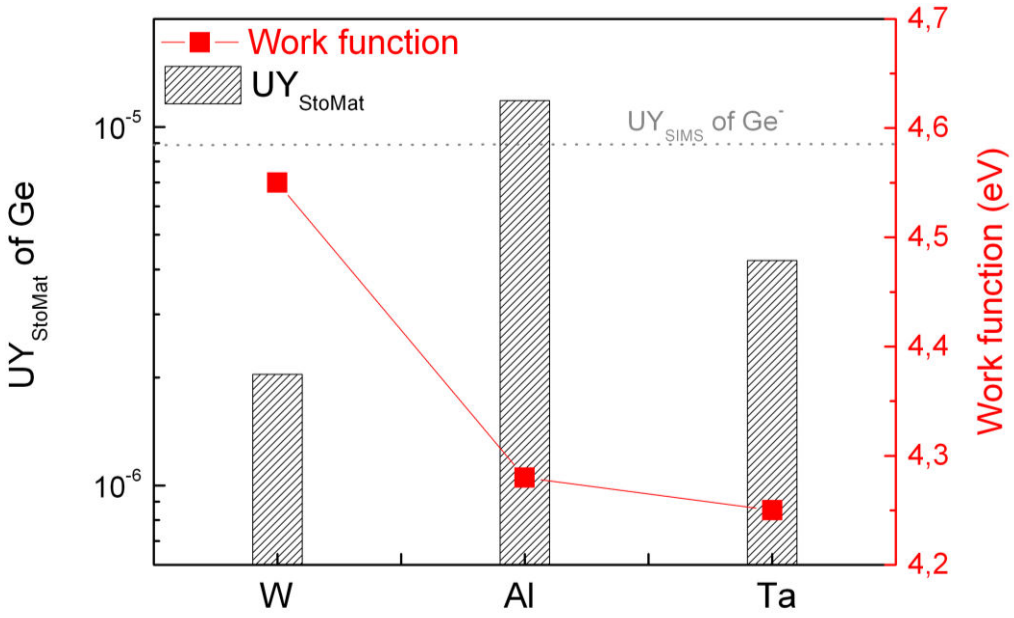

Fig. I-12: Useful yield of storing matter on Ge- for different collector surface [113].

Another application of storing matter to inorganic samples was investigated by C. Mansilla and T. Wirtz for the analysis of boron-doped and implanted SiO_2/Si [118]. In this work, they showed how the matrix effects can be avoided from traditional SIMS by using storing matter technique (Fig. 1-13).

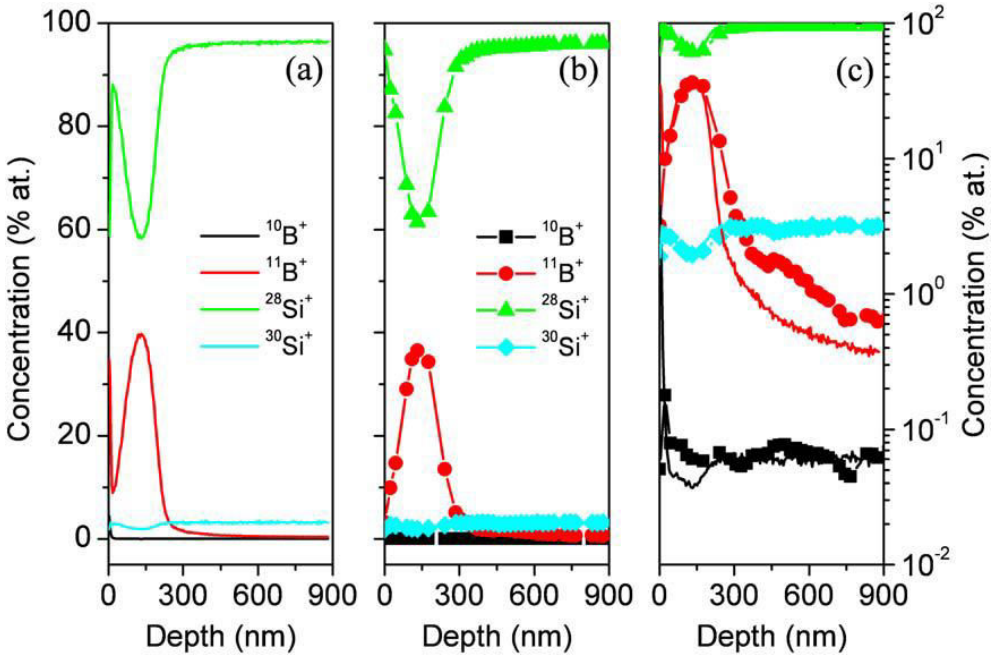

Fig. I-13: absolute concentration depth profiles for the B-implanted samples measured by (a) traditional SIMS (b) storing matter (c) as well as their overlay [118].

However, several other inorganic materials have been tested by other users for storing matter but experiments for the calculation of sticking coefficient for titanium and tungsten have not been done before. Calculation of useful yield of tungsten (W) as a collector surface on Ge (100) was performed by Mansilla et al. [113], and Philipp et al. [110] studied the useful yield of titanium (Ti) in storing matter instrument but sticking efficiency of Ti and W on Si (100) was never investigated before in storing matter instrument. Another material of interest to be tested was carbon on silicon on storing matter instrument but we did only simulation calculations for carbon as it is very prone to contaminations. In the following chapter, we will discuss details of the techniques and results related to sticking and deposition of carbon, titanium and tungsten on silicon surfaces.

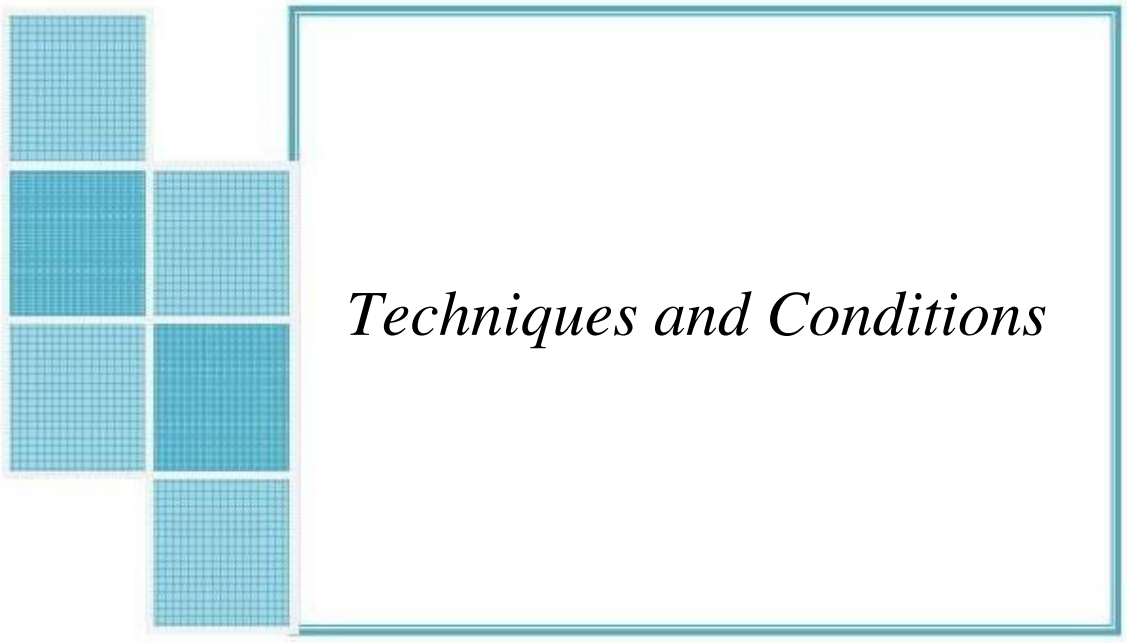

Techniques and Conditions

"This PhD work involves both experimental and simulation analysis. The details of techniques and conditions implemented for different inorganic particle interactions are discussed in this chapter."

Chapitre 2.
Techniques and conditions

1) Introduction

As the SubML project deals with a multidisciplinary approach, several techniques have been employed to accomplish the project targets. The main three techniques used in the SubML project are molecular dynamics simulations, sputter deposition in the storing matter instrument and SIMS analysis technique. We will describe first molecular dynamics simulation details followed by storing matter and SIMS description along with the conditions used during the project.

2) Simulation techniques

For the numerical simulation work of this project, we choose MD method as it is the most promising simulation tool to provide a totally predictable description of the system of interest over short span of time and it provides detailed explanations of the atomistic characteristics during the deposition process. For the simulations we used the MD code (FLX) developed by J. Kieffer et al.[61,61] which was developed for the modeling of materials with mixed ionic-covalent bonding character. As such, FLX offers a choice of interaction models, including Lennard-Jones, Coulomb, Born-Mayer-Huggins, three-body, and Kieffer's model of charge-transfer. FLX uses a fifth-order Gear predictor-correct scheme for the integration of the equations of motion.

FLX gathers input from one or maximally two files, the control file and a configuration file. The control file contains information about the chemical constitution of the system to be simulated and run-time options pertaining to the collection of statistical information. The configuration file contains the initial coordinates, velocities, instantaneous forces, 3^{rd} and 4^{th} derivatives of all dynamical variables. This file is only necessary if a system's evolution is observed over subsequent runs, i.e., the initial configuration of one run is typically the ending configuration of a preceding run. For new runs, the positions within a unit cell are defined within the control file. The configuration file also contains information about the run history of a configuration, allowing one to trace the evolution of a structure and the various conditions that it has been subjected to.

We will describe now the pressure and temperature algorithms used in FLX. Constant pressure general Parinello-Rahman (PR) (9 degrees of freedom) algorithm has been used in the calculations. The general PR algorithm includes 9 parameters to define the simulation box. They are 3 length and 3

angle parameters and rest of three parameters are used to describe the orientation of simulation box in space. Velocity rescaling has been implemented for temperature control.

FLX establishes and updates a nearest neighbour list to determine the atoms that are covalently bound. The neighbour list helps reducing the calculation time by limiting the calculation of the interatomic interactions to neighbouring atoms. For charge transfer and tree-body interactions, a list with the nearest neighbours is used. For the repulse term, an extended neighbour list is employed. The amount of charge transferred between pairs of atoms is δ_{ij} Moreover, the total amount of charge added or removed from any given atom depends on the amount of charge transferred from each neighbour. In the current model, charge transfer is limited to nearest neighbours.

A more detailed description of the Gear predictor-corrector algorithm is given below. The prediction step is based upon the Taylor expansion as follows:

$$\begin{pmatrix} r_0^p(t+\delta t) \\ r_1^p(t+\delta t) \\ r_2^p(t+\delta t) \\ r_3^p(t+\delta t) \\ r_4^p(t+\delta t) \end{pmatrix} = \begin{pmatrix} 1 & 1 & 1 & 1 & 1 \\ 0 & 1 & 2 & 3 & 4 \\ 0 & 0 & 1 & 3 & 8 \\ 0 & 0 & 0 & 1 & 4 \\ 0 & 0 & 0 & 0 & 1 \end{pmatrix} \begin{pmatrix} r_0(t) \\ r_1(t) \\ r_2(t) \\ r_3(t) \\ r_4(t) \end{pmatrix} \quad \text{.....(II-1)}$$

Where index 0 to 4 refer to the derivatives, $r_0$is the position at t=0, $r_1 = \left(\frac{\partial\, r_0}{\partial\, t}\right)\delta t$, $r_2 = \frac{1}{2}\left(\frac{\partial^2 r_0}{\partial\, t^2}\right)\delta t^2$, $r_3 = \frac{1}{6}\left(\frac{\partial^3 r_0}{\partial\, t^3}\right)\delta t^3$, $r_4 = \frac{1}{24}\left(\frac{\partial^4 r_0}{\partial\, t^4}\right)\delta t^4$ and superscript 'p' stands for predicted. The corrected positions are given by:

$$\begin{pmatrix} r_0^c(t+\delta t) \\ r_1^c(t+\delta t) \\ r_2^c(t+\delta t) \\ r_3^c(t+\delta t) \\ r_4^c(t+\delta t) \end{pmatrix} = \begin{pmatrix} r_0^p(t+\delta t) \\ r_1^p(t+\delta t) \\ r_2^p(t+\delta t) \\ r_3^p(t+\delta t) \\ r_4^p(t+\delta t) \end{pmatrix} + \begin{pmatrix} c_0 \\ c_1 \\ c_2 \\ c_3 \\ c_4 \end{pmatrix} \delta r \quad \text{.....(II-2)}$$

Where $\delta r = r_2^c - r_2^p$ and superscript 'c' stands for corrected. The coefficients c_i values can be obtained from the following table using the variable $r_n(t)$. These values of c_i are obtained from the FLX user manual guide (Table II-1) and can also be found in reference [119]. In this work, the values for the 5th order are taken.

order	c_0	c_1	c_2	c_3	c_4
3	0	1	1		
4	1/6	5/6	1	1/3	
5	19/120	3/4	1	1/2	1/12
6	3/20	251/360	1	11/1	1/6

Table II-1: Values of coefficients C_i during corrector steps.

We choose to use the reactive force field developed by J. Kieffer et al.[61-63,63]. This potential involves Coulomb interaction term, directional covalent bond terms, torsion and dispersion terms. The torsion and dispersion term are not required for this work. Important attributes of this force field for simulating systems which undergo significant structural reorganization are

(i) its ability to calculate the redistribution of electron density upon formation, ionization, or breaking of bonds, within a charge transfer term.

(ii) the fact that the angular constraints dynamically readjust whenever there is a change in the coordination number of an atom.

The force field as used in this work includes the Coulomb, Born-Huggins-Mayer and three-body term:

$$U(r_{ij}) = U(r_{ij})_{Coulomb} + U(r_{ij})_{BM-repulsive} + U(r_{ij})_{3-body} \quad \text{(II-3)}$$

The first term is Coulomb potential term:

$$U(r_{ij})_{Coulomb} = q_i \sum_{j=1}^{N} \frac{q_j}{4\pi\varepsilon_0 r_{ij}} \quad \text{(II-4)}$$

It is an effective pair potential that describes the interaction between two point charges and acts along the line connecting the two charges. Here q_i and q_j are the electronic charges localized at the location of atom i and j, r_{ij} is the distance between two particles i and j, ε_0 is the dielectric constant of vacuum. The charge transfer term permits for the atomic charge to be modified by $q_i = q_i^0 - \sum_{j=1}^{NC} \delta_{ij}\zeta_{ij}$ where ζ_{ij} is the cut off function having value $\zeta_{ij} = \frac{1}{1+e^{b(r_{ij}-a)}}$ (a and b are empirical parameters), q_i^0 is the

charge of the isolated atom, δ_{ij} is the amount of charge that can be transferred between the two atoms. The Ewald summation is used to calculate the Coulomb interactions.[120]

The second term in the force field is the Born-Huggins-Mayer repulsive term.

$$U(r_{ij})_{BM-repulsive} = \sum_{i=1}^{NC} C_{ij} e^{(\sigma_i + \sigma_j - r_{ij})\rho_{ij}} \quad \text{.....(II-5)}$$

It describes the short range repulsive interactions, where C_{ij} is pre-exponential factor and described by $C_{ij} = A_{ij}\left(1 + \frac{z_i}{n_i} + \frac{z_j}{n_j}\right)$,$z_i$ is the valence and n_i is the number of electrons in the outer shell of atom i, σ_i is the radius of atom i, A_{ij} and ρ_{ij} are adjustable constants [121].

The third term of the potential is a three-body attractive potential.

$$U(r_{ij})_{3-body} = \sum_{j=1}^{NC-1} \sum_{k=j+1}^{NC} (\varphi_{ij} + \varphi_{ik}) \Lambda(\theta_{ijk}) \quad \text{.....(II-6)}$$

The term $(\varphi_{ij} + \varphi_{ik})\Lambda(\theta_{ijk})$ provides the model for covalent bonding, and it acts in the radial and angular direction between triplets of particles, where θ_{ijk} is the angle formed by the bond directions r_{ij} and r_{ik}. The components of force acting between the centres of mass of the particles, $\varphi_{ij} = -C_{ij}\left(\frac{\rho_{ij}}{\eta_{ij}}\right)\zeta_{ij} e^{\lambda_{ij}\eta_{ij}} e^{-r_{ij}\eta_{ij}}$, are purely attractive, and ζ_{ij} is a cut-off function. The magnitude of this attraction is modulated by the multiple-coordination angular term, $\Lambda(\theta_{ijk}) = 4e^{-\gamma_{ijk}(\bar{\theta} - \theta_{ijk})^4} - 3$ where $\bar{\theta}$ is the equilibrium bond angle. A_{ij}, ρ_{ij}, θ_{ijk}, η_{ij}, C_Z, A_Z, γ_{ijk}, are adjustable parameters, which have been generated and fitted by a genetic algorithm used by another researcher in the project [121] or taken from previous works.

Finally, we have the potential form as follows:

$$U(r_{ij}) = q_i \sum_{j=1}^{N} \frac{q_j}{4\pi\varepsilon_0 r_{ij}} + \sum_{i=1}^{NC} C_{ij} e^{(\sigma_i + \sigma_j - r_{ij})\rho_{ij}} + \sum_{j=1}^{NC-1} \sum_{k=j+1}^{NC} (\varphi_{ij} + \varphi_{ik}) \Lambda(\theta_{ijk}) \text{.....(II-7)}$$

Fig. II- 1(a) shows how the cut-off function varies with the distance between two Si-Si atoms and Fig. II-1(b) describes the potential shape for the repulsive and attractive term, as well as the sum of the two for a Si-Si interaction. In Fig. II-1(b), the red line represents the repulsive term, the blue line represents the attractive term and the dashed green line represents the sum of the two. Fig. II-2 shows the potential shape for the angular term of the three body of the Kieffer potential. The 3D

configuration of three body potential term is shown in Fig. II-3. In Fig. II- 3, two red dots represent the positions of two atoms with fixed position during three body interactions. The potential well is shown for the third atom.

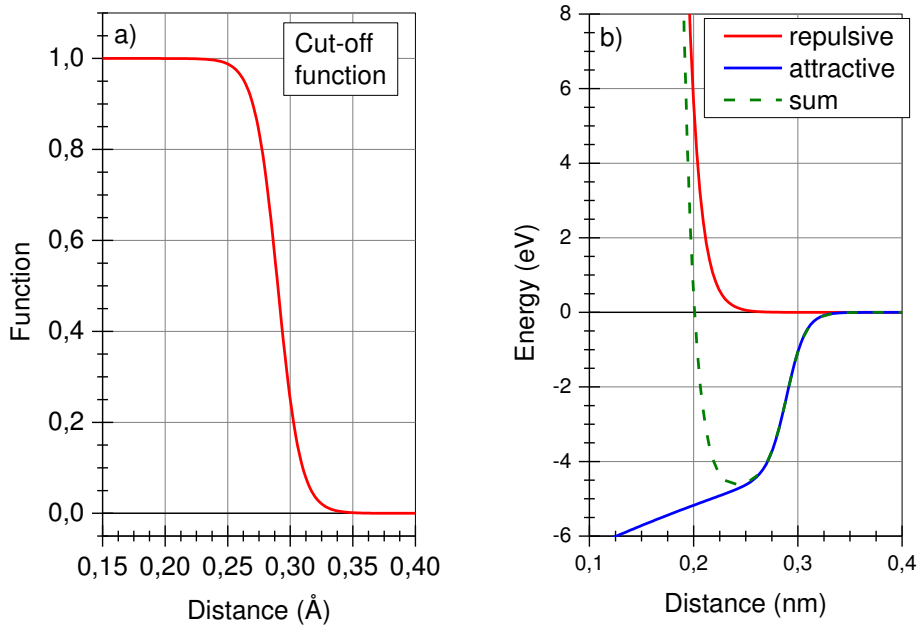

Fig. II-1: Charge transfer function (a) and potential energy variations (b) for Si-Si interaction. In Fig. II-1(b), red line represents repulsive term and blue line represents attractive term due to three body and the dashed green line represents sum of red line and blue line.

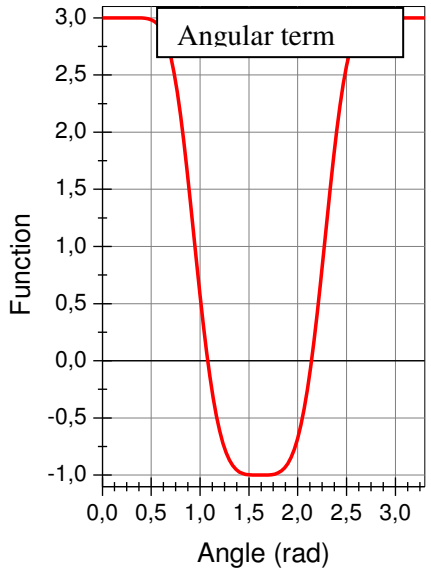

Fig. II-2: Potential shape for angular term of Kieffer force field.

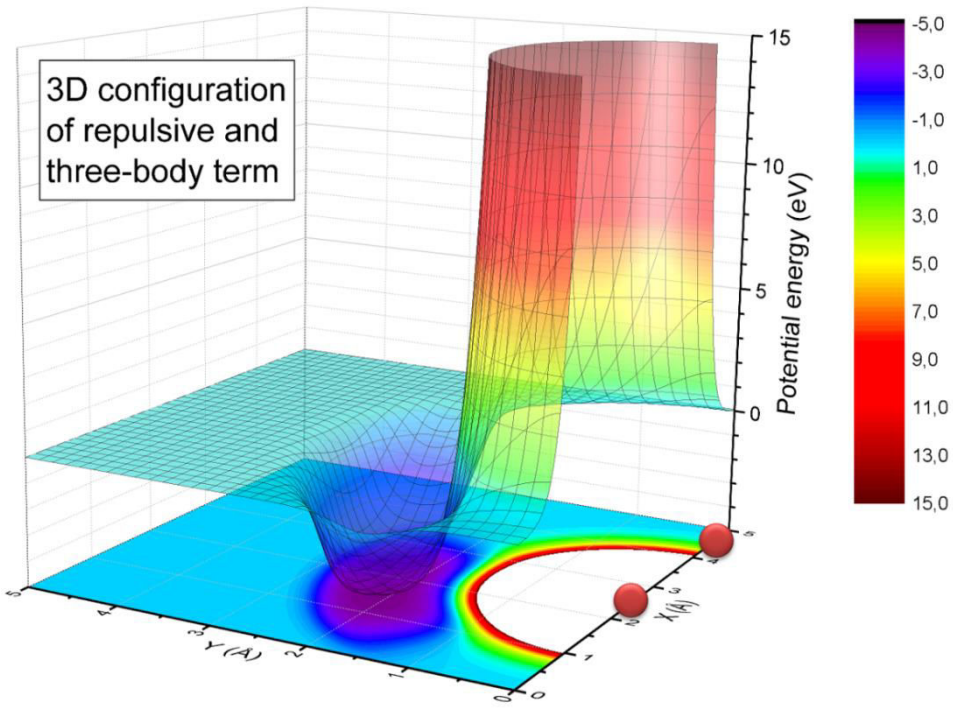

Fig. II-3: 3D configuration of repulsive and three body potential terms. For this three body interaction, two red dots represent the fix positions of two Si atoms and the potential well is represented for the third atom.

i) Simulation conditions for single C, Ti and W depositions on Si(100)

As the main three inorganic materials to be investigated in the project are C, Ti and W, the MD simulations have been performed for C, Ti and W deposition on Si (100). The parameters for the interatomic interactions were obtained by using a genetic algorithm. This work was carried out by other people in our group [121-123,123,124].

The simulation cell for the crystalline system within the Kieffer force field framework is a fixed 8x8x8 supercell containing 4096 Si atoms. The parameters used for this MD simulations work for Si-Si, Si-C, Si-Ti interactions will be discussed later [61-63,122]. For our simulation work, both crystalline and amorphous silicon surface has been used. The creation of crystalline surface is done as follows. First a larger supercell containing 4096 silicon atoms is created from the unit cell with 8 Si atom positions and some vacuum is inserted above and below the system by increasing the box size in the z direction by a factor 5 as shown in Fig II-4. The silicon (100) surface has been created by cutting Si unit cell (having diamond structure) in (100) direction. Then Si surface is relaxed during 100 ps at 300 K in NVT (constant number of particles, constant volume and constant temperature) ensemble, which results in the formation of silicon dimers on the surface. There are some randomness at the surface and the dimers are not all precisely aligned. Periodic boundary conditions are exercised in the three

directions of space. A 17 nm vacuum gap in the z direction is implemented to separate the silicon surface from its image.

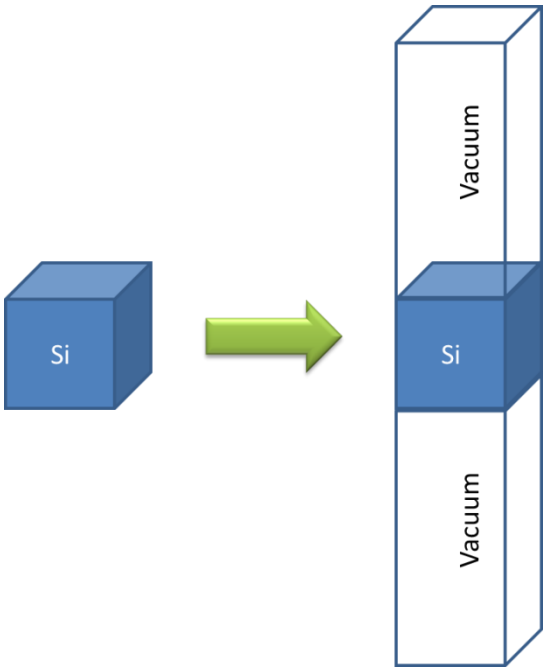

Fig. II-4: Increase of the box size in z direction to create some vacuum above and below the sample.

The creation of amorphous surface is done by using the Amorphous Silicon Surface Generator available on the website of Nanohub.org[125]. and it follows the method by Wooten et al. to create semi-conductor models[126]. Primarily, a crystalline (3x3x3) silicon supercell having 216 atoms is generated. Afterwards, 1000 random bond changes are applied to the structure. The structure is then annealed to a temperature (kbT) of 0.95eV and cooled down to 0.1eV with a step of 0.05eV. This is a normal temperature for the annealing of silicon. A large supercell having 5832 silicon atoms is then generated by repeating newly created simulation box (containing 216 atoms) in each direction of space. Afterwards, using the Kieffer potential and MD simulations, the system has been relaxed in the NPT (constant number of particles, constant pressure, and constant temperature) ensemble at 300 K for 50 ps with a time step of 0.5 fs. A amorphous silicon surface is then generated by cleaving the system in the NVT ensemble at 300K for 50 ps with a time step of 0.5 fs. One by one atom (C, Ti, W) is then sent randomly at a fixed distance from the surface with a constant downward velocity. Velocities are controlled according to the corresponding energies in the range of 1-50 eV. At the same time, incidence angles are varied between 0°, 30°, 45° and 60° with respect to the surface normal. For the single carbon deposition, the simulation has been performed for 15° incidence angle along with other angles. The initial directions of the incoming atom towards the silicon surface are randomly defined by the azimuth angle together with incidence angle for each simulation. 100 independent simulations are executed for each incidence angle and impact energy (*i.e.* each simulation equals to one atom impacting on a pristine surface) in order to achieve meaningful statistics.

Surface	Crystalline/Amorphous
Species	C/Ti/W
Time step	0.2 fs
Simulation Time	6 ps
Size of simulation box	4.2 nm x 4.2 nm x 4.2 nm
Surface exposed	(100)
Incidence angle	0°, 30°, 45°, 60°, (15° for single C)
Azimuth angle	Randomized
Deposition location	Randomized
Energy	1-50 eV, (100eV for single W)
#simulations	100

Table II-2: Simulation conditions for single C/Ti/W deposition.

The incoming atom carries no charge, as adding a charged particle would change the simulation box neutrality. The MD simulations have been executed for a simulation duration of 6 ps with a time step of 0.2

fs. The simulations are done in the NVE ensemble (constant number of particles, volume and energy) and during the simulation no energy scaling is utilized. This short time scale is enough for the system to dissipate the impact energy, considering that it does not exceed 50 eV. All the simulation conditions are given in Table II-2 below. Fig. II-5(a) describes the top view of crystalline silicon (100) surface used for this simulation work, While Fig. II-5(b) describes the top view of amorphous silicon surface used for some of the simulations.

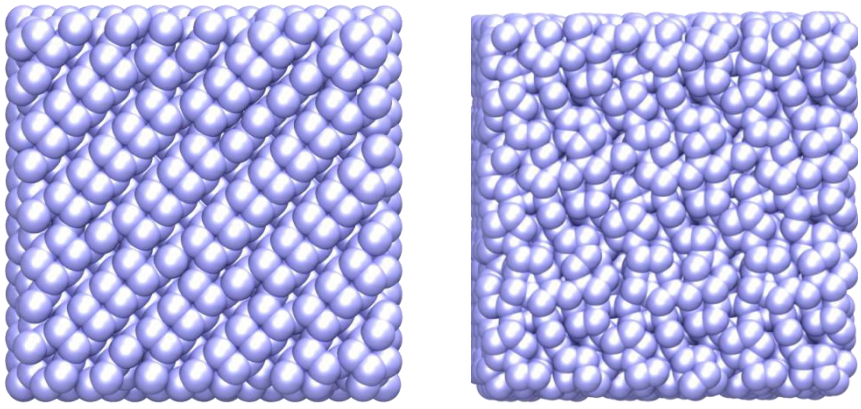

Fig. II-5: a) Top view with dimer reconstruction for a crystalline Si surface, b) Top view of an amorphous Si surface.

The following three tables contain the simulation parameters for the interaction of carbon (Table II-3), titanium (Table II-4) and tungsten (Table II-5) with silicon surface atoms.

Element		σ_i (nm)	n_i	z_i	q_i^0
Si		0.101	8	+4	0
C		0.095	8	+4	0
Pair	A_{ij} (10^{-19}J)	ρ_{ij} (nm^{-1})	λ_{ij} (nm)	η_{ij} (nm^{-1})	κ_{ij} (nm^{-1})
Si-Si	1.80	91.00	-1.31	2.00	91.00
Si-C	0.38	39.22	-10.99	0.22	36.59
C-C	0.012	87.22	1.24	1.79	140.31
Charge transfer		δ_{ij} (e)	a (nm)	b (nm^{-1})	
Si-Si		0.000	0.293	110.0	
Si-C		0.095	0.243	47.89	
C-C		0.000	0.199	85.61	
Triplet		γ_{ijk} (rad^{-n})	θ (rad)	n	m
Si-Si-Si		4.60	1.91	4	4
Si-C-Si		1.20	1.91	2	1
C-Si-C		0.55	1.91	2	1

Table II-3 : Parameters for C-Si interactions [122].

Element		σ_i (nm)	n_i	z_i	q_i^0
Si		0.101	8	+4	0
Ti		0.147	18	+4	0
Pair	A_{ij} (10^{-19}J)	ρ_{ij} (nm^{-1})	λ_{ij} (nm)	η_{ij} (nm^{-1})	κ_{ij} (nm^{-1})
Si-Ti	0.81	68.33	0.45	12.77	160.68
Charge transfer		δ_{ij} (e)	a (nm)	b (nm^{-1})	
Si-Ti		-0.157	0.27	154.28	
Triplet		γ_{ijk} (rad^{-n})	θ (rad)	n	m
Si-Ti-Si		1.93	1.57	2	1
Ti-Si-Ti		1.20	1.57	2	1

Table II-4 : Parameters for Ti-Si interactions [123].

Element		σ_i (nm)	n_i	z_i	q_i^0
Si		0.101	8	+4	0
W		0.135	32	+4	0
Pair	A_{ij} (10^{-19}J)	ρ_{ij} (nm^{-1})	λ_{ij} (nm)	η_{ij} (nm^{-1})	κ_{ij} (nm^{-1})
Si-W	0.56	83.55	0.26	056	111.88
Charge transfer		δ_{ij} (e)	a (nm)	b (nm^{-1})	
Si-W		-0.0043	0.31	204.32	
Triplet		γ_{ijk} (rad^{-n})	θ (rad)	n	m
Si-W-Si		0.78	1.31	2	1
W-Si-W		4.77	1.31	2	1

Table II-5 : Parameters for W-Si interactions [123,124].

ii) Simulation conditions for multiple impacts of C on Si (100)

Along with this, there was another simulation frame designed to execute continuous atom deposition in order to have better comparison with experimental observations. Here MD simulations are also performed using the reactive force field described by J. Kieffer and his co-workers [61-63]. The parameters for Si-Si and Si-C interactions are presented in [122] and in table II-3. For the continuous carbon deposition on the Si(100) surface, similar conditions have been used than for single carbon deposition [122] for the deposition of multiple carbon atoms on a Si(100) surface. The deposition of each carbon in a continuous fashion has to be divided into two steps: a deposition step and a cooling step. The cooling step, consisting of a ramping of the temperature back to 300 K during 4 ps, is used after the deposition of each atom. The azimuth angle for these simulations has been fixed at 0° and 45°.

For the results' analyses, the implantation depth is defined as the average vertical distance between the carbon atom at the end of each MD simulation and the surface plane. For the Si(100) surface, the surface plane is simply defined by the *z* coordinate of the topmost silicon atom. For all conditions, the reflected atoms are ignored in the calculations of depth and angular distributions. In order to get some information on the structure formed, the system has been divided in the z direction into different slabs. Each slab has a thickness of 5.0 Å. In the graphs they are identified by the centre position of the slab, i.e. 2.5 Å for the first slab, 7.5 Å for the second, etc. We choose 5 Å thick slab arbitrarily and it is quite close to the lattice dimensions for the Si diamond structure, which is 5.43 Å.

The simulation conditions are same as single carbon deposition except azimuth angle which are set at 0° and 45°.

3) Experimental techniques

In order to investigate the sticking, deposition and reorganization of the inorganic materials Ti and W on silicon Si(100) surfaces experimentally, we employed storing matter deposition technique along with dynamic SIMS analysis technique. We will first discuss the sputter deposition process in storing matter technique and used conditions for the deposits followed by the description of the SIMS instrument employed and the conditions used.

i) Storing matter technique: principle and instrumental description

Here we will focus on the description of several parts of the storing matter instrument.

As our main point of interest is to investigate deposition and sticking behaviour of inorganic materials on silicon substrate in the sub-monolayer range, the storing matter instrument is particularly suitable since it is specifically designed to achieve sub-monolayer deposits. Controlling primary current and the time of the deposit, several sub-monolayer deposits are achieved. Fig. II-6 shows the schematic diagram of prototype storing matter instrument.

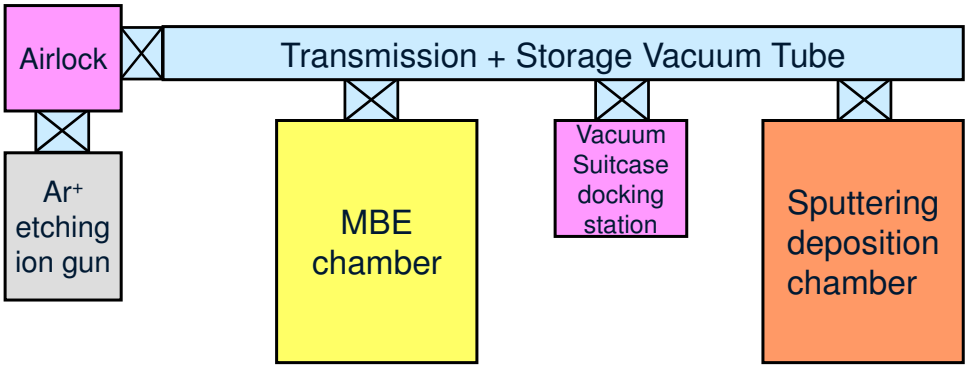

Fig. II-6: schematic diagram of prototype storing matter instrument.

Three main sections of the storing matter instrument can be identified:

(a) Collector preparation:

This section consists of an Ar^+ etching ion gun chamber and an MBE chamber. The collector (mainly Si collector) can be etched by an Ar^+ (10 keV) ion beam to remove the native oxide or surface contamination. In the MBE chamber, a metal coating can be deposited by means of thermal evaporation on the Si collector.

(b) Sputter deposition chamber:

This section describes the part highlighted by orange colour in Fig. II-6. The target material is sputtered by a floating low energy ion gun by controlling the fluence. The collector is placed two millimetres above the target.

(i) Sample and collector stage:

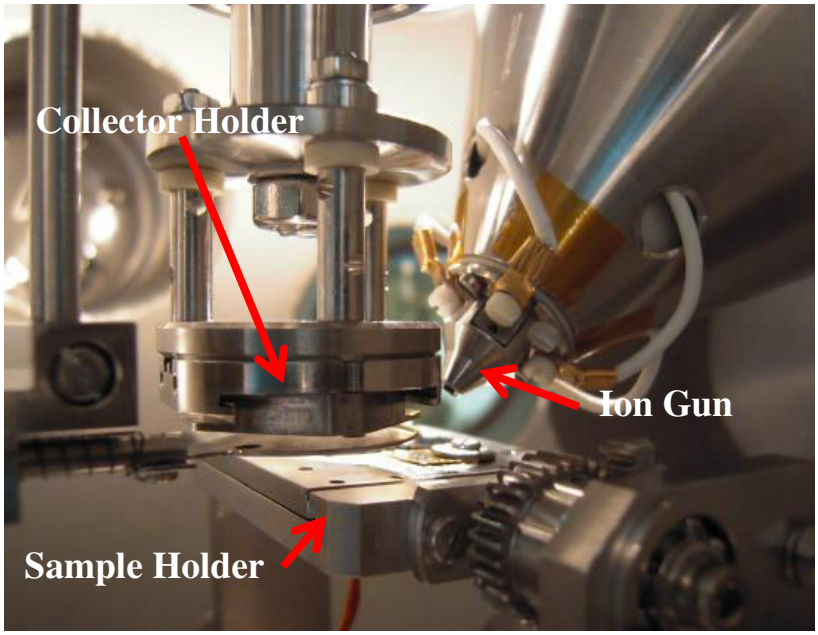

Fig. II-7: main deposition chamber of storing matter instrument.

Fig. II-7 shows the position of collector and sample (or target) while doing the sputtering processes. The collector stage is motorized and can be moved in X, Y and Z direction with high precision. The movement of collector stage can be read and controlled by a joystick (SPRITE XYZR Meca2000, Deben) with a precision of 1 µm; it can also be rotated if necessary. The position of the sample stage can be read and controlled by a controller in the X & Y direction with a precision of 1 µm (SPRITE HR2 stage controller joystick, Deben) . It can be moved manually in the Z direction and can also be rotated or tilted.

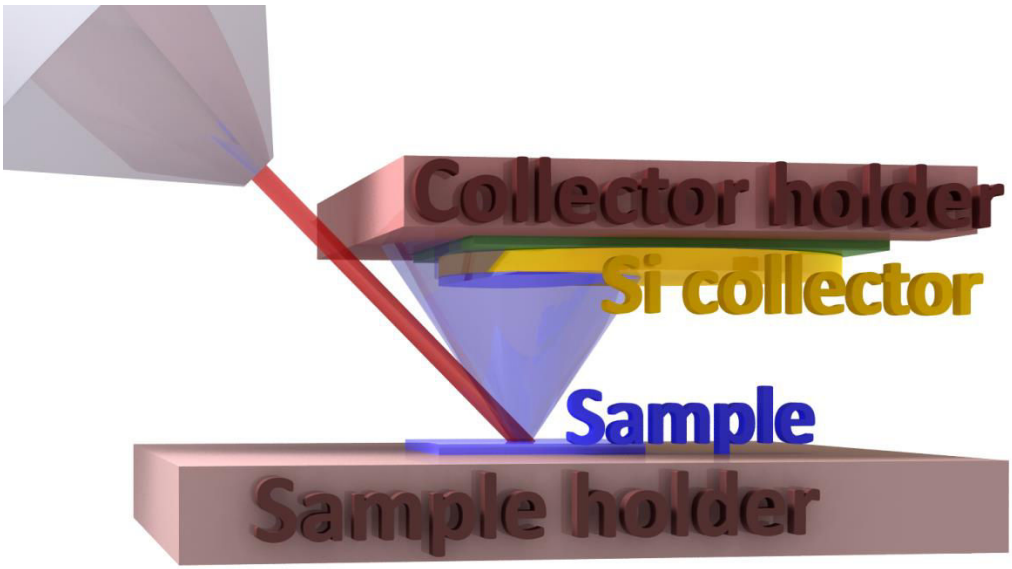

Fig. II-8: sputtering process during deposition.

The Fig. II-8 describes the experimental deposition processes while doing deposits. The primary beam hit the sample surface at 45. In this case positioning of collector is an important factor which decides how much of sputtered materials could be collected. After collecting the sputtered particles, depth profiles in the analysing instrument are done to characterise the deposit.

(ii) Floating low energy ion gun:

The floating low energy ion gun (FLIG) was designed to keep the control on impact energies and beam current while the ion beam hits the target materials. With the use of FLIG, the energy can be varied from 100 eV to 10 keV and the current can be controlled from few nA to several hundred nA. The impact angle to the substrate surface for the ion beam is adjusted at 45°. Depending upon the goal of experiments, there are several possibilities to choose primary ions (Ar^+, Xe^+ or O_2^+) which are generated by a cold cathode duoplasmatron source.

(iii) Electron detector and raster controller:

It is possible to raster the ion beam while doing sputtering. The ion beam can be rastered by four deflectors which exist in the FLIG section. For this work, a raster voltage up to 440 V corresponding to the raster area of 1.5 x 1.5 mm^2 at 10 keV impact energy is chosen. The rastering is basically controlled by the software installed in the computer and synchronized with a secondary ion/electron detection system (IGM 300, Ionoptika). The spot size is focussed and adjusted by using a grid, which comes in the range of few μm^2.

(iv) Electron gun:

There is an electron gun inside the sputter deposition chamber. The electron gun is basically used to do the charge compensation during the sputtering of insulating samples. The electron gun can be operated up to 30 keV energy.

(c) Storage and transfer of the collector:

A portable suitcase is equipped in this section to transfer the deposit to analytical chamber without breaking the ultra-high vacuum conditions. At the same time the collector can be stored in the storage section of storing matter configuration without changing the UHV conditions.

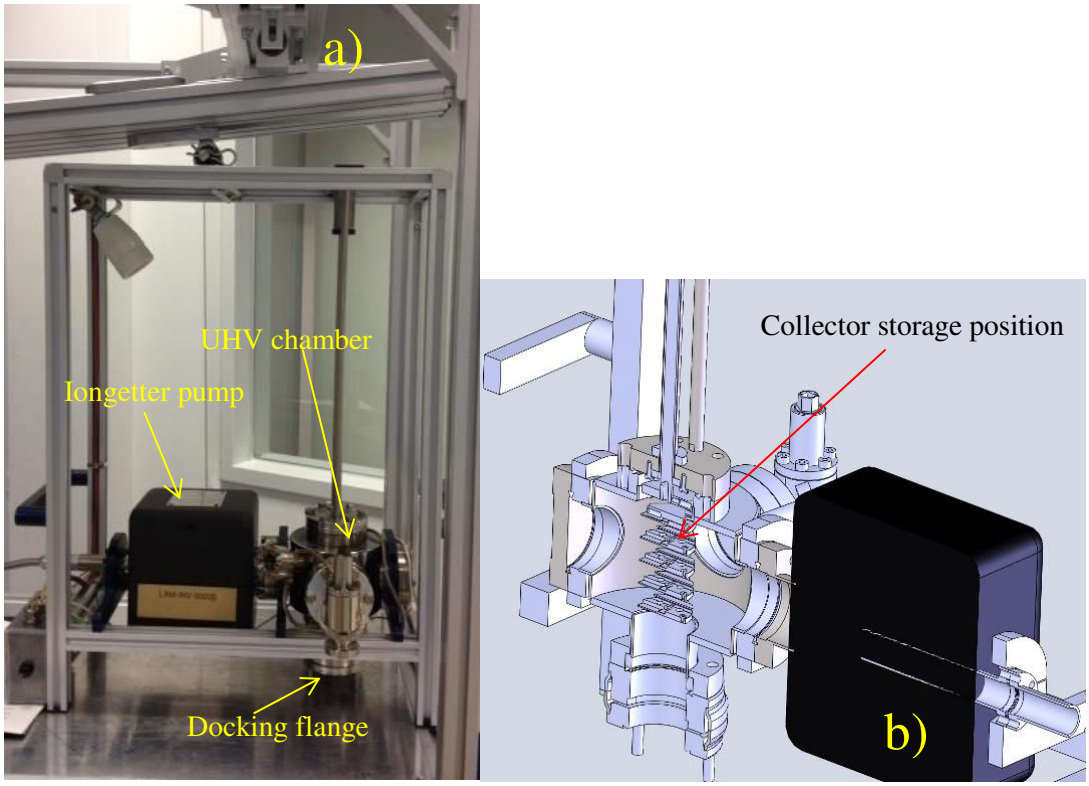

Fig. II-9: UHV suitcase (a) used for transfer and cross-sectional view (b) for collector storage position inside the UHV suitcase chamber.

It is possible to prepare several collectors in the same time and store them for analysis in a specially designed cart with 10 sample positions in the storing matter instrument. The cart is moved from one position to another by a magnet. Later the collectors are moved from the cart to the suitcase for the transfer into an analytical instrument. During all these transfers, the UHV conditions are always maintained below 10^{-8} mbar to minimize contamination or oxidation of the deposit. Only exception is the airlock of the different analysis instrument, where the pressure might be higher.

Fig. II-9 shows the structure of the suitcase for transferring the collectors to analytical chamber (Static SIMS; dynamic SIMS, NanoSIMS50, AES or XPS). This suitcase is specially developed to maintain the UHV conditions and is having 5 independent sample positions [Fig. II-9(b)] [127]. All the analytical instruments in SAM have adapted docking chambers and specially designed collector holders for the analysis purpose. Table II-6 summarizes the conditions used while preparing the storing matter deposits.

Parameters	Values
Impact Energy	10 keV (Ar^+)
Incidence Angle	45°
Ion Current	40-200 nA
Time	30-600 sec
Raster Size	1.5x1.5 mm^2
Species	Ti, W

Table II-6: Conditions for sputter deposition in storing matter instrument.

ii) Secondary Ion Mass Spectroscopy: Instrumental description

After getting the sub-monolayer deposit in storing matter instrument, we wanted to use a sensitive technique to quantify our results and we used dynamic SIMS (Cameca IMS 6f) for the analysis of the deposits. The IMS 6f at CRP Gabriel Lippmann has a primary column at 60° with a Cs^+ ionization source and O_2^+ source. There is an airlock system connected to the analysis chamber in order to do the sample transfer.

All experiments were done using the Cs^+ source. O_2^+ would have been a better choice for detecting Ti^+ and W^+ ions. However, there was already enough signal using Cs^+ for detecting Ti^+. For W^+

detections, O_2^+ ions would have been a better choice, but the duoplasmatron was out of service or not working reliably over a long period of time. The impact energy for Cs^+ source was 10 keV and we used low primary ion current (2-3 nA) in order to avoid a too quick sputtering of the sub-monolayer deposit. The raster can be changed but for most of my experiments I used a raster size of 500 µm x 500 µm. In the mass spectrometer, I used two field apertures for the analysis (1800 µm or 750 µm). This leads to diameters of the analysed area of 150 µm or 62.5 µm. The contrast aperture of 400 µm was used. The sample stage of the IMS 6f can be moved vertically and horizontally to change to area to be analysed, while keeping the z position unchanged to stay in the focal plane of the mass spectrometer. By changing the horizontal or vertical position, a line scale is possible to do. More details about the analysis conditions are listed in the Table II-7.

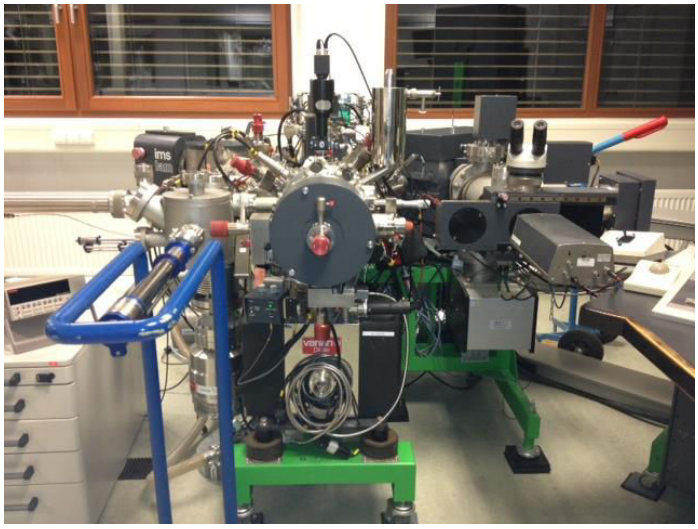

Fig. II-10: Cameca IMS 6f at CRP Gabriel Lippmann.

Parameters	Values
Source Energy	10 keV
Sample Voltage	4.5 keV
Impact Energy	5.5 keV
Incidence Angle	60°
Primary Current	2-3 nA
Raster size	500 µm
Field Aperture	1800 or 750 µm
Field of view	150 or 62.5 µm
Contrast aperture	400 µm
Mass resolution $\frac{M}{\Delta M}$	400

Table II-7: Analysis conditions for a deposit analysed in IMS 6f.

The several sections of IMS 6f at CRP Gabriel Lippmann instrument are discussed in the following paragraphs.

(a) Primary ion source.

The IMS 6f at CRP Gabriel Lippmann consists of three ion sources (duoplasmatron, Cs source and Ga source). For my studies, I used Cs source for analysing the deposits of both Ti and W on silicon.

Cs Ion beam can be used in positive and negative secondary ion mode depending upon the element to be characterized. The Cs source produces Cs^+ ions via vaporization of Cs atoms through a porous tungsten plug. The schematic diagram shows how exactly Cs source is heated and how the Cs^+ ions get extracted.

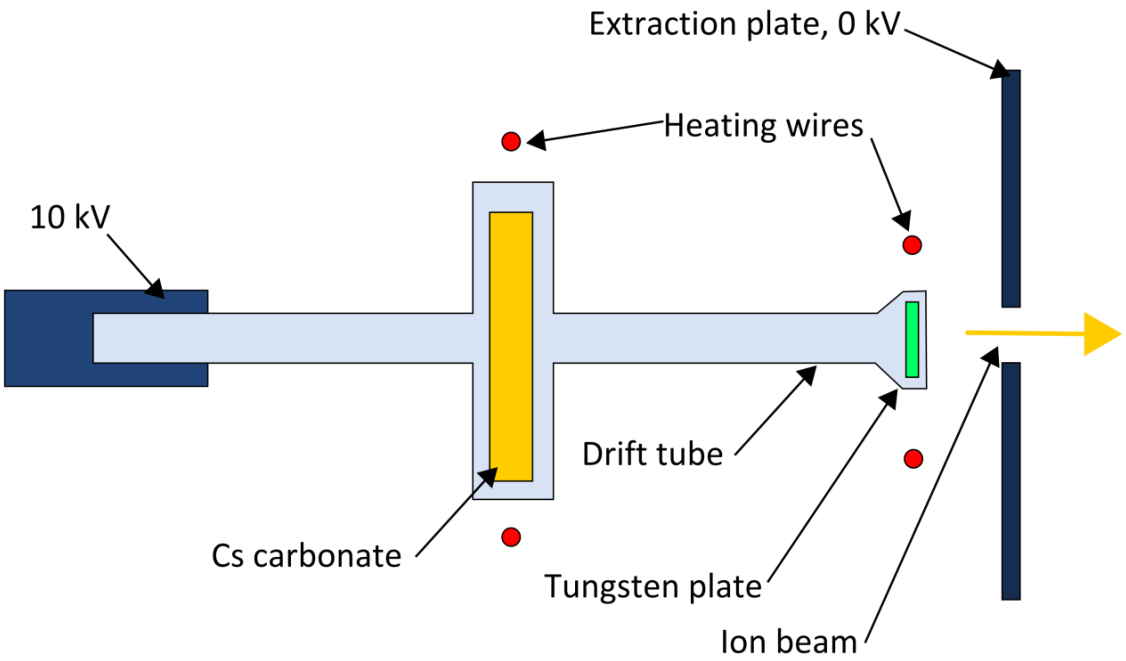

Fig. II-11: schematic diagram of Cs source.

(b) Primary Ion beam:

Fig. II-12 describes different parts of the primary column of IMS 6f used at CRP Gabriel Lippmann. The primary column consists of deflectors, lenses, apertures, filters, quadrupoles, and deflection plates which help to filter, focus, shape and raster the primary ion beam and to get a primary ion current in the desirable range.

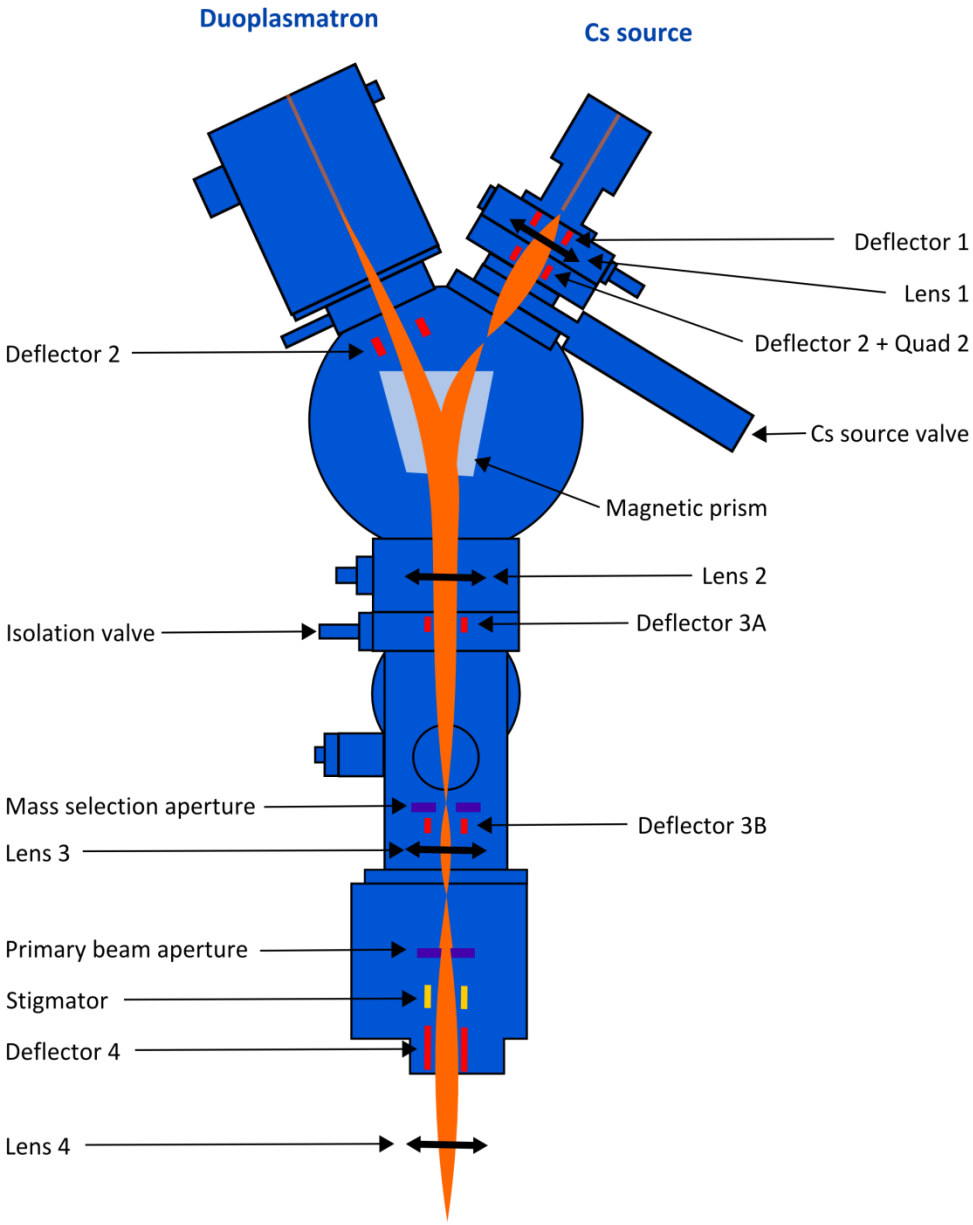

Fig. II-12: Schematic diagram of primary column of IMS 6f [128].

(c) Secondary Ion Extraction

Secondary ions are formed due to the bombardment of energetic primary beam at the surface of sample. The secondary ions are immediately extracted by an immersion lens. In the instrument I used, the sample voltage can be varied from 4 kV to 10 kV and the first electrode of the immersion lens is grounded. Depending upon the polarity of the sample, negative or positive secondary ions can be extracted. The user has the influence to select the polarity of secondary ions by machine settings.

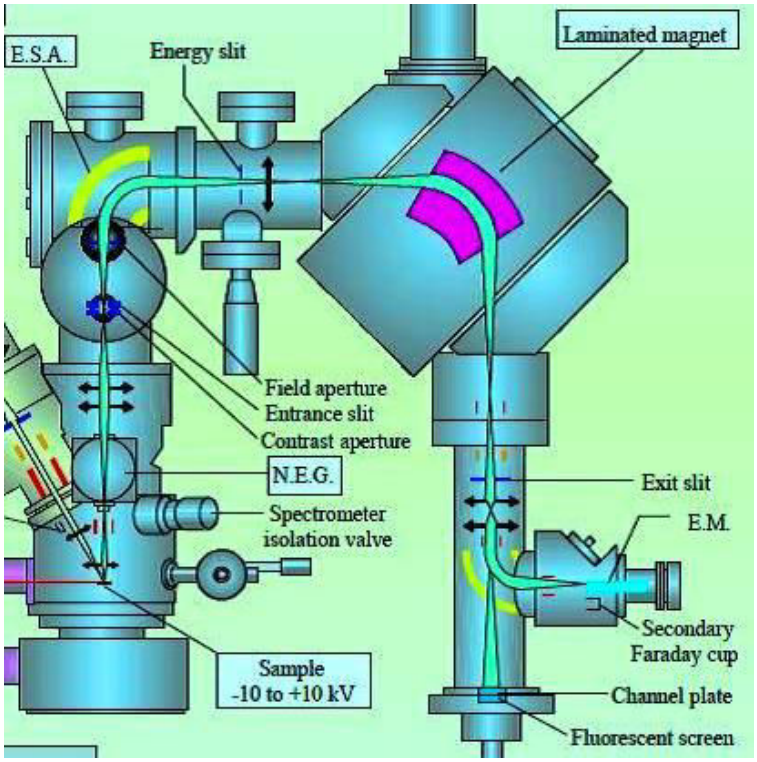

Fig. II-13: Secondary ion extraction and transfer set up for IMS 6f [128].

(d) Secondary Ion Transfer:

After the extraction of the secondary ions by the immersion lens, the ions are transferred to the electrostatic sector and then into the magnetic sector. The main reason to use this transfer lens is to magnify the image of the sample surface at the position of field aperture and to get well focused beam into the entrance slit of the spectrometer. The field apertures used for this work were first (1800 µm) and second field (750 µm) aperture of the IMS 6f. The field visualised with the first aperture is 150 µm and that with the second field aperture is 62.5 µm. There are different transfer lenses in this sector and mostly depend upon the user to choose as each lens gives a different magnification of the sample surface in the field of the field aperture.

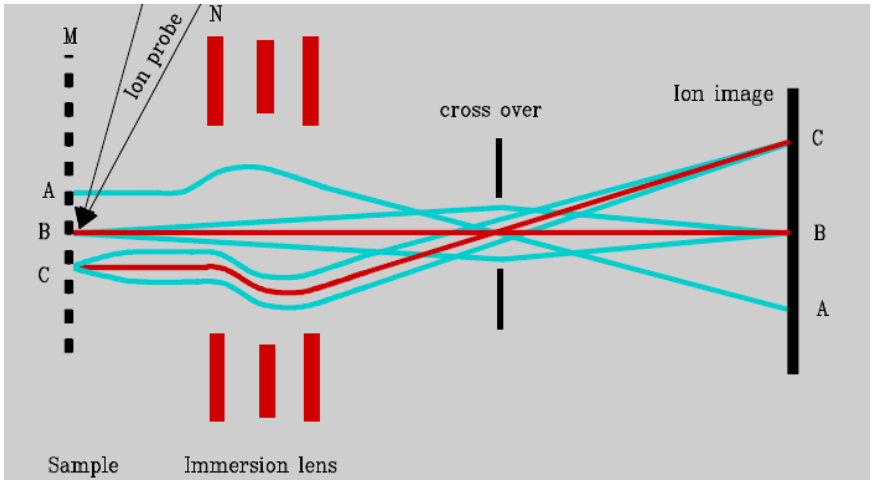

Fig. II-14: Secondary ion transfer process [128].

(e) Ion Energy Analyser

The secondary ions are having a wide range of energies after the sputtering process. These secondary ions are allowed to pass through the electrostatic energy analyser. While passing through the energy analyser, the low energy ions are more deflected than the high energy ones. An energy selection slit can be chosen to pass through the dispersed secondary ions in required range. The outer and inner spherical electrode surfaces of the energy analyser are having voltages of opposite polarities. There is an electrostatic spectrometer lens in between energy analyser and magnetic analyser, which aligns the energy filtered ion beam into the magnetic sector.

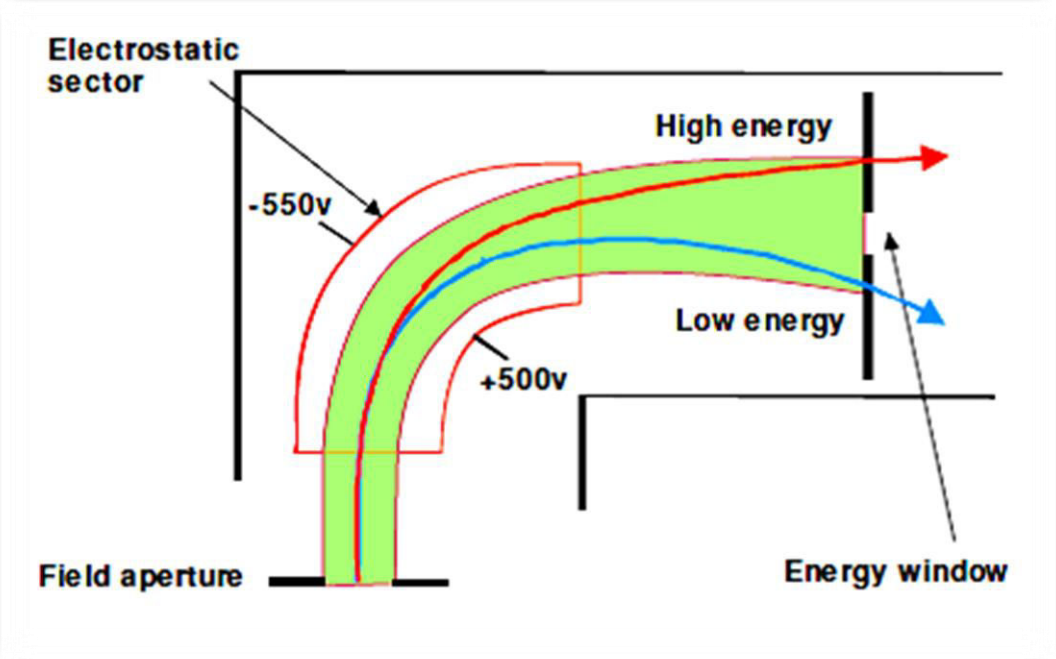

Fig. II-15: Diagram for an ion energy analyser [129].

(f) Mass Analyser:

After crossing through the electrostatic energy sector, the ion beam enters into the magnetic sector. In the magnetic sector, the mass analyser includes a magnetic field which plays the part of a mass dispersing prism. The deviation produced by magnetic prism depends on the momentum of the particles. This angular deviation is a function of mass. Fig. II-16 illustrates how different ions differing by one mass unit are separated. The selection slit isolates every ionic species. The width of the mass selection slit is adjusted according to the size of the cross-over image and hence the virtual image made up of ions having a well-defined mass. How accurate the mass is defined depends on the size of the cross-over image and the width of the slit, i.e., mass resolution M/ΔM. A minimum mass resolution of 300 is obtained on the IMS 6f. The transmission depends upon: (i) the transfer lens which is energized, (ii) the contrast aperture, (iii) the mass resolving power which is related to the width of the entrance and exit slit and the aperture angle of the spectrometer. In IMS 6f, contrast

apertures have a diameter of 100 µm to 400 µm and several field apertures of 1800 µm, 750 µm and 100 µm are available. The width of the energy slit, entrance slit and exit slit are kept wide open during the analysis.

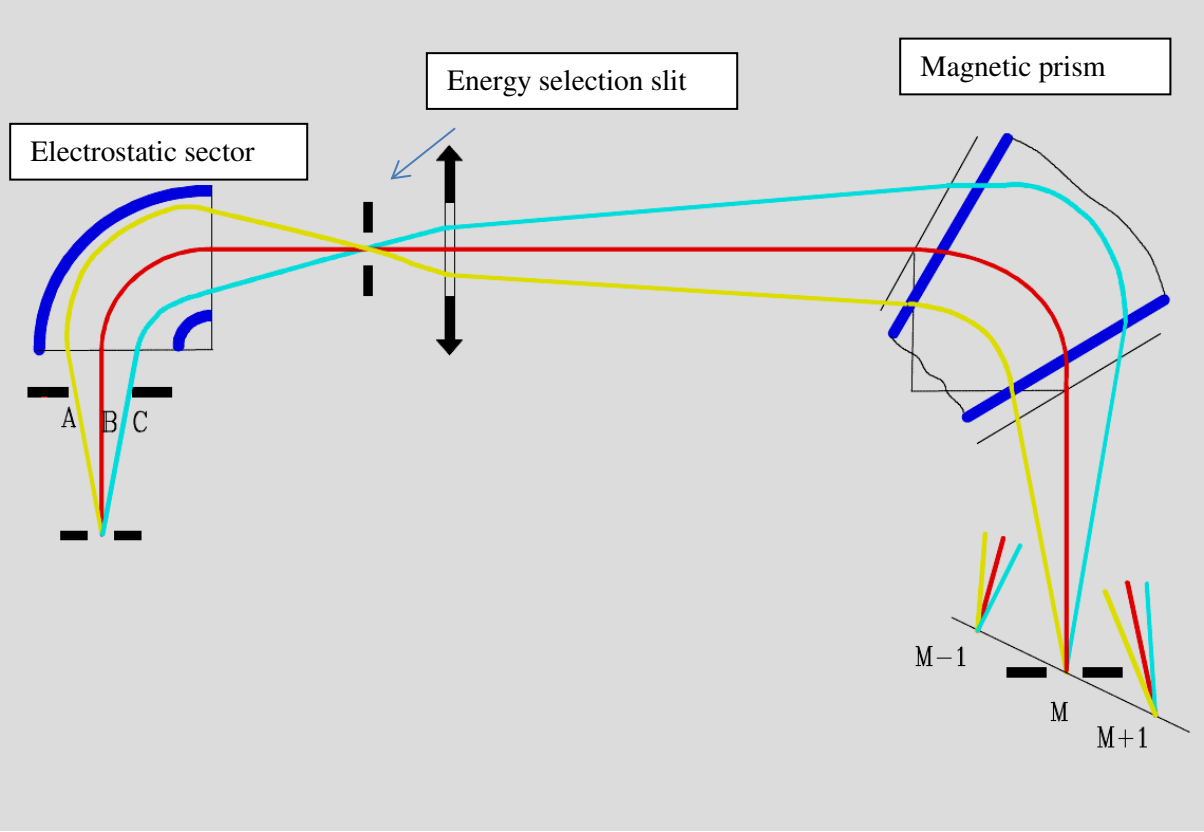

Fig. II-16: Diagram for an ion energy analyser [128].

The techniques and conditions explained here will be referred to in the next chapters while we describe the simulation and experimental results and their discussions.

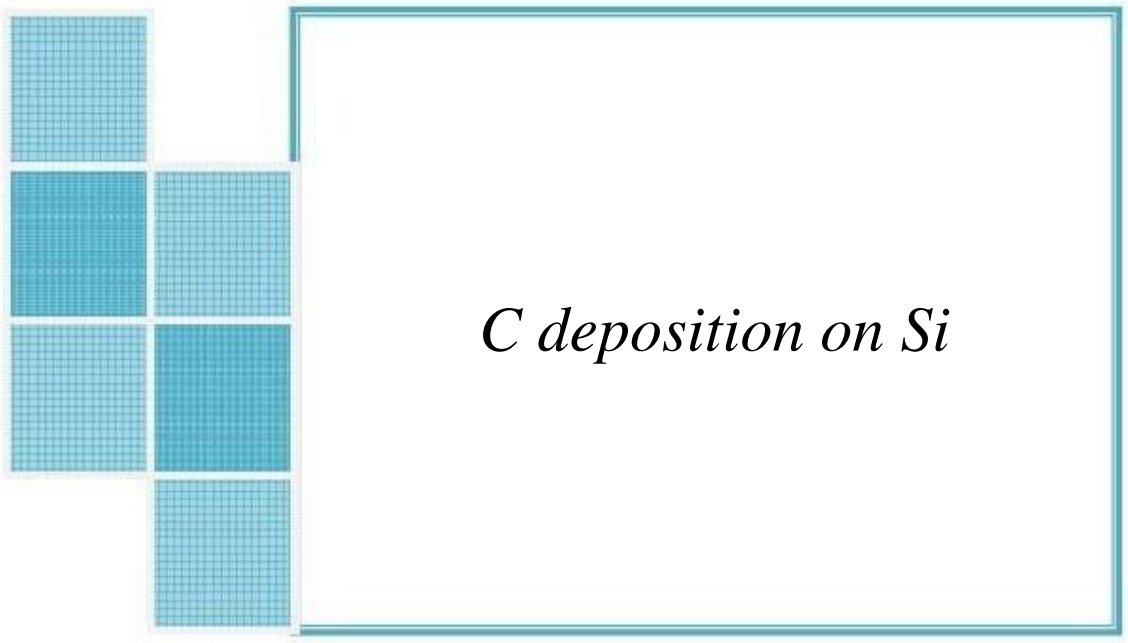

C deposition on Si

"Influence of angle and energy on sticking, deposition and implantation of carbon atoms on silicon surface has been investigated for single carbon depositions. Similarly, multiple carbon depositions have been investigated to observe several issues regarding deposition and implantation processes, as well as diffusion mechanism and damage formation."

Chapitre 3.
Carbon (C) deposition on Si (100) by Molecular Dynamics Simulations

1) Introduction:

The properties of the materials to be deposited on the surface and the properties of the surface are very important because it determines the properties of the interface to be formed. In this chapter, the deposition and sticking of carbon on silicon (100) will be investigated by molecular dynamics simulations. The main objective to deposit carbon on silicon was to understand the very first steps of the formation mechanisms of SiC and the sticking of carbon in the sub-monolayer range in the storing matter instrument [109] using silicon wafers as collector. How and where carbon gets deposited or implanted, as well as the evolution of the sample composition and structure with increasing carbon fluence is studied.

In order to understand in detail the atomic scale mechanisms, the carbon-silicon interaction plays an important role and we use MD simulations with the reactive force field developed by John Kieffer and co-workers[61,62,67] to gain a better understanding how the angle and energy influence the deposition mechanisms and the formation of SiC compound. This force field allows for the possibility to account for the breaking and formation of bonds as well as for a dynamic charge transfer between pair of atoms, which is important for the Si-C system. During the interactions between Si and C, the possible interactions may occur are Si-Si, Si-C and C-C interactions. The different parameters and their ability to model silicon carbide, including formation energy of several point defects in these structures, were already tested previously.

The results for carbon deposition will be discussed in two parts. We start the investigation by depositing single carbon atoms by MD simulations. The results we get with the Kieffer force field for single impacts have been compared with the well-tested Erhart-Albe interatomic potential in order to validate our results. The part with the Erhart-Albe potential has been carried out at the University of Helsinki. The results have been published in the Journal of Physics;: condensed matter[122].

Next, the deposition of multiple carbon atoms will allow for the simulation of the sub-monolayer deposition process and to understand how and where the carbon atoms deposit.

The results for single deposition of carbon on silicon will be discussed first followed by the multiple carbon deposition.

2) Section 1: results for single carbon deposition

The computational details for this single carbon deposition on Si (100) are described in chapter 2. So, we will directly go to the results and discussion part of the single carbon deposition. The results described here for single carbon deposition are adapted from the paper published within our group, where I am a co-author. Only my contributions from the published paper are included here. In a first step, simulation results for single carbon are carried out for the Kieffer and the Erhart-Albe interatomic potentials in order to validate the parameter set for Si-C. The simulations with the Erhart-Albe potential were done at the University of Helsinki.[122]

i) Deposition, implantation and backscattering of carbon atoms.

In the whole thesis, implantation is defined as the deposition of carbon atoms below the first two silicon monolayers. The proportions of carbon being implanted, deposited and backscattered are computed using both the Kieffer and the Erhart-Albe interatomic potentials at selected impact energies and angles. A carbon atom is considered as being implanted after impact with the silicon surface if its position at the end of the MD simulation is beneath a virtual plane located 0.5 Å below the topmost silicon atom of the surface. Carbon atoms which are located above that virtual plane at the end of the MD simulation and which are not backscattered are considered as being deposited. Blue lines in Fig. III-1 show the backscattering yields for carbon deposition on a flat surface at different deposition angles and energies. For incidence angles of 0°, 15°, and 30°, a backscattering yield lower than 11 % is always observed. Increasing the incidence angle to 45° and 60° will gradually lead to a significant direct loss of matter at higher energies via backscattering of the incoming particle upon impact with the silicon surface. With an incidence angle of 0°, the backscattering yield stands between 0 and 0.08, while it is in the range 0-0.05, 0-0.07, 0-0.14%, and 0-0.27 for 15°, 30°, 45°, and 60°, respectively. The backscattering yields for 0° and 30° are very close to the ones computed with the Erhart-Albe potential, as the observed range with this potential is 0-0.05 for 0° and 0.02-0.11 for 30°. At 60°, the agreement between the two potentials is not as good since the Erhart-Albe potential predicts a higher backscattering yield at low deposition energies. This little discrepancy between the potentials at 60° can also, albeit to a lesser extent, be observed in the deposition and implantation yields. Here it should be recalled that there is a small difference in the reconstruction of the silicon surfaces with the Kieffer potential (presence of randomness) and with the Erhart-Albe potential (dimers aligned). Tests using a non-reconstructed (100) surface and the randomly reconstructed (100) surface with the Erhart-Albe potential at 60° incidence angle enables us to rule out an effect of the surface relaxation on the deposition and backscattering rates. We presume that the slight discrepancy

at 60° is due to the fact that the two force fields use very different approaches and hence the forces acting between atoms may be different.

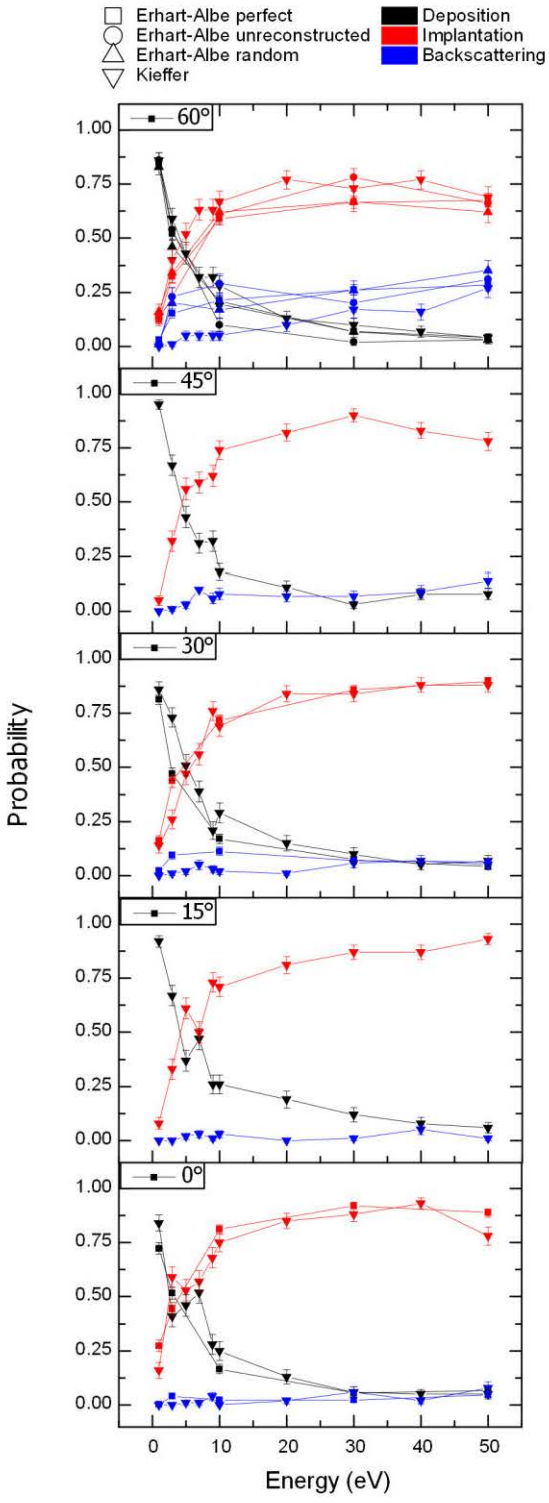

Fig. III-1: Ratios between deposition (black), implantation (red) and backscattering (blue). Deposition is defined as a carbon atom on top of the silicon surface, while implantation means a carbon atom beneath the silicon surface plane.

ii) Implantation of the carbon atoms.

Next, we address the issue of whether the carbon deposits on the silicon surface, or goes beneath the first silicon plane of the surface. To answer this question, Fig. III-1 presents for each impact angle the proportion of carbon atoms that stay on the surface (deposited – black lines) or go deeper into the material (implanted – red lines). As could be expected, the lower the energy, the more likely is deposition compared to implantation. At 1 eV and for all angles, the deposition/implantation ratios are within 83/17 and 95/5 for both potentials, meaning a vast majority of the carbon atoms stay on top of the surface. When increasing the energy of the carbon, the ratio deposition/implantation rapidly drops. Broadly speaking, and for all incidence angles tested with the Kieffer potential, the implantation rate overcomes deposition when the energy of the carbon atom is higher than 5 eV. Increasing the energy to values higher than 20 eV does not have an impact on the deposition/implantation ratios, as most of the carbon atoms are implanted.

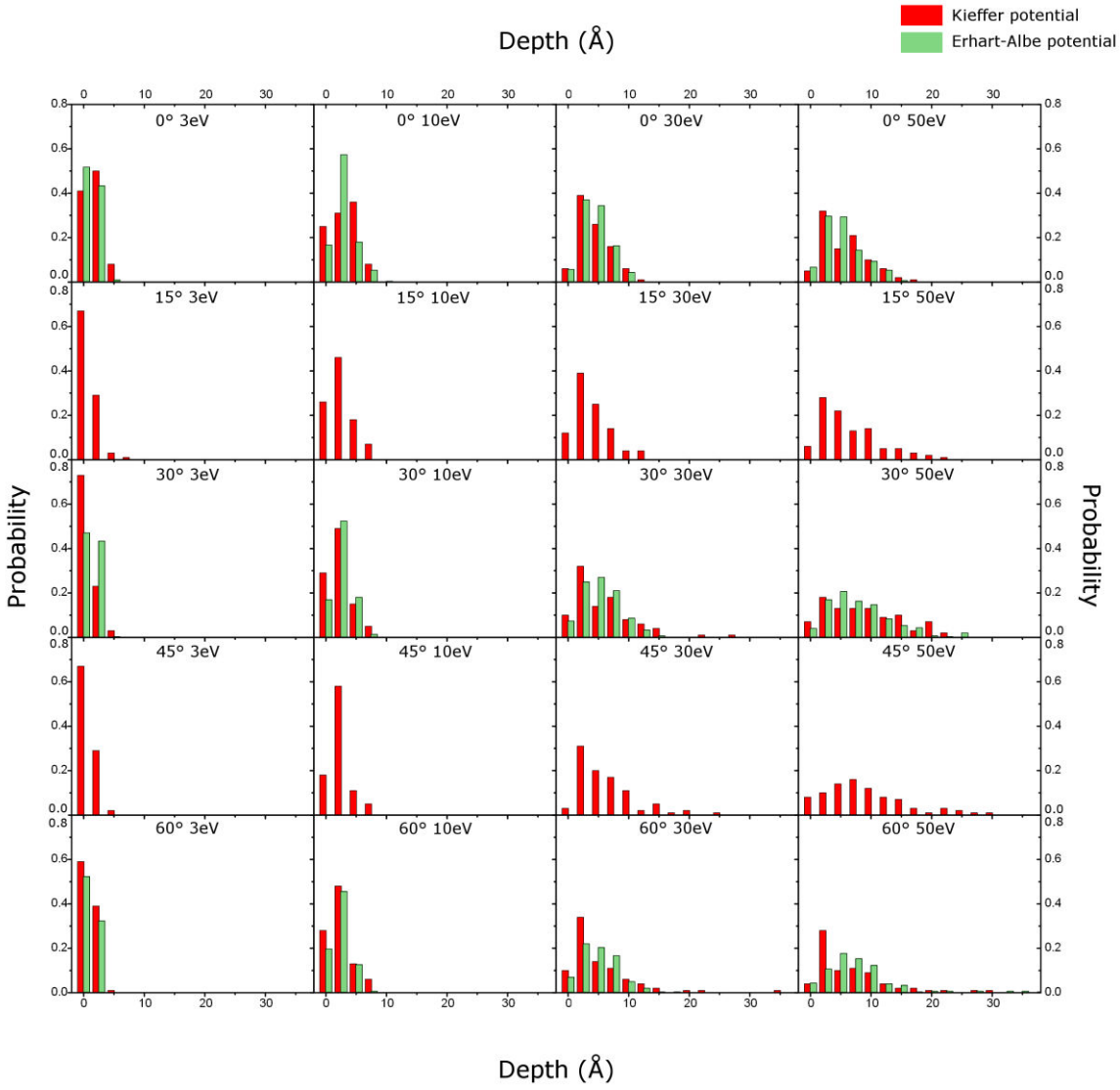

Fig. III-2: Depth distributions computed with Kieffer (red) and Erhart-Albe (green) potential for selected incidence angles and energies.

In Fig. III-2 the dispersion of deposition depths for selected energies and incidence angles are presented. Fig. III-3 shows the average depth reached by the carbon projectile for each impact and incidence angle. The depth is computed by taking the difference in z coordinates of the impact point on the substrate and of the final configuration of the carbon atom. Backscattered atoms are ignored whenever averages are computed. The data for both potentials is presented in Fig. III-2 and Fig. III-3 and no major systematic differences can be observed. The higher backscattering yields that have been observed in Fig. III-1 for deposition at low energies coupled with a 60° incidence angle have no impact on the depth reached by the carbon. Instead, the largest differences in the implantation depths between the two potentials are observed for the higher deposition energies at 30° and 60° incidence angles. These divergences stay within the error bars and are not systematic, since at 50 eV – 60° the Erhart-Albe potential provides a slightly deeper implantation and at 50eV – 30°, it is the Kieffer potential that provides the deepest implantation. From Fig. III-2, it can be seen that the shallower implantation for the Kieffer potential at 50eV – 60° is due to a higher stopping power of the material at shallow depths. Similarly, the deeper implantation at 50eV – 30° for the Kieffer potential is due to a tail in the depth distribution extending deeper than for the Erhart-Albe potential.

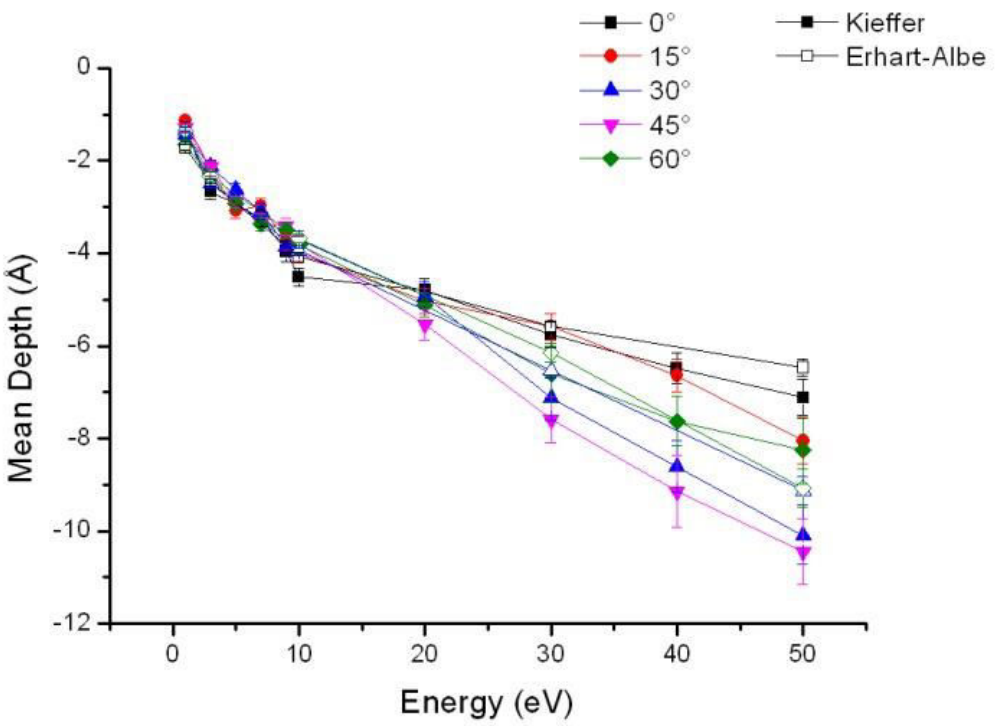

Fig. III-3: Evolution of the average depth versus the deposition energy as computed using Kieffer and Erhart-Albe potentials. The depths are computed as the differences in the z coordinates of the impact location and the final location of the carbon atom.

Looking at Fig. III-3, one can observe that the incidence angle has no influence on the average depth of the deposited carbon at energies up to 20 eV. The trend in dispersion of depths for the lower half of

the deposition energies (Fig. III-2) is the same when comparing the incidence angles at selected energies, confirming the incidence angle does not influence the depth reached by a carbon projectile having a kinetic energy lower than 20 eV. At higher energies, this is not true anymore, since incidence angles of 30° and 45° lead to the deepest mean deposition depth and incidence angles of 0° and 15° to the shallowest. The average depths reached by deposition performed at 60° incidence angle lie in-between these two extremes. The analysis of the depth dispersion on Fig. III-2 brings some useful insights on the issue.

The dispersions of depths at 30 eV and 50 eV are very similar when comparing simulations at 0° and 15° incidence angles. The most probable depth reached by carbon is 2.5 Å. The probability to find the carbon atom at a selected depth then gradually decreases when going deeper into the sample. For energies of 30 eV, this probability virtually reaches 0 after a depth of 10 Å for both incidence angles, while at 50 eV this point is reached at 17.5 Å for normal incidence and 20.0 Å for 15° incidence. At incidence angles of 30° and 45°, the situation is completely different. The most probable depth at 30 eV is still located within 2.5 – 5.0 Å for both incidence angles, but the absolute probability to find a carbon at that depth is lower than the absolute probability observed at normal and 15° incidence. In addition, the tails of the distributions extend much deeper into the sample (down to 15 Å at 30° incidence and to 20 Å at 45°). Looking at the depth distributions for simulations carried out at 50 eV, the difference with the 0°-15° incidence angles is even more flagrant, as the depth distributions for 30° and 45° is nearly flat, with an almost constant probability to find the carbon atom between depth 0 Å and depth 20 Å. In addition, it should be noted that only few carbon atoms were observed far deeper than 20 Å for the 30° and 45° incidences. At the most grazing angle of 60°, the shapes of the depth dispersions computed with Kieffer potential are in between the ones of 0° - 15° incidence angle and the ones of 30°- 60°. For both 30 eV and 50 eV energies, the most probable depth is clearly at 2.5 Å but as for the 30° -60° incidence angle simulations, the tail extends very deep inside the silicon bulk and few carbon atoms can be observed at depths much deeper than 20 Å.

Raineri *et al*. have reported that when implanting boron and phosphorus in crystalline silicon at several directions, the depth profiles present a single maximum intensity for all directions except the (110), where a second intensity maximum is observed at significantly deeper depths[130]. Similarly, as seen in the previous paragraph, when depositing carbon at angles close to 45° incidence angles, part of the flux is stopped at a shallow depth, while the rest of the flux can reach a deeper part of the silicon sample. The reason for these different behaviours in the dependence of the depth distribution on the incidence angles is attributed to narrow channels running through the bulk structure in the (110) direction and its symmetry-equivalent directions. Part of these channels indeed intersect the Si(100) surface plane with an angle of 45° relative to the normal of the surface and are available to the carbon atoms. Fig. III-4 shows the (101) projection of the accessible surface area for a carbon atom of size 1.5 Å. The colouring is set depending on the achievable depths and the channels are clearly

visible as black dots. As a consequence of this orientation, only the carbons having an incidence angle close to 45° are allowed to enter the channels. Carbon depositing with an incidence angle of 0° and 15° are too far from this 45° optimum and are stopped at very shallow depths. Our simulations also show that incidence angles of 30° and 60° are still within the correct window, to allow the carbon to enter the channels and reach a deeper part of the silicon sample.

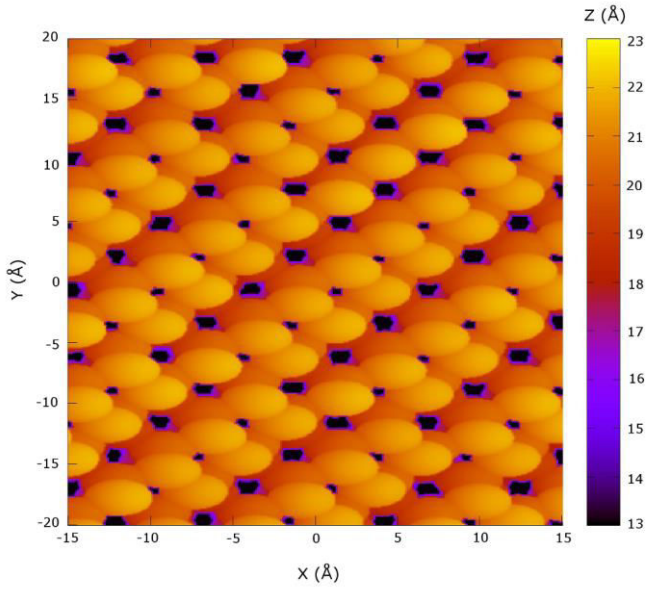

Fig. III-4: Accessible surface area for a 1.5 Å radius atom having a trajectory at 45° from the (100) Si normal.

There are four equivalent directions to the (110) vector going through the (100) plane, meaning that on an azimuth plane parallel to the surface, four orthonormal channels meet the (100) plane (Fig. III-5). This explains why there is such a wide distribution of achievable depths for 30°, 45°, and 60° incidence angles. Carbon projectiles that do not possess the right azimuth trajectory cannot enter the channel and are stopped at shallow depths, while others will go deeper inside the silicon surface. From the very flat depth distribution of simulations at 50 eV and 45° incidence angle, we can conclude that the proportion of atoms effectively entering the channels versus those not entering is about 50/50, which sets the window on an azimuth plane to enter the channel to about 45°. This is supported by experimental results reported in[3]where both maxima in the intensities of the depth profiles in the (110) direction have equal intensities.

Next the reasons for the different depth distributions at 50 eV – 60° observed with Kieffer and Erhart-Albe potentials are analysed in depth. It is known that energies and forces between carbon and silicon increase faster at higher energies for the Erhart-Albe than for the Kieffer potential [122]. These steeper forces mean that it is easier for the carbon atom to enter the channel when outside the correct azimuth window, effectively widening it. With the weaker repulsive forces of the Kieffer potential, the carbon

is more likely to form bonds with silicon atoms before being deviated into the channels. This effect can also be observed, albeit to a lesser extent, for deposition at 30°. At 0° no differences between the potentials can be observed because the channel is completely out of reach for the carbon atom. This explains the stronger stopping power at shallow depth for incoming directions slightly out of the perfect channel window, i.e. 45°.

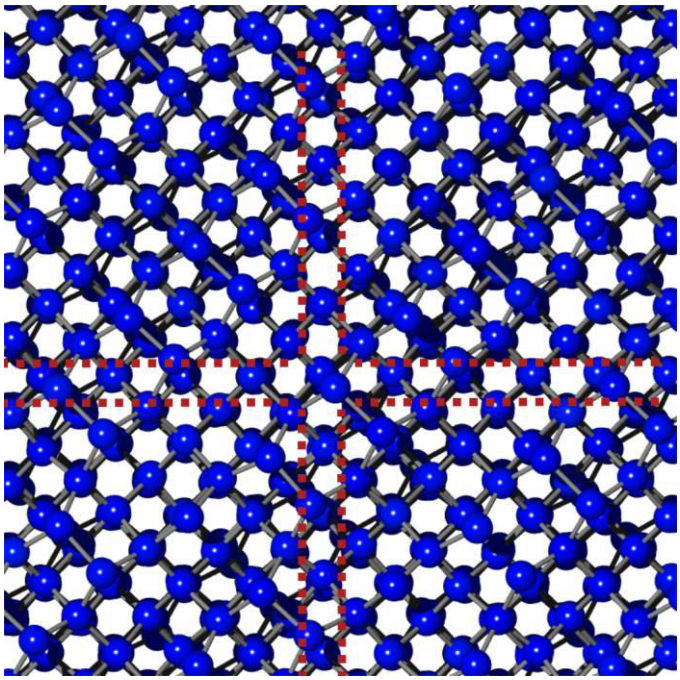

Fig. III-5: <100> top view representation of the directions followed by the (101) and (011) channels inside the silicon structure.

iii) Comparison with DFT.

The MD results obtained during the PhD work are now compared to some DFT data obtained by another researcher during the project. DFT calculations for carbon adsorption have been performed on different sites on and underneath the surface plane. The adsorption energies for the different sites will allow to support, or not, the MD results. On the surface, two adsorption sites have been identified with very similar adsorption energies of 7.26 and 7.16 eV. The most stable geometry is when carbon adsorbs *vis-à-vis* of a surface silicon dimer, creating bonds with three silicon atoms (Fig. III-6a). The three Si-C bond lengths are 1.76 Å, 1.90 Å and 1.90 Å. On the side of the silicon dimer where the carbon adsorbs, the dimer is now only linked to the material through the carbon atom, breaking two Si-Si bonds at the benefit of three Si-C bonds. The other adsorption site (Fig. III-6b) is located in between two silicon dimers. The distortion of the silicon surface is lower, but the carbon atom is only bound with two silicon atoms (1.82 Å both), explaining the slightly lower adsorption energy.

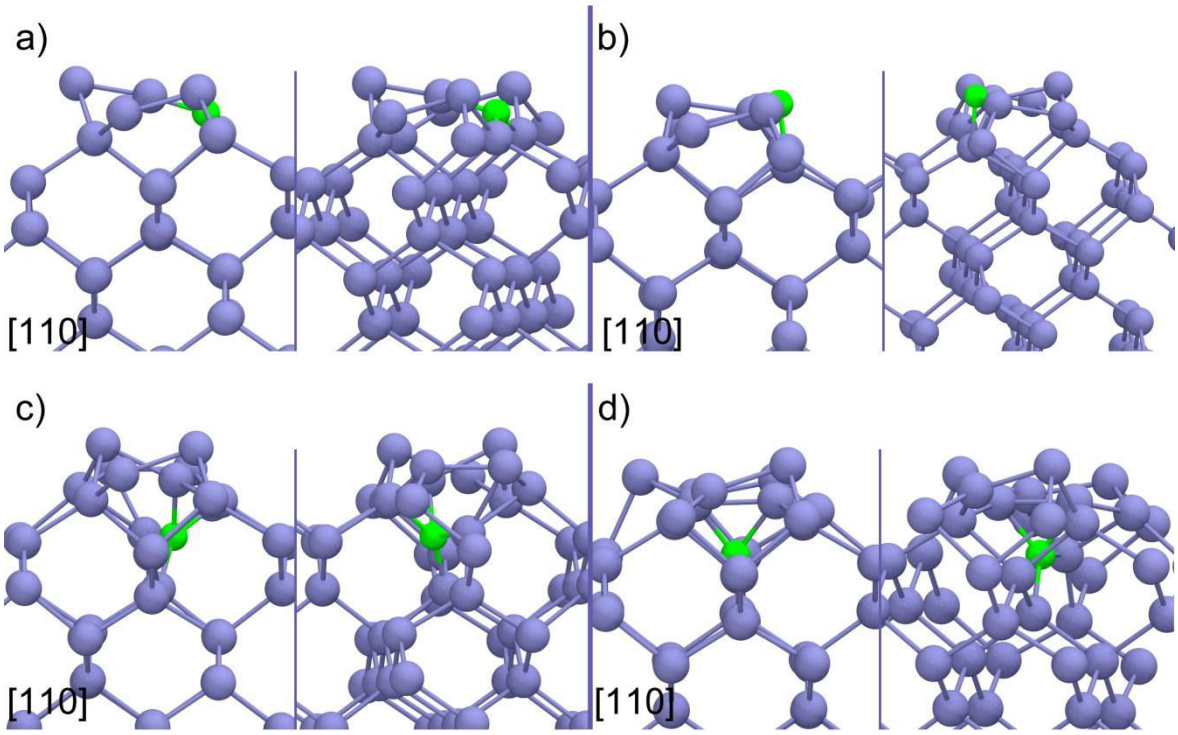

Fig. III-6: Top and side views of four adsorption sites for carbon on the (100) surface as computed by DFT.

In parallel to these two surface adsorption sites, we have identified two other sites for carbon deposition under the surface plane (Fig. III-6c and 6d) with adsorption energies of 7.87 eV and 8.10 eV, which are significantly more stable than those on the surface plane. In both subsurface sites, the carbon atom sits tetrahedrally bound beneath a surface silicon dimer. In the most stable configuration (Fig. III-6d), there is a strong distortion of the silicon structure around the carbon defect, with a silicon atom now protruding on the surface between two silicon dimers. The four Si-C bond lengths are 1.82 Å, 1.82 Å, 1.92 Å, and 2.04 Å. On the other sub-surface site (Fig. III-6c), no silicon atom is pushed out of its initial location. Its higher energy shows that the distortion observed in Fig. III-6d allows the structure to decrease the internal stress induced by the interstitial carbon atom. These DFT results show a qualitative agreement with the MD simulations presented above, as both methods show that carbon atoms tend to favour subsurface deposition sites. Indeed Fig. III-6 shows that, provided it has enough energy to pass through the first layer of the surface, the carbon deposit is more likely to stay 2.5 Å below the surface plane.

iv) Sticking coefficient

Due to the short simulation times, 6 ps for the Kieffer potential and 5 ps for the Erhart-Albe potential, the sticking coefficient of carbon on silicon includes only immediate backscattering events. It should also be noted that all carbon atoms come to rest during the simulation, so that the probability of later

desorption is small. Some deposited matter may eventually desorb from the collector by simple thermal activation, leading to a lower sticking coefficient than the one measured within the first 6 ps of the deposition. This loss of matter by thermal activation is not easy to quantify as, ideally, one would need to perform kinetic Monte-Carlo simulations knowing the activation energy for carbon desorption from different deposition sites as well as the activation energies for surface diffusion, coalescence, etc [9]. An easier way, albeit still computationally expensive, to assess this loss due to thermal activation is to let the MD simulations run for significantly longer times. Two deposition conditions using the Kieffer potential are selected to run the extra MD simulations for significantly longer timing using the last configuration of their corresponding simulation as starting point. The first condition is the one with deposition at 50 eV – 60° in order to have a highly energetic system and a relatively shallow deposit. The second run has deposition conditions of 1 eV – 0° to have a high load of carbon deposit at very shallow depths. Simulations are run using a 1fs time step for 200 ps. No desorption of carbon from the collector due to thermal activation could be observed within the 200 ps of the simulations. This leads us to conclude that the thermal desorption of carbon from the silicon wafer is very low and the backscattering yields observed in Fig. III-1 may be a reasonable first approximation to assess the sticking coefficients, as they are the inverse of the backscattering yields. Deposition incidence angle close to the normal gives always high sticking coefficients. Depending on the initial energy of the carbon atom, the sticking coefficients range from 100 to 92 %, 100-95 %, 100-93%, 100-90 % for 0°, 15°, 30° , 45° and 60° incidence angles respectively. The differences in sticking coefficients found at different angles are small.

v) Conclusion and outlook

With the view of performing analyses of alloy materials using the Storing Matter technique developed at the Centre de Recherche Public- Gabriel Lippmann in Luxembourg, the first steps of a MD investigation of carbon deposition on silicon surfaces have been discussed . The reactive force field developed by John Kieffer et al. is selected, as it enables the formation and breaking of bonds via an adaptive and environment sensitive charge transfer.

The deposition of a single carbon atom on a (100) reconstructed silicon surface at energies lower than 50 eV is investigated and compared to similar MD simulations performed using the well-established Erhart-Albe potential. 100 independent simulations are run in order to have significant statistics. Results using both potentials are similar, although slight divergences appear at grazing angles and for the higher end of the deposition energies.

3) Section 2: Results for Continuous Carbon Deposition

i) Introduction

Silicon Carbide (SiC) is a semiconductor material with a wide band gap which has interesting properties for many applications, including among other high-power and high-frequency electronic devices [131], nuclear technology, deep-space missions and in the semiconducting industry [132,133]. At the same time, the performances of such devices significantly depend on the defects formed during crystal growth or ion implantation processes. In order to investigate the influence of the defects on the SiC film properties, several theoretical and experimental studies have been carried out. Both, the electrical and physical properties of SiC films, or devices made of SiC, change with the SiC crystalline structure [134]. As per example, the fabrication of light emitting diodes depends on the intrinsic defects in Silicon carbide [135]. In order to understand how the material properties depend on growth conditions, a detailed insight into the sputtering/deposition of carbon materials on silicon substrates is of key importance for thin film growth via plasma deposition techniques and sputter deposition.

In this section of carbon deposition on silicon, we describe the deposition of multiple carbon atoms on a crystalline silicon (Si) surface modelled at 1, 5, 10, 20, 30 eV energies with initial directions of 0°, 30°, 45° and 60° to the normal of the silicon surface by using molecular dynamics simulations combined with the afore-described force field that includes bond breaking and formation. In this section we use the MD simulations to investigate how continuous or multiple carbon deposition on the silicon surface may influence substrate amorphization and carbon implantation mechanism as compared to what was observed on crystalline and amorphous silicon surfaces. These simulations allow for atomic scale insights into the deposition mechanisms and an easier comparison with experimental observations. The results, including distributions of implantation depth, carbon concentrations, sticking coefficients, radial distribution function, angular distribution function and coordination are compared for different incidence angles, energies and fluences. Due to the deposition of carbon inside the silicon structure, silicon - carbon compound starts to form. The crystalline structures have been investigated for different conditions to get a better understanding of the damaging and growth mechanisms. It is found that a lot of damage is accumulated in the area of deposition near to the surface but underneath the surface the silicon has still a more crystalline structure. The variation of the silicon structure slightly depends on the angle of incidence. For the conditions used for these simulations, the sticking probability is always high and varies between 95% and 100%, which can be attributed to the high affinity of carbon for silicon.

ii) Results and discussion

The results for continuous carbon deposition have been analysed in three approaches to observe the influence of energy, angle and fluence of the incoming carbon atoms on the deposition mechanisms. First, the angular influence on deposition and implantation mechanism at a constant energy of 5 eV is

described. The 5 eV energy has been chosen because it is within the typical energy range for magnetron sputtering in plasma deposition processes and sputter deposition. The azimuth angle for these simulations has been fixed to 45°, which, together with the incident angle, defines the initial direction of the carbon atoms with respect to the silicon surface. Secondly, the energy influence on deposition and implantation mechanisms has been investigated for a constant angle after 100 carbon depositions. Energies of incoming carbon have been varied at 1 eV, 5 eV, 10 eV, 20 eV, 30 eV. The observation for different energies have been done at 0° and also comparison of the outcome parameters at another extreme angle for 60° have been discussed in order to have meaningful conclusions. The azimuthal angle is fixed at 45° for each case. In third approach, the evolution of the system structure has been investigated with change in deposition dose. For a particular impact energy and incidence angle, dose of incoming carbon atoms has been varied and outcome parameters for system structure have been observed. In this case also, the azimuthal angle is fixed at 45°.

iii) Results for multiple carbons at constant energy

We will present and discuss how low 5 eV deposition of multiple carbon atoms modifies the silicon structure.

(a) Depth distribution and concentration

Fig. III-7 presents the depth distributions after the deposition of 100 carbon atoms for incidence angles of 0°, 30°, 45° and 60°. More than 90% of the atoms get implanted in the first 10 Å of the sample, independent of the angle of incidence. The number atoms at the surface is relatively low (8 – 16 counts) and increases to a maximum of 25 – 30 counts at a depth of 5 Å below the surface. The difference in counts between the different angles is not significant. At a depth of 16.25 Å, the number of counts is almost zero, and no atoms get implanted to a depth of 17.5 Å or deeper. At a depth of 5.0 Å, there is an abrupt fall in counts for the 30° angle, which is due to statistical fluctuations related to the relatively small number of deposited atoms. The general trend of Fig. III-7 is visible in the average implantation depths, which are also quite similar for the different angles, with 6.9 Å at 0°, 6.2 Å at 30°, 6.7 Å at 45° and 6.0 Å at 60°.

Fig. III-8 shows the variation of carbon concentration versus depth. On the graph, the points refer to the middle of the slabs. For the angle of incidence at 60°, the concentration is maximum right at the surface, i.e. in the first slab with a thickness of 2.5 Å, and for the other angles the maximum in between 2.5 Å and 5.0 Å. The concentration of carbon atoms becomes zero after a depth of 22.5 Å, and this for all conditions. The maximum concentration does not exceed 14 atomic% which shows that we model only the beginning of the film

growth and that the concentrations are far from a stoichiometric carbide. Apparent contradictions between Fig. III-7 and Fig. III-8, like higher C surface concentration for an incidence angle of 60° versus highest counts for carbon atoms at 30° for the depth distribution is due to changing number of atoms in the topmost slabs. This is due to slight roughening of the surface as well as density variations in the topmost slab due to damage formation. This effect is not visible in Fig. III-7. In general, Fig. III-8 shows that more grazing incidence leads to higher surface concentrations. The apparent slightly shallower implantation depth at 60° might be not relevant because of the small difference to the other incidence angles.

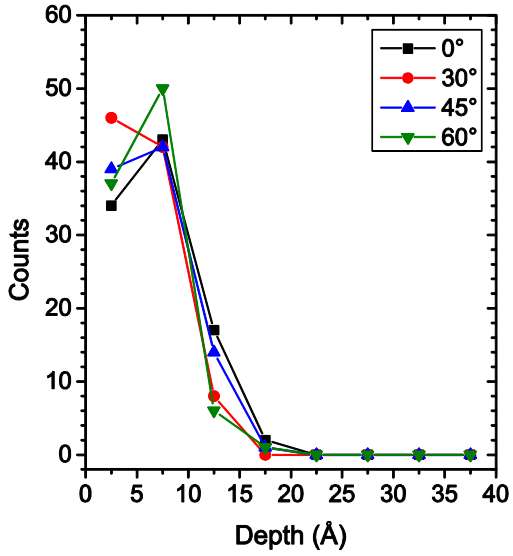

Fig. III-7: Depth distribution of implanted atoms for the incidence angles of 0°, 30°, 45° and 60°.

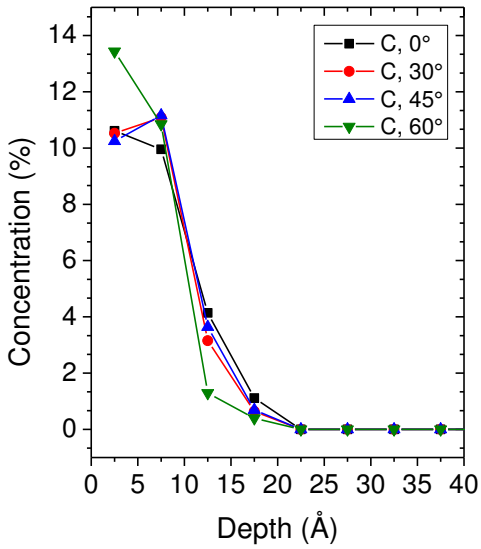

Fig. III-8: Variation of the concentration of the carbon atoms with depth for the deposition of 100 C on a Si(100) surface. The data is shown for the 4 incidence angles.

(b) Radial distribution function

The formation or deformation of the silicon structure with increasing depth can be studied by the radial distribution function. The radial distribution function g(r) has been calculated for various slabs, each slab having a thickness of 5 Å. Fig. III-9 shows its variation at 0°, 30°, 45° and 60° incidence for the different slabs. It clearly shows that the peaks are more distinct for the slab at 17.5 Å compared to the other slabs. As the slab with centre at 17.5 Å is quite far from the surface, only few carbon atoms get implanted to that depth and the structure is less damaged. The other slabs are closer to the surface with more implanted carbon atoms and the silicon structure is already more damaged, which results in broader and less separated peaks. For the slabs closer to the surface, a first smaller peak at a distance of about 1.9 Å from the central is due to Si-C first-neighbour contributions. The higher peak at 2.3 Å is due to Si-Si first neighbours. The broadening of the second-nearest Si-Si peaks at a depth of 3.4 Å is partially due to Si-C contributions. Comparing the peaks corresponding to Si-C and Si-Si interactions allows us to conclude that the structure of the system is amorphous, or at least heavily damaged, near to the surface and has a more crystalline structure in deeper regions as they are less affected by the C implantation.

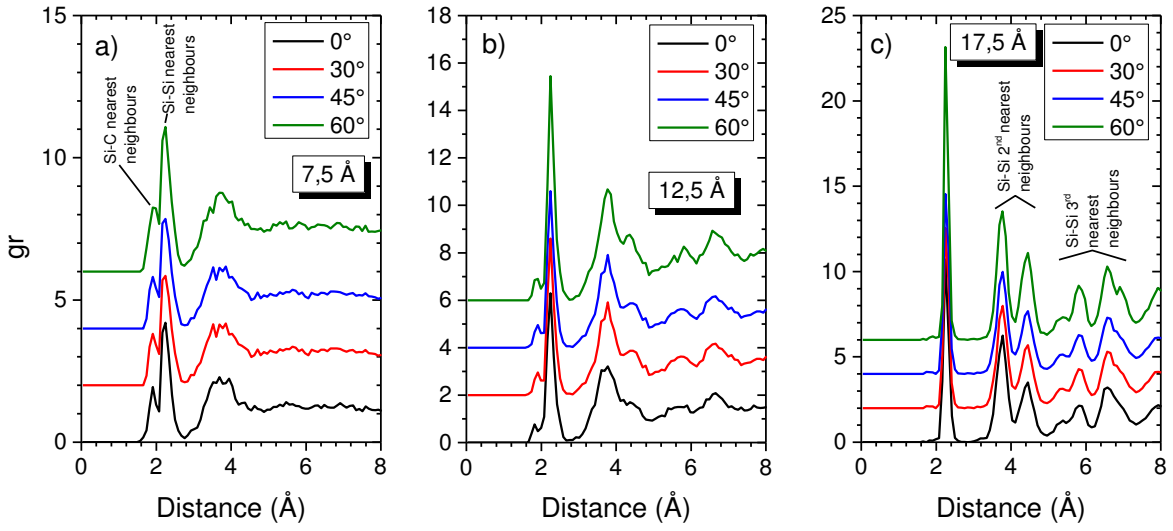

Fig. III-9: Radial distribution function for different angles for the slabs centred on a) 7.5 Å, b) 12.5 Å and c) 17.5 Å.

In addition, an influence of the incidence angle on the radial distribution function is also visible in Fig. III-9. The peaks for Si-Si and Si-C first-neighbour interactions at 60° incidence angle for the slab with centre at 7.5 Å show no major dependence on the angle of incidence. For larger depths, differences become however apparent. At 12.5 Å, the two Si-Si second-

nearest neighbour peaks at 3.8 Å and 4.4 Å are better separated at 60° than for the other angles. This becomes even more pronounced at 17.5 Å for the Si-Si second- and third-nearest neighbour peaks. At 60° incidence, more energy gets deposited closer to the surface, which results in less damage at 12.5 Å or deeper inside the Si substrate.

(c) Angular distribution function

Beyond the radial distribution functions, it is also interesting to note how the angular distributions vary for the different slabs with the incidence angles. In order to interpret the results, we consider the same three slabs (centred on 7.5 Å, 12.5 Å and 17.5 Å) (Fig. III-10). Close to the surface, the angular distribution is much broader than inside the sample with low or no carbon implantation. In the slab centred at 7.5 Å, the peaks are wider compared to the other slabs, which is an indicator of heavier damage in that slab. There are two distinct peaks: one around 55° and another around 110°, which proves that the angular distribution is really broad in this case. Contributions to angles below 80° in the crystalline structure are due to carbon atoms which implanted into interstitial positions in the silicon lattice. During the initial implantation of carbon and SiC formation, this seems to be a preferred site in the Si lattice. In the case of the slabs centred on 12.5 Å and 17.5 Å, the peaks are sharp and well distinct, which reveals that the structures are less damaged in these slabs. Still, the 12.5 Å slab, some carbon atoms in interstitial sites contribute to angles below 80° and the main peak is still larger than at 15.5 Å.

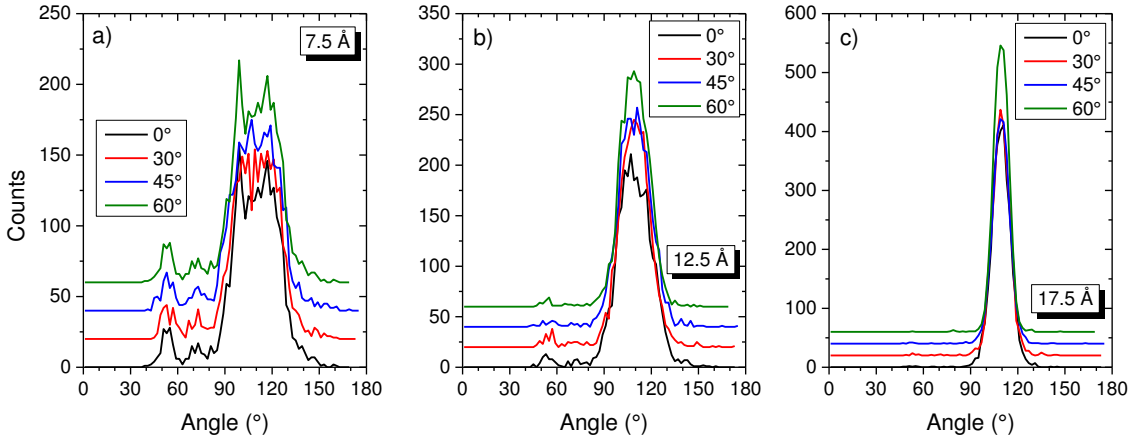

Fig. III-10: Angular distribution for the slabs at a) 7.5 Å, b) 12.5 Å and c) 17.5 Å for the different incidence angles.

Here we observed the change in outcome parameters for different angles. There are some significant changes in the deposition mechanisms between 0° and 60°. In the next paragraph, we will discuss the influence of energies in deposition mechanisms.

iv) Results for continuous C deposition at constant angle for different energies

Previously, we observed how the change in angles influences different mechanisms for continuous carbon deposition at a constant energy. In this section, we investigate how it influences several parameters (radial distribution function, depth distribution, angular distribution function, coordination, concentration) for continuous carbon deposition while the impact energies of incoming carbon have been changed for a constant angle. Like for the previous section, the results have been analysed after 100 carbon depositions. The results have been analysed first at a constant angle of 0° for several energies (1 eV, 5 eV, 20 eV, 30 eV) and also at 60° for the same energy variations. Two constant angles are chosen to verify if there are significant contributions of angles while the energies are varied to study the outcome parameters. For both cases, the azimuthal angle is fixed at 45°. In the following paragraphs we will discuss the outcome of continuous carbon depositions by calculating the parameters such as radial distribution function, depth distribution, coordination, angular distribution function, and concentration successively for a constant angle at different energies.

(a) Radial Distribution Function

The outcome of different structures formed during continuous carbon depositions and implantations with increasing depth and energy can be studied and explained by the radial distribution functions. The radial distribution function g(r) has been calculated for various slabs, each slab having a thickness of 5 Å. Fig. III-11 shows its variation at 1 eV, 5 eV, 20 eV and 30 eV for different slabs at 0° incidence angle while the azimuthal angle is fixed at 45°. The peaks are more distinct for the slab at 12.5 Å compared to the other slabs. As the slab with centre at 12.5 Å is quite far from the surface, only few carbon atoms get implanted to that depth and the silicon structure is less damaged. The other slabs which are closer to the surface are already damaged due to the excess number of presence of carbon atoms than the available lattice sites. For the slabs closer to the surface, it can be observed that there is a first smaller peak at a distance of about 1.9 Å from the central. This is due to Si-C first-neighbour contributions. The higher peak at 2.3 Å from the central is due to Si-Si first neighbours. The peaks corresponding to Si-C and Si-Si interactions give ideas about the structure of the system. Now we will investigate how energy can influence the system structure by observing variations in radial distribution function as depicted in Fig. III-11. For the slab with centre at 2.5 Å, the peaks for Si-C first-neighbour at a distance about 1.9 Å for 1 eV have higher

values compared to other energies as most of the carbon atoms stay just near to the surface for 1 eV incident energy. The case is opposite for the slab having centre at 12.5 Å as carbon atoms do not have sufficient energy to be implanted in this slab while being incident at 1 eV. The peak amplitude for Si-C first neighbour is almost negligible for 1 eV in the 12.5 Å slab but still there are small number of carbon atoms. It is not expected to be implanted 12.5 Å deep for 1 eV carbon atom but it is due to the formerly implanted carbon atoms have been pushed downwards by the lately arrived carbon atoms. This will be discussed in more detail in the section on the changes with fluence. For higher energies, the ratio of Si-C to Si-Si peaks has lower value than at 1 eV in 2.5 Å slab and higher value in 12.5 Å slab. This reflects that energy has a certain influence in the variation of structure formed due to the carbon implantation. At 12.5 Å, the two Si-Si second-nearest neighbour peaks at 3.8 Å and 4.4 Å have higher values at 1 eV energy than at other energies. At 1 eV incident energy, more carbon atoms get deposited closer to the surface, which results in less damage at 7.5 Å and 12.5 Å or deeper inside the Si system. The distributions of carbon atoms will be seen in a clearer aspect while we discuss the depth distribution of carbon atoms in different slabs in next section.

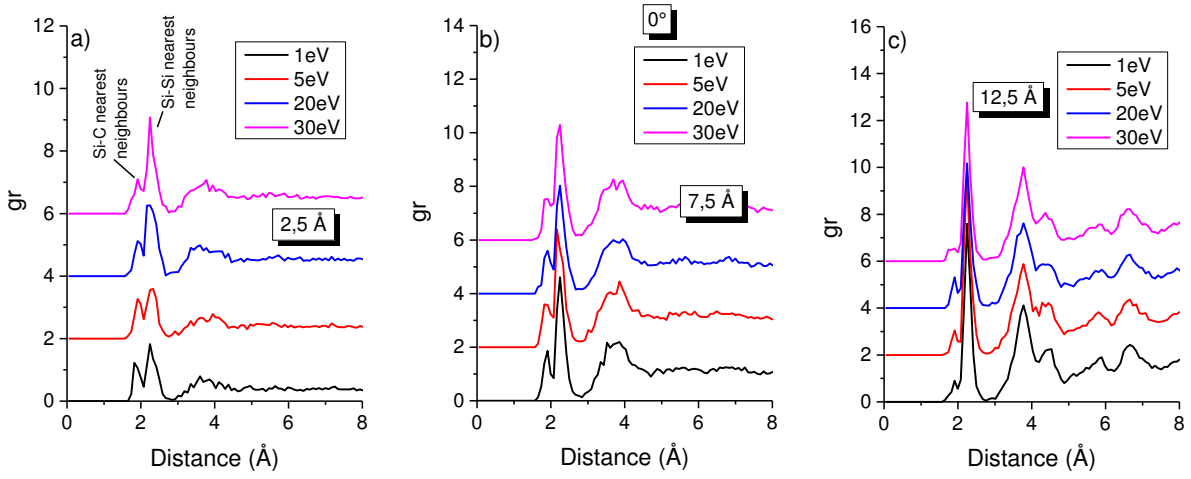

Fig. III-11 :Radial distribution function for different energies at 0° for the slabs centred on a) 2.5 Å, b) 7.5 Å and c) 12.5 Å.

Next, we will describe here the variations in radial distribution functions with energies for another extreme angle at 60°(Fig. III-13). The variation is quite similar compared to 0° incidence angle but there are changes in values of radial distribution function for both angles. If we consider the ratio between the Si-C and Si-Si nearest neighbour peaks at different energies for both 0° and 60° angles,

certainly the Si-C peak has higher amplitude values at 60°. This proves that there are more carbon atoms near to the surface at 60° than at 0°.

In order to understand the mechanism in a better way, we took snapshots at 0° and 60° for 5 eV incident energy after 100 carbon depositions. The other energies gave similar results. Fig. III-12 (a) describes the snapshot at 0° and Fig. III-12 (b) describes the snapshot at 60°. The white line is drawn 12.5 Å beneath the surface. It is seen from the Fig. III-12 that there are quite a few carbon atoms under the line for 0° but the number is pretty less for 60°. So, majority of carbon atoms stay near to the surface for 60° incidence angle and it contributes to higher Si-C peaks.

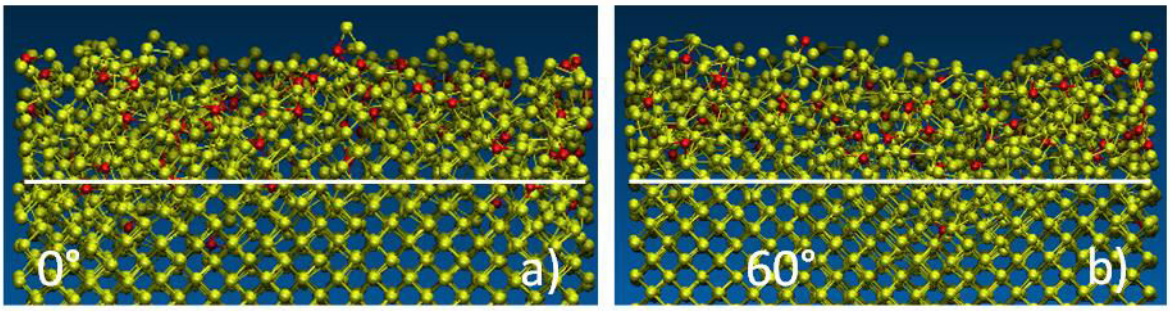

Fig. III-12: Snapshots at 0° and 60° after 100 carbon depositions for 5 eV incident energy.

The Si-Si 2nd and 3rd peaks are more sharp and prominent in 12.5 Å slab compared to the slab centred at 7.5 Å and 2.5 Å. This proves also that there is less implantation of carbon atoms and the structure is more like silicon structure.

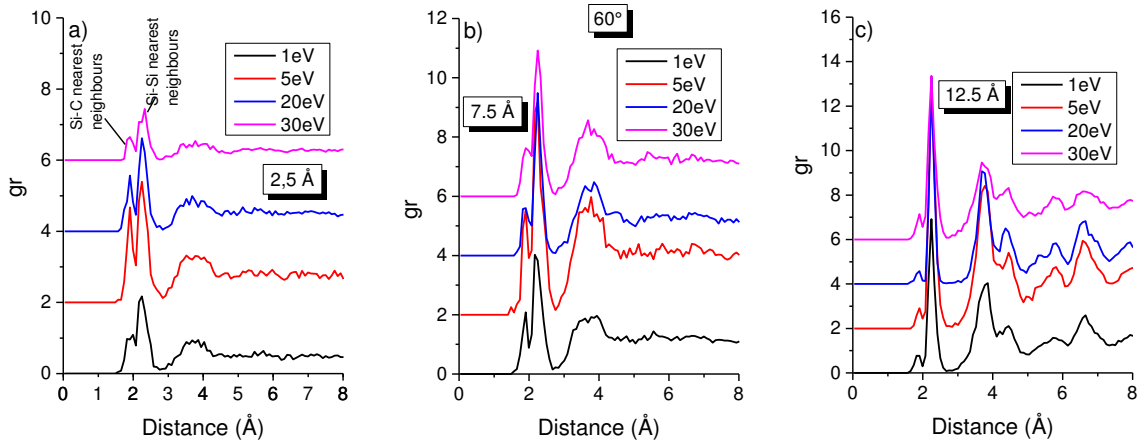

Fig. III-13: Radial distribution function for different energies at 60° for the slabs centred on a) 2.5 Å, b) 7.5 Å and c) 12.5 Å.

(b) Depth distribution

The distribution of carbon atoms along the depth for different energies is shown in Fig. III-14 and Fig. III-15. Fig. III-14 and 15 give the information about the number of carbon atoms present in a bin at a

particular depth. The depth distributions are done by histogram analysis having the bin size of 2.5Å. It is observed from the distribution of carbon atoms for the first slab that the number of carbon atoms increases from 1st bin to 2nd bin for all four energies in Fig. III-14 and 15. So, it is obvious that the number of carbon atoms is not maximum just near to the surface but it is maximum a monolayer beneath the surface. Considering the number of carbon atoms deposited beneath 10 Å distance from the surface for both 0° and 60°, the counts are always maximum for 0° incidence angle for a particular energy that means the atoms stay comparatively closer to the surface in case of 60° incidence angle.

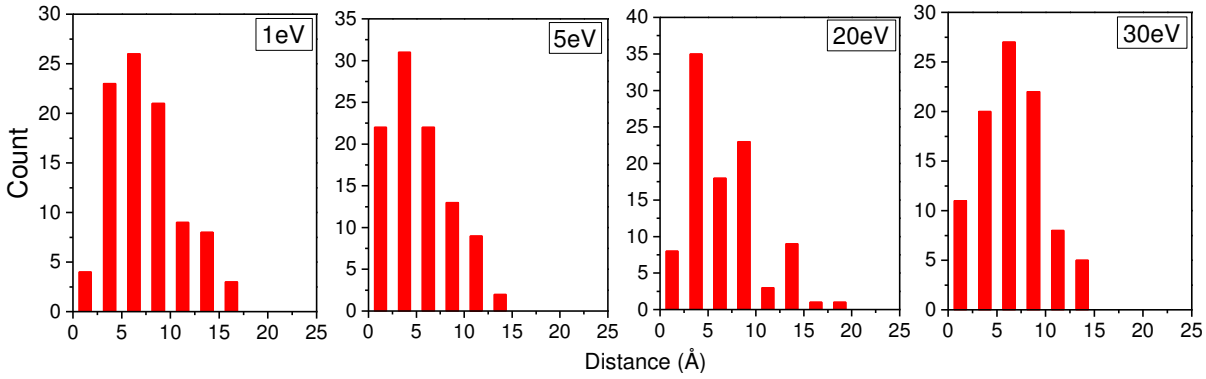

Fig. III-14: Depth distribution of implanted atoms for the energies of 1 eV, 5 eV, 20 eV and 30 eV at 0°.

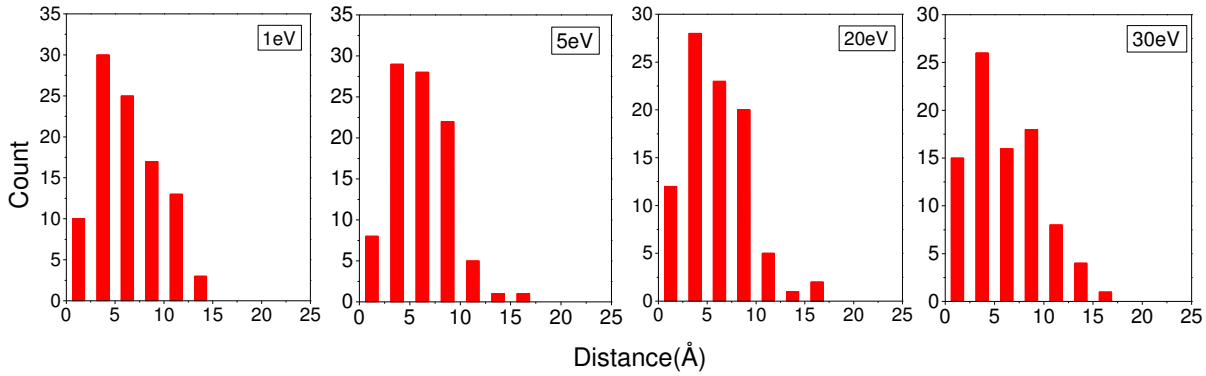

Fig. III-15: Depth distribution of implanted atoms for the energies of 1 eV, 5 eV, 20 eV and 30 eV at 60°.

(c) Coordination calculations

The coordination number of an atom defined as the number of nearest neighbours and it is estimated by counting the other nearby atoms to which it is bound. Along with radial distribution calculations, coordination calculations help to describe the bonding structure after the carbon atoms got deposited or implanted in the silicon system. Here we will investigate and determine how the energy of the carbon atom influences to the bonding with their nearest neighbours in three different slabs by calculating the coordination number. First, the results for coordination calculations have been described at 0° incidence angle for energies at 1 eV, 5 eV, 20 eV and 30 eV (Fig. III-16). In order to interpret the results, we consider three slabs (centred on 2.5 Å, 7.5 Å and 12.5 Å) at 0° incidence angle. The trend in variations in coordination number is almost same for three slabs but the number of carbon atoms being coordinated varies for different slabs. It is observed that most of the carbon atoms

are being bound to four neighbours in three slabs but still there are some carbon atoms which is bound to 3 or 2 neighbours and even 1 neighbour (at 1 eV incident energy for 2.5 Å slab). This unusual positioning of carbon atoms and getting coordinated with one neighbour in the silicon system can be due to the defects and damage already created nearer to the surface of the system. The counts of carbon atoms coordinated with four neighbours is maximum in 7.5 Å slab and the value of counts varies from 46 to 48 for all the different energies in the slab. The average number of carbon atoms having coordination 4 varies between 24 to 32 for 2.5 Å slab and 17-28 for 12.5 Å slab for all the energies. There are some carbon atoms having coordination number 2 at 30 eV incident energy in the 2.5 Å slab, which might come due to the defects created already nearer to the surface.

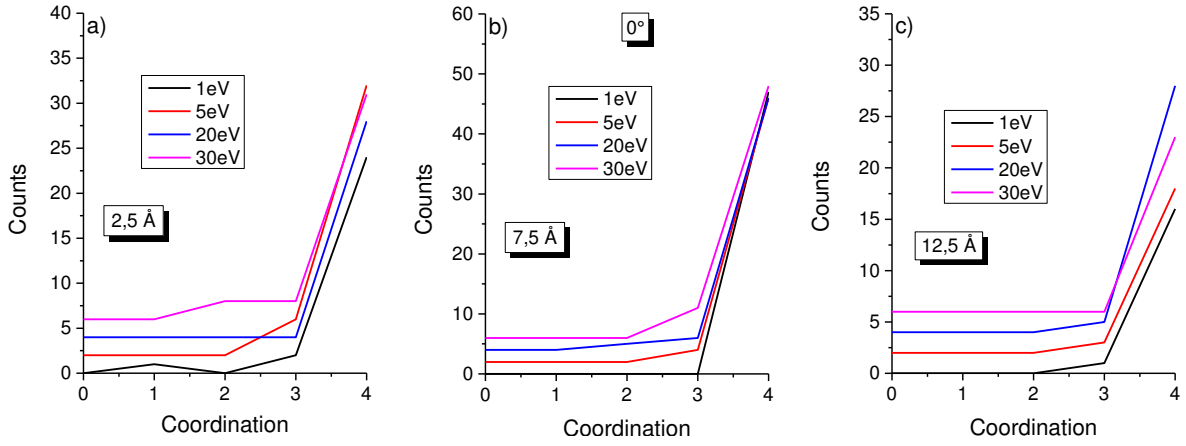

Fig. III-16: Coordination values for different energies at 0° for the slabs centred on a) 2.5 Å, b) 7.5 Å and c) 12.5 Å.

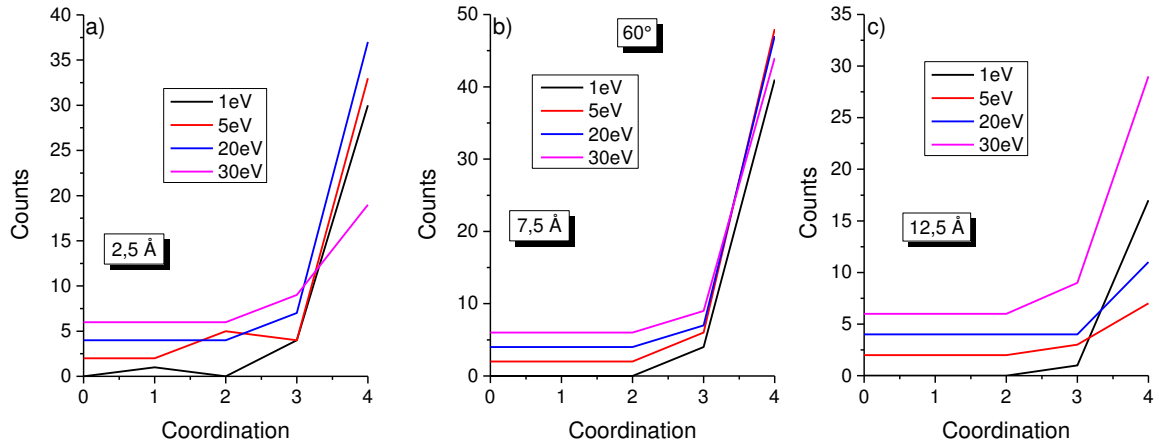

Fig. III-17 :Coordination values for different energies at 60° for the slabs centred on a) 2.5 Å, b) 7.5 Å and c) 12.5 Å.

Now, we will discuss the coordination of carbon atoms in case of 60° incidence angle (Fig. III-17). In case of 30 eV incident energy, the coordination of carbon atoms with four neighbours is lowest compared to others energies in the 2.5 Å slab and highest in the 12.5 Å slab than other energies. If we

consider the coordination mechanism of the carbon atoms for three slabs, it is found that the carbon atoms are well coordinated in 7.5 Å slab. At 5 eV energy, some of the carbon atoms having two neighbours and in this case the structure is more damaged compared to the structure nearer to the surface at 0°.

(d) Angular Distribution function

Angular distribution is also another important parameter, which can give a clear picture of the implantation and deposition mechanism and locations of carbon inside silicon structure. Along with that, a clear idea about silicon carbide formation can be obtained from layer to layer. In this paragraph, we will describe the variation of angular distribution function with energies for different slabs. In order to interpret the results, we consider the same three slabs (centred on 2.5 Å, 7.5 Å and 12.5 Å) for 0° incidence angle and the energies are varied for 1 eV, 5 eV, 20 eV and 30 eV. Close to the surface, the angular distribution is much broader than inside the sample with low or no carbon implantation. In the slab centred at 2.5 Å and 7.5 Å, there are several smaller peaks except the larger peaks near at 55° and 110°. These numbers of smaller peaks comes due to the amorphized structure of the system and several extra bond angles appear between Si-Si-Si and Si-C-Si and C-Si-C. There are certain differences in peak values for different energies as the implantation mechanism is different for different cases. In the 7.5 Å slab, there are two smaller peaks in the larger peak itself around 55° for 1 eV energy and this behaviour is not visible for other energies. As expected due to less implantation energy, most of the carbon atoms do not go to the 12.5 Å slab and sits in 7.5 Å slab. Due to the presence of a large number of carbon atoms, the lattice gets more distorted than for the other energies.

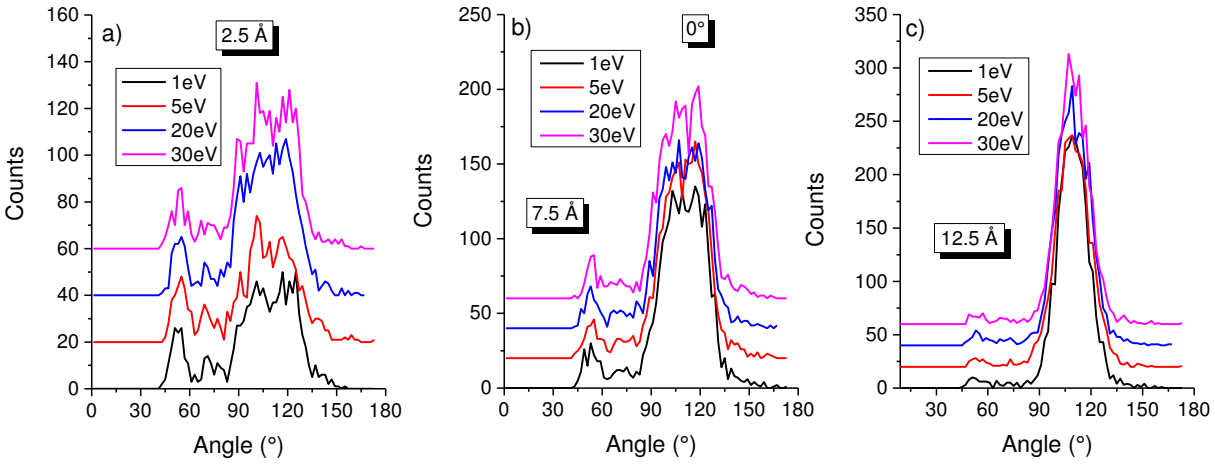

Fig. III-18: Angular distribution function for different energies at 0° for the slabs centred on a) 2.5 Å, b) 7.5 Å and c) 12.5 Å.

Along with 0° incidence angle, we analysed the angular distribution results for 60° as well. Fig. III-19 explains several peaks due to Si-C and Si-Si interactions. The nature of distribution of angular function is almost similar like the case of 0°. There are also several peaks in between 55° and 110° for 2.5 Å and 7.5 Å slabs like at 0° but here the counts are more. This suggests that the structure is even more amorphized in the case of 60°.

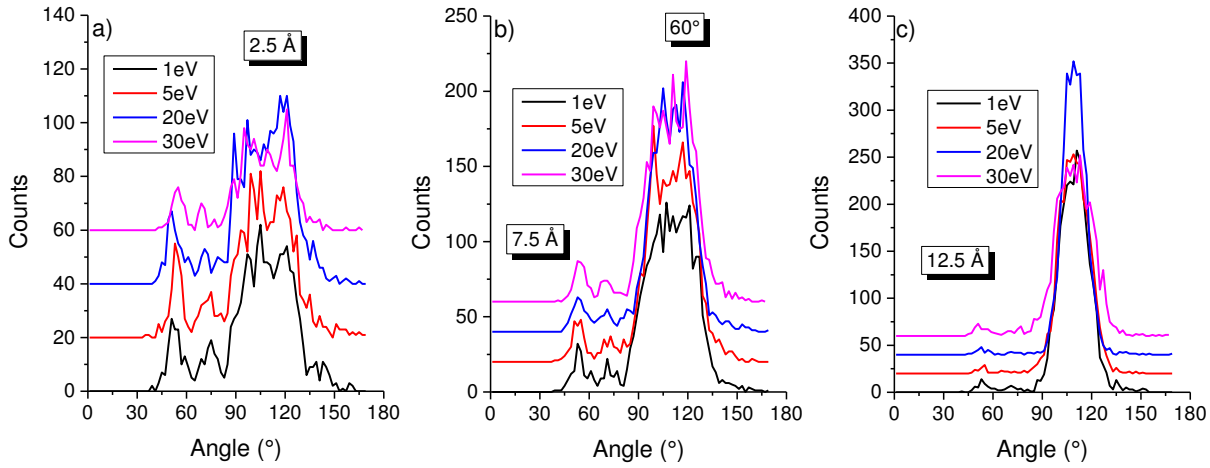

Fig. III-19: Angular distribution function for different energies at 60° for the slabs centred on a) 2.5 Å, b) 7.5 Å and c) 12.5 Å.

(e) Concentration

The Fig. III-20 describes the carbon concentration in the whole slab for several energies at 0° and at 60°. The variation of concentration according to the length of the slab changes for carbon. While going more deep inside the slab, the carbon concentration decreases and this reveals the fact that, most of the carbon atoms sit near to the surface. In case of 0° incidence, it is observed that, the concentration increases first and later decreases for 20 eV and 30 eV incident energy. The increment of concentration at 20 eV and 30 eV proves that higher energies prompt more implantation and the number of carbon atoms near to the surface is less. For all other energies, the concentration decreases right from the surface.

For all the other energies, the decrement of carbon concentration is almost in a similar fashion. The concentration near to the surface is higher at 5 eV for both the angles, followed by the concentration at 1 eV. Due to less initial energy, carbon atoms do not have sufficient energy to be implanted deeply and increase the concentration near to the surface. The concentration is almost zero at a distance of 22.5 Å from the surface for both angles and no carbon atoms got implanted far beyond this depth. The natures in variation in concentration for all the energies are similar for both 0° and 60°. For both

angles, Fig. III-20 describes that concentration just near to the surface is maximum for 5 eV and minimum at 30 eV for 60° and at 20 eV for 0°.

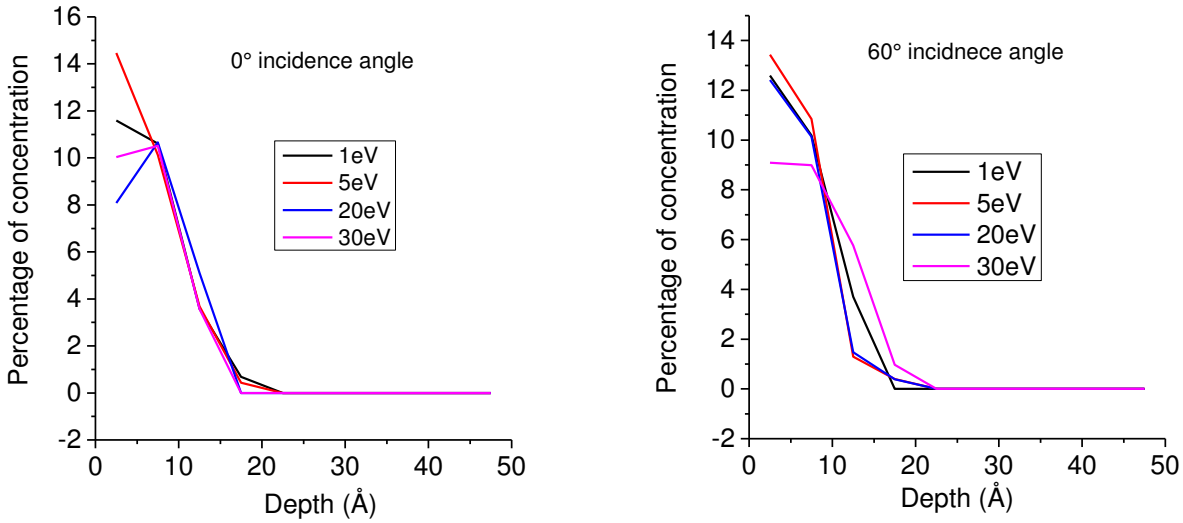

Fig. III-20: Concentration variation of carbon for different energies at 0° and 60°for the whole structure.

v) Evolution of the system with deposition dose

In order to understand how the dose of carbon during continuous carbon deposition influences the mechanism inside the silicon system, we have investigated the structure formed in several steps (after 30, 50, 70 and 100 carbon depositions). To analyse the results, we have described here the deposition of carbon atoms at a lower energy (1 eV) and at a higher energy (30 eV) for 0° incidence angle while the azimuthal angle is fixed to 45° for both cases. To describe the structure formed, we analysed the system structure by calculating radial distribution function, depth distribution, angular distribution function and coordination number. First we will investigate by radial distribution function calculations followed by depth distribution, angular distribution function and coordination number calculations at 1 eV and 30 eV for several cases.

(a) Radial distribution function

Like the previous analyses, we divide the whole structure in three slabs having a thickness of 5 Å each. If we consider the slab (centre at 2.5 Å) at the surface, the 1st Si-Si interaction peak is higher for 30 carbon deposition than for 100 carbon deposition and the 1st Si-Si interaction peaks for all other cases are in between them. This is due to the presence of more carbon atoms in case for 100 carbon deposition in the same slab. This reveals also that most of the silicon atoms are involved t in bonds with carbon atoms. The Si-Si peak amplitude is getting lower because of a decreasing density due to the damage introduced by the carbon deposition. At the same time due to the same reason, the Si-C interaction peak amplitude is lower for 30 carbon deposition in the slab centred at 2.5 Å. Comparing

Si-C first interaction peak for all cases in three slabs, it is found that the peak has higher values for the slab centred at 2.5 Å, which means that the majority of the carbon atoms is implanted in that slab. The nature of peak distributions is similar for all the three slabs. The Si-C first interaction peak is only visible in 2.5 Å slab for 30 carbon deposition and there is no contribution due to Si-C peaks in 7.5 Å slab and in 12.5 Å slab for 30 carbon depositions. This reveals that there are enough lattice sites available in the first slab to accommodate 30 carbons which also can be seen in the snapshot taken in Fig. III-25. Comparing the sharpness of the peaks for Si-Si 2nd neighbour and 3rd neighbour for all the slabs, it is observed that the peaks are very broad for 100 carbon depositions than the cases for 30, 50 and 70 carbon depositions. The Si-Si peaks are very broad due to the presence of large number of carbon atoms after 100 carbon depositions and the structure is much more amorphized. And if we measure the amplitude of the Si-Si peaks for 2nd and 3rd neighbour, there is certainly some difference between several deposition fluencies. The peaks amplitude is certainly higher for 30 carbon deposition and decreases gradually for 50, 70 and 100 carbon depositions. These changes reveal that the structures are different for individual dose. It is more amorphous in case of 100 depositions and less amorphous in case of 30 depositions.

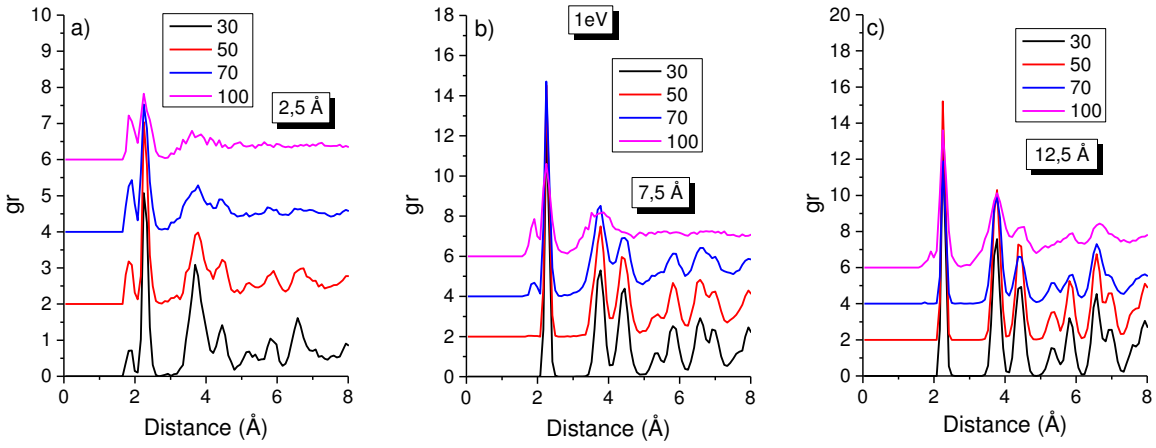

Fig. III-21: Radial distribution function for different fluence for 1 eV carbons at 0° for the slabs centred on a) 2.5 Å, b) 7.5 Å and c) 12.5 Å.

Now we will consider the same case but changing the energy to a higher value to 30 eV in order to observe if there are some changes in parameters for radial distribution function. Fig. III-22 describes that there are some peaks for Si-C first neighbor interaction for 30 carbon depositions at 7.5 Å slab and even at 12.5 Å slab for 50 carbon depositions, which was not visible in case of 1 eV energy depositions. This proves that there are certain influences of energies for deposition and implantation processes for carbon depositions. The amplitude of Si-Si peaks are higher at 2.5 Å slab than at 1 eV as high energy prompts more deep implantation. At 30 eV energy the distribution area is more broad

than at 1 eV and that is why Si-Si 2nd and 3rd neighbors are also more distinct and separated than at 1 eV for 100 carbon depositions.

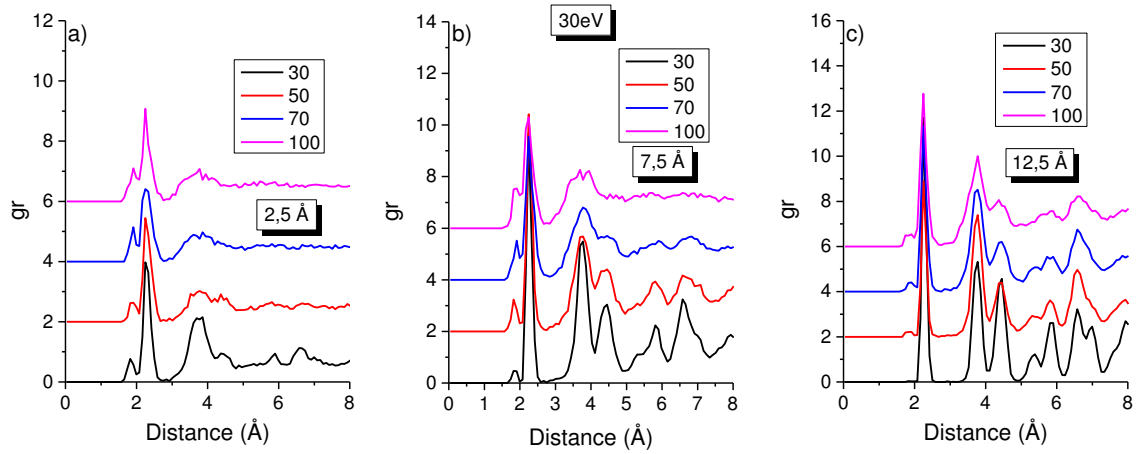

Fig. III-22: Radial distribution function for different fluence for 30 eV carbons at 0° for the slabs centred on a) 2.5 Å, b) 7.5 Å and c) 12.5 Å.

(b) Depth distribution with change in dose

Fig. III-23 and Fig. III-24 show the depth distribution calculations after 30, 50, 70 and 100 carbon depositions. Radial distribution gives the idea of the structure of the compound after depositions but depth distribution provide a clearer view how the carbon atoms have been distributed according to the depth while the dose has been changed. In the Fig. III-23 it is seen that almost all the carbon atoms deposited in the first slab, i.e., above 5 Å distance from the surface for 30 and 50 carbon depositions. But while the dose has been increased the carbon atoms can be found at 10 Å and at 17.5 Å for 70 and 100 carbon depositions. This observation is done at 1 eV incident energy of carbon and it is possible to find carbon atom at 17.5 A deep. Due to the increase in number of carbon atoms at the surface, it might possible that the carbon atoms already in the below layer have been pushed further down as we explained also in earlier sections. This phenomenon can be explained by following the trajectory of a carbon atom which is deposited earlier in the process.

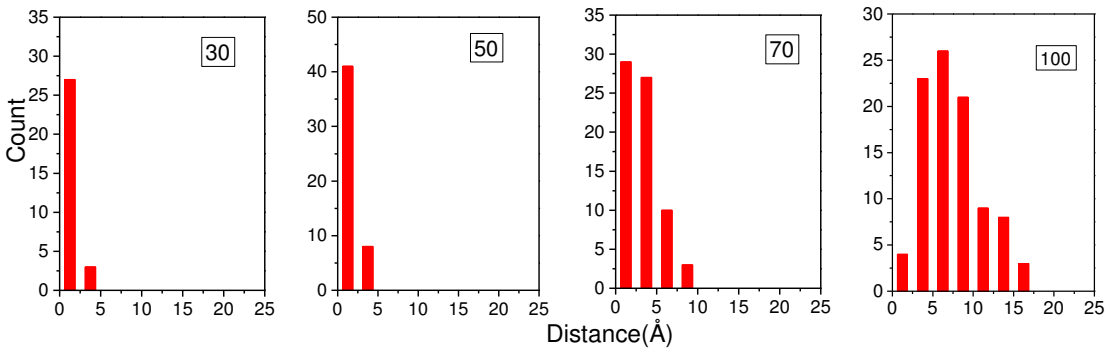

Fig. III-23: Depth distribution of C atoms after 30, 50, 70 and 100 depositions at 1eV at 0°.

In order to investigate the same issue, the analysis has been done at higher 30 eV energy for different doses. From Fig. III-24, it is observed that the atoms are already in 2nd and 3rd slabs for 30 and 50 deposition dose, which was not visible in case of 1 eV. It basically happened due to high impact energy of incoming carbon atoms.

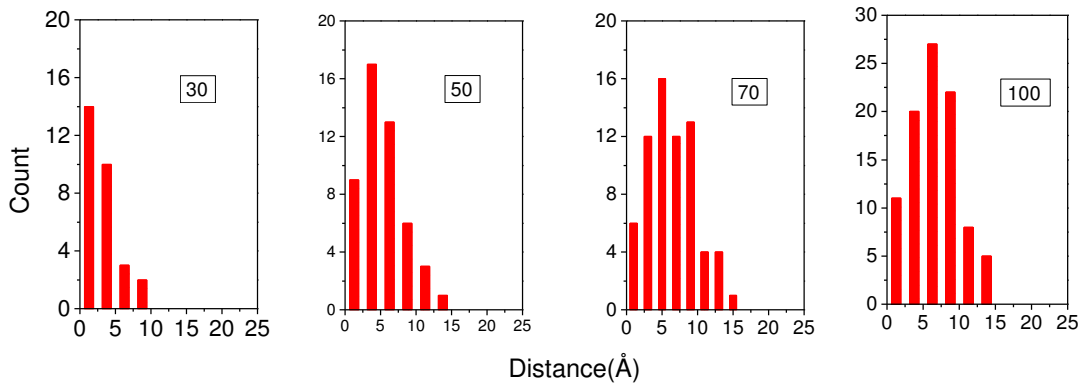

Fig. III-24: Depth distribution of C atoms after 30, 50, 70 and 100 depositions at 30eV and at 0°.

Some snapshots are taken to observe the deposition and implantation mechanism while the fluence has been changed. Fig. III-25 (a), (b), (c) and (d) represent successively the system structure for 30, 50, 70 and 100 carbon depositions. For 30 and 50 carbon depositions, the carbon atoms sit just near to the surface and make systematic bonding with silicon neighbors. And while the number of carbon atoms have been increased to 70 and 100, the suface looks more amorphized.

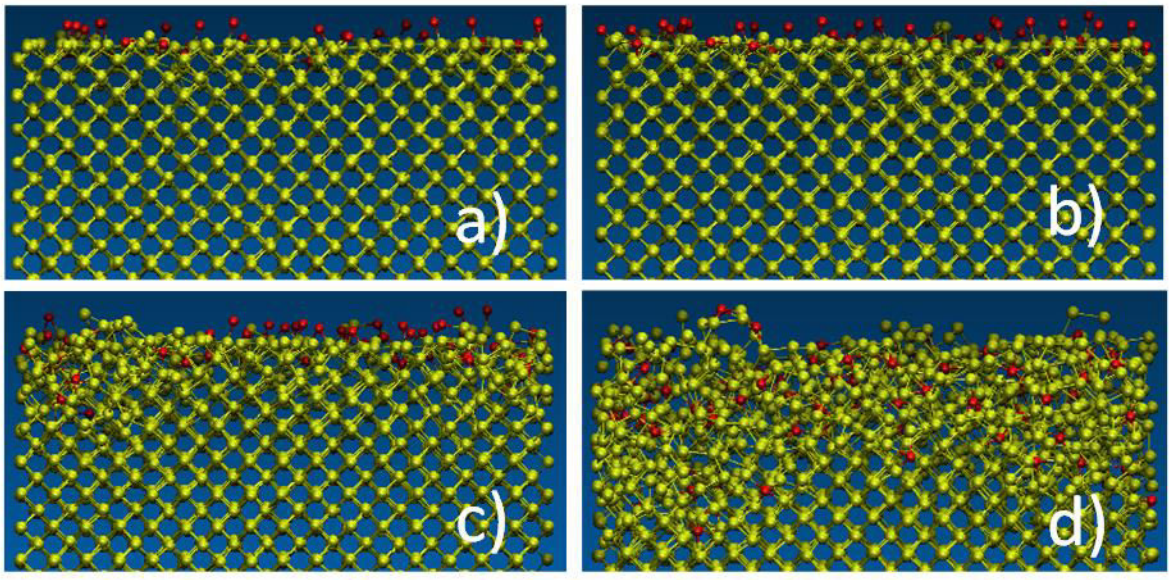

Fig. III-25: Snapshot of the system structure after 30(a), 50(b), 70(c) and 100(d) carbon depositions at 1 eV incident energy.

Some snapshots are also taken at 30 eV keeping the same conditions like at 1 eV. Fig. III-26 (a), (b), (c) and (d) represent successively system structure for 30, 50, 70 and 100 carbon depositions at 30 eV. At 1 eV, most of the carbon atoms stay near to the surface for 30 and 50 carbon depositions but here in case of 30 eV incident energy, the carbon atoms already start to be implanted and very rare carbon atoms can be found to be sitted on the surface after 30 and 50 carbon depositions. If we compare the snapshots for 30, 50 and 70 depositions at 1 eV and 30 eV, significant differences can be found for the deposition and implantation mechanisms. Due to high energy, the implantation depth is higher for 30, 50 and 70 carbon depositions at 30 eV.

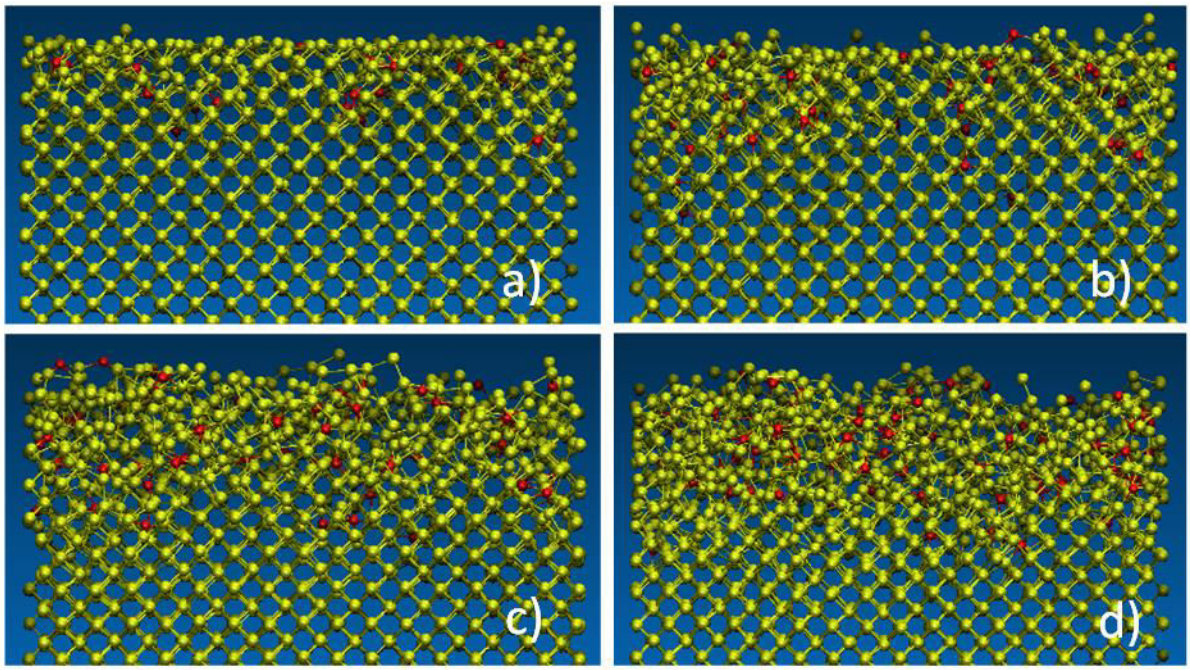

Fig. III-26: Snapshot of the system structure after 30(a), 50(b), 70(c) and 100(d) carbon depositions at 30 eV incident energy.

(c) Angular distribution function

Angular distribution function calculates the probability of finding bond angles formed in a certain crystal structure. Hence calculating angular distribution function and determining the bond angles, we can estimate the structure formed during deposition and implantation of carbon atoms. Here we will first describe the results for several fluencies (after 30, 50, 70 and 100 carbon depositions) at 1 eV energy (Fig. III-27) followed by 30 eV energy (Fig. III-28) for 0° incidence angle and azimuth angle fixed at 45°. Similarly as described in radial distribution function calculation, we consider three slabs having 5 Å widths each (centered at 2.5 Å, 7.5 Å and 12.5 Å). We observed that there are several peaks occurred at different angles in the 2.5 Å, which comes due to the several bond angles between Si and C in the slab. The number of small peaks decrease for the slab centered at 7.5 Å. The angular distribution is broad due to several peaks near to the surface and it is sharp in deep inside the structure

(at 12.5 Å slab). There are two distinct peaks at 55° and another close to 110°. There are several other small peaks in between 55° and 110°. The peaks near to 110° at 2.5 Å slab has higher amplitude value for 30 carbon depositions and decreases for 50, 70 and then become minimum for 100 carbon depositions. Due to less presence of carbon atoms, these peaks are higher for minimum carbon depositions. The peaks near to 55° diminishes at 7.5 Å slab for 30 and 50 carbon depositions, which reveals that the structure is more like silicon structure due to less implantation of carbon atoms. Still, in the 7.5 Å slab, some carbon atoms in interstitial sites contribute to angles below 80° and the main peak is still larger than at 12.5 Å. The peaks at 55° totally diminishes for all conditions at 12.5 Å slab and the peaks are sharp and well distinct.

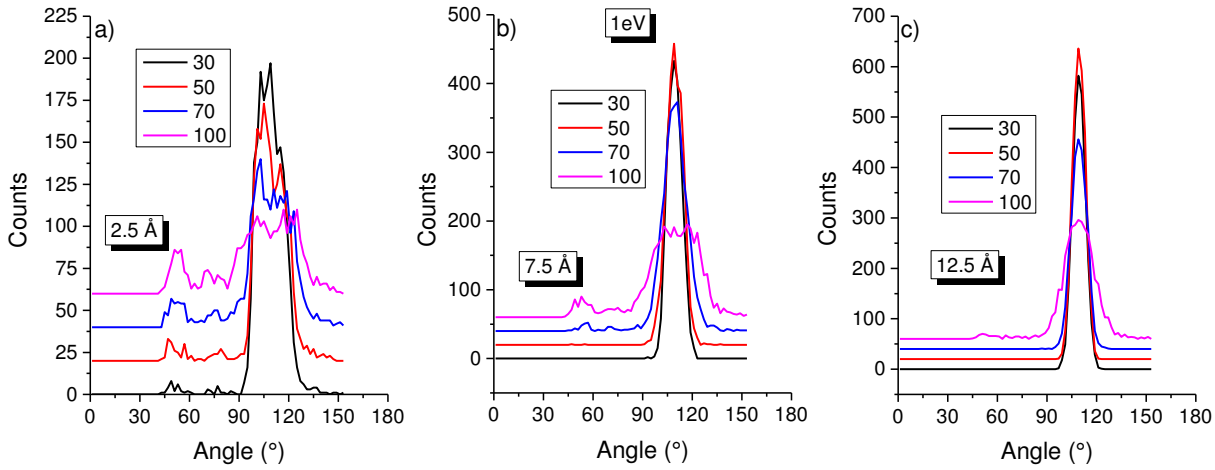

Fig. III-27: Angular distribution function for different fluencies for 1 eV carbons at 0° for the slabs centred on a) 2.5 Å, b) 7.5 Å and c) 12.5 Å.

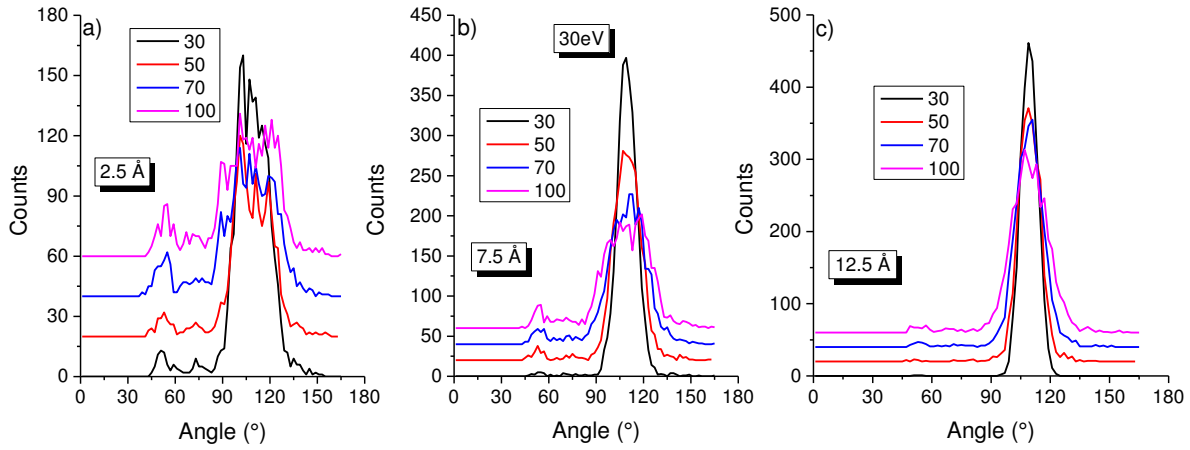

Fig. III-28: Angular distribution function for different fluencies for 30 eV carbons at 0° for the slabs centred on a) 2.5 Å, b) 7.5 Å and c) 12.5 Å.

The angular distribution calculations have been observed also for another condition for 30 eV at the same angle (Fig. III-28). Due to high energy, there are some peaks come at 55° angle for 7.5 Å slab, which was not visible in case of 1 eV energy. So, there are certain changes in structure while energy has been varied in implantation mechanism. The variations in nature of the peaks found at 55° and at 110° are similar like those at 1 eV but there are certain changes in the mean value of amplitudes.

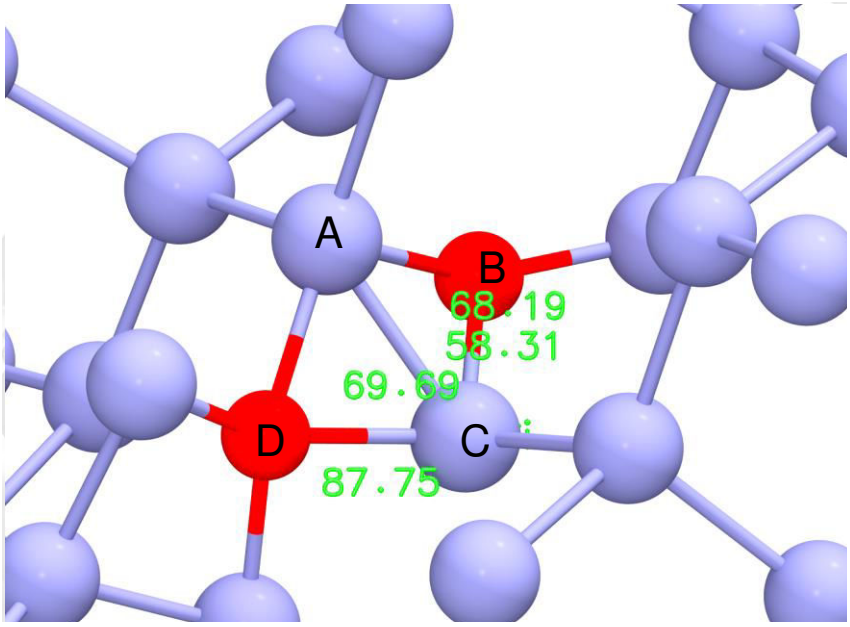

Fig. III-29: Several angular bonds formed between Si and C at 1eV.

From the angular distribution function in Fig III-27 (a), it is seen that there are two peaks between 45° and 90°. These angles formed are identified in the Fig III-29. The angle ABC has a value of 68.19° which is due to bonds between Si-C-Si and the angle BCA has a value of 58.31° which is due to bonds between C-Si-Si. This means that the angle Si-C-Si (ABC) has greater value than the angle C-Si-Si (BCA).

Considering all the deposition conditions for continuous carbon depositions, we can expect a high sticking probability due to the high affinity of Si for C. This is confirmed in our simulations where we found that the sticking probability of carbon atoms on the Si(100) surface is always higher than 90%. The sticking coefficient increases from 0.94 at 60° up to 0.99 at normal incidence. At 30° and 45°, intermediate values of 0.97 have been obtained. However, it should be noted that the differences between these values are not significant.

In several sections during our discussions, we found that there are atoms implanted 15 Å deep even at 1 eV. This has happened due to pushing and migration mechanism. In order to investigate the phenomenon we followed one carbon atom from one location to the end of simulation after 100 carbon depositions (Fig. III-30).

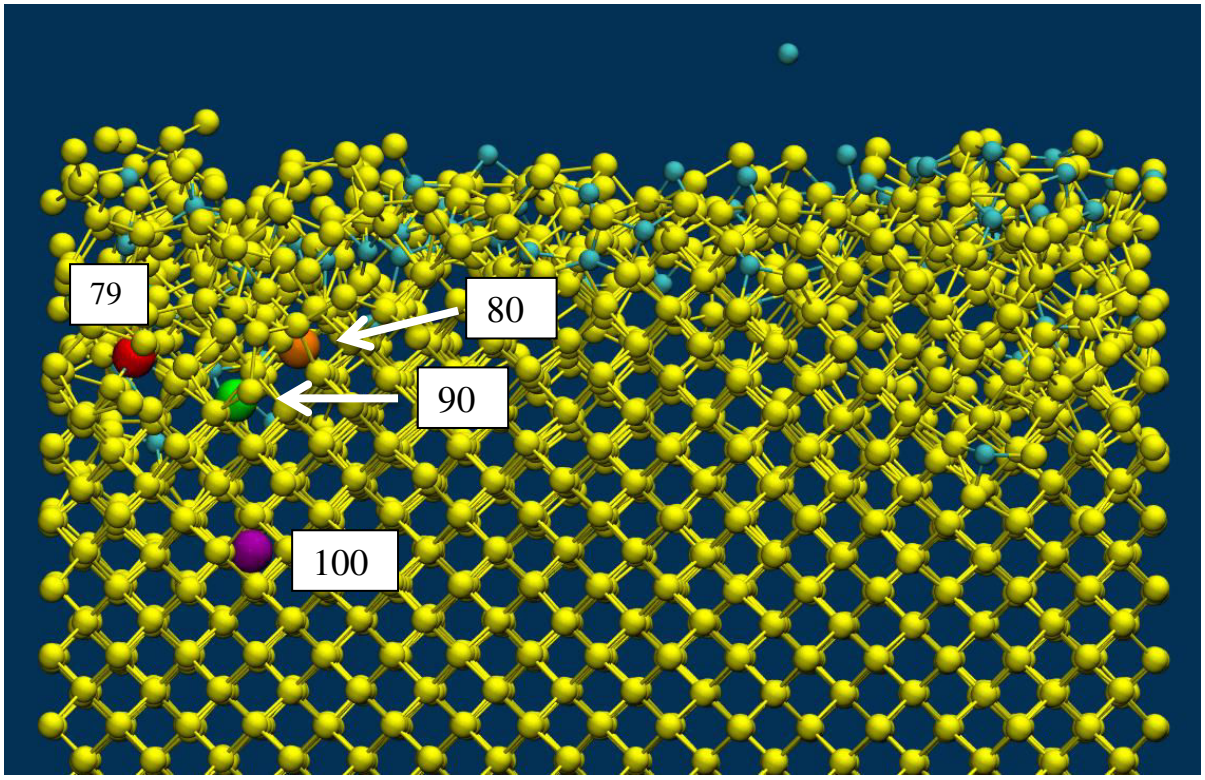

Fig. III-30: Diffusion and migration mechanism during the continuous deposition at 1 eV. Red sphere represents the location of a carbon atom at 79th carbon deposition to the system. Orange, green and purple spheres represent successively the locations of same carbon atom after the 80th, 90th and 100th carbon atom come into the system.

We have described here the trajectory of a carbon atom from the 79th carbon deposition to the 100th carbon deposition. During interaction of the 79th carbon atom to the system, we identified location of a carbon atom highlighted in red sphere in Fig. III-30. Immediately after next carbon comes into the system ,i.e., the 80th carbon interaction to the system, the identified carbon atom (red sphere) migrate to the location of orange sphere in Fig. III-30. Again after additional 10 carbon depositions (i.e., after the 90th carbon deposition) we followed the trajectory of the identified carbon atoms and it was found at the position of green sphere in Fig. III-30. Again after additional 10 carbon depositions (i.e., after the 100th carbon deposition), we followed the trajectory of the same identified carbon atom and it was finally located at the location of purple sphere in Fig. III-30. So, certainly, the carbon atoms being pushed down from the 79th position (red sphere) to 100th position (purple sphere) due to addition of extra carbon atoms. The insertion of carbon atoms into the silicon lattice deforms the latter and leads to defects which facilitate the diffusion of atoms.

The snapshots give the impression of an amorphous Si-C structure. XRD analysis using the Debyer software[136] shows only Si peaks, but no peaks related to SiC (Fig III-31), which confirms the initial impression from the snapshots.

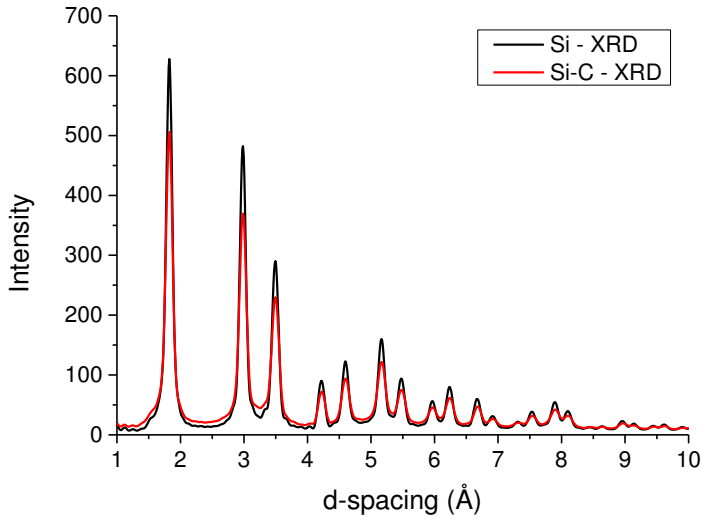

Fig. III-31: X-ray diffraction patterns of pure silicon and after deposition 100 C atoms

4) Conclusion

MD investigation of carbon depositions on silicon surfaces have been discussed both for single and multiple carbon depositions. The reactive force field developed by John Kieffer is selected, as it enables the formation and breaking of bonds via an adaptive and environment sensitive charge transfer for both cases. In single carbon deposition, the deposition and implantation mechanism of a single carbon on a (100) reconstructed silicon surface have been investigated and the comparison are made using the well-established Erhart-Albe potential. Results of depth distribution, deposition and implantation ratio, back-scattering probability etc. using both potentials are similar, although slight divergences appear at grazing angles and for the higher end of the deposition energies.

Afterwards, multiple carbon deposition on a similar crystalline silicon surface using the third generation force field by Kieffer *et al,* is modelled in order to get a better understanding of carbon deposition and implantation and damage formation during low-energy carbon atom interactions with a Si(100) surface. The result has been analysed in three parts (at constant energy, at constant angle and at constant doses). The main parameters to investigate the system structures include radial distribution function, depth distribution, coordination number and angular distribution function.

The radial distribution function reveals the damaging of the Si structure as a function of incidence angle, incidence energy, deposition dose and depth in the sample. We found an amorphous, or at least heavily damaged, structure just near to the surface and a more ordered crystalline structure at depths exceeding 10 Å. Similar conclusions can be drawn from the angular distributions, depth distributions and coordination number. The variation of carbon concentrations with depth are similar for the angles at 0°, 30° and 45°, while 60° incidence produces a slightly higher carbon concentration of the sample

surface at constant incident energy 5eV. The results at different doses show how the deposition mechanism changes while the fluencies have been varied. Some snapshots also confirm the mechanisms. Finally, the results of radial distribution functions, depth distributions, coordination number and angular distributions give several aspects of deposition and implantation mechanism for continuous carbon depositions. The results might give some important insight in SiC formation and interface formation as the properties of SiC devices and films largely depend on defects.

Importantly, even in the sub monolayer range the carbon deposition strongly modifies the top layer of silicon surface, which gives important insights into the deposition process and which should be accounted for in future studies.

Ti deposition on Si

"Sticking coefficient of titanium on silicon surfaces has been investigated by storing matter and SIMS technique as well as by numerical simulations."

Chapitre 4.

Titanium (Ti) deposition on Silicon (Si)

1) Introduction:

This chapter deals with fundamental aspects of depositing titanium (Ti) on silicon (Si) in the sub-monolayer range in order to understand where and under which conditions the atoms stick on the substrate. Hence, the sub-monolayer film deposition of Ti on Si(100) is discussed for various fluences by changing the primary current and the deposition time.

The choice of key parameters for the deposition conditions in storing matter chamber have been chosen for sub-monolayer films. The parameters for the analyses by dynamic SIMS also were chosen for very dilute deposits in order to obtain sufficiently low sputter rates. The sputtered particles consisting of charged and neutral atoms or particles are sputtered by Ar^+ ions from the sample and collected on the substrate surface with a certain angular distribution depending upon the positioning of collector, target and ion beam. The ejected particles are thus non-uniformly spread over a certain area of the collector (Si) to form the deposit. In order to investigate the distribution of the atoms in the collector surface, several dynamic SIMS analyses were done across the deposit along vertical and horizontal directions to find the centre of the deposit and record its shapes. A maximum intensity is found near to the edge of the collector. In order to collect a maximum of the sputtered particles, the substrate Si collector should be placed closer to the FLIG (Floating Low Energy Ion Gun). In that case, special care should be taken that some part of the substrate should not cut the incident ion beam. The shape of all the deposits is same, which reveals that the angular distribution is similar for all deposits.

In this chapter along with experimental results, we will describe some molecular dynamics and DFT results for titanium, which were previously obtained by a postdoc researcher in our group [123]. Later some comparisons will be made between the simulation and experimental results. The parameter by which both methods can be compared is the sticking coefficient.

2) Experimental setup and conditions

i) Collector (Si) and Target (Ti) preparation process

Silicon wafers of 1 inch diameter have been chosen as collector material. In order to remove surface contaminations, the Si wafer is cleaned successively with deionised water, acetone and ethanol in an

ultrasonic bath. This is followed by nitrogen blow in the clean room. The cleaned wafer is then introduced into the ultra-high vacuum (UHV) deposition chamber (having a pressure of 10^{-8} to 10^{-9} mbar) via an airlock. The target (Ti) to be sputtered and deposited on the Si collector is cleaned using the same process than for Si. Afterwards, it is introduced into the main deposition chamber.

ii) Storing matter set up and conditions

The storing matter technique, which is a prototype instrument at the CRP – Gabriel Lippmann has been used for preparing the titanium sub-monolayer deposits. In this work, titanium is sputtered by an argon beam with energy of 10 keV and an angle of incidence of 45° with respect to the surface normal. The sputtered titanium particles are collected on the 1 inch Si wafer collector placed above the titanium sample. The intensity of the raster-scanned Ar^+ beam has been varied from 40 nA to 180 nA and the deposition time from 200 s to 600 s in order to change the primary ion fluence from 1.5 x 10^{14} to 4.5 x 10^{14} ions/cm^2. This corresponds to 5.55 x 10^{14} to 1.25 x 10^{15} sputtered titanium atoms. For all the deposits, the position of the silicon collector relative to the titanium sample should remain unchanged. Before starting the deposition process, the titanium target is sputtered for a sufficient time in order to remove the native oxide layer. Keeping the collector with the deposit under UHV conditions throughout the whole process is essential in order to minimize the oxidation of the deposit and the deposition of contaminations.

iii) Analysis conditions in SIMS

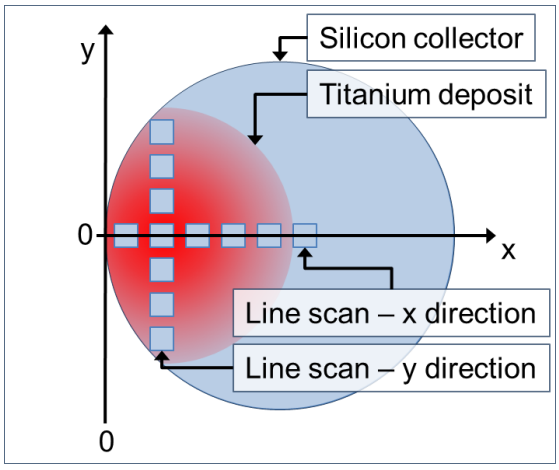

Fig. IV-1: Line scans during SIMS analysis in x and y directions.

After preparing the deposits, the collectors have been transferred to the SIMS instrument via a portable UHV suitcase (10^{-8} to 10^{-9} mbar) [137]. SIMS analyses have been carried out on a Cameca IMS-6f instrument. A 5.5 keV Cs^+ primary ion beam is chosen for the analysis of the deposits. The sample voltage is set to 4.5 keV. The beam is raster-scanned over an area of 500 x 500 µm^2.The analysed ions are $^{48}Ti^+$, $^{46}Ti^+$, and $^{28}Si^+$. The field aperture is set to1800 µm and the contrast aperture to 400 µm.

The important parameters used for storing matter and analysis in SIMS are given in Table IV-1

Analysis condition	Storing matter technique	Dynamic SIMS analysis
Primary Ion	Ar^+	Cs^+
Impact energy	10 keV	5.5 keV
Impact angle	45° (solid angle)	60°
Primary current	40-180 nA	2-3 nA
Raster	1.5 mm x 1.5 mm	500 µm
Analysed ions		$^{28}Si^+$, $^{46}Ti^+$, $^{48}Ti^+$
Time	200-600 s	XX s

Table IV-1: Deposition and analysis conditions.

Table IV-2 gives the details of the deposition conditions for several primary current and time of the deposit for which the results will be explained.

Condition reference	Primary current (nA)	Time (s)	Total number of Ar^+ ions
a)	160	200	$2.00x10^{14}$
b)	180	200	$2.25x10^{14}$
c)	155	350	$3.39x10^{14}$
d)	180	400	$4.50x10^{14}$
e)	60	420	$1.57x10^{14}$
f)	160	300	$3.00x10^{14}$
g)	155	250	$2.42x10^{14}$
h)	40	600	$1.5x10^{14}$
i)	180	300	$3.37x10^{14}$

Table IV-2: Deposition conditions for nine deposits.

For each deposit, several depth profiles were carried out in the form of line scans along the x and y directions as shown in Fig. IV-1. A line scan in the y direction is used to localize the centre of the deposit and the one in x direction is used to characterize the deposit.

3) Results and discussion: Experimental

i) Depth profile of a Ti deposit:

For the analysis of the deposits, several line scans containing a series of SIMS depth profiles are carried out. One of the depth profiles is shown in Fig. IV-2. The depth profile confirms the theoretical isotopic ratio between ^{46}Ti and ^{48}Ti and shows that no mass interferences are present. As $^{28}Si^{+}$ is the matrix signal for all the deposits, we normalize the secondary ion signals with respect to the matrix signal in order to correct for any changes in primary ion current and mass spectrometer transmission between the different depth profiles of a same deposit. The depth profile gives the total number of counts for the analysed area.

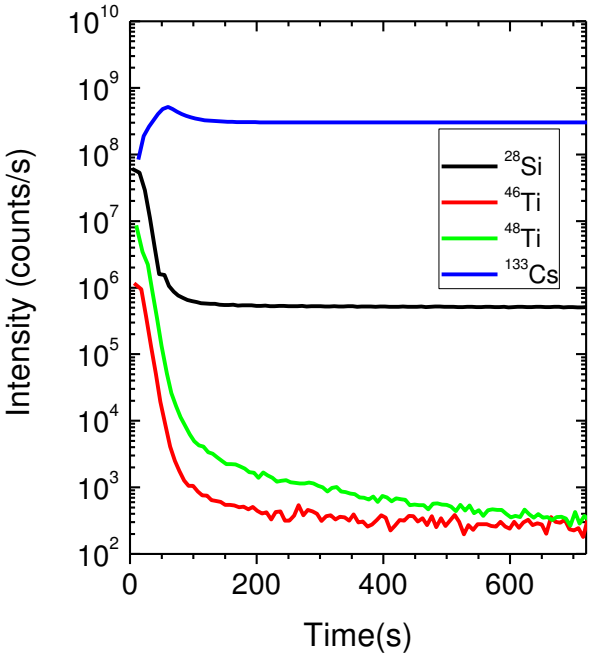

Fig. IV-2: Depth profile of a sub-monolayer Ti deposit.

For each deposit, the counts for a depth profile at the centre of the deposit is maximum and drops to lower value towards the edge and becomes minimum at a distance of 8 – 10 mm from the centre. The intensity of silicon signal is higher than expected at the beginning of analysis due to the presence of an oxide layer on the collector surface and it decreases after the removal of the oxide layers by the sputtering. The presence of oxygen is due to the oxidation of the deposit (even under UHV conditions) and the silicon wafer.

ii) Characterisation of the sub-monolayer deposits

The SIMS analyses are carried out as explained in chapter 2. Fig. IV-3 shows the depth profiles for the different analysis points of the line scan in the x direction for nine deposition conditions (Table IV-2). $^{48}Ti^+$ secondary ion intensities which are of interest for the characterisation of the profiles are shown. The $^{133}Cs^+$ and $^{28}Si^+$ intensities are identical for the different profiles. Although the Ti deposits are in the sub-monolayer area, the $^{48}Ti^+$ counts stay above the background noise up to sputtering time of 400 s in SIMS. This is due to the mixing of the Ti atoms into the Si collector by the Cs^+ primary ion beam. At the same time, quite a large number of Ti atoms is available in the analysis area with a diameter of 150 µm.

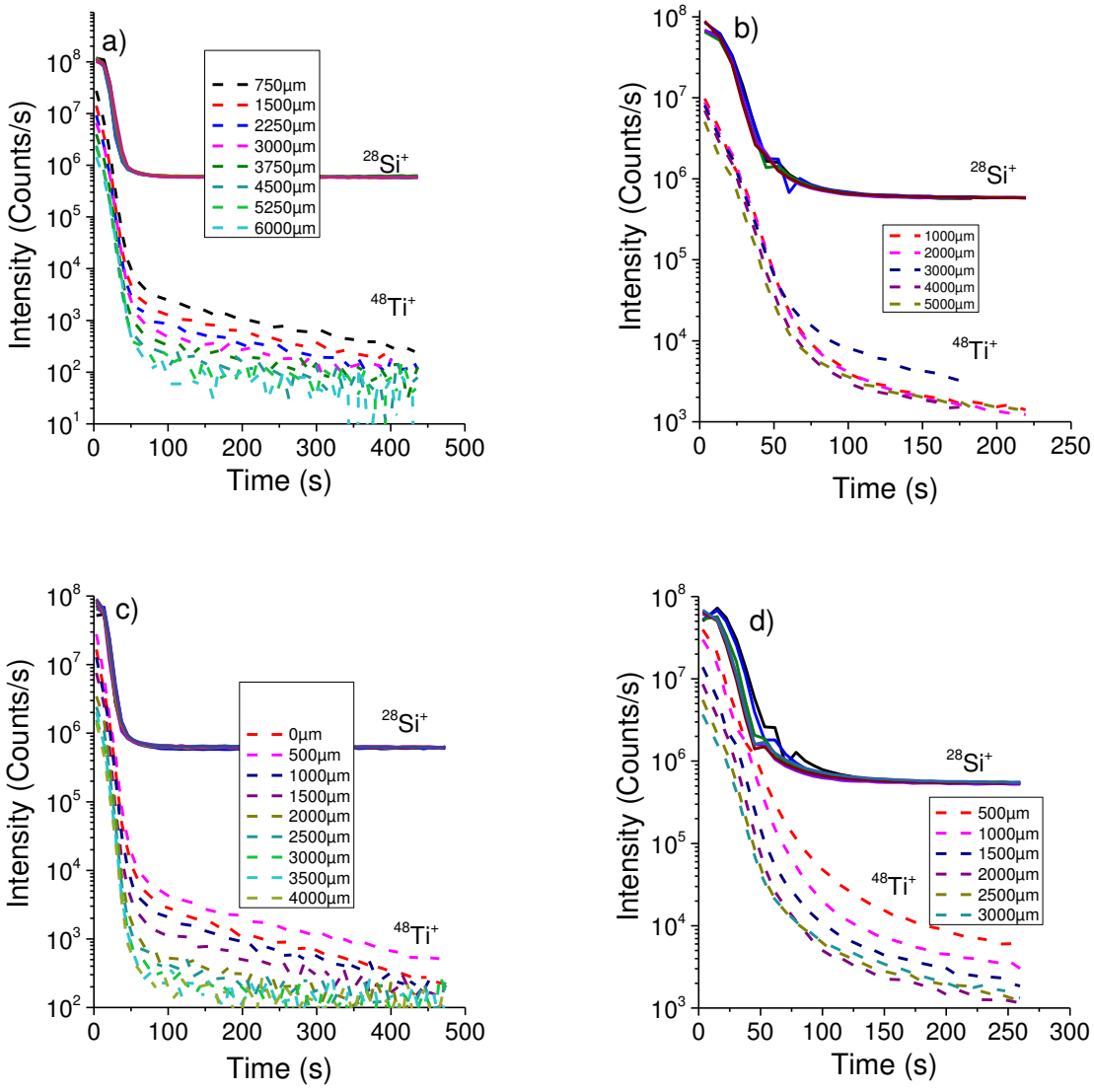

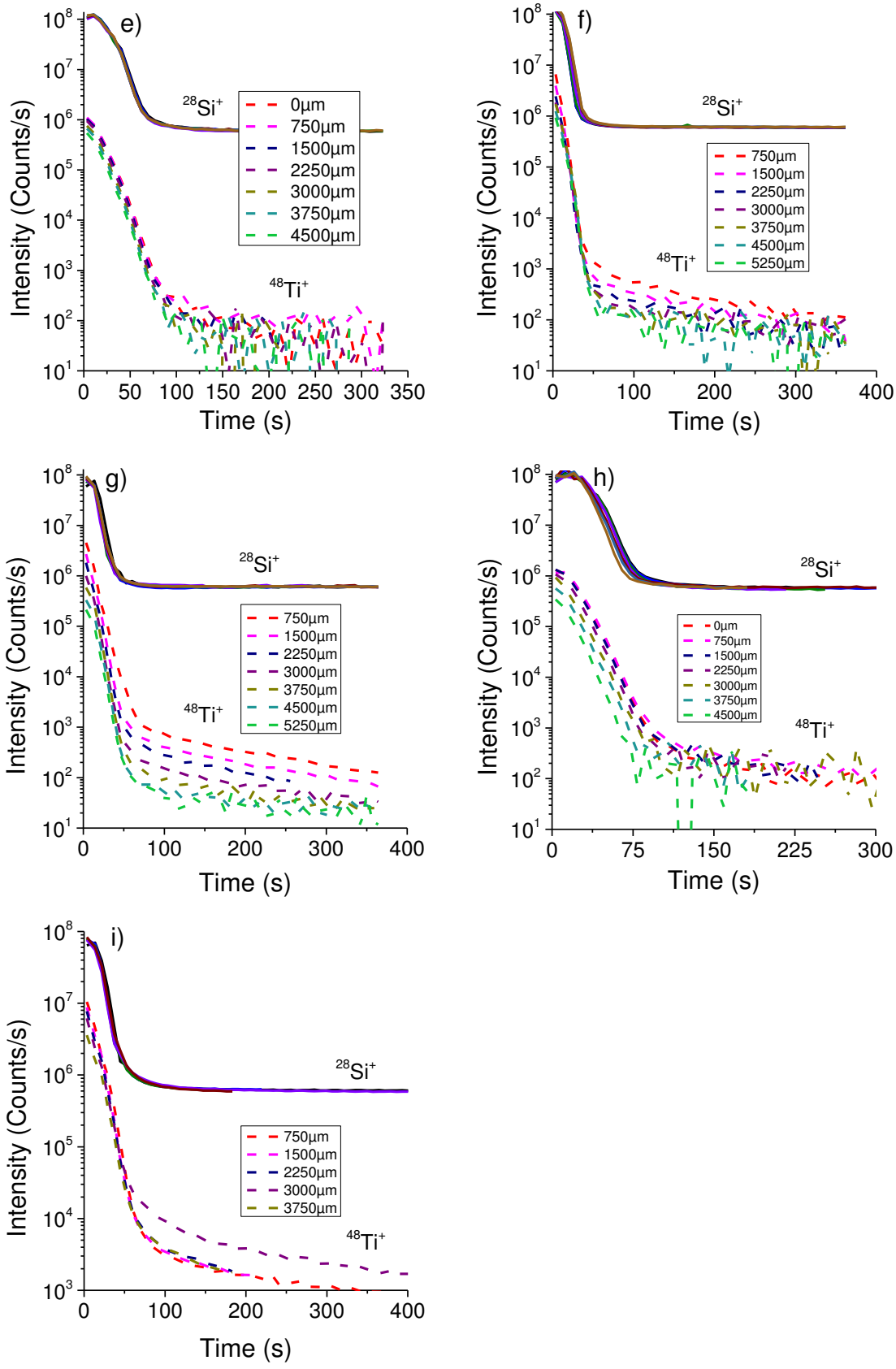

Fig. IV-3: Depth profiles of a line scan in x direction for nine sub-monolayer titanium deposits on silicon. (a)-(i) correspond to deposit conditions reported in Table IV-2.

For each depth profile, the area under the $^{48}Ti^{+}$ curve is integrated in order to get the total number of counts detected for each analysis point. The intensity is maximum at the centre of the deposit and decreases successively and becomes minimum at a distance of 10 mm from the centre. The centre of the deposit is close to one border of the collector. Our experimental setup does not allow for a positioning more towards the centre of the deposit without that the collector cuts the Ar^{+} beam during the deposition process. For further calculations we assume that the deposit is symmetric and that the data can be fitted to a Lorentz curve.

The ability of this function to fit the data can be explained as follows: the ion beam with a Gaussian density profile is raster scanned across the surface. As the beam diameter is relatively small compared to the raster-scanned area and the angular distribution of the sputtered matter follows a cosine law (reference to chapter 1), the projection of the angular distribution on a plane above the surface corresponds to a Lorentz function. Fig. IV-4 shows the shape of a Lorentz curve after the convolution for 1 mm raster size.

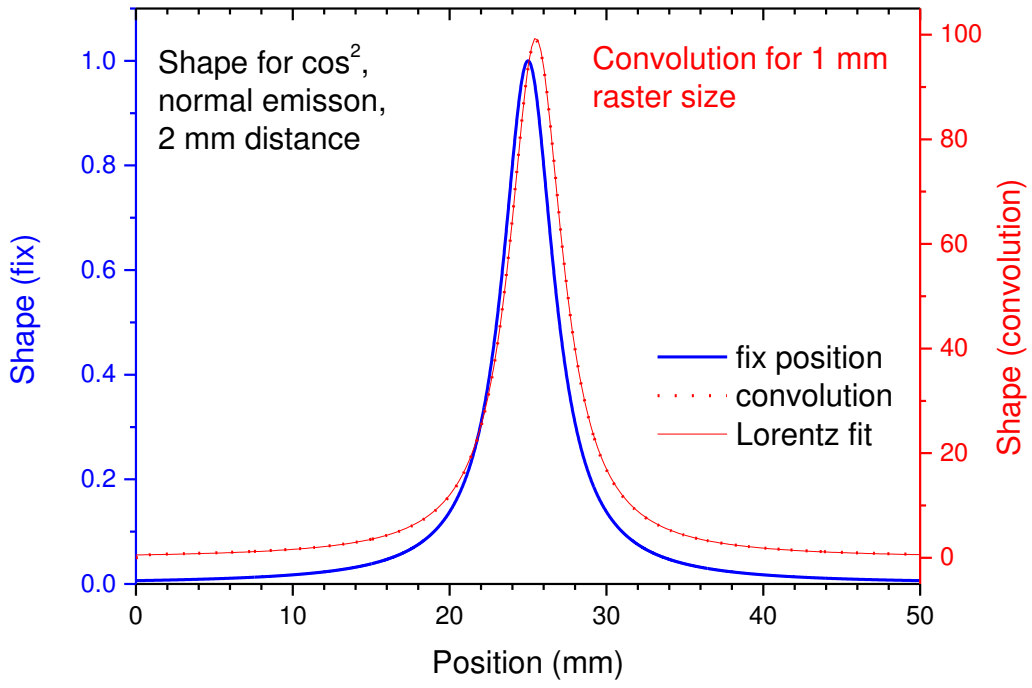

Fig. IV-4: Convolution of Lorentz function.

The symmetry of the deposit is also confirmed by the line scan in y direction. Fig. IV-5 shows the Lorentzian fit in one dimension for the nine Ti deposits shown in Fig. IV-3.

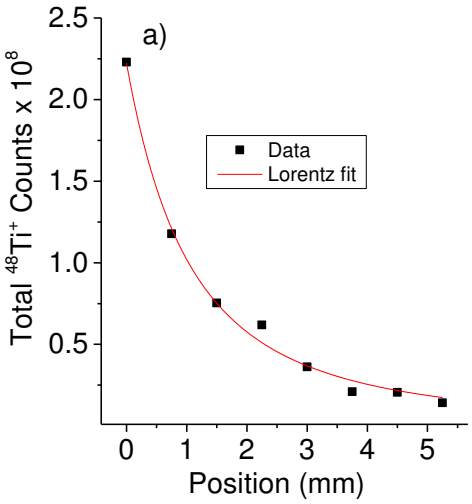
a)
Data
Lorentz fit
Total $^{48}Ti^{+}$ Counts x 10^{8}
Position (mm)

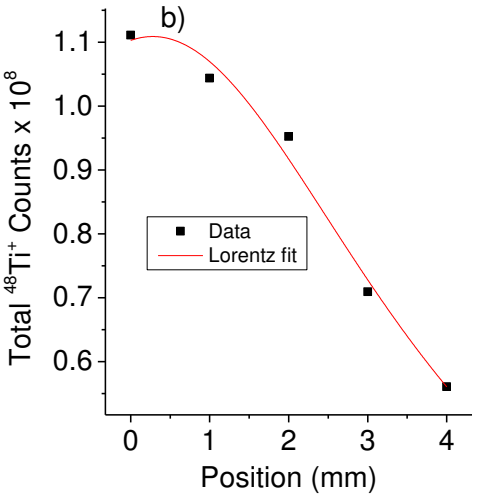
b)
Data
Lorentz fit
Total $^{48}Ti^{+}$ Counts x 10^{8}
Position (mm)

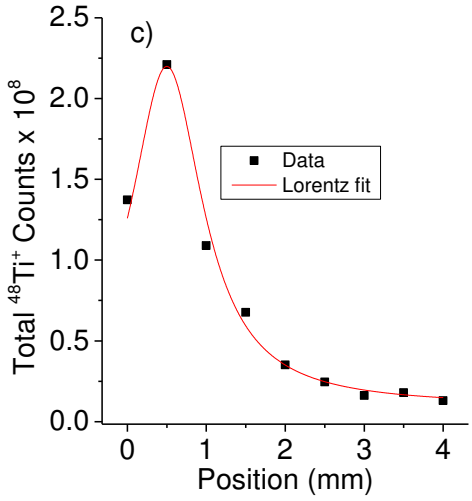
c)
Data
Lorentz fit
Total $^{48}Ti^{+}$ Counts x 10^{8}
Position (mm)

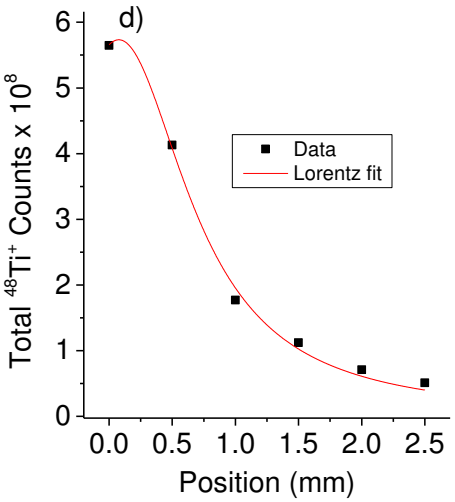
d)
Data
Lorentz fit
Total $^{48}Ti^{+}$ Counts x 10^{8}
Position (mm)

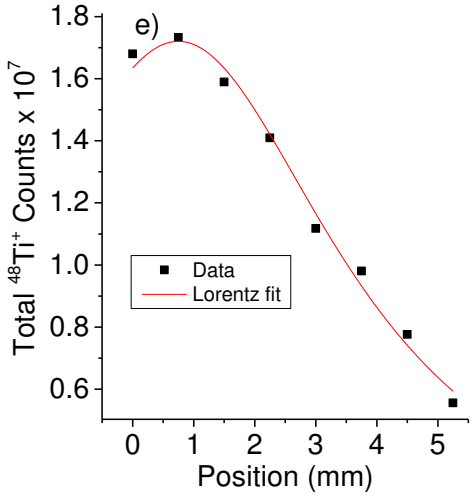
e)
Data
Lorentz fit
Total $^{48}Ti^{+}$ Counts x 10^{7}
Position (mm)

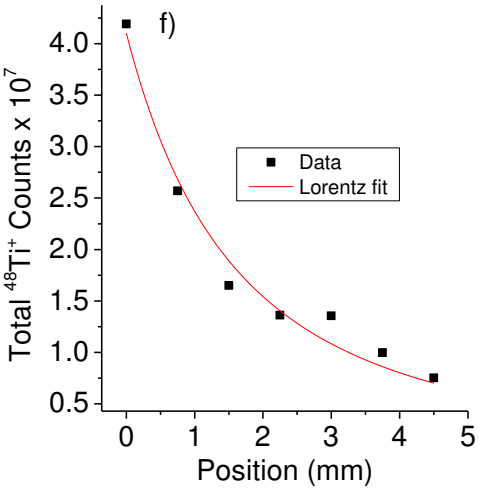
f)
Data
Lorentz fit
Total $^{48}Ti^{+}$ Counts x 10^{7}
Position (mm)

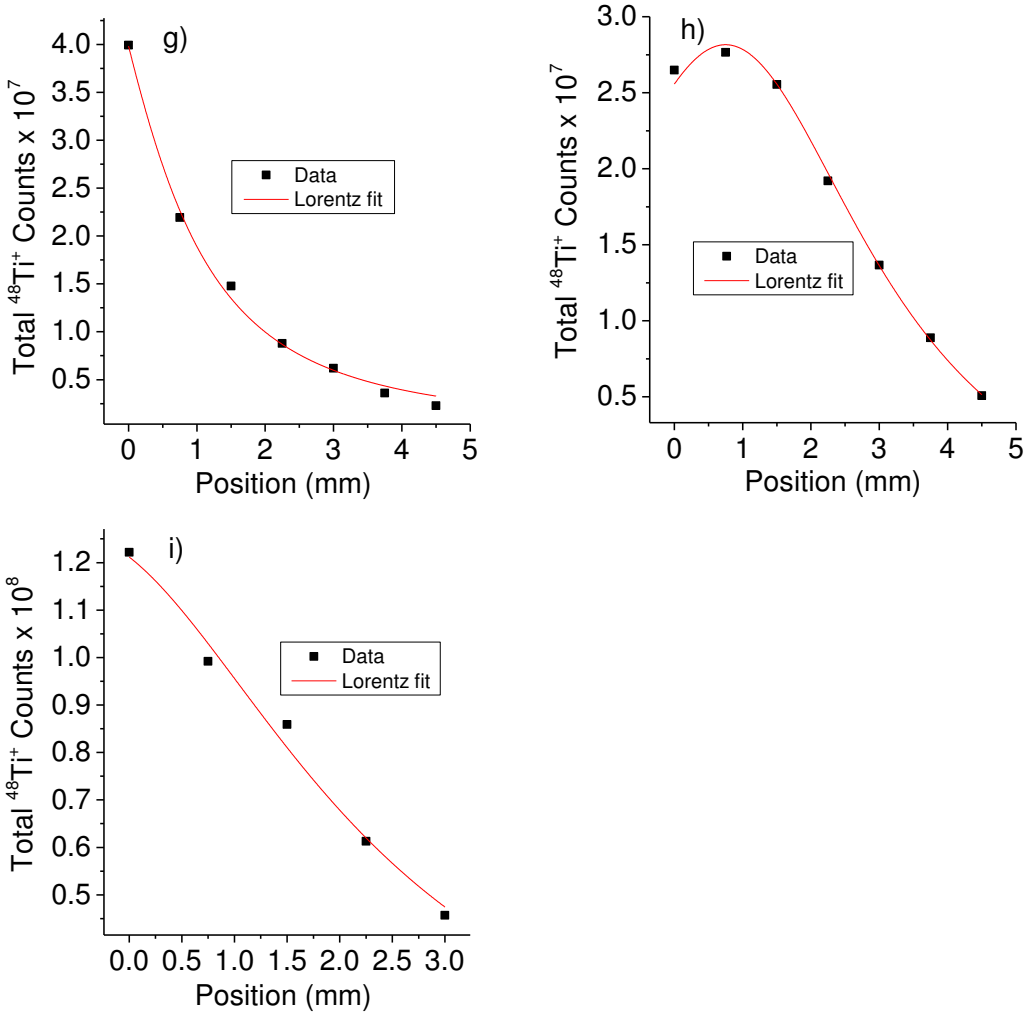

Fig. IV-5: Lorentz curve fitting in 1D along the distance from the edge of the substrate, where a), b), c), d), e), f), g), h) and i) correspond to the same profile as in Fig. IV-3.

In order to calculate the total amount of Ti atoms deposited on the Si collector, the 1D Lorentz curve needs to be transformed into polar coordinates and the volume under the 3D curves needs to be integrated. The function used for the fitting is given by:

$$f(x) = z_0 + \frac{2A}{\pi}\frac{w}{w^2+4(x-x_c)^2} \qquad \text{(IV-1)}$$

The function for the 2D fitting is given by:

$$f(x) = z_0 + \frac{2A}{\pi}\frac{w}{w^2+4(x-x_c)^2+4(y-y_c)^2} \qquad \text{(IV-2)}\ ^{138}$$

Where x_c and y_c are the position of the center of the deposit, z_0 is the asymptotic value corresponding to the background noise (in our case it should be zero), w is the full width at half maximum and A is the area. After converting the function into a 2D Lorentz curve using polar coordinates and by

assuming that the deposit is symmetric, the volume below the curve, i.e. the total number of atoms detected, is given by:

$$C_{SIMS} = \frac{2A}{\pi}\int_0^R \int_0^{2\pi} \frac{w}{w^2+4(r-r_c)^2} r dr d\theta \quad \text{(IV-3)}$$

which after integration leads to:

$$C_{SIMS} = \frac{Aw}{2}[\ln(w^2 + 4R^2) - lnw^2] \quad \text{(IV-4)}$$

The values of *A* and *w* are obtained from the one dimensional Lorentz fit, while the *R* value was taken equal to 10000 µm because beyond this value no titanium was detected. The values of *A* and *w* of the fit of all deposits of Fig. IV-5 are given in Table IV-3.

Condition reference	Total number of Ar^+ ions	Area (A)	Width (w)
a)	$2.00x10^{14}$	$7.30x10^{11}$	1441.51
b)	$2.25x10^{14}$	$3.19x10^{11}$	7971.45
c)	$3.39x10^{14}$	$5.50x10^{11}$	1666.84
d)	$4.50x10^{14}$	$1.20x10^{12}$	1327.60
e)	$1.57x10^{14}$	$1.76x10^{11}$	6524.01
f)	$3.00x10^{14}$	$1.96x10^{11}$	3332.70
g)	$2.42x10^{14}$	$2.45x10^{11}$	2623.08
h)	$1.50x10^{14}$	$2.82x10^{11}$	5241.33
i)	$3.37x10^{14}$	$1.09x10^{12}$	6110.18

Table IV-3: Values of A and w for nine deposits.

From the values of *A* and *w*, the number of counts can be estimated. However, this number does not take an ionisation probability less than one and the transmission of the mass spectrometer into account, i.e. the volume of the deposit is underestimated for the moment.

Knowing the total counts after integrating the Lorentz fit, the total number of actual deposited Ti particles N_{Ti} on the substrate is calculated using the useful yield of Ti in Si:

$$UY_{SIMS} = \frac{N_{Ti\ detected}^{in\ SIMS}}{N_{Ti\ sputtered}^{in\ SIMS}} \quad \text{(IV-5)}$$

Where $N_{Ti\ detected}^{in\ SIMS}$ is the number of Ti atoms detected in SIMS and $N_{Ti\ sputtered}^{in\ SIMS}$ is the number of Ti atoms sputtered during the analysis. A reference sample with Ti implanted into Si has been used to calculate the useful yield of SIMS UY_{SIMS}.

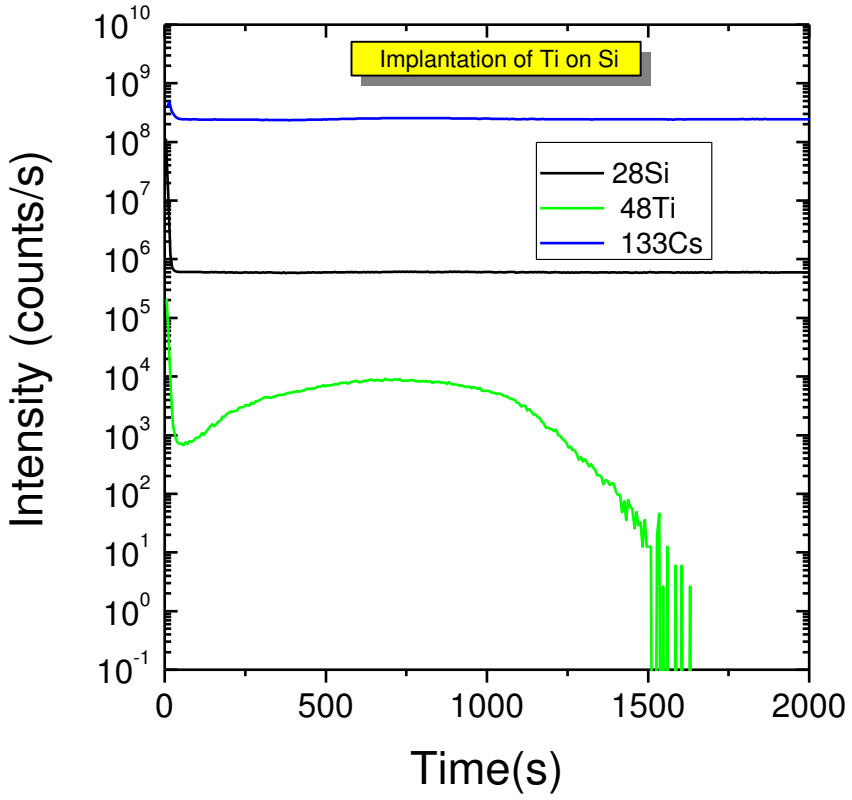

Fig. IV-6: Implant of Ti analysed in SIMS.

The 10 keV implant of Ti with a fluence of 10^{16} atoms/cm^2 has been used. $N_{Ti\ detected}^{in\ SIMS}$ is obtained by integrating the area below the $^{48}Ti^+$ curve and UY_{SIMS} for $^{48}Ti^+$ is found to be 1.4×10^{-4} (Fig. IV-6). The analytical conditions for the Ti implanted sample are the same than for the deposits. The useful yield is used to convert the integrated $^{48}Ti^+$ counts from the deposit into the total number of Ti atoms deposited $N_{Ti\ deposited}^{in\ Storing\ Matter}$ on the collector surface by multiplying this number with UY_{SIMS}.

Now using the useful yield of SIMS, we can have the expression of $N_{Ti\ deposited}^{in\ Storing\ Matter}$ as below.

$$N_{Ti\ deposited}^{in\ Storing\ Matter} = \frac{C_{SIMS}}{UY_{SIMS}} \quad \text{(IV-6)}$$

Before calculating the sticking coefficient, the number of atoms sputtered during the deposition process $N_{Ti\ deposited}^{in\ Storing\ Matter}$ needs to be known. This requires the knowledge of the sputtering yield:

$$Y = \frac{N_{Ti\,sputtered}^{in\ Storing\ Matter}}{N_{Ar+}} \quad \text{(IV-7)}$$

Where N_{Ar+} is the number of Ar^+ ions hitting the Ti sample during the deposition process. Y for 10 keV Ar^+ ion bombardment of Ti has been experimentally determined by measuring a crater sputtered into Ti. A sputtering yield of 3.7 ± 0.2 has been found which is in good agreement with simulations using the 2008 version of TRIM [139,140].

Using the sputtering yield, the number of Ti atoms sputtered during the deposition process is given by:

$$N_{Ti\ sputtered}^{in\ Storing\ Matter} = \mathrm{Y} \cdot \mathrm{N_{Ar^+}} \quad \text{(IV-8)}$$

Next, the sticking coefficient SC is calculated using:

$$SC = \frac{N_{Ti\,deposited}^{in\ Storing\ Matter}}{N_{Ti\,sputtered}^{in\ Storing\ Matter}} = \frac{C_{SIMS}}{UY_{SIMS} * Y * N_{Ar+}} \quad \text{(IV-9)}$$

The sticking coefficients evaluated for the nine deposits are listed in Table IV-4.

Condition references	Sputtered Ar^+ ions	Sputtered Ti particles	Sticking coefficients (SC)
a)	2.00×10^{14}	7.40×10^{14}	0.93
b)	2.25×10^{14}	8.32×10^{14}	0.31
c)	3.39×10^{14}	1.25×10^{15}	0.43
d)	4.50×10^{14}	1.66×10^{15}	0.66
e)	1.57×10^{14}	5.82×10^{14}	0.27
f)	3.00×10^{14}	1.11×10^{15}	0.19
g)	2.42×10^{14}	8.96×10^{14}	0.29
h)	1.5×10^{14}	5.55×10^{14}	0.50
i)	3.37×10^{14}	1.24×10^{15}	0.81

Table IV-4: Values of number of sputtered particles and SC (sticking coefficient) for nine deposits.

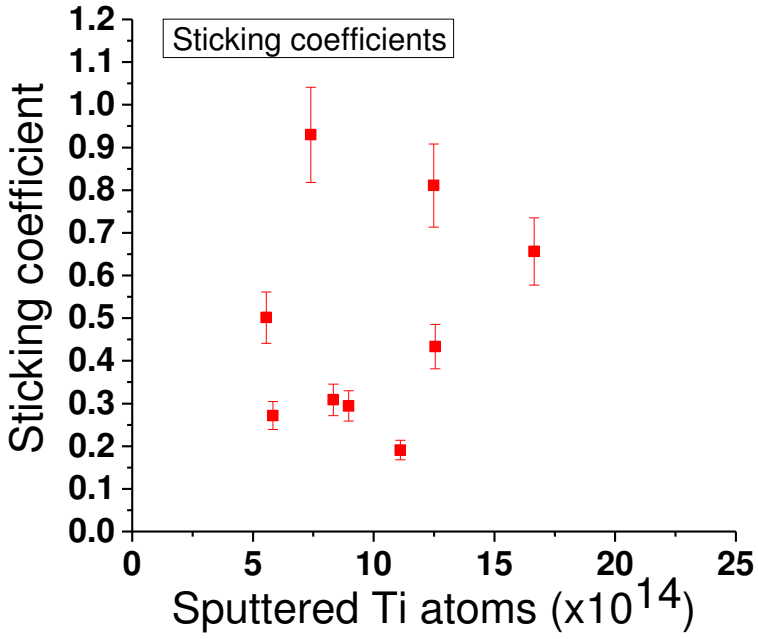

Fig. IV-7: Variation of the sticking coefficient as a function of Ti atoms sputtered during the deposition process.

The sticking coefficient distributes from 0.19 to 0.93 as shown in Fig. IV-7. There is no particular trend in the variation of the sticking coefficient with fluence. As long as the coverage of Ti atoms is in the sub-monolayer range (5.55×10^{14} – 1.66×10^{15} ions/cm^2), no particular dependence of the sticking probability on the surface coverage is expected.

Even if the centre of the deposit is not in the collector, the Lorentz fit assuming a symmetric deposit gives us the total number of deposited counts. The major reason for not getting particular trend in sticking values comes due to error in predicting line scan during SIMS analysis and also during the fitting of the Lorentz curve for some deposits. Indeed, for some deposits, the centre of the deposit is not on the collector, which means that the Lorentz fit is done using points which describe a relatively small part of the deposit shape. This may lead to a not so robust fit, and hence some significant error. The contributions due to SIMS experimental error are discussed in more detail below. The uncertainty in the measurements during the SIMS analysis is given by the error bars.

Here we will describe the contribution to the uncertainty is the positioning of the collector in the SIMS analysis chamber.

Indeed, the manipulator with the sample holder allows only for a positioning with a given uncertainty. For the first line-scan in the y direction, this has no huge effect. However, after finding the centre of the deposit, the sample needs to be repositioned for the line-scan in x direction. For the latter, an uncertainty of about 100 µm might be expected. In addition, depth profiles are carried out every 700 µm on average. With these two contributions, the line-scan might be carried out in worse case

about 500 µm off the centre of the deposit. If we consider Fig. IV-8, where two Lorentzian curves with amplitude value H= $5.67x10^8$ and H=$4.81x10^8$ are taken, the committed error is in this situation almost 14%. We did this calculation by reconstructing a 3D Lorentz function taking the parameters of Fig. IV-5(a) and the error for misalignment for 500 µm was estimated.

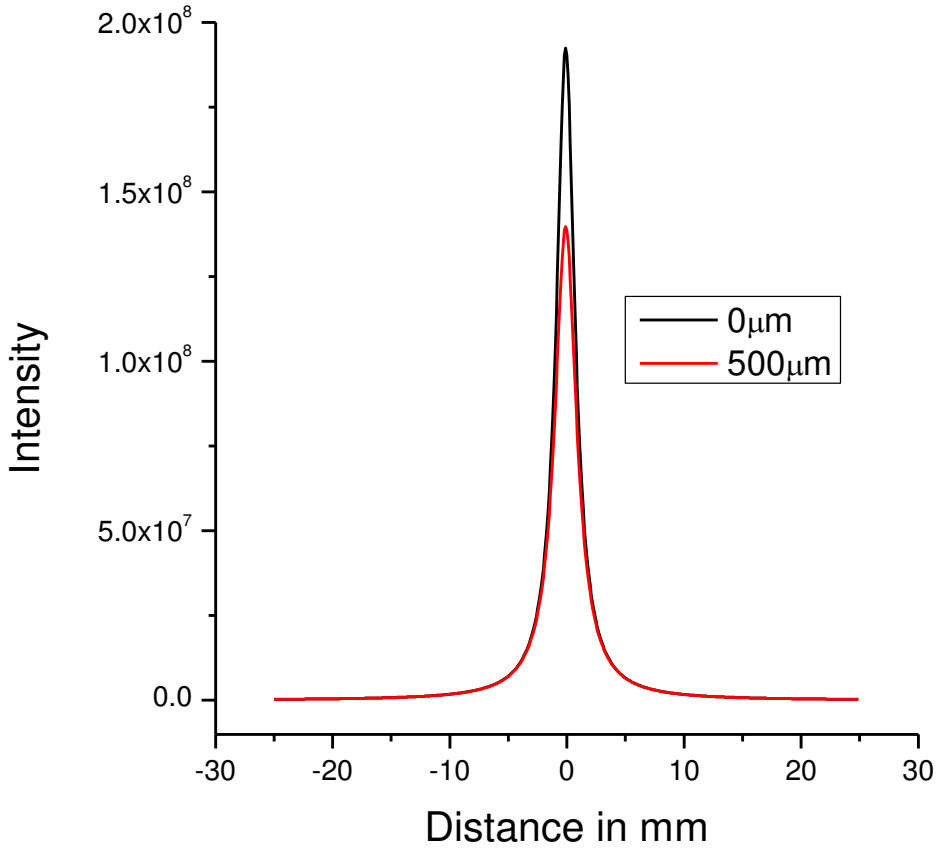

Fig. IV-8: Shape of the Lorentz curve at correct position and at the position due to misallocation of 500µm during analysis in SIMS.

4) Simulation results:

In the previous section, the sticking coefficient has been experimentally determined for several amounts of Ti deposited onto the Si collector. It is also obvious from the results that the experimental error for a sub-monolayer deposit by this technique is quite high. At the same time, the maximum values obtained should give a good idea of the actual sticking probability. Molecular dynamics simulations are used to validate the experimental numbers and gain some insights into the atomic-scale mechanisms, i.e. how and where the Ti atoms adsorb. The MD simulations of Ti deposition on Si(100) and amorphous Si have been carried out for different energies and angles of incidence. Information obtained by the simulation process includes mean implantation depth, depth distribution and the backscattering probability for a crystalline and amorphous sample. The conditions for the MD simulations are described in section 2.2.

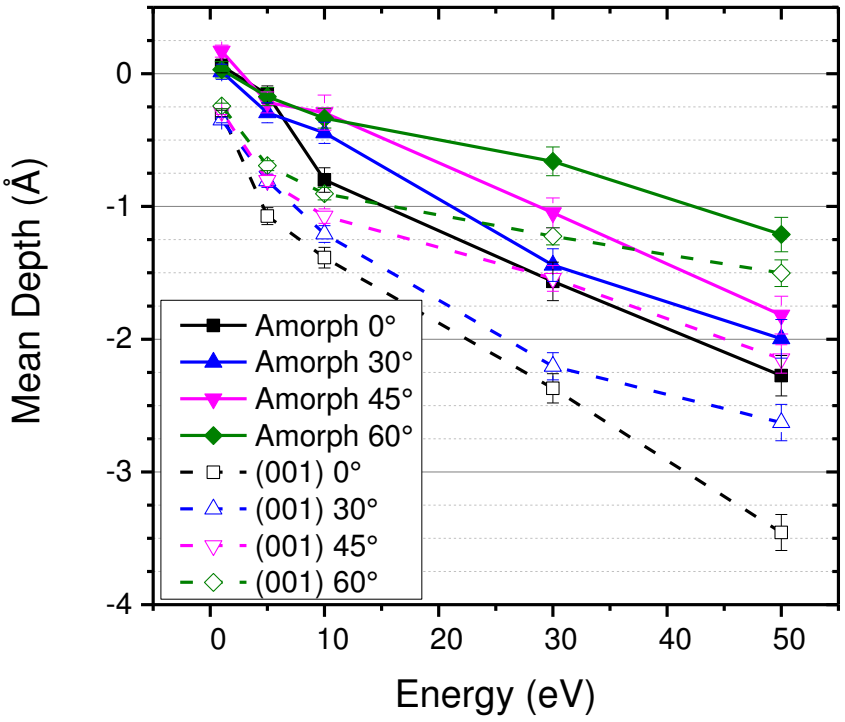

Fig. IV-9: Average depth as a function of deposition energy for different incidence angles.

Fig. IV-9 shows the variation of the average depth with the deposition energy for amorphous and crystalline silicon surfaces. The average depth has been calculated taking the final position of z coordinate of the deposited Ti atoms. They may deposit on the silicon surface or up to several monolayers deep. At very low energies, i.e. below 10 eV, there is no significant variation in the average depth with the incidence angle. At higher energies, the implantation depth increases and the incidence angle has a significant influence on the mean depth of the implanted Ti atoms. The average depth is highest at normal incidence and lowest at 60° with respect to the surface normal. This is explained by the normal component of the velocity vector of the Ti atom which is highest at normal incidence. This shows also that there is no, or at least no pronounced, channelling effect for the Ti deposition on contrary to the carbon deposition. At 50 eV, which is also the highest impact energy, the average depth of a Ti atom is highest in our simulations and reaches 2.2 Å for the amorphous sample and 3.5 Å for the crystalline sample. In general, the mean implantation depth is higher for the crystalline surface. The crystalline surface has a more order structure which helps the Ti atoms to implant deeper using low density channels which is not possible in the amorphous structure. However, the trend of the depth variation with the incidence angle does not depend on the sample structure.

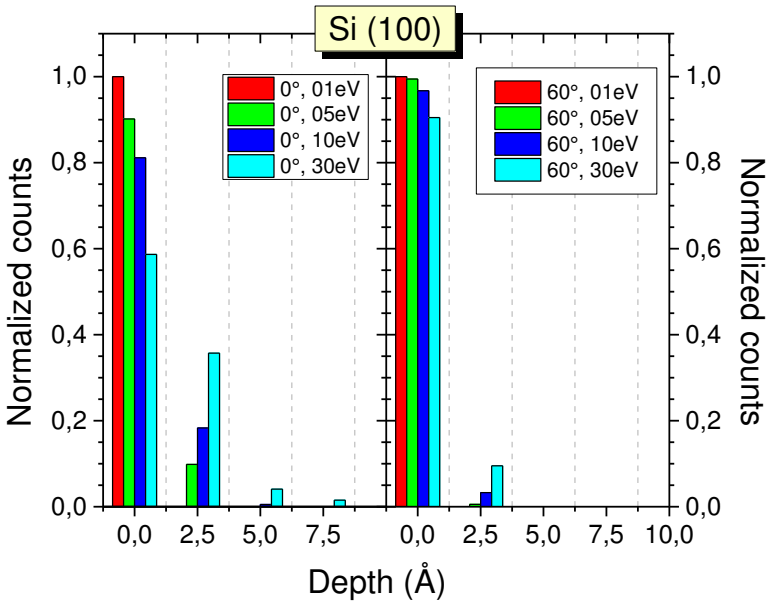

Fig. IV-10: Depth distribution for Ti atoms implanted into a Si(100) surface.

Fig. IV-10 shows how the Ti atoms are distributed inside the silicon for slabs with a thickness of 2.5 Å. The comparison is shown for the two extreme incidence angles of 0° and 60°. The graphs clearly show that most of the atoms stay on or very close to the surface. At 60°, more than 90% of the atoms stay in the topmost slab. In case of the 0° incidence angle and energy of 30 eV, Ti atoms can implant down to a depth of 7.5 Å. For the other energies, atoms implant deeper than at 60°, but stay in the two topmost slabs. Only at 1 eV, the Ti atoms stay always in the topmost 2.5 Å. Most even adsorb on one of the dimer atoms or adsorb in between two dimer rows (Fig. IV-11). For higher energies, the titanium atoms can still deposit on a dimer row, or in between two rows (Fig. IV-12a and b). If they stay on the Si(100) most often some silicon atoms of the dimer reconstruction gets displayed, leading to the deposition of the titanium atom into the dimer row and sputtering on silicon atom or displacing it on the surface.(Fig. IV-12c and d). Implanted titanium atoms can be found in two different kinds of sites. Either they implant into interstitial sites (Fig. IV-13a and b), or in substitution sites. The latter cause always some distortion of the silicon lattice (Fig. IV-13c and d). Except to some distortions, the implantation of the titanium atoms does not cause the formation of some additional damage.

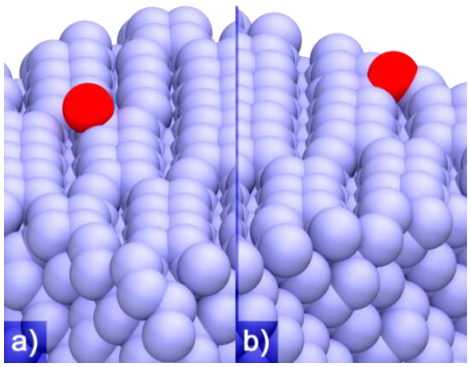

Fig. IV-11: Adsorption sites for Ti atoms deposited at 1 eV.

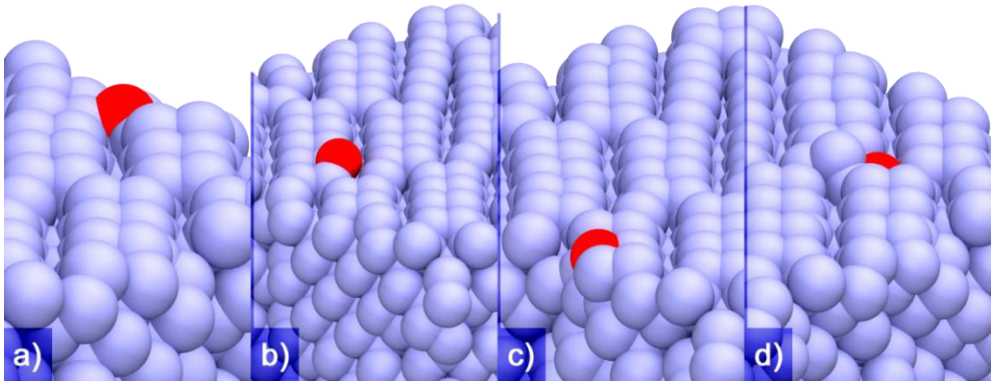

Fig. IV-12: Deposition sites for 50 eV titanium atoms on the Si(100) surface.

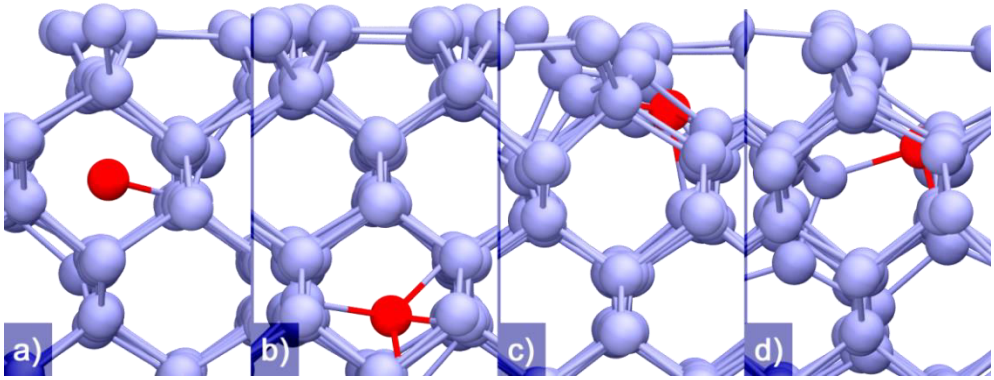

Fig. IV-13: Implantation sites for 50 eV titanium atoms inside the silicon lattice.

The main idea for carrying out MD simulations was the missing information on reliable sticking behaviour of Ti on Si in the sub-monolayer range as well as the underlying mechanisms. Information from experiments is limited to average data and macroscopic insights. The sticking probability of Ti on Si was calculated by taking the ratio between Ti atoms deposited in the surface and the number of Ti atoms sent towards the surface. (Fig. IV-14). Fig. IV-14 shows the sticking probability of titanium atoms for different energies and angles on both amorphous and crystalline Si surface.

It is found that the sticking probability is low at 5 eV and is significantly higher at 10 eV. This is due to energy of incoming Ti atom and how it is transferred to the substrate. At 1 eV, the deposition energy is lower than the Si-Ti bond energy, meaning that the Ti atoms will stick for most combinations of impact position and incidence energy. For 5 eV, the Si-Ti bond energy is close to the depositon energy and when the Ti atoms interact with the silicon surface, there are possibilities of resonance effect depending on the impact position. Indeed when Ti lands on Si atoms the backscattering probability is increased. .In the case of 10 eV, the scenario is different; the Ti atoms have sufficient energy to pass through the Si surface, leading already to some implantation below the topmost monolayer. Fig. IV-14 shows also that the sticking probability remains almost constant also for the higher incident energies of 30 eV and 50 eV, except for the 60° incidence angle. It is found that the sticking probability at 60° incidence in the case of both amorphous and crystalline silicon

decreases for the higher deposition energies. This is due to the component of the velocity vector parallel to the surface being higher than the normal component and it prompts more backscattering. In general the sticking probability at 10 eV or higher energy values vary between 0.95 to 0.99, i.e. it is close to unity. At 5 eV, the sticking coefficient varies in between 0.85 to 0.96.

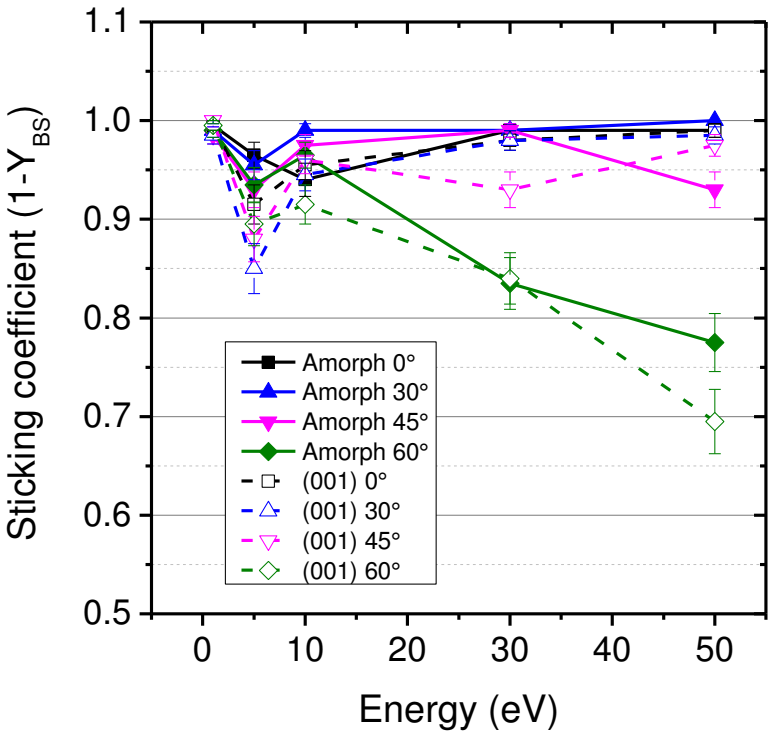

Fig. IV-14: Sticking probability for Ti on amorphous and crystalline silicon.

When comparing now the simulation to the experimental data, it is important to mention that in the sputter deposition process the most probable energy of the sputtered particles is in the 5-10 eV range, i.e. the energy range where the backscattering probability in the MD simulations is highest. Hence, the agreement between simulation and the three highest experimental data points is good. The values of sticking for 5 and 10 eV averaged over the angles are 0.88 and 0.94 for crystalline surface and 0.94 and 0.96 for amorphous surface. The MD simulations indicate also that the Ti atoms tend to stay in the Si lattice once they get implanted. This agrees with a previous study using density functional theory (DFT) calculations which show that both the adsorption on the silicon surface or in sub-surface sites leads to adsorption energies in the range of 5 to 6 eV per atom. However, activation energies between different adsorption sites are relatively high (4.59eV to 5.67eV), so that the titanium atoms will mostly stay in the positions they got deposited.

5) Conclusions:

In conclusion, we can say that a sub-monolayer film was grown for Ti on Si and sticking coefficient was measured, which was almost close to unity by molecular dynamics simulation approach. The

experimental sticking coefficient has on average a fluctuation. As we discussed, there were possible amount of uncertainty during the measurement of sticking coefficient in experimental approach, otherwise we expect sticking coefficient to be more or less constant in the sub-monolayer range and to change for a larger coverage. The method we employed here for the measurement of sticking coefficient is quite large in steps and involves mathematical and statistical estimations. Somehow we are able to estimate the sticking coefficient but improving the system set up and reducing the error, more reliable sticking values can be achieved.

The conditions in experiments and simulations were also not exactly the same. Modelling the deposition of titanium up to the coverage reached in the experimental work would have been a tedious job and there was no time left for the optimisation of Ti-Ti interaction parameters to make such multiple Ti depositions. But at least single Ti depositions give us an insight into the behaviour of sticking of Ti while the angles and energies are changed keeping the flux in a constant rate.

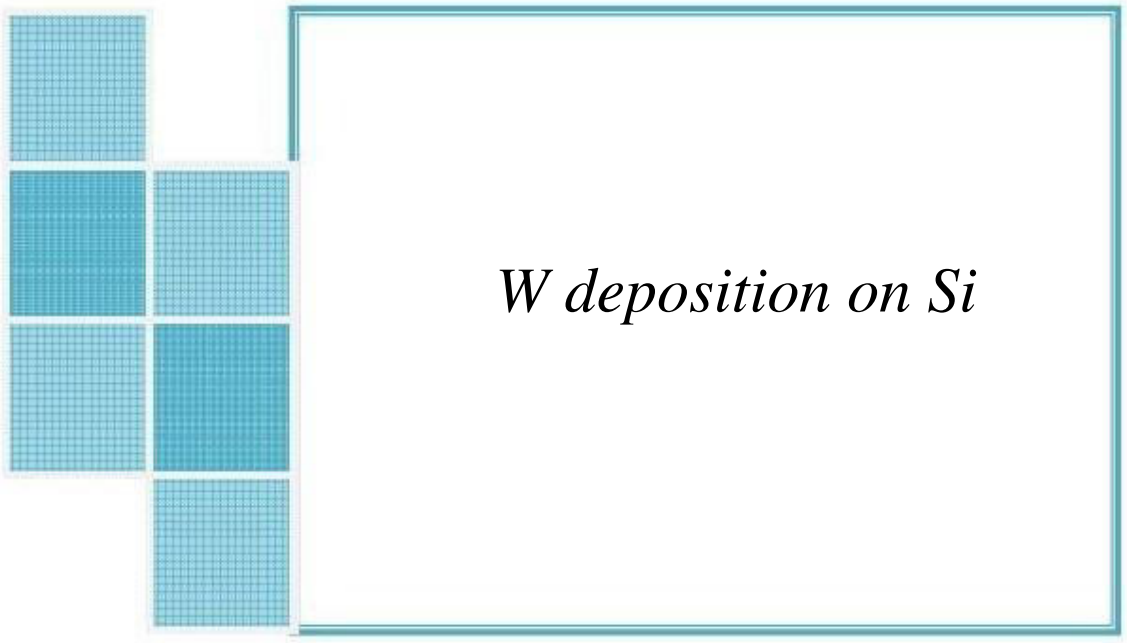

W deposition on Si

"Sticking and deposition mechanism of tungsten on silicon surfaces has been investigated by storing matter technique as well as by numerical simulations."

Chapitre 5.

Tungsten (W) deposition on Silicon (Si)

1) Introduction:

Here in this chapter we will discuss about the deposition process of sub-monolayer tungsten (W) film at room temperature by the storing matter technique by changing the fluence of argon ions during the deposition process. Later the deposited tungsten sub-monolayer film has been analysed in secondary ion mass spectrometry instrument to estimate the deposition and sticking behaviour of tungsten on silicon surface. The key parameters for making deposit in storing matter technique are chosen to achieve sub-monolayer deposits. The parameters in SIMS analysis are chosen also cautiously to get low sputter rates as the deposits are dilute. The ejected sputtered particles are spread over a certain area of the collector to form the deposit. Like titanium deposits, in order to investigate the distribution of the atoms in the collector surface, several dynamic SIMS analyses were done across the deposit along vertical and horizontal directions to find the centre of the deposit and record its shapes. A maximum intensity is always found almost at the edge of the collector for tungsten deposits. The silicon (Si) collector used for making tungsten deposit is same as for the titanium deposit described in previous chapter and also the cleaning procedures of silicon collectors is similar as before. One 10 mm x 15 mm foil of tungsten was used as a target.

Along with the experimental deposition process, molecular dynamics investigation for deposition and implantation mechanism of tungsten atoms in silicon structure have been done by post-doc researcher using the Kieffer force field. The sticking and deposition behaviour of the tungsten atoms in silicon have been investigated by depth distribution, mean depth variations, lateral displacement, sticking probability calculations using MD simulations. The details of the MD results will be given in later section of this chapter after experimental results.

2) Experimental setup

i) Storing matter conditions for W deposits

The storing matter conditions to achieve W deposits are the same as those used in the case of titanium (cf Table II-6 in chapter 2), except the fluency of incoming atoms. During the tungsten deposition preparation, the intensity of the raster-scanned Ar^+ beam has been varied from 100 nA to 160 nA and the deposition time from 200 s to 480 s in order to change the primary ion fluence from1.62 x 10^{14} to 4.80 x 10^{14} ions/cm^2. This corresponds to 9.26 x 10^{14} to 2.73 x 10^{15}sputtered tungsten atoms. For all

the deposits, the position of the silicon collector relative to the tungsten sample should be the same, but the results show that the positioning is not completely reproducible. In order to remove the native oxide layer on the sample (tungsten) surface, the surface has been sputtered for 1 hour.

ii) Analysis conditions in SIMS

The SIMS analysis conditions used for tungsten deposits are similar as titanium deposit analysis conditions. Similarly, a 5.5 keV Cs^+ primary ion beam is chosen for the analysis of the deposits. The sample voltage is set to 4.5 keV. Since the deposit is very dilute, the primary current is fixed to 1-2 nA in order to avoid a too fast sputtering of the deposited material. The beam is raster-scanned over an area of 500 x 500 μm^2.The analysed ions are $^{184}W^+$, $^{186}Wi^+$, and $^{28}Si^+$. The field aperture is set to1800 µm and the contrast aperture to 400 µm. For each deposit, several depth profiles were carried out in the form of line scans along the x and y directions like the line scan performed for titanium deposit in Fig. IV-2 (chapt 4). Line scan in the x direction has been used to characterize the deposit. The important parameters used for storing matter and analysis in SIMS are the similar as it is used for titanium deposit.

Table V-1 gives the details of the deposition conditions for several primary current and time of the W deposit for which the results will be explained.

Condition reference	Primary current (nA)	Time (s)	Total number of Ar^+ ions
a)	160	480	$4.80x10^{14}$
b)	130	200	$1.62x10^{14}$
c)	130	350	$2.84x10^{14}$
d)	140	400	$3.50x10^{14}$
e)	160	300	$3.00x10^{14}$
f)	100	320	$2.00x10^{14}$

Table V-1: Deposition conditions for 6 deposits.

3) Results and discussion

i) Depth Profile of a W deposit:

Depth profiles are done to analyse the deposits. One of the depth profiles for tungsten deposit is shown in Fig. V-1. Actually, line scans which are a series of depth profiles are executed along vertical and horizontal directions. The depth profile confirms the theoretical isotopic ratio between ^{186}W and ^{184}W and shows that no mass interferences are present. As $^{28}Si^+$ is the matrix signal for all the deposits, we normalize the secondary ion signals with respect to the matrix signal in order to correct for any changes in primary ion current and mass spectrometer transmission between the different depth profiles. The depth profile gives the total number of counts for the analysed area.

The counts for a depth profile at the centre of the deposit is maximum and drops to lower value towards the edge and become minimum at a distance of 8-10 mm from the centre similar to the deposits of titanium discussed in previous chapter. The intensity of silicon signal is higher at the beginning of analysis due to the presence of oxidised W deposit and native Si oxide on the collector surface and it decreases after the removal of the oxides.

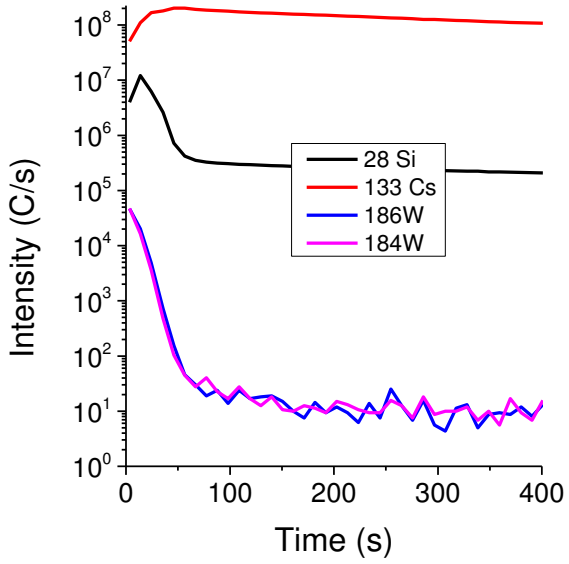

Fig. V-1: Depth profile of a sub-monolayer W deposit.

ii) Characterisation of the sub-monolayer deposits

Fig. V-2 shows the depth profiles for the different analysis points of the line scan in the x direction for six deposits conditions (Table V-1).. Only the $^{184}W^{+}$ secondary ion intensities which are of interest for the characterisation of the profiles are shown. The $^{133}Cs^{+}$ and $^{28}Si^{+}$ intensities are identical for the different profiles. Although the W deposits are in the sub-monolayer area, the $^{184}W^{+}$ counts stay above the background noise up to sputtering time of 200 s in SIMS. This is due to the mixing of the W atoms into the Si collector by the Cs^{+} primary ion beam. At the same time, quite a large number of W atoms is available in the analysis area with a diameter of 150 µm.

For each depth profile, the area under the $^{184}W^{+}$ curve is integrated in order to get the total number of counts detected for each analysis point. The intensity is maximum at the edge of the collector and decreases successively and becomes minimum at a distance of 10 mm from the edge on average. Our experimental setup does not allow for a positioning more towards the centre of the deposit without that the collector cuts the Ar^{+} beam during the deposition process as described for titanium deposits in chapter 4. For further calculations we assume that the deposit is symmetric and that the data can be fitted to a Lorentz curve as described in the chapter 4. Following six figures describe the Lorentz fit for six deposits explained on Fig. V-2 and Table V-1 above.

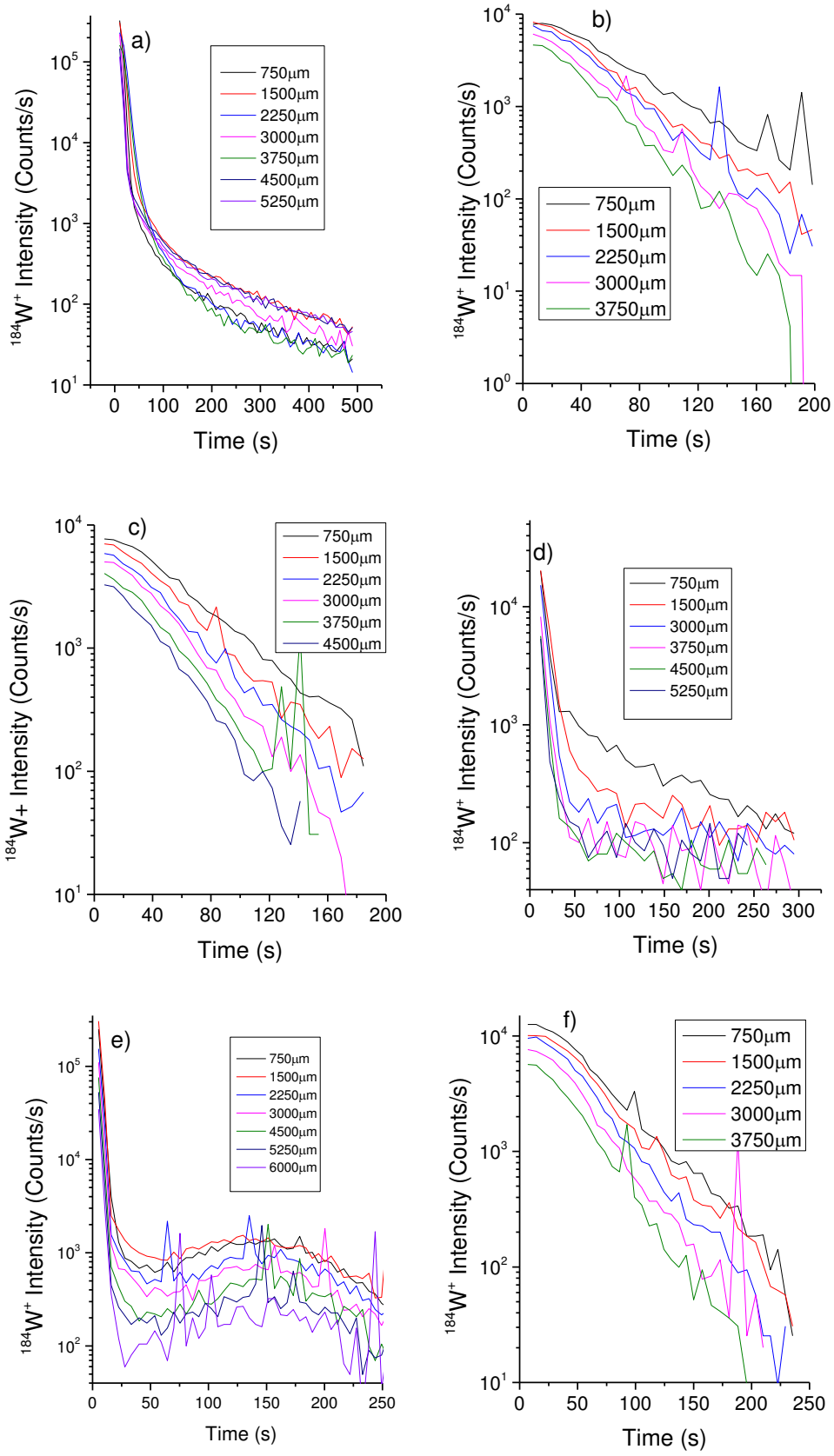

Fig. V-2: Depth profiles of a line scan in x direction for six sub-monolayer tungsten deposit on silicon. (a)-(f) correspond to deposit conditions reported in Table V-1.

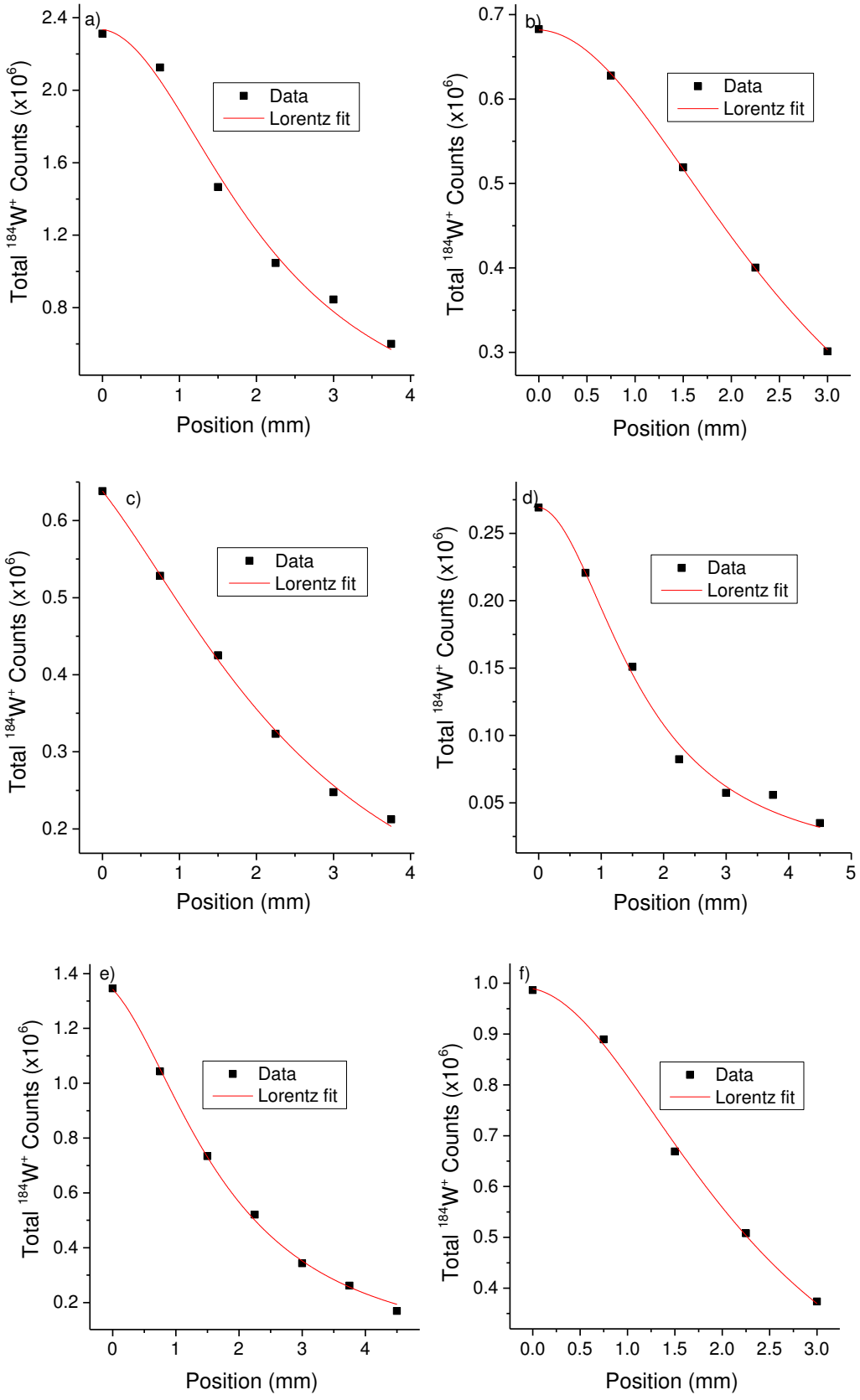

Fig. V-3: Lorentz curve fitting in 1D along the distance from the edge of the substrate, where a), b), c), d), e), and f) correspond to the same profile as in Fig. V-2.

The value of the area (A) and width (w) of the Lorentz fit of all deposits of Fig. V-3 are given in Table V-2.

Condition reference	Total number of Ar^+ ions	Area (A)	Width (w)
a)	$4.80x10^{14}$	$1.58x10^{10}$	4314.40
b)	$1.62x10^{14}$	$5.80x10^{09}$	5415.85
c)	$2.84x10^{14}$	$6.72x10^{09}$	6027.27
d)	$3.50x10^{14}$	$1.40x10^{09}$	3314.28
e)	$3.00x10^{14}$	$8.51x10^{09}$	3907.96
f)	$2.00x10^{14}$	$7.46x10^{09}$	4790.39

Table V-2: Values of A and w for six tungsten deposits.

From the values of *A* and *w*, total number of counts detected can be estimated. The rest of the process for calculating the sticking coefficient is identical to the one for Ti explained in chapter 4 (from equation IV-1 to equation IV-9 in chapter 4). However, there are two parameters which have different values from titanium while doing the step explained in chapter 4. One of them is sputter yield (Y) of W in the storing matter and another one is useful yield of SIMS (UY_{SIMS}) for tungsten. A sputtering yield of 5.7 ± 0.3 has been found for tungsten, which is in good agreement with simulations using the 2008 version of TRIM.

And during this process of estimating sticking coefficient, a 10keV implant of W on Si with a fluence of 10^{16} atoms/cm^2 has been used to obtain the useful yield of SIMS and UY_{SIMS} for $^{184}W^+$ is found to be $8.25x10^{-5}$ (Fig. V-4).

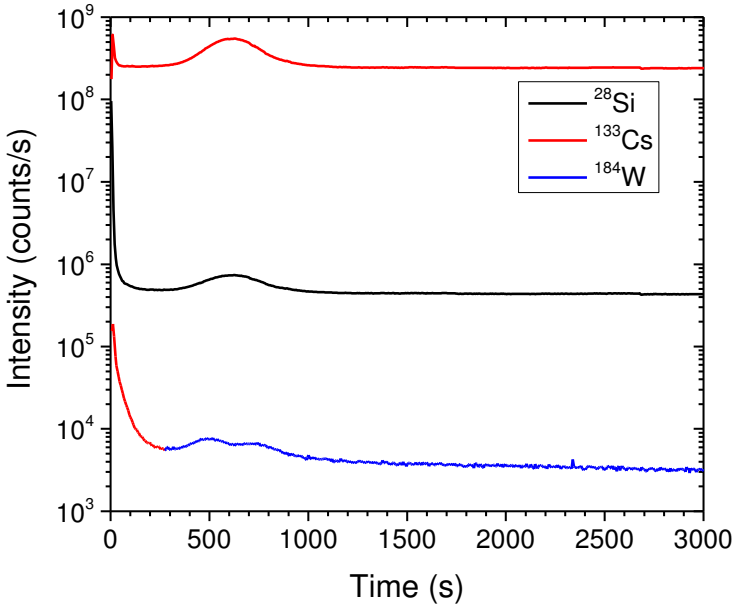

Fig. V-4: Implantation of W on Si analysed in SIMS having value of Useful yield = $8.25x10^{-5}$.

Table V-3 gives the values of sticking coefficients with sputtered particles for six tungsten deposits.

Condition references	Sputtered Ar^+ ions	Sputtered W particles	Sticking coefficients (SC)
a)	$4.80x10^{14}$	$2.73x10^{15}$	1.02
b)	$1.62x10^{14}$	$9.26x10^{14}$	1.03
c)	$2.84x10^{14}$	$1.62x10^{15}$	0.65
d)	$3.50x10^{14}$	$1.99x10^{15}$	0.13
e)	$3.00x10^{14}$	$1.71x10^{15}$	0.90
f)	$2.00x10^{14}$	$1.14x10^{15}$	1.13

Table V-3: Sticking coefficient values for different sputtered particles.

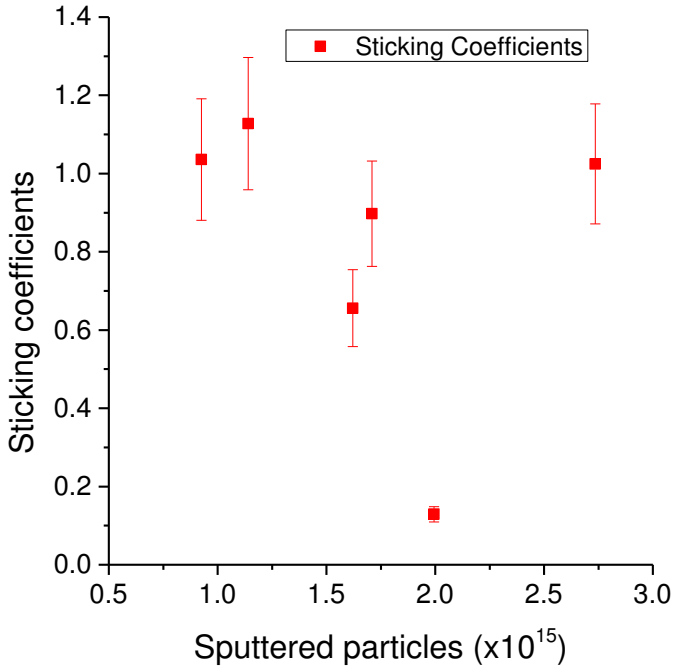

Fig. V-5: Sticking coefficients vs Sputtered particles for tungsten deposits.

It is seen in the figure that there are some sticking coefficients with values over unity. But considering the error bar (calculated from SIMS misalignment), the sticking coefficient could have value less than unity. Another reason for higher sticking values might be the matrix effect while measuring the useful yield of SIMS using the implant. From Fig. V-4, it is seen that there are sudden bumps for the intensity profile. This bumps come due to the well-known matrix effect in SIMS. The bumps are not only visible for $^{184}W^+$, which is expected because of the implant, but also for $^{28}Si^+$ and $^{133}Cs^+$, and all are located at the position of the W implant, indicating that the presence of W is responsible for the matrix effect. The ionization efficiency of the ejected tungsten, silicon and cesium particles strongly depends on the chemical environment. As the chemical environment in the background is not fixed, tungsten changes the sample work function and the matrix effect occurs.

Like titanium, no particular trend was found between sticking coefficients and sputtered particles for tungsten as the deposit is in the sub-monolayer range.

4) Simulation results:

As discussed in the earlier chapters, molecular dynamics simulation is an alternative complementary approach to support experimental observations. Here we employed MD simulation technique also for tungsten deposition. The MD simulations give us in detailed insights into the atomic scale mechanisms of deposition and implantation of tungsten atoms on silicon surfaces and also how and where the tungsten atoms adsorb. The MD simulations of tungsten (W) on Si (100) have been carried out for different angles and energies. The analysis of the simulation results have been done in the form of mean depth variations, depth distributions, lateral displacement, sputter yield variation and sticking probability. The simulation conditions employed for performing MD simulations for the tungsten deposition on silicon have been described in the Table II-2 of chapter 2.

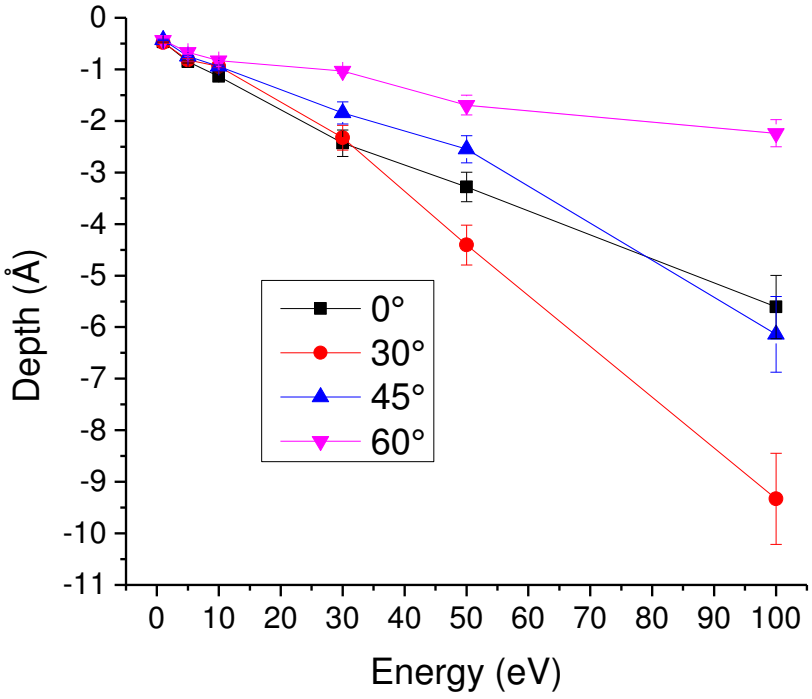

Fig. V-6: Average implantation depth as a function of deposition energy for different incidence angles.

Fig. V-6 shows the average implantation depth variation with the deposition energy for tungsten atoms on a crystalline silicon surfaces. The average depth has been calculated taking the final position of z coordinate of the deposited W atoms. Unlike the cases for carbon and titanium depositions, the primary energy of incoming tungsten atom has been varied up to 100 eV in order to see if there is any large variation in the deposition and implantation process, as well as the sputtering yield. At very low energies, i.e. below 10 eV primary energy of tungsten atoms, there is no significant change in the

average depth. Almost all the tungsten atoms stay near to the surface. At 30 eV impact energy, the mean depth of the tungsten atom goes up to 2.5Å. As depicted in Fig. V-6, the implantation depth increases at higher energies and the incidence angle has a significant influence on the mean depth of implanted W atoms.

Till 30 eV incident energy, the average depth of tungsten is highest at normal incidence and lowest at 60° with respect to the surface normal. This is due to the normal component of the velocity vector of the W atoms which is highest at normal incidence. At 100 eV incident energy, the average depth of W atom is maximum and reaches 9.5 Å for the incidence angle of 30°. We observe a significant change in mean depth at 30° incidence angle for 50 eV and 100 eV compared to other angles. We observed that there is a diffusive channeling for tungsten deposition at 30° as could be seen in Fig. V-7 For other angles this effect is less probable.

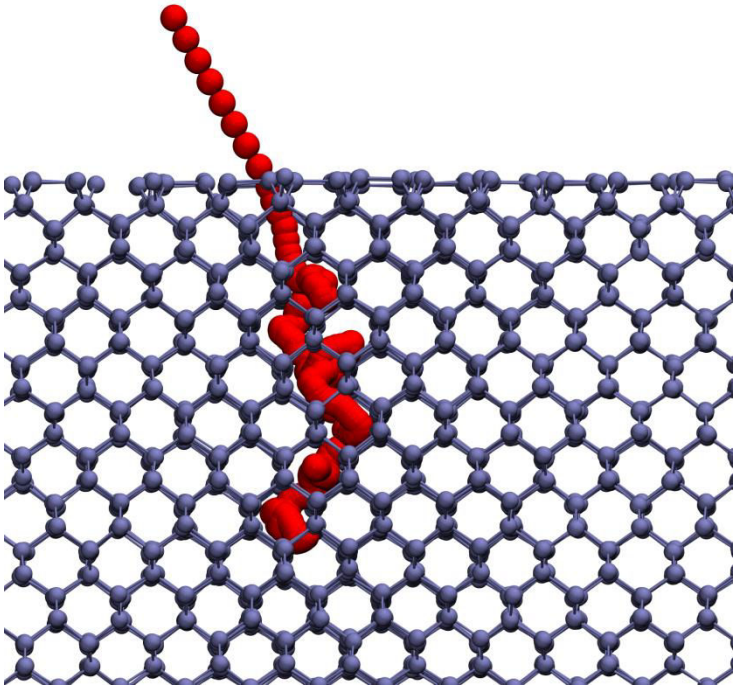

Fig. V-7: diffusive channelling for tungsten atom deposited at 30° incident angle.

Even at 100 eV, the mean depth is low at 60° compared to the other angles. Most of the tungsten atoms just stay near to the surface even at 100 eV for 60°. This reveals that the angle of an incoming atom has large influence in deposition and implantation process. We took some snapshots from our simulation to observe exact location of tungsten atom when deposited with 50 eV and 100 eV energy at 30° incidence angle. From the Fig. V-8, it can be seen that tungsten atom goes very deep for these two particular cases compared to all other cases. The Fig. V-9 shows the snapshot of tungsten atom sitting just on the surface and the snapshot is taken at 50 eV energy and 60° incidence angle.

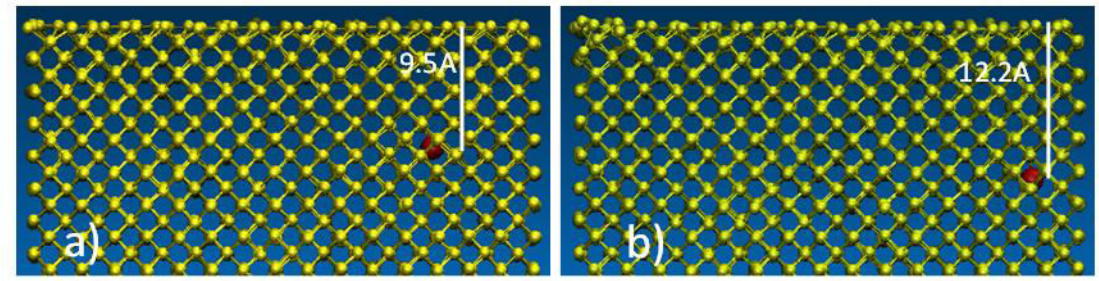

Fig. V-8: Snapshot of a tungsten atom implanted at 50 eV (a) and 100 eV(b) at 30° incidence angle.

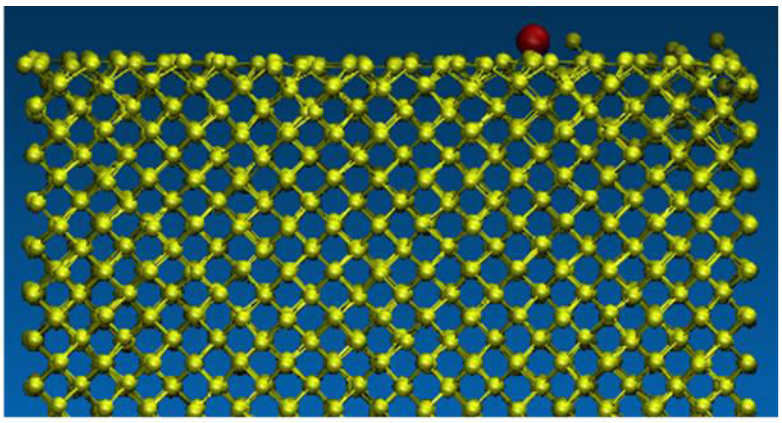

Fig. V-9: Snapshot of a tungsten atom just deposited on the Si (100) surface.

Fig. V-10 describes the depth distributions of tungsten atoms inside the silicon structure for several angles and energies. The comparison is shown for five different energies of 1 eV, 5 eV, 30 eV, 50 eV and 100 eV for incidence angles of 0°, 30°, 45° and 60°. For higher energies, the implantation depth is longer and conversely implantation depth is shorter for lower energies. So, in order get better view of depth distributions, we took smaller bin size (2.5 Å) for low energies at 1 eV and 5 eV depositions and larger bin size (5 Å) for higher energies 30 eV, 50 eV and 100 eV.

The maximum depth is always for 0° and minimum for 60° for all the energies. Fig. V-10 clearly shows that the implantation depth increases with increment of incidence energy. For the incident energies of 1eV and 5eV, majority of tungsten atoms are deposited between 0 Å and 2.5 Å down to the surface. And there is no atom being implanted down to 2.5 Å depth for 1 eV but some atoms are found at a depth between 2.5 Å and 5 Å for 5eV case. The case is different for tungsten atoms deposited with initial energies of 30eV, 50eV and 100eV. Tungsten atoms have been implanted up to 27.5Å down into the sample for 30 eV and 50 eV incident energy according to the Fig. V-10 c) and d). The maximum implantation depth is reached to 40Å for the tungsten atoms deposited with initial energy 100 eV according to Fig. V-10 e). This proves that there is a certain influence on implantation depth distribution while energies are increased. There is certain trend in the distribution of tungsten

atoms at different depths with energies. From Fig. V-10, it is seen that almost 200 tungsten atoms deposited at a depth between 0 Å and 2.5 Å for 1 eV and 5 eV incident energies while the number drops for other energies (30 eV, 50 eV and 100 eV).

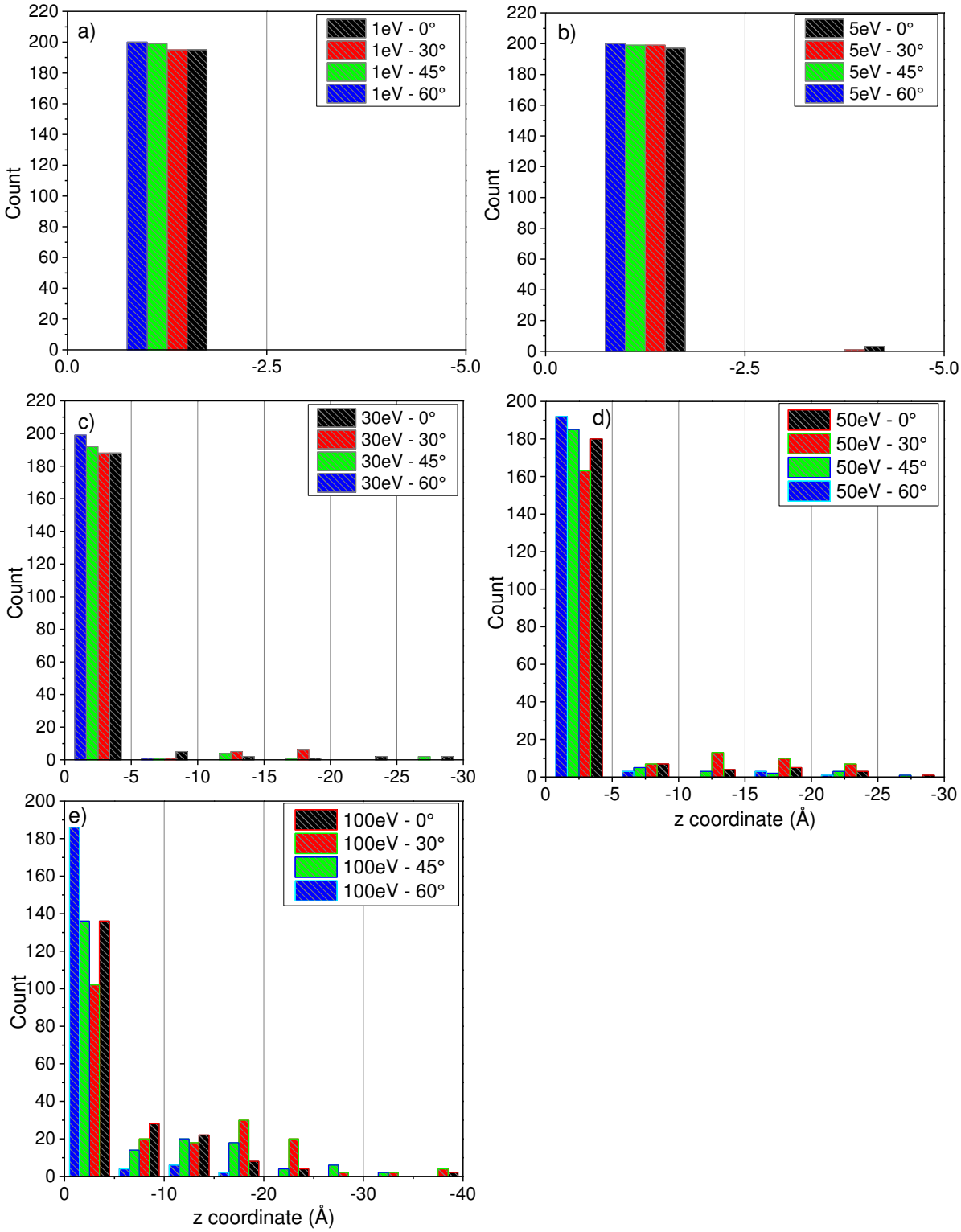

Fig. V-10: Depth distribution for W atoms implanted into a Si(100) surface where (a), (b), (c), (d), (e) are the corresponding depth distributions at 1 eV, 5 eV, 30 eV, 50 eV and 100 eV.

For 30 eV, 50 eV and 100 eV incident energies, there are certainly several number of tungsten atoms implanted at a depth below 5 Å.. The distribution of tungsten atoms below the 5Å depth is much similar for 30 eV, 50 eV and 100 eV incident energies but the number of counts is maximum for 100 eV energies. During the mean depth analysis (Fig. V-6), we find that the average depth is higher for 30° incidence angle at 50 eV and at 100 eV. The similar nature can be confirmed in the Fig. V-10 as the counts at larger depth for 30° (red slab) is always maximum compared to other angles for 50 eV and 100 eV. Considering implantation at all angles and energies, it is observed that majority number of tungsten atoms just deposited near to the surface.

Fig. V-11 shows how the energy and angle influence lateral displacement of tungsten on silicon surface. The lateral displacement is larger for higher slanting angle, which is quite logical as the tangential component of velocity is higher for larger slanting angles. The difference in lateral displacement value from 0° to other three angles (30°, 45°, 60°) is higher but the difference in lateral displacement value among these angles (30°, 45°, 60°) is low. At the same time Si (100) diamond crystal structure orientation also might have some influence for the lateral displacement of tungsten atoms while it comes at larger slanting angle. The lateral displacement for all cases increases linearly with energy.

The highest lateral displacement is achieved for 100 eV, which is 10.5 Å for 60° incident angle. At 5 eV for 0° incidence angle, the lateral displacement is lowest, which is 1.1 Å. There is a sudden increase in lateral displacement at 50 eV for 30° than other larger slanting angles (45° & 60°). This support also the unusual behavior at 30° while describing mean depth calculations for tungsten atom deposited at 50 eV incident energy.

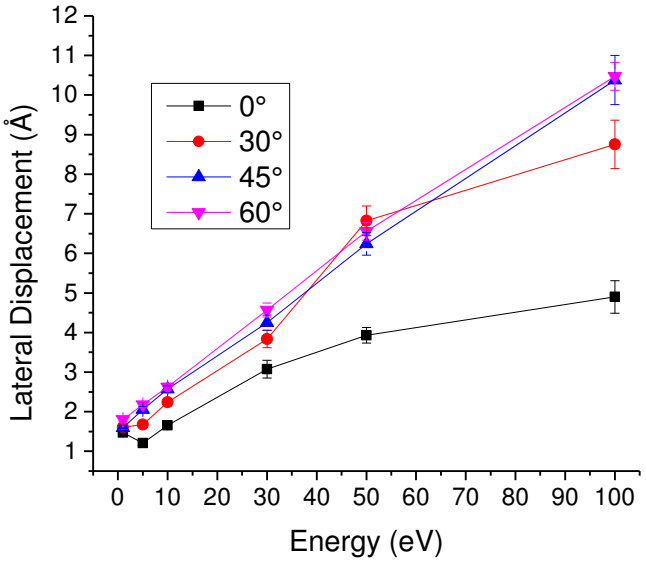

Fig. V-11: Lateral displacements of W atoms on Si(100) surface.

The Fig. V-12 describes the deposition and implantation ratios of tungsten atoms at 0°, 30°, 45° and 60° incidence angles for energies varied from 1 eV to 100 eV. A tungsten atom is accounted as being implanted if its final location is beneath a virtual plane located 2.5 Å below the topmost silicon atom of the surface at the end of the MD simulation. Tungsten atoms are treated as being deposited if its final location is above that virtual plane and not reflected from the surface at the end of the MD simulation.

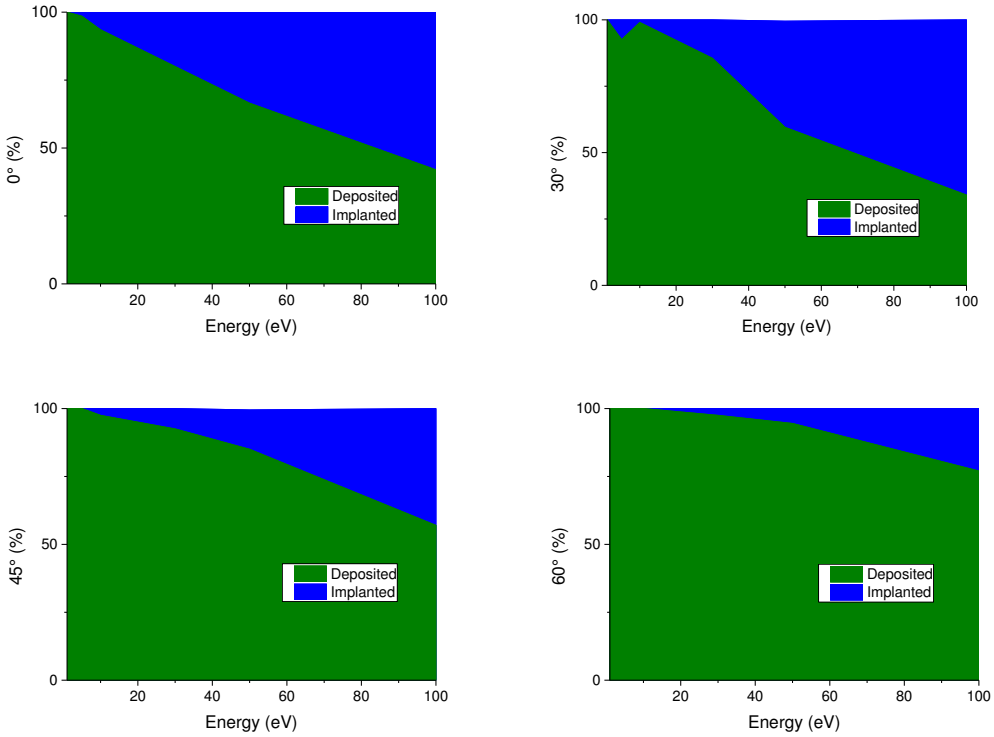

Fig. V-12: Deposition to implantation ratio of W atoms on Si(100) surface.

As expected, the deposition is higher compared to implantation at lower energy. At 1 eV and for all angles, the ratios of deposition to implantation found higher, which reveals that a vast amount of tungsten atoms sit on top of the surface. With increment of energy of the incident tungsten atom, the ratio deposition/implantation falls. Fig. V-12 describes that the implantation is highest at 100 eV. Increasing the energy to values higher than 20 eV does not have an impact on the deposition/implantation ratios, as most of the carbon atoms are implanted.We observed that the ratio between implanted and deposited tungsten atoms is higher at lower angles and decreases with the increment of angles. The deposition/implantation ratio is maximum at 60° and minimum at 0°, which reveals the fact that implantation is maximum when tungsten atoms are deposited in normal direction.

During these simulation studies, we also investigate sputtering yield of tungsten atoms on silicon increasing energies up to 100 eV (Fig. V-13).

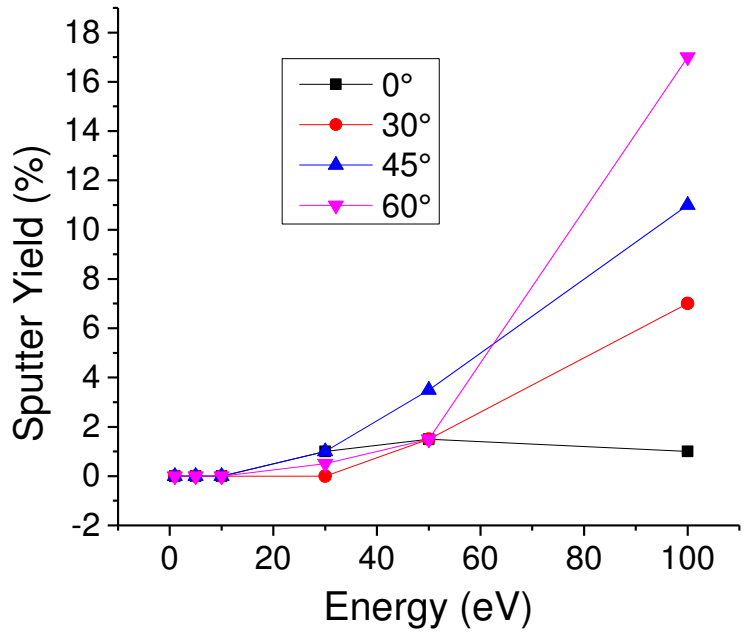

Fig. V-13: Variation of sputtering yield with W-atom energy on Si(100) surface.

We observed that there is no sputtering until 10eV incident energy but immediately after the sputtering of silicon happens to start. There are significant numbers of silicon atoms sputtered at 30 eV and the numbers increase further for 50 eV and 100 eV. It is observed that the sputter yield suddenly changed to a higher value for 30°, 45° and 60° but it remains quite low at 0°.

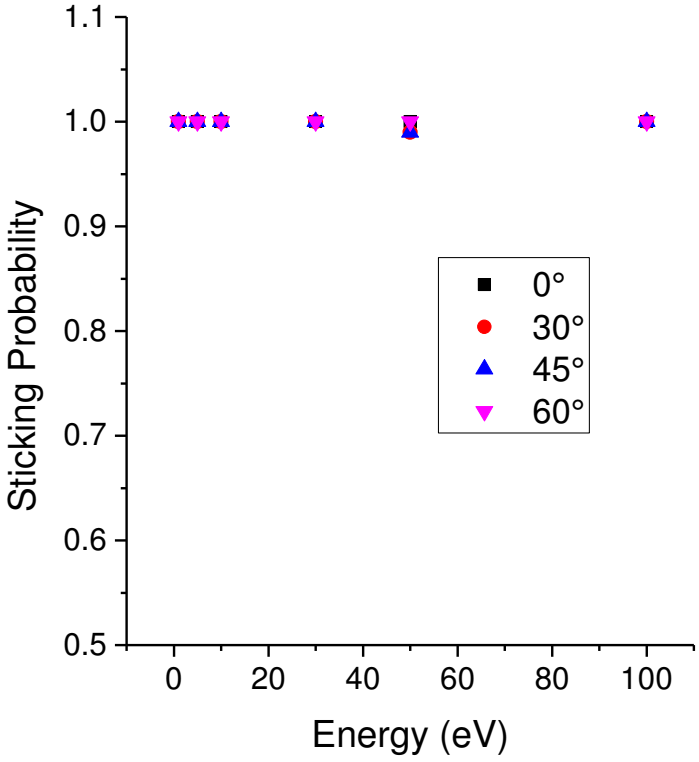

Fig. V-14: Sticking probability of W on Si (100).

Along with the sputtering yield observation, we also investigate the sticking probability of the tungsten particles (Fig. V-14). Sticking probability has been calculated by removing back scattering atoms from the incoming atoms. During the observation, it is found that there are very less backscattering tungsten atoms for all the angles and energies and almost all the tungsten particles sit on the silicon surface. The sticking coefficient is almost unit for all cases. In case of titanium and carbon depositions on silicon, we still find sticking coefficient which is less than 0.9 but here sticking coefficient for tungsten has higher values. In order to explain this behaviour, we calculated the bond energies. The bond energies for Si-C, Si-Ti and Si-W are found to be 4.6 eV, 5.5 eV, and 10.6 eV. Hence we find that the bond energy for Si-W is almost twice the value for Si-Ti. Due to this higher bond energy the sticking probability is higher for tungsten and it reaches almost unit value.

5) Conclusions:

Attempts are made to calculate the sticking coefficients of tungsten on silicon experimentally and sticking coefficient values are found to be high. The matrix effect during the calculation of useful yield using the implant might partially contribute to sticking coefficient with values close to unit value. However, these values agree also well with the numerical simulations. Several other investigations are made by molecular dynamics approach. Depth distribution provides the influence of energies in implantation mechanisms. Lateral displacement and sputter yield calculations provide also important information about deposition and implantation mechanisms. When lateral displacement is high, the implantation depth is lower and vice versa. From the sputter yield calculations, it can be seen that energy and angle both have influence in sputtering. Higher energy prompts high sputtering. Finally, we calculated sticking coefficients also for tungsten on silicon. The investigation reveals that the sticking coefficient is almost unit for all the cases, which proves that tungsten has very high affinity for silicon.

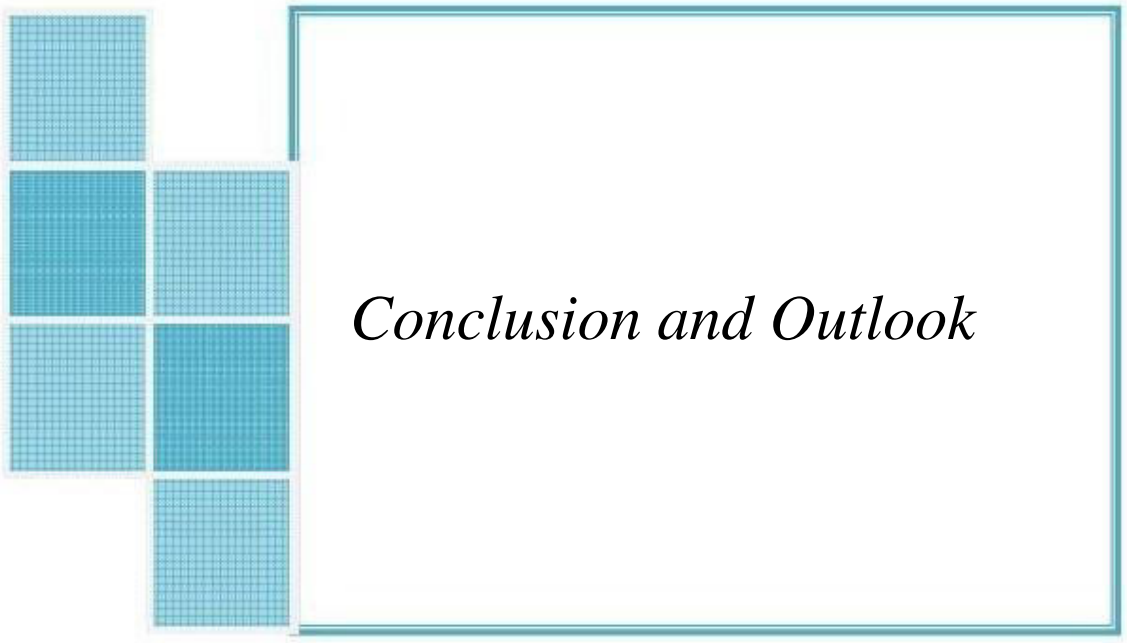

Conclusion and Outlook

"This chapter summarises the objectives of the work and results achieved as well as the difficulties encountered and future perspectives."

Chapitre 6. Conclusion and Outlook

1) Conclusion

The sticking, deposition and reorganization of atoms in the sub-monolayer range is of great importance for the field of surface science. Sticking of any material to a product surface is an important industrial problem with many applications in the field of packaging, electronic and material industries In order to well understand the interaction phenomenon between atom and surface, as could be the case in plasma surface treatments, it is essential to get a perfect knowledge on the sticking mechanisms during the early stage of interactions since these mechanisms control the interface properties.

The main goal of this work was to investigate sticking and deposition behaviour of inorganic particles on silicon surfaces during growth of interface in sub-monolayer regime at few eV energy. Along with experimental investigations, numerical simulation approach has been used to achieve these objectives. Large-scale MD simulations making use of first-principles based reactive force fields are used to understand the atomistic processes underlying the adhesion and reorganization of atoms on the substrates for numerical approach. Only in this way, a better understanding and control of tailor-designed surface properties can be obtained.

Furthermore, these studies enhance the comprehension of the deposition process in the sub-monolayer regime during the collector preparation for the surface analysis technique “Storing Matter”. The results of Sub-ML give contributions and suggestions to further improve this technique. The influences of atom and cluster energies and incidence angles on sticking and surface diffusion have been investigated for different surfaces with respect to surface coverage. The plasma by itself is not investigated in this project but it is treated as a source of atoms. The major parameters explored in this project include the particle properties (size, energy and angular distributions) as well as the substrate composition and roughness.

Sticking and deposition mechanism of C, Ti and W have been studied and discussed by both experimental and numerical approaches. Along with experimental work, numerical analysis brings atomic scale insight to deposition and implantation mechanisms. No experimental study has been carried out for carbon deposition on Si. Experimental observations were not possible for carbon as with our setup, carbon contaminations could not be reduced to the degree where they did not interfere significantly with the sub-monolayer deposits. Therefore, additional simulation work has been carried out for carbon, i.e. the continuous deposition of carbon on silicon.

Molecular dynamics investigation of carbon on silicon brings detailed atomic scale insight for carbon while interacting with silicon at low energies. Continuous carbon deposition along with single impact of carbon on silicon surfaces describes several aspects of deposition and implantation mechanism for carbon. The reactive force field developed by John Kieffer is selected, as it permits the formation and breaking of bonds via an adaptive and environment sensitive charge transfer for both cases. The results for single carbon deposition mainly consist of mean depth variations, depth distributions, deposition to implantation ratio, back scattering probability. The comparisons and validations are made with well-established Erhart-Albe potential for these results. The results using both potentials are similar, although slight divergences appear at grazing angles and for the higher end of the deposition energies. The studies of single carbon depositions were extended to multiple carbon deposition to get a better understanding of carbon deposition and implantation and damage formation during low-energy carbon atom interactions with a Si(100) surface and also to explain the results in more experimental prospects as we were not able to execute experimental work for carbon due to contamination problems. We explained the results in different approaches but the main idea was to observe and interpret multiple carbon deposition and implantation mechanism at different conditions. The main parameters to investigate the system structures after continuous deposition include radial distribution function, depth distribution, coordination calculation, concentration and angular distribution function.

Radial distribution function along with angular distribution function reveals the damaging information of Si-C structure as a function of incidence angle, incidence energy, deposition dose and depth in the sample. It is observed that the structure is heavily distorted just near to the surface and a more ordered structure at depths exceeding 10 Å. Similar conclusions can be drawn from the concentrations, depth distributions and coordination number calculations. The influence of angle and energy on the structure formed has been explained in different sections. It is found that energy has larger influence than angle for the damage formed. Analysis of the results at different steps varying the incoming dose of carbon atoms brings also several aspects of deposition and implantation process for carbon. There were some carbon atoms found even at 15 Å depth at 1 eV, which was mainly due to some deposition induced diffusion mechanism. Some snapshots were taken to support this phenomenon. Finally, the results of radial distribution functions, depth distributions, coordination number and angular distributions give several aspects of deposition and implantation mechanism for continuous carbon depositions. The results might give some important insight in Si-C bond formation but do not bring complete information on silicon carbide.

In chapter 4, several aspects regarding sticking and deposition mechanisms for titanium on silicon have been described and discussed. Experimental observation along with numerical investigation provides detailed understanding of atomic scale mechanism of titanium on silicon surfaces. Interface mechanisms during the sub-monolayer film growth have been discussed. Sticking behaviour of

titanium during the sub-monolayer film growth has been understood. Experimental investigation of sticking behaviour does not provide any particular trend with sputtered particles. As could be expected, it is tricky also to find any particular sticking trend for such a thin deposit. In order to support these experimental observations, MD simulation studies were carried out. The sticking coefficient for titanium is found to be higher having values between 0.8 to 0.99. It would have been more significant to correlate experimental and simulation results if we would have found out sticking and deposition behaviour of titanium in multiple deposition condition as we studied for carbon deposition. But optimisation of the Ti-Ti force field parameters would have been a tedious job and beyond the possibilities of this project. But at least single Ti depositions give us an insight into the behaviour of sticking of Ti while the angles and energies are changed keeping the flux in a constant rate.

Similar approaches were considered for the investigation of tungsten deposition behaviour on silicon substrate. The experimental investigation shows that the values of sticking coefficients are high, which correlates well with the molecular dynamics studies. One of the reasons for higher sticking values could be the higher bond energy between W-Si. Several other investigations are made by molecular dynamics approach. Depth distribution provides the influence of energies in implantation mechanisms. Lateral displacement and sputter yield calculations provide also important information about deposition and implantation mechanisms. When lateral displacement is high, the implantation depth is lower and vice versa. From the sputter yield calculations, it can be seen that energy and angle both have influence in sputtering. Higher energy prompts high sputtering. Finally, we calculated sticking coefficients also for tungsten on silicon. The investigation reveals that the sticking coefficient is almost unit for all the cases, which proves that tungsten has very high affinity for silicon.

Globally, it can be concluded that sticking and deposition behaviour of inorganic particles (C/Ti/W) on silicon surfaces during the growth of interface in sub monolayer range at low energies have been understood and explored both by experimental and simulation approach. While there are experimental limits, analyses are explored in simulation approach. Perfect parallelization of conditions for both simulation and experimental approach was not possible, at least basic ideas regarding deposition and sticking have been achieved. Among all three materials, tungsten seems to have higher sticking probability compared to other two (Ti and C) due to its higher bond energy with silicon.

2) Outlook

Sticking coefficient values using storing matter and SIMS techniques are determined but more accuracy can be achieved by reducing the length of the process. In the scale of accuracy, this experimental techniques used here cannot be competitive to other traditional sticking coefficient measurement instrument like Rutherford Backscattering method. The main application of the Storing Matter technique for inorganic samples is quantitative depth profiling. But during doing depth profiles

in SIMS, there were always uncertainty to choose the right spot in the deposit. Including a scale in the collector holder could reduce the error till some extent.

Control of contaminations with the current set-up is too limited for some elements, and only sputter deposition and analysis in one chamber can reduce the errors. In this way, we can avoid using suitcase to transfer the samples. Eventually, it will result less contaminations.

While comparing the results by both simulation and experimental approach, there are several conditions which could be considered carefully. Although we maintain to keep our deposit from deposition till the analysis process under UHV conditions, still there are always native oxide layers on silicon surfaces. But while determining simulation conditions, there is no possibility for silicon surface to be oxidized. While doing simulations, the angles are perfectly defined but there is no defined angle within the storing matter set up. In fact, all the sputtered particles distribute through a solid angle. Similarly, the energy of the incoming atom is fixed and defined in simulation process but the sputtered particles in storing matter have a distribution of energies. For single atom deposition, only Si-Ti or Si-W interactions are considered and other interactions are neglected, which is not the same for experimental interaction among particles in storing matter deposit. A perfect alignment between simulation and experimental conditions could provide more meaningful comparisons of phenomenon. For carbon deposition, along with single carbon deposition, we have performed continuous carbon deposition and different conclusions have been made. It would be better also to execute continuous titanium and tungsten investigation on silicon surface. Although we could expect the nature of distribution of titanium /tungsten along the silicon slab might be similar like carbon but several other findings on the film growth could be investigated. For future aspect, these multiple titanium and tungsten deposition should be carried out in order to have more realistic comparisons with sputter deposition techniques at low energies.

Using of implant to calculate the useful yield of SIMS was not the best choice to have competitive results. But there was no other possibility to measure useful yield except the use of implant. Sometimes matrix effect during the analysis of implant could bring error in measurement of useful yield of SIMS. MC simulations, MD simulations, Rutherford backscattering processes could be the alternatives to avoid the use of implant.

This PhD work is an important first step before investigating deposition mechanism of SiC, TiC and WC on substrate surface, which has several industrial applications. So, as a continuation of this PhD work, deposition mechanisms of SiC, TiC and WC on Si substrate could be studied next.

For the current work, only single atom deposition in the few eV range has been carried out but future work on deposition of small clusters of various sizes using molecular dynamics simulations could be interesting and could be comparable with plasma deposition process.

Several other aspects also could be interesting to investigate, such as island formation, diffusion during physical characterization of the inorganic Storing Matter deposits. This would provide a deeper insight into the fundamental processes involved in the deposition processes.

References

1. Graves, D. B.; Jensen, K. F. Continuum model of dc and rf discharges. *IEEE Trans. Plasma Sci.* **1986,** *PS-14* (2), 78-91.

2. Boeuf, J. P. Numerical model of rf glow discharges. *Phys. Rev. A* **1987,** *36* (6), 2782-2792.

3. Hancock, G.; Compton, R. G. *Applications of Kinetic Modelling;* 1 ed.; Elsevier: 1999.pp. 1-713.

4. Surendra, M.; Graves, D. B. Particle simulations of radio-frequency glow discharges. *Plasma Science, IEEE Transactions on* **1991,** *19* (2), 144-157.

5. Birdsall, C. K. Particle-in-cell charged-particle simulations, plus Monte Carlo collisions with neutral atoms, PIC-MCC. *Plasma Science, IEEE Transactions on* **1991,** *19* (2), 65-85.

6. Graves, D. B.; Brault, P. Molecular dynamics for low temperature plasma-surface interaction studies. *Journal of Physics D-Applied Physics* **2009,** *42* (19), 194011.

7. Bogaerts, A.; van Straaten, M.; Gijbels, R. Monte Carlo simulation of an analytical glow discharge: motion of electrons, ions and fast neutrals in the cathode dark space. *Spectrochimica Acta Part B: Atomic Spectroscopy* **1995,** *50* (2), 179-196.

8. Bogaerts, A.; Gijbels, R.; Goedheer, W. J. Hybrid Monte-Carlo Fluid Model of A Direct-Current Glow-Discharge. *J. Appl. Phys.* **1995,** *78* (4), 2233-2241.

9. Brault, P.; Range, H.; Toennies, J. P. Molecular beam studies of sticking of oxygen on the Rh(111) surface. *J. Chem. Phys.* **1997,** *106* (21), 8876-8889.

10. Neyts, E.; Bogaerts, A.; Gijbels, R.; Benedikt, J.; van de Sanden, M. C. M. Molecular dynamics simulations for the growth of diamond-like carbon films from low kinetic energy species. *Diamond and Related Materials* **2004,** *13* (10), 1873-1881.

11. Konoplev, V.; Caturla, M. J.; Abril, I.; Gras-Marti, A. Bulk atomic relocation in low-energy collision cascades in silicon: Molecular Dynamics versus Monte Carlo simulations. *Nuclear Instruments and Methods in Physics Research Section B: Beam Interactions with Materials and Atoms* **1994,** *90* (1-4), 363-368.

12. Guvenc, Z. B.; Hippler, R.; Jackson, B. Bombardment of Ni(100) surface with low-energy argons: molecular dynamics simulations. *Thin Solid Films* **2005,** *474* (1-2), 346-357.

13. Gleason, K. K.; Wang, K. S.; Chen, M. K.; Reimer, J. A. Monte Carlo simulations of amorphous hydrogenated silicon thin-film growth. *Journal of Applied Physics* **1987,** *61* (8), 2866-2873.

14. McCaughey, M. J.; Kushner, M. J. Simulation of the bulk and surface-properties of amorphous hydrogenated silicon deposited from silane plasmas. *J. Appl. Phys.* **1989,** *65* (1), 186-195.

15. Ohira, T.; Ukai, O.; Noda, M. Fundamental processes of microcrystalline silicon film growth: a molecular dynamics study. *Surf. Sci.* **2000,** *458* (1-3), 216-228.

16. Bakos, T.; Valipa, M.; Aydil, E. S.; Maroudas, D. Temperature dependence of precursor-surface interactions in plasma deposition of silicon thin films
8. *Chem. Phys. Lett.* **2005,** *414* (1-3), 61-65.

17. Bakos, T.; Valipa, M. S.; Maroudas, D. Interactions between radical growth precursors on plasma-deposited silicon thin-film surfaces. *J. Chem. Phys.* **2007,** *126* (11), 114704.

18. Pandey, S. C.; Singh, T.; Maroudas, D. On the growth mechanism of plasma deposited amorphous silicon thin films. *Appl. Phys. Lett.* **2008,** *93* (15), 151913.

19. Valipa, M. S.; Sriraman, S.; Aydil, E. S.; Maroudas, D. Atomic-scale analysis of fundamental mechanisms of surface valley filling during plasma deposition of amorphous silicon thin films. *Surface Science* **2005,** *574* (2-3), 123-143.

20. Gordiets, B. F.; Andujar, J. L.; Corbella, C.; Bertran, E. Kinetic model of thin film growth by vapor deposition. *Eur. Phys. J. D* **2005,** *35* (3), 505-511.

21. Rosen, J.; Schneider, J. A.; Larsson, K. Ab initio studies of adsorption and migration surface processes on an alpha-Al2O3 surface. *Solid State Commun.* **2005,** *135* (1-2), 90-94.

22. Wijesundara, M. B. J.; Hanley, L.; Ni, B. R.; Sinnott, S. B. Effects of unique ion chemistry on thin-film growth by plasma-surface interactions. *Proceedings of the National Academy of Sciences of the United States of America* **2000,** *97* (1), 23-27.

23. Abrams, C. F.; Graves, D. B. Three-dimensional spatiokinetic distributions of sputtered and scattered products of Ar+ and Cu+ impacts onto the Cu surface: Molecular dynamics simulations. *IEEE Trans. Plasma Sci.* **1999,** *27* (5), 1426-1432.

24. Gou, F.; Chen, L. Z. T.; Meng, C.; Qian, Q. Molecular dynamics simulations of reactive etching of SiC by energetic fluorine. *Appl. Phys. A-Mater. Sci. Process.* **2007,** *88* (2), 385-390.

25. Battaile, C. C.; Srolovitz, D. J.; Butler, J. E. A kinetic Monte Carlo method for the atomic-scale simulation of chemical vapor deposition: Application to diamond. *J. Appl. Phys.* **1997,** *82* (12), 6293-6300.

26. Dawnkaski, E. J.; Srivastava, D.; Garrison, B. J. Growth of diamond films on a diamond {001}(2x1):H surface by time dependent Monte Carlo simulations. *J. Chem. Phys.* **1996,** *104* (15), 5997-6008.

27. Brenner, D. W. Empirical potential for hydrocarbons for use in simulating the chemical vapor-deposition of diamond films. *Phys. Rev. B* **1990,** *42* (15), 9458-9471.

28. Gou, F.; Meng, C. L.; Zhouling, Z. T.; Qian, Q. Hydrocarbon film growth by energetic CH3 molecule impact on SiC (001) surface. *Appl. Surf. Sci.* **2007,** *253* (20), 8517-8523.

29. Stillinger, F. H.; Weber, T. A. Computer-simulation of local order in condensed phases of silicon. *Phys. Rev. B* **1985,** *31* (8), 5262-5271.

30. Pailthorpe, B. A.; Mitchell, D.; Bordes, N. S. Thermal diffusion in molecular dynamics simulations of thin film diamond deposition. *Thin Solid Films* **1998,** *332* (1-2), 109-112.

31. Samela, J.; Nordlund, K.; Keinonen, J.; Popok, V. N. Comparison of silicon potentials for cluster bombardment simulations. *Nucl. Instrum. Methods Phys. Res. B* **2007,** *255*, 253-258.

32. B.A.Helmer; D.B.Graves Molecular dynamics simulations of fluorosilyl species impacting fluorinated silicon surfaces with energies from 0.1 to 100 eV. *Journal of Vacuum Science and Technology A* **1997,** *15*, 2252.

33. Posselt, M.; Gabriel, A. Atomistic simulation of amorphous germanium and its solid phase epitaxial recrystallization. *Phys. Rev. B* **2009,** *80* (4), 045202.

34. Gärtner, K.; Stock, D.; Weber, B.; Betz, G.; Hautala, M.; Hobler, G.; Hou, M.; Arite, S.; Eckstein, W.; Jiménez-Rodríguez, J. J.; Pérez-Martín, A. M. C.; Andribet, E. P.; Konoplev, V.; Gras-Marti, A.; Posselt, M.; Shapiro, M. H.; Tombrello, T. A.; Urbassek, H. M.; Hensel, H.; Yamamura, Y.; Takeuchi, W. Round robin computer simulation of ion transmission through crystalline layers. *Nucl. Instrum. Methods Phys. Res. B* **1995,** *102* (1-4), 183-197.

35. Tersoff, J. New empirical-model for the structural-properties of silicon. *Phys. Rev. Lett.* **1986,** *56* (6), 632-635.

36. Tersoff, J. Empirical interatomic potential for carbon, with applications to amorphous-carbon. *Phys. Rev. Lett.* **1988,** *61* (25), 2879-2882.

37. Brenner, D. W. Empirical potential for hydrocarbons for use in simulating the chemical vapor deposition of diamond films. *Physical Review B* **1990,** *42* (15), 9458.

38. Abell, G. C. Empirical chemical pseudopotential theory of molecular and metallic bonding. *Phys. Rev. B* **1985,** *31* (10), 6184-6196.

39. Ni, B.; Lee, K. H.; Sinnott, S. B. A reactive empirical bond order (REBO) potential for hydrocarbon-oxygen interactions. *J. Phys. : Condens. Matter* **2004,** *16* (41), 7261-7275.

40. Heo, S.; Sinnott, S. B. Computational investigation of the mechanical properties of nanomaterials. Taipei, Taiwan, 2008; pp 438-442.

41. Betz, G.; Husinsky, W. Molecular-Dynamics Studies of Cluster Emission in Sputtering. *Nucl. Instrum. Methods Phys. Res. B* **1995,** *102* (1-4), 281-292.

42. Hsu, W. D.; Jang, I.; Sinnott, S. B. Computational investigation of the chemical modification of polystyrene through fluorocarbon and hydrocarbon ion beam deposition. *Chemistry of Materials* **2006,** *18* (4), 914-921.

43. Hu, Y.; Irving, D. L.; Sinnott, S. B. Ion deposition induced modification of carbon nanopeapods: A computational study. *Chemical physics letters* **2006,** *422* (1), 137-141.

44. Jang, I. K.; Sinnott, S. B. Molecular dynamics simulations of the chemical modification of polystyrene through CxFy+ beam deposition. *J. Phys. Chem. B* **2004,** *108* (49), 18993-19001.

45. Jeong, B. W.; Lim, J. K.; Sinnott, S. B. Tensile mechanical behavior of hollow and filled carbon nanotubes under tension or combined tension-torsion. *Applied Physics Letters* **2007,** *90* (2), 023102.

46. van Duin, A. C. T.; Dasgupta, S.; Lorant, F.; Goddard, W. A. ReaxFF: A reactive force field for hydrocarbons. *J. Phys. Chem. A* **2001,** *105* (41), 9396-9409.

47. Rappe, A. K.; Goddard, W. A. Charge equilibration for molecular-dynamics simulations. *J. Phys. Chem.* **1991,** *95* (8), 3358-3363.

48. Chenoweth, K.; Cheung, S.; van Duin, A. C. T.; Goddard, W. A.; Kober, E. M. Simulations on the thermal decomposition of a poly(dimethylsiloxane) polymer using the ReaxFF reactive force field. *J. Am. Chem. Soc.* **2005,** *127* (19), 7192-7202.

49. van Duin, A. C. T.; Strachan, A.; Stewman, S.; Zhang, Q. S.; Xu, X.; Goddard, W. A. ReaxFF(SiO) reactive force field for silicon and silicon oxide systems. *J. Phys. Chem. A* **2003,** *107* (19), 3803-3811.

50. Cheung, S.; Deng, W. Q.; van Duin, A. C. T.; Goddard, W. A. ReaxFF(MgH) reactive force field for magnesium hydride systems. *J. Phys. Chem. A* **2005,** *109* (5), 851-859.

51. Goddard, W. A.; Zhang, Q.; Uludogan, M.; Strachan, A.; Cagin, T. *The ReaxFF polarizable reactive force fields for molecular dynamics simulation of ferroelectrics*. IOP Institute of physics publishing LTD: 2002; pp 45-55.

52. Ludwig, J.; Vlachos, D. G.; van Duin, A. C. T.; Goddard, W. A. Dynamics of the dissociation of hydrogen on stepped platinum surfaces using the ReaxFF reactive force field. *J. Phys. Chem. B* **2006,** *110* (9), 4274-4282.

53. Liu, B.; Lusk, M. T.; Ely, J. F.; van Duin, A. C. T.; Goddard, W. A. Reactive molecular dynamics force field for the dissociation of light hydrocarbons on Ni(111). *Molecular Simulation* **2008,** *34* (10-15), 967-972.

54. Jarvi, T. T.; Kuronen, A.; Hakala, M.; Nordlund, K.; van Duin, A. C. T.; Goddard III, W. A.; Jacob, T. Development of a ReaxFF description for gold. *The European Physical Journal B* **2008,** *66* (1), 75-79.

55. Chenoweth, K.; van Duin, A. C. T.; Goddard, W. A. ReaxFF reactive force field for molecular dynamics simulations of hydrocarbon oxidation. *J. Phys. Chem. A* **2008,** *112* (5), 1040-1053.

56. Chenoweth, K.; van Duin, A. C. T.; Persson, P.; Cheng, M. J.; Oxgaard, J.; Goddard, W. A. Development and application of a ReaxFF reactive force field for oxidative dehydrogenation on vanadium oxide catalysts. *J. Phys. Chem. C* **2008,** *112* (37), 14645-14654.

57. Nielson, K. D.; van Duin, A. C. T.; Oxgaard, J.; Deng, W. Q.; Goddard, W. A. Development of the ReaxFF reactive force field for describing transition metal catalyzed reactions, with application to the initial stages of the catalytic formation of carbon nanotubes. *J. Phys. Chem. A* **2005,** *109* (3), 493-499.

58. Yu, J. G.; Phillpot, S. R.; Sinnott, S. B. Interatomic potential for the structure and energetics of tetrahedrally coordinated silica polymorphs. *Phys. Rev. B* **2007,** *75* (23), 233203.

59. Yu, J. G.; Sinnott, S. B.; Phillpot, S. R. Charge optimized many-body potential for the Si/SiO2 system. *Phys. Rev. B* **2007,** *75* (8), 085311.

60. Yasukawa, A. Using an extended Tersoff interatomic potential to analyze the static-fatigue strength of SiO2 under atmospheric influence. *Jsme International Journal Series A-Mechanics and Material Engineering* **1996,** *39* (3), 313-320.

61. Huang, L. P.; Kieffer, J. Molecular dynamics study of cristobalite silica using a charge transfer three-body potential: Phase transformation and structural disorder. *J. Chem. Phys.* **2003,** *118* (3), 1487-1498.

62. Huang, L. P.; Durandurdu, M.; Kieffer, J. Transformation pathways of silica under high pressure. *Nature Materials* **2006,** *5* (12), 977-981.

63. Huang, L. P.; Kieffer, J. Thermomechanical anomalies and polyamorphism in B_2O_3 glass: A molecular dynamics simulation study. *Phys. Rev. B* **2006,** *74* (22), 224107.

64. Huang, L. P.; Durandurdu, M.; Kieffer, J. New B_2O_3 crystals predicted from concurrent molecular dynamics simulations and first-principles calculations. *J. Phys. Chem. C* **2007,** *111* (37), 13712-13720.

65. Huang, L.; Nicholas, J.; Kieffer, J.; Bass, J. Polyamorphic transitions in vitreous B_2O_3 under pressure. *J. Phys. : Condens. Matter* **2008,** *20* (7), 075107.

66. Bhattacharya, S.; Kieffer, J. Fractal dimensions of silica gels generated using reactive molecular dynamics simulations. *J. Chem. Phys.* **2005,** *122* (9), 094715.

67. Bhattacharya, S.; Kieffer, J. Fractal dimensions of silica gels generated using reactive molecular dynamics simulations. *The Journal of chemical physics* **2005,** *122* (9), 094715.

68. Huang, L. P.; Kieffer, J. Amorphous-amorphous transitions in silica glass. II. Irreversible transitions and densification limit. *Phys. Rev. B* **2004,** *69* (22), 224204.

69. Huang, L. P.; Kieffer, J. Amorphous-amorphous transitions in silica glass. I. Reversible transitions and thermomechanical anomalies. *Phys. Rev. B* **2004,** *69* (22), 224203.

70. Zhou, J.; Kieffer, J. Molecular dynamics simulations of monofunctionalized polyhedral oligomeric silsesquioxane C6H13(H7Si8O 12). *Journal of Physical Chemistry C* **2008,** *112* (10), 3473-3481.

71. Gilmore, C. M.; Sprague, J. A. Molecular-dynamics simulation of the energetic deposition of Ag thin films. *Phys. Rev. B* **1991,** *44* (16), 8950-8957.

72. Sprague, J. A.; Gilmore, C. M. Molecular dynamics simulations of film-substrate interface mixing in the energetic deposition of fcc metals. *Thin Solid Films* **1996,** *272* (2), 244-254.

73. Schwebel, C.; Pellet, C.; Gautherin, G. Angular distributions of heavy particles emitted from a Si target during an ion beam sputter process. *Nuclear Instruments and Methods in Physics Research Section B: Beam Interactions with Materials and Atoms* **1986,** *18* (1), 525-528.

74. Tarus, J.; Nordlund, K. Molecular dynamics study on Si20 cluster deposition on Si(001). *Nuclear Instruments and Methods in Physics Research Section B: Beam Interactions with Materials and Atoms* **2003,** *212* (0), 281-285.

75. Biswas, R.; Grest, G. S.; Soukoulis, C. M. Molecular-dynamics simulation of cluster and atom deposition on silicon (111). *Phys. Rev. B* **1988,** *38* (12), 8154-8162.

76. Betz, G.; Husinsky, W. A combined molecular dynamics and kinetic Monte Carlo calculation to study sputter erosion and beam assisted deposition. *Nuclear Instruments and Methods in Physics Research Section B: Beam Interactions with Materials and Atoms* **2002,** *193* (1-4), 352-358.

77. Ju, S. P.; Weng, C. I.; Chang, J. G.; Hwang, C. C. A molecular dynamics study of deposition rate dependence of film morphology in the sputtering process. *Surface and Coatings Technology* **2002,** *149* (2-3), 135-142.

78. Hu, Y.; Sinnott, S. B. A molecular dynamics study of thin-film formation via molecular cluster beam deposition: effect of incident species. *Surface Science* **2003,** *526* (3), 230-242.

79. Hui Qing Lan; Zheng Ling Kang Molecular Dynamics Simulations of Structures of Amorphous Carbon Films via Deposition. *Advanced Materials Research* **2011,** *194-196*, 2220-2224.

80. Chen, H.; Hagiwara, I.; Kiet Tieu, A.; Kishimoto, K.; Liu, Q. Theoretical investigation about secondary deposition of thin-film formation by molecular dynamics simulation. *Journal of Crystal Growth* **2007,** *303* (2), 530-536.

81. Ishikawa, Y.; Mateo, J. J.; Tryk, D. A.; Cabrera, C. R. Direct molecular dynamics and density-functional theoretical study of the electrochemical hydrogen oxidation reaction and underpotential deposition of H on Pt (111). *Journal of Electroanalytical Chemistry* **2007,** *607* (1), 37-46.

82. Zaminpayma, E.; Nayebi, P.; Mirabbaszadeh, K. A Study About Nanocluster Deposition of Thin-film Formation by Molecular Dynamics Simulation. *J Clust Sci* **2008,** *19* (4), 623-629.

83. Lee, S. G.; Choi, H.; Chung, Y. C. Molecular dynamics simulation of film growth characterization of Fe and Cu on Cu(111) surface in the early stages of the deposition process. *Current Applied Physics* **2011,** *11 (4, Supplement)*, S65-S68.

84. Zhang, H.; Xia, Z. N. Molecular dynamics simulation of cluster beam Al deposition on Si (100) substrate. *Nuclear Instruments and Methods in Physics Research Section B: Beam Interactions with Materials and Atoms* **2000,** *160* (3), 372-376.

85. Fang, T. H.; Chang, W. J.; Lin, C. M.; Lien, W. C. Molecular dynamics and experimental studies on deposition mechanisms of ion beam sputtering. *Applied Surface Science* **2008,** *254* (11), 3436-3441.

86. Tomasch, G. A.; Kim, Y. W.; Markert, L. C.; Lee, N. E.; Greene, J. E. Growth of homoepitaxial Ge(001)2 x 1 by ultrahigh vacuum ion beam sputter deposition. *Thin Solid Films* **1993,** *223* (2), 212-217.

87. K.Miyake; K.Ohashi Superior Corrosion Resistance of Ion Beam Deposited Iron Film. *Japanese Journal of Applied Physics* **1993,** *32*, L120.

88. Jimenez-Saez, J. C.; Perez-Martin, A. M. C.; Said-Ettaoussi, M.; Jiménez-Rodríguez, J. J. Molecular dynamics simulation of Ni cluster deposition on Cu(0 0 1) surfaces. *Nuclear Instruments and Methods in Physics Research Section B: Beam Interactions with Materials and Atoms* **2005,** *228* (1-4), 64-68.

89. Bunnik, B. S.; de Hoog, C.; Haddeman, E. F. C.; Thijsse, B. J. Molecular dynamics study of Cu deposition on Mo and the effects of low-energy ion irradiation. *Nuclear Instruments and Methods in Physics Research Section B: Beam Interactions with Materials and Atoms* **2002,** *187* (1), 57-65.

90. Raizer, Y. P.; Kisin, V. I.; Allen, J. E. *Gas discharge physics;* 1 ed.; Springer-Verlag Berlin: 1991.pp. 1-449.

91. Baumjohann, W.; Treumann, R. A. *Basic space plasma physics;* World Scientific: 1997.pp. 1-340.

92. Fukushima, K.; Kusano, E.; Kikuchi, N.; Saito, T.; Saiki, S.; Nanto, H.; Kinbara, A. Ion fraction and energy distribution of Ti flux incident to substrate surface in RF-plasma enhanced magnetron sputtering. *Vacuum* **2000,** *59* (2-3), 586-593.

93. Chiba, Y.; Kashiwagi, K.; Kokai, H. Plasma surface treatment effect of TiO2 thin film. *Vacuum* **2004,** *74* (3-4), 643-646.

94. Wan, G. J.; Yang, P.; Fu, R. K. Y.; Mei, Y. F.; Qiu, T.; Kwok, S. C. H.; Ho, J. P. Y.; Huang, N.; Wu, X. L.; Chu, P. K. Characteristics and surface energy of silicon-doped diamond-like carbon films fabricated by plasma immersion ion implantation and deposition. *Diamond and Related Materials* **2006,** *15* (9), 1276-1281.

95. Zhang, X.; Huang, Y.; Wang, T. Surface analysis of plasma grafted carbon fiber. *Applied Surface Science* **2006,** *253* (5), 2885-2892.

96. Rai, P.; Park, J. S.; Park, G. G.; Lee, W. M.; Yu, Y. T.; Kang, S. K.; Moon, S. Y.; Hong, B. G. Influence of carbon precursors on thermal plasma assisted synthesis of SiC nanoparticles. *Advanced Powder Technology* **2014,** *25* (2), 640-646.

97. Zalm, P. C. Ultra shallow doping profiling with SIMS. *Rep. Prog. Phys.* **1995,** *58*, 1321.

98. Zalm, P. C. Secondary ion mass spectrometry. *Vacuum* **1996,** *45(6/7)*, 753.

99. Behrisch, R.; Eckstein, W. Introduction and Overview. In *Sputtering by Particle Bombardment*, Rainer Behrisch, Wolfgang Eckstein, Eds.; Springer: 2006; pp 1-20.

100. P.Sigmund Sputtering by ion bombardment theoretical concepts. In *Sputtering by Particle Bombardment I, Top. Appl. Phys. 47*, Rainer Behrisch, Ed.; Springer: Berlin, Heidelberg, 1981.

101. P.Sigmund Fundamental Processes in Sputtering of Atoms and molecules (SPUT92). *K. Dan. Vidensk. Selsk. Mat. Fys. Medd.* **1993,** *43*.

102. Wilson, R. G.; Stevie, F. A.; Magee, C. W. *Secondary Ion Mass Spectrometry: A Practical Handbook for Depth Profiling and Bulk Impurity Analysis;* John Wiley & Sons, Inc: 1989.

103. Guzman de la Mata, B.; Dowsett, M. G.; Twitchen, D. Sputter yields in diamond bombarded by ultra low energy ions. *Applied Surface Science* **2006,** *252* (19), 6444-6447.

104. K.Rodelsperger; A.Scharmann Angular distribution measurements of sputtered atoms with characteristic X-ray emission. *Nuclear Instruments and Methods in Physics Research Section B* **1976,** *132*, 355-362.

105. G.Brauer; D.Hasselkamp; W.Kruger; A.Scharmann The angular distribution of particles sputtered from Cu, Zr, and Au surfaces by ion bombardment at grazing incidence. *Nuclear Instruments and Methods in Physics Research Section B* **1985,** *12*, 458-463.

106. W.Kruger; A.Scharmann; H.Afridi; G.Brauer Application of pixe to the measurement of sputter deposits. *Nuclear Instruments and Methods Physics Research Section B* **1980,** *168*, 411-414.

107. Wolfgang O.Hofer Angular, Energy, and Mass Distribution of Sputtered particles. In *Topics in Applied Physics*, R.Behrisch, K.Wittmaack, Eds.; Springer-Verlag: 1991; Vol. 64.

108. Lee, C. S.; Liu, Y. C.; Chen, Y. H.; Lee, S. Angular distribution of sputtered particles induced by ion bombardment. *Nuclear Instruments and Methods in Physics Research Section B: Beam Interactions with Materials and Atoms* **2004,** *219-220* (0), 221-225.

109. Wirtz, T.; Migeon, H. N. Storing Matter: A new quantitative and sensitive analytical technique. *Applied Surface Science* **2008,** *255* (4), 1498-1500.

110. Philipp, P.; Douhard, B.; Lacour, F.; Wirtz, T.; Houssiau, L.; Pireaux, J. J.; Migeon, H. N. The Storing Matter technique: Preliminary results on PS and PVC. *Appl. Surf. Sci.* **2008,** *255* (4), 866-869.

111. Becker, N.; Mansilla, C.; Wirtz, T.; Migeon, H. N. The Storing Matter technique applied to PVC: Effect of the primary ion fluence on the sputter-deposition. *Nucl. Instrum. Methods Phys. Res. B* **2011,** *269* (9), 1029-1031.

112. Becker, N.; Wirtz, T.; Migeon, H. N. The Storing Matter technique: Application to PVC using Au and Ag collectors. *Surf. Interface Anal.* **2011,** *43* (1-2), 502-505.

113. Mansilla, C.; Wirtz, T.; Verdeil, C. Study of the useful yield of the Storing Matter technique using Ge(100) as a sputter target. *Nuclear Instruments and Methods in Physics Research Section B: Beam Interactions with Materials and Atoms* **2009,** *267* (16), 2589-2591.

114. Mansilla, C.; Wirtz, T. Application of the Storing Matter technique to the analysis of semiconductor materials. *J. Vac. Sci. Technol. B* **2010,** *28* (1), C1C71-C1C76.

115. Mansilla, C.; Wirtz, T. Storing Matter: a new analytical technique developed to improve the sensitivity and the quantification during SIMS analyses. *Surf. Interface Anal.* **2010,** *42* (6-7), 1135-1139.

116. G.Slodzian Enveloppe Soleau No. 13852 deposited by Cameca. on behalf of G.Slodzian, Ed.; 1998.

117. Becker, N.; Wirtz, T.; Migeon, H. N. The Storing Matter technique: Application to polymer samples using Ag collectors. *Surf. Interface Anal.* **2011,** *43* (1-2), 413-416.

118. Mansilla, C.; Wirtz, T. Application of the storing matter technique to the analysis of boron doped and implanted SiO2/Si. *Applied Surface Science* **2012,** *258* (10), 4813-4818.

119. D.C.Rapaport *The art of molecular dynamics simulation;* Cambridge University Press: 2004.

120. Ewald, P. P. Die Berechnung optischer und elektrostatischer Gitterpotentiale. *Ann. Phys.* **1921,** *369* (3), 253-287.

121. L.Angibaud; L.Briquet; P.Philipp; T.Wirtz; J.Kieffer Parameter optimization in molecular dynamics simulations using a genetic algorithm. *Nuclear Instruments and Methods in Physics Research B* **2011,** *269*, 1559-1563.

122. Briquet, L. G. V.; Jana, A.; Mether, L.; Nordlund, K.; Henrion, G.; Philipp, P.; Wirtz, T. Reactive force field potential for carbon deposition on silicon surfaces. *J. Phys. : Condens. Matter* **2012,** *24* (39), 395004.

123. L.G.V.Briquet; T.Wirtz; P.Philipp First principles investigation of Ti adsorption and migration on Si (100) surfaces. *Journal of Applied Physics* **2013,** *114*, 243505.

124. Briquet, L. G. V.; Philipp, P. First principles investigation of the electronic, elastic and vibrational properties of tungsten disilicide. *Journal of Alloys and Compounds* **2013,** *553* (0), 93-98.

125. Johlin, E. C.; Wagner, L.; Grossman, J. C.; Riley, J. Amorphous Silicon Generator. *http://nanohub. org/resources/asilicon. (DOI: 10. 4231/D30K26B35).* **2013**.

126. Wooten, F.; Winer, K.; Weaire, D. Computer generation of structural models of amorphous Si and Ge. *Physical Review Letters* **1985,** *54* (13), 1392-1395.

127. Bendler, B.; Barrahma, R.; Philipp, P.; Wirtz, T. New neutral cesium evaporation chamber and UHV suitcase. *Surf. Interface Anal.* **2011,** *43* (1-2), 514-517.

128. Cameca IMS6f user manual.
Ref Type: Generic

129. Secondary ion mass spectrometry (SIMS). *School of Geosciences,University of Edinburgh, http://www. geos. ed. ac. uk/facilities/ionprobe/SIMS4. pdf* **2014**.

130. Raineri, V.; Privitera, V.; Galvagno, G.; Priolo, F.; Rimini, E. Channeling implants in silicon crystals. *Materials Chemistry and Physics* **1994,** *38* (2), 105-130.

131. Negoro, Y.; Kimoto, T.; Kataoka, M.; Takeuchi, Y.; Malhan, R. K.; Matsunami, H. Embedded epitaxial growth of 4H-SiC on trenched substrates and pn junction characteristics. *Microelectronic Engineering* **2006,** *83* (1 SPEC. ISS.), 27-29.

132. Gao, F.; Du, J.; Bylaska, E. J.; Posselt, M.; Weber, W. J. Ab Initio atomic simulations of antisite pair recovery in cubic silicon carbide. *Applied Physics Letters* **2007,** *90* (22), 221915.

133. Casady, J. B.; Johnson, R. W. Status of silicon carbide (SiC) as a wide-bandgap semiconductor for high-temperature applications: A review. *Solid-State Electronics* **1996,** *39* (10), 1409-1422.

134. Agueev, O. A.; Svetlichny, A. M.; Izotovs, D. A.; Melnikov, A. V.; Voronko, A. B. Temperature dependence simulation of electrophysical properties of silicon carbide. *ASDAM Int. Conf.*, **2000**; proc. pp 295-298.

135. Fuchs, F.; Soltamov, V. A.; Väth, S.; Baranov, P. G.; Mokhov, E. N.; Astakhov, G. V.; Dyakonov, V. Silicon carbide light-emitting diode as a prospective room temperature source for single photons. *Sci. Rep.* **2013,** *3* (1637).

136. http://code.google.com/p/debyer/

137. Bendler, B.; Philipp, P.; Wirtz, T. Neutral cesium deposition prior to SIMS depth profiling - preliminary results on organic samples. *Surf. Interface Anal.* **2013,** *45* (1), 57-60.

138. Filipovic, L.; Selberherr, S. A Two-Dimensional Lorentzian Distribution for an Atomic Force Microscopy Simulator. In *Monte Carlo Methods and Applications*, Sabelfeld, K. K., Dimov, I., Eds.; De Gruyter: 2012; pp 97-104.

139. Biersack, J. P.; Haggmark, L. G. A Monte Carlo program for the transport of energetic ions in amorphous targets. *Nucl. Instrum. Methods* **1980,** *174*, 257.

140. Biersack, J. P.; Eckstein, W. Sputtering studies with the Monte Carlo program TRIM.SP. *Appl. Phys. A-Matter* **1984,** *34*, 73.

Collage et adhérence de particules dans le domaine de la sous-monocouche

Résumé

Au cours d'un traitement de surface de type dépôt assisté par plasma, les caractéristiques et propriétés de l'interface entre le dépôt et le substrat sont déterminées par la première couche atomique du dépôt, voire les premiers atomes qui commencent à recouvrir la surface du substrat. Aussi, la parfaite connaissance du comportement des particules incidentes et du réarrangement des atomes suite à l'impact d'une particule du plasma est-elle un élément essentiel à la description du comportement de la surface en cours de traitement et donc de ses propriétés ultérieures. Au cours de cette thèse, nous avons entrepris d'étudier, par une approche combinant expériences et simulation numérique par dynamique moléculaire, l'interaction d'espèces (C, Ti, W) avec une surface de silicium en fonction de paramètres tels que l'énergie, la fluence ou encore l'incidence des particules arrivant sur la surface. Une part importante de ce travail a consisté à adapter les codes de dynamique moléculaire (utilisation des champs de force réactifs) aux systèmes étudiés. La partie expérimentale a nécessité la mise en place de procédures spécifiques pour l'utilisation de l'équipement *Storing Matter*. Les résultats montrent que, quelles que soient l'espèce incidente, parmi celles étudiées, le coefficient de collage (SC) est dans la gamme [0.7 – 1] ; dans le cas de W, quasiment tous les atomes incidents restent sur la surface (SC≈1). Outre la détermination du coefficient de collage, pour différentes conditions initiales des espèces incidentes (énergie, incidence, fluence) les modifications apportées à la surface ont également été déterminées en termes d'implantation et de trajectoire dans le matériau des espèces incidentes, et de pulvérisation de la surface du substrat.

Mots-Clés : Dynamique moléculaire, coefficient de collage, SIMS, Storing Matter, sous-monocouche.

Sticking and deposition of atoms in the sub-monolayer range

Abstract

During plasma assisted deposition, properties of the coating substrate interface depend on the first atomic layer of the deposit, or the atoms that first start to cover the surface. Therefore the good knowledge of the sticking coefficient and the reorganization of the surface following particle impact is an essential issue to achieve the description of the behavior of the processed surface and, therefore, its expected properties. Consequently, we investigated the interaction between incoming particles (C, Ti, W) and a silicon surface by using an approach combining molecular dynamic simulations and experiments. Various initial conditions were studied, energy, fluence and incidence angle of the incoming particles. An important part of this work has consisted in adapting the molecular dynamic codes (using reactive force fields) to the investigated systems. Meanwhile, experimental procedure specifically devoted to the use of the *Storing Matter* facility was also developed. Results show that the sticking coefficient (SC) value is in the range [0.7 – 1] irrespectively of the incoming species; in the case of W, almost all atoms stick on the surface (SC≈1). Besides the determination of sticking coefficient, the surface modification resulting from the particles impingement were determined for various initial conditions (energy, fluence, angle) in terms of implantation and displacement of the incoming species, and surface sputtering as well.

Keywords: Molecular dynamic simulations, sticking coefficient, SIMS, Storing matter, Sub monolayer.